Measurement of the top quark mass in the all-jets final state at $\sqrt{s} = 13\,\text{TeV}$ and combination with the lepton+jets channel

Dissertation
zur Erlangung des Doktorgrades

an der Fakultät für
Mathematik, Informatik und Naturwissenschaften

Fachbereich Physik
der Universität Hamburg

vorgelegt von

Johannes Lange

Hamburg
2020

Gutachter der Dissertation:	Prof. Dr. Peter Schleper
	Dr. Christian Schwanenberger
Zusammensetzung der Prüfungskommission:	PD Dr. Andreas Meyer
	Prof. Dr. Arwen Pearson
	Prof. Dr. Peter Schleper
	Dr. Christian Schwanenberger
	Prof. Dr. Géraldine Servant
Vorsitzende der Prüfungskommission:	Prof. Dr. Arwen Pearson
Datum der Disputation:	04.03.2020
Vorsitzender des Fach-Promotionsausschusses PHYSIK:	Prof. Dr. Günter Hans Walter Sigl
Leiter des Fachbereichs PHYSIK:	Prof. Dr. Wolfgang Hansen
Dekan der Fakultät MIN:	Prof. Dr. Heinrich Graener

Abstract

A measurement of the top quark mass using LHC proton-proton collision data with an integrated luminosity of $35.9\,\mathrm{fb}^{-1}$ is presented. The dataset has been recorded with the CMS detector in LHC Run 2 at a center-of-mass energy of 13 TeV in the 2016 data taking period.

Events are selected in which a top quark and a top antiquark are produced and both decay exclusively to jets. This $\mathrm{t\bar{t}}$ all-jets final state is characterized by six jets in the detector and therefore contaminated by multijet background, which is estimated from data in a control region. A kinematic fit is utilized to reconstruct the full $\mathrm{t\bar{t}}$ system, improving the invariant mass resolution for the top quark candidates and at the same time reducing the multijet background by requiring a goodness-of-fit criterion. The top quark mass is extracted using the ideogram method, simultaneously constraining an additional jet energy scale factor (JSF) to reduce systematic uncertainties. The top quark mass is found to be $m_{\mathrm{t}} = 172.34 \pm 0.20\,(\mathrm{stat{+}JSF}) \pm 0.70\,(\mathrm{syst})\,\mathrm{GeV}$, agreeing well with previous measurements.

Furthermore, a combined top quark mass measurement using the all-jets and lepton+jets final states simultaneously is performed. For this, a combined likelihood including the events of both final states is constructed and the same mass extraction is applied as for the all-jets final state. The resulting measurement is $m_{\mathrm{t}} = 172.26 \pm 0.07\,(\mathrm{stat{+}JSF}) \pm 0.61\,(\mathrm{syst})\,\mathrm{GeV}$. This is the first time a top quark mass measurement combining both final states in a single likelihood function is presented. The result is consistent with other measurements at the LHC.

A global electroweak fit employing this measurement shows the importance of the top quark mass for consistency checks of the standard model of particle physics.

Kurzfassung

Es wird eine Messung der Topquarkmasse vorgestellt, für die LHC-Proton-Proton-Kollisionsdaten aus Run 2 verwendet werden. Der Datensatz mit einer integrierten Luminosität von 35.9 fb^{-1} wurde 2016 mit dem CMS-Detektor bei einer Schwerpunktsenergie von 13 TeV aufgezeichnet.

Es werden Ereignisse selektiert, in denen ein Topquark und ein Topantiquark produziert werden und beide ausschließlich zu Jets zerfallen. Dieser voll-hadronische $\mathrm{t\bar{t}}$-Endzustand wird duch sechs Jets im Detektor charakterisiert und ist daher von Multijet-Untergrund kontaminiert, welcher aus Daten in einer Kontrollregion abgeschätzt wird. Ein kinematischer Fit wird genutzt, um das gesamte $\mathrm{t\bar{t}}$-System zu rekonstruieren. Durch diesen wird die Auflösung der invarianten Masse der Topquarkkandidaten verbessert und gleichzeitig kann der Multijet-Untergrund reduziert werden, indem ein Fitgütekriterium angewandt wird. Die Topquarkmasse wird mittels der Ideogrammmethode extrahiert, während gleichzeitig ein zusätzlicher Jet-Energie-Skalierungsfaktor (JSF) eingeschränkt wird, um systematische Unsicherheiten zu reduzieren. Die Bestimmung der Topquarkmasse liefert $m_{\mathrm{t}} = 172.34 \pm 0.20\,(\mathrm{stat+JSF}) \pm 0.70\,(\mathrm{syst})$ GeV, was in guter Übereinstimmung mit früheren Messungen ist.

Des Weiteren wird eine kombinierte Messung der Topquarkmasse durchgeführt, bei der der voll-hadronische und der lepton+jets-Zerfallskanal simultan verwendet werden. Dazu wird eine kombinierte Likelihoodfunktion konstruiert, die die Ereignisse aus beiden Zerfallskanälen enthält. Die Massenextraktion wird wie für den voll-hadronischen Endzustand angewandt. Die resultierende Messung ergibt $m_{\mathrm{t}} = 172.26 \pm 0.07\,(\mathrm{stat+JSF}) \pm 0.61\,(\mathrm{syst})$ GeV. Dies ist das erste Mal, dass eine Messung der Topquarkmasse präsentiert wird, bei der beide Endzustände in einer einzelnen Likelihoodfunktion kombiniert wurden. Das Ergebnis ist konsistent mit anderen Messungen am LHC.

Ein globaler elektroschwacher Fit, für den diese Messung verwendet wird, zeigt wie wichtig die Topquarkmasse für Konsistenztests des Standardmodells der Teilchenphysik ist.

List of publications

During the research work in the years of my doctoral studies at the University of Hamburg, I have been the (main) author of the following publications, which are based on the results presented in this dissertation.

- CMS Collaboration, "Measurement of the top quark mass in the all-jets final state at $\sqrt{s} = 13$ TeV", CMS Physics Analysis Summary CMS-PAS-TOP-17-008, 2018.
- J. Lange (on behalf of the CMS Collaboration), "Top quark mass measurement in the $\mathrm{t\bar{t}}$ all-jets final state with the CMS experiment at $\sqrt{s} = 13\,\mathrm{TeV}$", in *Proceedings of the 11th International Workshop on Top Quark Physics (TOP2018) Bad Neuenahr, Germany, September 16-21, 2018 (SLAC eConf C1809161)*, `arXiv:1812.05394`.
- CMS Collaboration, "Measurement of the top quark mass in the all-jets final state at $\sqrt{s} = 13$ TeV and combination with the lepton+jets channel", *Eur. Phys. J. C* **79** (2019) 313, `doi:10.1140/epjc/s10052-019-6788-2`, `arXiv:1812.10534`.

In addition, these experiment-internal documents have been prepared:

- J. Lange, C. Garbers, N. Kovalchuk, P. Schleper, H. Stadie, F. Stober, and D. Lincoln, "Measurement of the top quark mass in the all-jets final state at 13 TeV", CMS Analysis Note CMS AN-2017/064 v10 [CMS internal], 2017.
- J. Lange, C. Garbers, N. Kovalchuk, P. Schleper, H. Stadie, F. Stober, and D. Lincoln, "Combined measurement of the top quark mass in the lepton+jets and all-jets final states at 13 TeV", CMS Analysis Note CMS AN-2018/076 v9 [CMS internal], 2018.

Contents

1

Introduction

Chapter contents

In this thesis, a measurement of the top quark mass (m_t) is presented using proton-proton collision data recorded with the CMS detector at the CERN LHC in 2016 at a center-of-mass energy of 13 TeV. The results presented here have been published by the CMS Collaboration [1] and presented as a preliminary result [2]. While both of these documents have mainly been written by the author of this thesis, several people within the CMS Collaboration have been involved in the review of the analysis and the presented documents. Furthermore, a summary has been prepared for a conference report [3]. Experiment-internal analysis notes (ANs), only accessible for collaboration members, have also been created [4, 5]. Figures and tables which are exactly those contained in Ref. [1] are referenced in the caption[1]. In addition, the plots contain a "CMS" label.

The sections of Chapter 1 contain an overview of the standard model of particle physics with a focus on the role of the top quark, its production in proton-proton collisions, and the different decay modes. Also, previous measurements of the top quark mass are discussed.

In Chapter 2, the experimental setup including the LHC and the CMS detector are described. Chapter 3 contains a description of the event reconstruction and the Monte-Carlo event simulation.

The actual analysis is presented in Chapters 4 and 5. Chapter 4 is about the top quark mass measurement in the all-jets channel, including the event selection, a kinematic fit, the background estimation, the m_t extraction, and the determination of the systematic uncertainties. In Chapter 5, a combined measurement using $\mathrm{t\bar{t}}$ all-jets and lepton+jets events is presented, which is performed using a single combined likelihood. In addition, the result is compared to BLUE combinations.

---

[1] In accordance with the recommendations of the *Konferenz der Fachbereiche Physik*: "Gute wissenschaftliche Praxis bei wissenschaftlichen Qualifikationsarbeiten in der Physik" / "Good scientific practice for scientific qualification reports and theses in physics" (18th May 2016)

The result of the top quark mass measurement is interpreted in terms of a global electroweak fit in Chapter 6. A summary of the measurements presented in this thesis is given in Chapter 7, as well as an outlook for possible future versions of the top quark mass measurement.

1.1 The standard model of particle physics

The most successful model for the interaction of fundamental particles is the standard model of particle physics (SM). It includes electromagnetic, weak, and strong interactions, which are described using quantum field theory. Gravitation is the only known force not included in the SM, which is described by general relativity. It is weak compared to the other interactions and thus negligible at typical energy scales and distances described using quantum field theories, like high-energy particle collisions. However, several models beyond the standard model (BSM) attempt to unify all interactions in a single theory, requiring a relativistic quantum theory of gravitation.

Although the SM cannot be a complete model of nature, its predictions are verified in a multitude of measurements, the latest being the discovery of the Higgs boson in 2012 by the CMS and ATLAS experiments at the LHC [6–9]. The most striking evidence that the SM is incomplete are astrophysical observations requiring the existence of dark matter (DM) [10, 11], which is interacting gravitationally, but neither electromagnetically nor strongly. It is estimated that a quarter of the energy density in the universe consists of DM [12], which cannot be explained with the particle content of the SM. However, since no direct evidence for BSM particles or interactions could be observed at the LHC yet, precision tests of the SM are important to potentially find inconsistencies hinting at possible directions for needed extensions of the SM.

In the following, a unit system is used in which the speed of light and the reduced Planck constant are set to unity ($c = \hbar = 1$), called natural unit system of particle physics. In this system, units are given in powers of the energy unit eV, or more commonly in GeV for energy scales in collider physics. Energies and momenta thus share the same dimension and become equal in the high-energy limit.

The particles in the SM are categorized as fermions, carrying half-integer spin in units of $\hbar$, and bosons, carrying integer spin. A summary of the SM particle content is shown in Fig 1.1. The fermions are ordered in three generations, where only the first one is making up ordinary matter, while the second and third generation are heavier copies of the particles of the first generation. Charged leptons carry electrical charges of $-1\mathrm{e}$, where e is the elementary electrical charge, while the neutrinos are electrically neutral. The quarks carry electrical charges of $+2/3\mathrm{e}$ (up-type) or $-1/3\mathrm{e}$ (down-type). In addition they possess color charge, i.e., they take part in the strong interactions. For each fermion there is an antifermion, having opposite charges. In the case of neutrinos, it is yet an open questions whether they are Dirac fermions, i.e., possess an antiparticle, or if they are Majorana particles, meaning that the neutrino is its own antiparticle.

The spin-1 vector bosons are the force carriers. Gluons mediate the strong force between quarks and gluons themselves. The photon is responsible for the electromagnetic force between electrically charged particles and the $\mathrm{W}^{\pm}$ and Z^{0} bosons mediate the weak

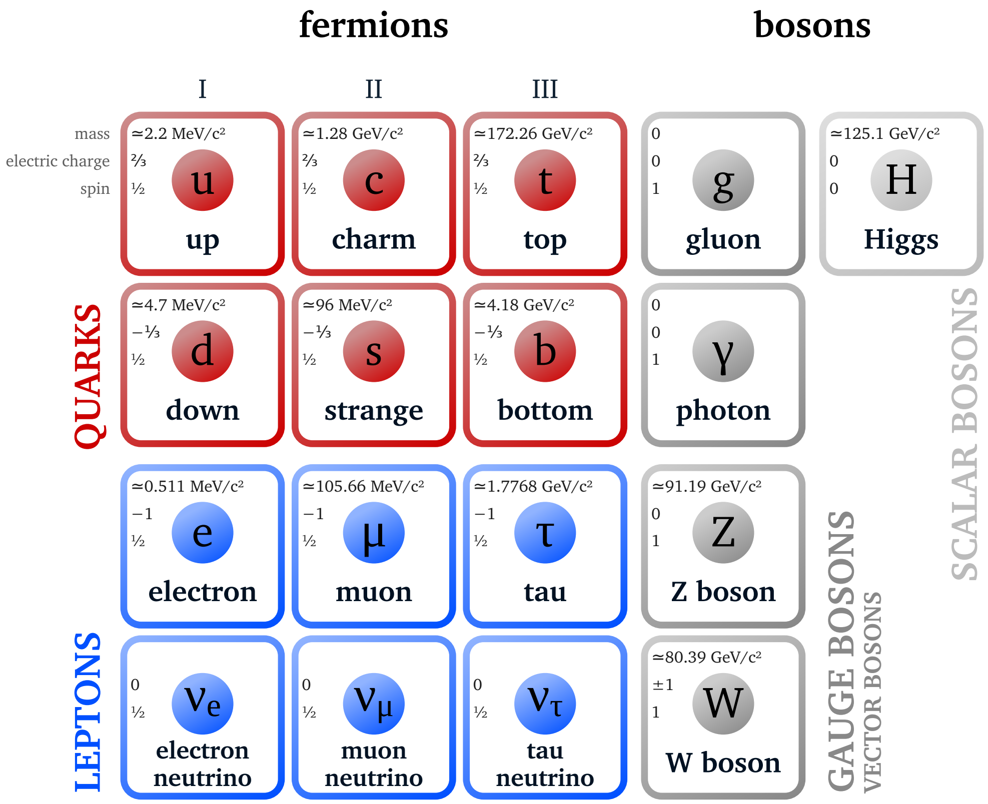

Figure 1.1: Particle content of the standard model of particle physics. Modified from Ref. [13]. The result of the top quark mass measurement presented in Chapter 5 is displayed here.

force. The spin-0 Higgs boson is a manifestation of the electroweak symmetry-breaking mechanism in the SM responsible for generating particle masses.

All elementary particles in the SM are described as quantum fields. Formally, it is a locally gauge invariant quantum field theory based on the $\mathrm{SU}(3)_{\mathrm{C}}\times\mathrm{SU}(2)_{\mathrm{L}}\times\mathrm{U}(1)_{\mathrm{Y}}$ gauge group. The structure of the interactions of the fields ϕ is encoded in a Lagrangian density $\mathcal{L}$ and the dynamics, i.e., the equations of motion are given by the Euler-Lagrange equations

$$\partial_{\mu}\left(\frac{\partial\mathcal{L}}{\partial\left(\partial_{\mu}\phi\right)}\right)=\frac{\partial\mathcal{L}}{\partial\phi}.$$

The strong interactions, based on the $\mathrm{SU}(3)_{\mathrm{C}}$ group, are described by quantum chromodynamics (QCD). They are mediated by gluons. All particles in the SM carrying color charge take part in this interaction, i.e., the quarks and the gluons themselves. The eight massless gluons carry color and anticolor. Particles with net color charge cannot exist freely and thus form hadrons, which are color neutral bound states. Quarks and gluons produced in particle collisions with high momenta will form pairs of quarks and antiquarks and further gluons that finally arrange to hadrons. These are mostly collimated and can be observed as hadronic jets.

The $\mathrm{SU}(2)_{\mathrm{L}}\times\mathrm{U}(1)_{\mathrm{Y}}$ group is related to the electroweak sector, which unifies the electromagnetic and weak interactions. The gauge eigenstates are the W^1, W^2, W^3, and B bosons, while the observable mass eigenstates γ, Z^0, and $\mathrm{W}^\pm$ are given by

$$\begin{bmatrix} \gamma \\ \mathrm{Z}^0 \end{bmatrix} = \begin{bmatrix} \cos\theta_W & \sin\theta_W \\ -\sin\theta_W & \cos\theta_W \end{bmatrix} \begin{bmatrix} \mathrm{B} \\ \mathrm{W}^3 \end{bmatrix},$$

$$\mathrm{W}^\pm = \frac{1}{\sqrt{2}} \left(\mathrm{W}^1 \mp \mathrm{W}^2 \right),$$

with the weak mixing angle θ_W with $\sin^2\theta_W \approx 0.23$ [12]. This transformation is called electroweak symmetry breaking. The photon γ is the mediator of the electromagnetic force and couples to electrically charged partiles. Weak interactions are mediated by the $\mathrm{W}^\pm$ and Z^0 bosons, coupling to quarks and leptons. In addition, there are triple and quartic gauge-boson couplings. At an interaction vertex with a $\mathrm{W}^\pm$ boson, a charged lepton changes its flavor to the corresponding neutrino and vice-versa. Similarly, an up-type quark changes to a down-type quark. For quarks, this flavor change occurs mostly within the same generation, but cross-generation transitions are possible. The transitions are given by the Cabibbo-Kobayashi-Maskawa (CKM) Matrix

$$V_{\mathrm{CKM}} = \begin{bmatrix} V_{\mathrm{ud}} & V_{\mathrm{us}} & V_{\mathrm{ub}} \\ V_{\mathrm{cd}} & V_{\mathrm{cs}} & V_{\mathrm{cb}} \\ V_{\mathrm{td}} & V_{\mathrm{ts}} & V_{\mathrm{tb}} \end{bmatrix}.$$

The probability for a transition from flavor x to a different flavor y is proportional to $|V_{xy}|^2$. While the matrix is not diagonal, the off-diagonal elements are small compared to the generation-internal elements [12]. Especially relevant for this thesis is the value of $|V_{\mathrm{tb}}| \approx 1$, as discussed in the next section.

The massive vector bosons $\mathrm{W}^\pm$ and Z with $m_{\mathrm{W}^\pm} = 80.4\,\mathrm{GeV}$ and $m_{\mathrm{Z}^0} = 91.2\,\mathrm{GeV}$ [12] cannot be inserted into the theory directly, because they break gauge invariance, which is a key principle of the formalism. Therefore, the masses are generated using a spontaneous symmetry breaking, which is called the Higgs mechanism. The Higgs potential

$$V(\phi) = -\mu^2 \phi^\dagger \phi + \lambda (\phi^\dagger \phi)^2 \qquad (\mu^2, \lambda > 0)$$

is added to the Lagrangian density, where ϕ is a scalar complex doublet field. It is symmetric in ϕ, but the minimum ϕ_0 is not located at the central symmetry point $\phi = 0$. Owing to the non-zero vacuum expectation value v, finite masses are generated for the three heavy vector bosons without violating local gauge invariance. In this minimal Higgs sector in the SM, one of the four real degrees of freedom introduced with the field ϕ remains and appears as a new scalar boson H. This Higgs boson is electrically neutral, has spin 0 and is massive, as experimentally confirmed, with $m_{\mathrm{H}} = 125.1\,\mathrm{GeV}$ [12]. Larger Higgs sectors like in two-Higgs-doublet models, generally considered BSM scenarios, would be possible, introducing more fields and therefore creating more Higgs bosons. Fermions in the SM can acquire mass via couplings to the Higgs field with a finite vacuum expectation value. This Yukawa coupling y_f for a fermion f is proportional to its mass,

$$m_f = \frac{1}{\sqrt{2}} v y_f \, .$$

Direct evidence for Yukawa couplings has been established by searching for H → $\mathrm{b\bar{b}}$ and H → $\tau^+\tau^-$ decays [14–18]. The Yukawa coupling of the top quark has been indirectly confirmed by the cross section of the gluon-gluon fusion channel for Higgs boson production, for which the top quark loop contribution is the strongest. This is very model dependent, though, and might receive contributions from BSM particles. A direct handle on the coupling is provided by $\mathrm{t\bar{t}H}$ production [19].

Higher-order quantum corrections in the SM lead to divergent loop momentum integrals. This would mean that infinitely large cross sections would be predicted. However, the SM is a renormalizable theory[2], which means that infinities can be absorbed in parameters of the theory, allowing to make finite predictions again. For this, a parameter $g \equiv g_{\text{bare}}$, like a coupling constant or particle mass, is replaced with a renormalized parameter $g_{\text{renorm.}}$ using a renormalization transformation

$$g_{\text{bare}} = g_{\text{renorm.}} + \delta g,$$

where δg is called the counter term. Different renormalization schemes exist with different choices for the transformation, which in principle result in the same predictions. The renormalized parameters are scheme-dependent, but can be transformed to the parameters in any other scheme. Popular choices are the on-shell scheme, the minimal-subtraction (MS) scheme, and the modified minimal-subtraction scheme ($\overline{\text{MS}}$ scheme). The latter two make the parameters dependent on a scale, like for the running strong coupling $\alpha_{\text{s}}(\mu)$.

Generally, particle mass parameters are subject to renormalization. For example, the propagators for scalar particles are of the form

$$\Delta(p) = \frac{\mathrm{i}}{p^2 - m^2 + \hat{\Sigma}(p^2)},$$

with the renormalized self energy $\hat{\Sigma}(p^2)$, including the loop contributions. A pole at M^2 is present for $M^2 - m^2 + \hat{\Sigma}(p^2) = 0$. The renormalization transformation is given by

$$m^2_{\text{bare}} = m^2_{\text{renorm.}} + \delta m^2 .$$

For the on-shell renormalization, the counter term is the unrenormalized self energy, $\delta m^2 = \Sigma(p^2)|_{p^2=m^2}$. The pole of the propagator is given by $p^2 = m^2$ and m is called pole mass. It can be considered a “long-distance mass”, inspired by the concept of a free particle, like for the electron. In the MS scheme, only the divergent part of the corrections is absorbed into the counter term, $\delta m^2 = a/\varepsilon$, where a is a constant and ε the dimensional regularisation parameter. For the $\overline{\text{MS}}$ scheme, also an additive constant $\gamma_E + \ln 4\pi$ is included in the counter term. The $\overline{\text{MS}}$ mass is regarded as a “short-distance mass”.

---

[2] The paragraphs on renormalization are mainly compiled from personal notes on the lecture “Renormalisation of spontaneously broken gauge theories and related phenomenological aspects” by Georg Weiglein given in the summer term 2018 as a *Lecture Course in the Integrated Research Training Group (IRTG) of the SFB 676 “Particles, Strings and the Early Universe”*.

1.2 The top quark

The top quark is the up-type quark of the third generation and has first been observed at the Tevatron by the CDF and D0 Collaborations in proton-antiproton collisions [20, 21]. It is the most massive particle in the SM, as shown in Fig. 1.2, and was therefore the last quark to be discovered, because enough energy is necessary to produce it. Its extremely large mass makes it extraordinary in several regards and the top quark mass (m_t) an important parameter of the SM.

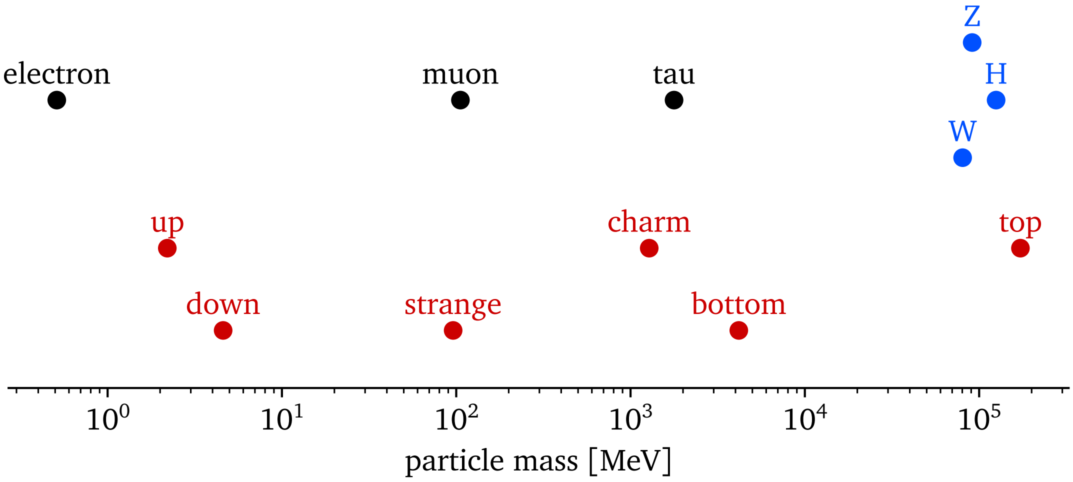

Figure 1.2: The spectrum of particle masses in the standard model. Charged leptons are shown in black. Quarks, shown in red, are divided in up-type quarks (upper row) and down-type quarks (lower row). The massive vector and scalar bosons are shown in blue. Massless bosons and neutrinos are not shown, since for the latter only upper mass limits exist.

Figure 1.2 shows the large hierarchy present in the SM particle mass spectrum, spanning six orders of magnitude without considering neutrinos. The only fermion with a mass in the order of the vector bosons and the Higgs boson itself is the top quark. Its mass is of the order of the vacuum expectation value v of the Higgs field, i.e., the top quark has a Yukawa coupling of $y_\mathrm{t} \simeq 1$. This is why the top quark is of particular interest in the examination of the Higgs sector and also in many BSM models. For example, the radiative corrections to the Higgs boson mass from fermions depend on the Yukawa coupling of the fermion f,

$$\Delta m_\mathrm{H}^2 \propto y_f^2 \Lambda_\mathrm{UV}^2 .$$

Figure 1.3 shows the Feynman diagram for the one-loop contribution from a top quark loop. These corrections drive the Higgs boson mass towards the ultra-violet cut-off scale Λ_UV of the theory beyond which the SM cannot be valid any more. This is generally assumed to be the Planck scale ($\approx 10^{19}$ GeV) which is many orders of magnitude higher

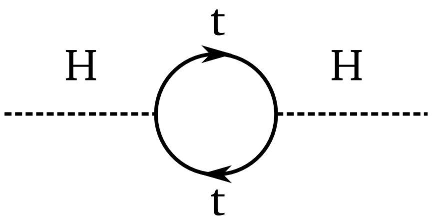

Figure 1.3: Feynman diagram for the one-loop correction to the Higgs boson mass via a top quark loop. In the used convention, the time direction is pointing horizontally to the right. A fermion arrow direction backwards in time indicates an antiparticle, while no bars over the labels are used.

than the electroweak scale ($\approx 10^2$ GeV) at which the measured Higgs boson mass is located [22]. This discrepancy is called the hierarchy problem. The loop corrections to m_H from the top quark are the strongest, owing to the large Yukawa coupling and models that try to address the hierarchy problem, such as supersymmetry [23–29], propose, e.g., top-quark partners that (partially) cancel the contributions to the Higgs boson mass.

The exact shape of the Higgs potential is not predicted by the SM, but the simplest form providing the spontaneous symmetry breaking is assumed. Depending on the Higgs quartic coupling parameter λ, it is possible that the current minimum is only a local minimum. If another lower-energy minimum exists or the potential does not even have a lower bound, the current state would not be stable and tunneling out of the current state would be possible. The exact shape of the potential dictates a mean half life. If this is smaller than the age of the universe, the electroweak vacuum is considered unstable, and if it is larger, it is considered metastable. One of the parameters with the strongest influence on the vacuum stability is the top quark mass. This is shown in Fig. 1.4 for the stability regions in the m_t-m_H and m_t-α_S planes for different parameter ranges [30]. The current values suggest that the current state is metastable.

Although the top quark mass is a free parameter of the SM, there are relations to other parameters which can be used to test the self consistency of the theory. A precise determination of the top quark mass is a crucial ingredient to these tests, formulated as global electroweak fits [31–36]. In the SM, the electroweak mixing angle is given by

$$\sin^2\theta_\mathrm{W} = 1 - \frac{m_\mathrm{W}^2}{m_\mathrm{Z}^2}\,.$$

This relation is modified by radiative corrections. For example, the top/bottom quark loop shown in Fig. 1.5 provides correction terms to m_W. Using an effective mixing angle and effective couplings, the W boson mass can be expressed as

$$m_\mathrm{W}^2 = \frac{m_\mathrm{Z}^2}{2}\left(1 + \sqrt{1 - \frac{\sqrt{8}\pi\alpha(1-\Delta r)}{G_F m_\mathrm{Z}^2}}\right),$$

with a form factor Δr, which depends nearly quadratically on the top quark mass and logarithmically on the Higgs boson mass [31]. Since Δr itself depends on m_W [37], an

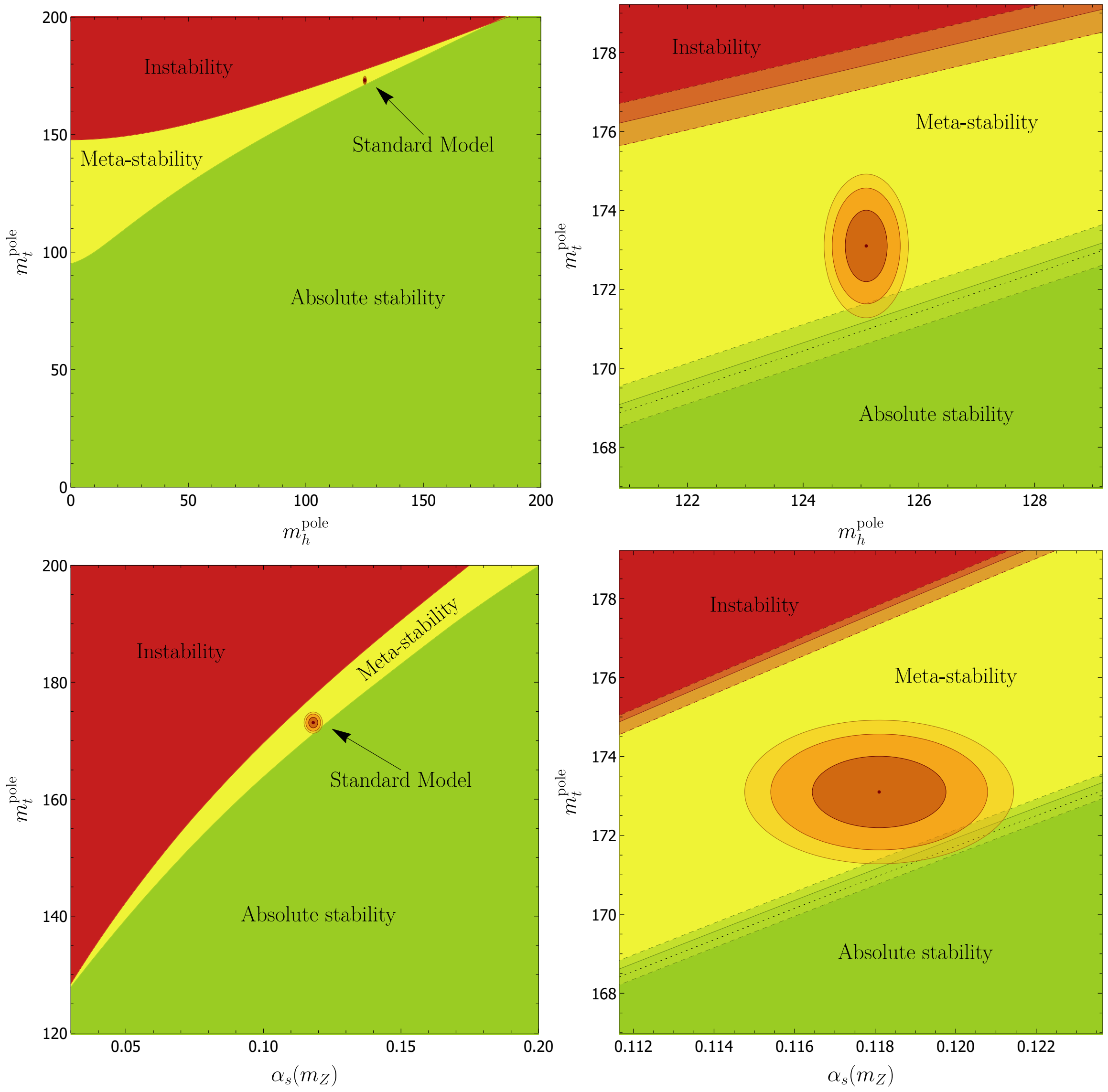

Figure 1.4: Regions of instability, metastability, and stability of the electroweak vacuum [30]. Top: $m_{\rm t}$-$m_{\rm H}$ plane. Bottom: $m_{\rm t}$-α_S plane. The ellipses show the 68%, 95%, and 99% confidence-level contours, where $m_{\rm t} = 173.1 \pm 0.6\,\text{GeV}$ is used.

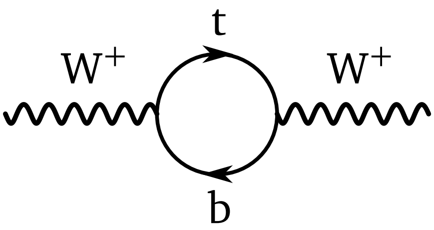

Figure 1.5: Feynman diagram for the one-loop correction to the W boson mass via a top/bottom quark loop. The same conventions as in Fig. 1.3 are used.

iterative method is utilized for the numerical calculation and a parametrization is used for fast evaluation in the GFITTER 2.2 software [31–34]. The global fit performed by the Gfitter Group for the parameters in the electroweak sector using a number of different input measurements yields a χ^2 of 18.6 for 15 degrees of freedom, corresponding to p-value of 0.23 [38]. Figure 1.6 shows the two-dimensional parameter scan of the global electroweak fit in the m_W-m_t plane. There is a slight tension between the global fit and the direct measurements, which is not significant, though. All in all, good compatibility of the SM parameters is observed, but the sensitivity to the top quark mass is demonstrated. Any significant discrepancies would hint at physics beyond the SM. This kind of SM consistency test is performed with the result of this thesis in Chapter 6. It is also used to, e.g., indirectly measure the W and Higgs boson masses.

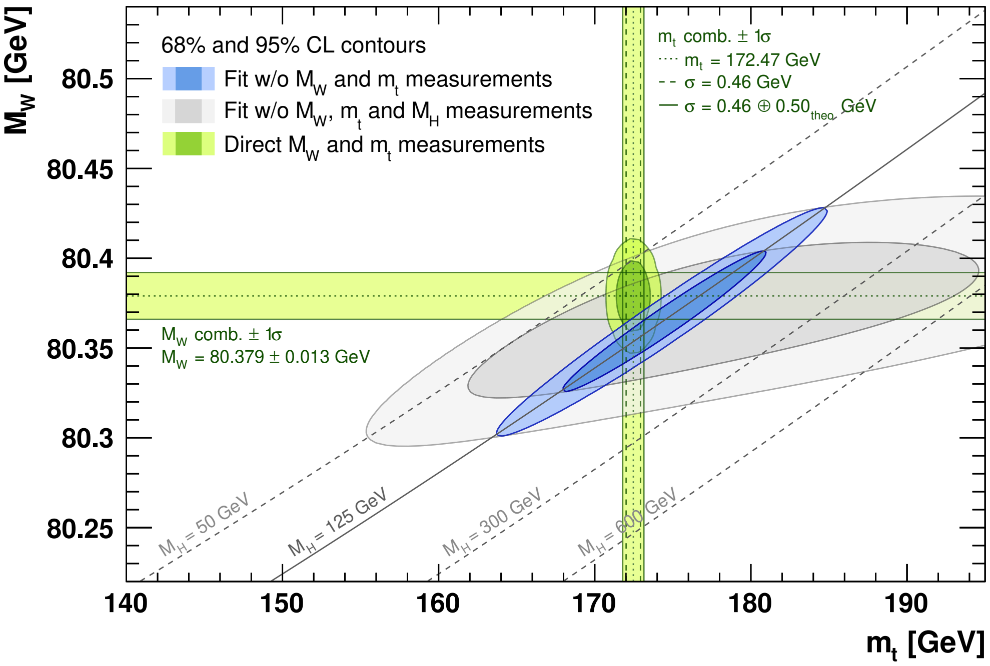

Figure 1.6: Two-dimensional parameter scan of the global electroweak fit in the M_W-m_t plane. The contours are shown for $\Delta\chi^2 = 2.3$ and 5.99, corresponding to 68% and 95% CL, respectively. The lines and bands represent the direct measurements [38].

1.3 Top quark production and decay in proton-proton collisions

At the LHC, top quarks are mainly produced as particle-antiparticle pairs ($\mathrm{t\bar{t}}$), via quark-antiquark annihilation or gluon-gluon fusion, the latter having the larger contribution due to the parton distribution functions at the LHC. Figure 1.7 shows Feynman diagrams for these processes. Top-quark-pair production is dominant due to the involved strong interaction leading to a higher rate than for single top quark production, which is induced by the weak interaction. Other even less frequent production modes are the production of four top quarks and $\mathrm{t\bar{t}}$ production in association with vector bosons or a Higgs boson, which are interesting processes on their own.

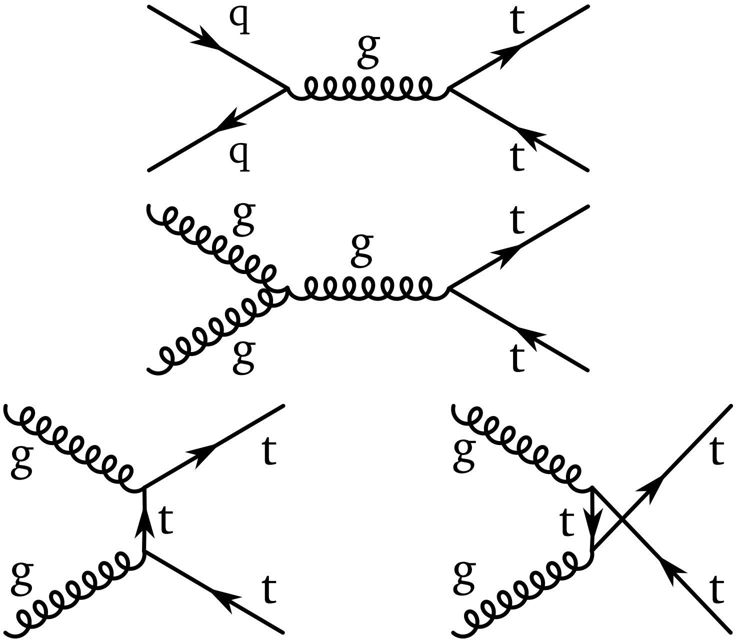

Figure 1.7: Feynman diagrams for leading-order $\mathrm{t\bar{t}}$ production in pp collisions for quark-antiquark annihilation (top), s-channel gluon-gluon fusion (middle), and t- and u-channel gluon-gluon fusion (bottom left and right). In the used convention, the time direction is pointing horizontally to the right. A fermion arrow direction backwards in time indicates an antiparticle, while no bars over the labels are used.

The $\mathrm{t\bar{t}}$ production cross section as a function of the center-of-mass energy is shown in Fig. 1.8. It is rising with the center-of-mass energy, i.e., higher energies are desirable to collect a large number of $\mathrm{t\bar{t}}$ events. For a top quark mass of $m_\mathrm{t} = 172.5\,\mathrm{GeV}$, the next-to-next-to-leading order (NNLO) cross section is $\sigma_{\mathrm{t\bar{t}}} = 831.76\,\mathrm{pb}$ for $\sqrt{s} = 13\,\mathrm{TeV}$, as calculated with the TOP++ program [39].

The top quark decays with a very short mean life time of $\tau_\mathrm{t} \approx 1/\Gamma_\mathrm{t} \approx 5 \cdot 10^{-25}\,\mathrm{s}$, for which a decay width of $\Gamma_\mathrm{t} = 1.3\,\mathrm{GeV}$ [41] has been used. Because this is shorter than the hadronization time of $\tau_\mathrm{had} \approx 1/\Lambda_\mathrm{QCD} \approx 3 \cdot 10^{-24}\,\mathrm{s}$, the top quark does not form hadrons, but directly decays, making it necessary to study it via its decay products.

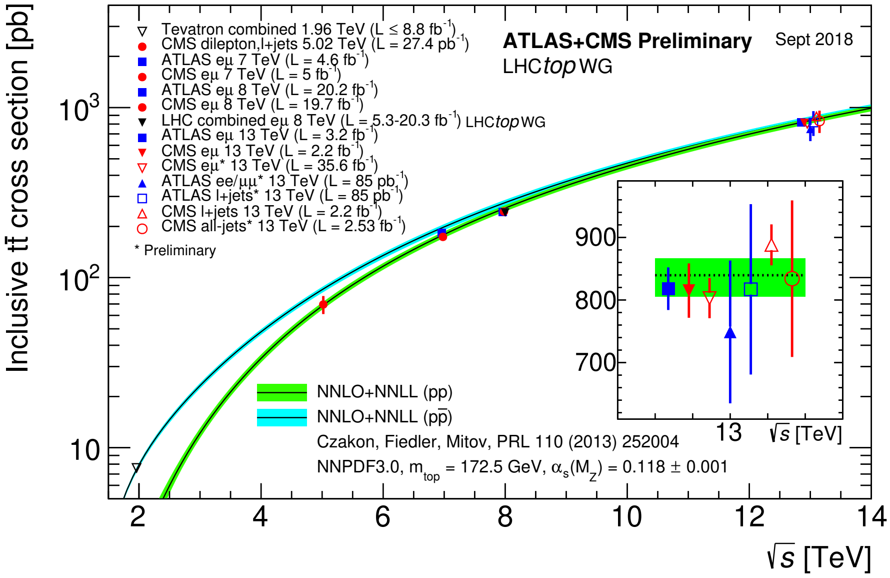

Figure 1.8: Summary of LHC and Tevatron measurements for the $t\bar{t}$ production cross-section as a function of the center-of-mass energy compared to the NNLO QCD calculation complemented with NNLL resummation (top++2.0) [40].

The top quark decays exclusively to a W boson and a down-type quark, which is almost always a b quark, owing to the corresponding CKM matrix element of $|V_{tb}| \approx 1$. In the following, only $t \rightarrow W^+ b$ (and $\bar{t} \rightarrow W^- \bar{b}$) are assumed. The W boson subsequently decays to a $\ell \nu_\ell$ pair (leptonic decay) of any generation $\ell = e, \mu, \tau$ or a quark-antiquark pair $q\bar{q}'$ (hadronic decay), as illustrated in Fig. 1.9.

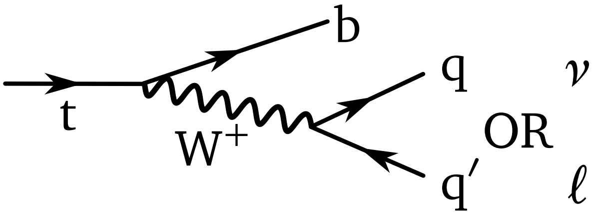

Figure 1.9: Top quark decay. Assuming a corresponding CKM matrix element of $|V_{tb}| \approx 1$, the top quark decays to a b quark and a W boson. The latter decays to a $q\bar{q}'$ pair or to a charged antilepton ℓ^+ and the corresponding neutrino ν_ℓ.

Since three color configurations are possible for each of the two allowed $q\bar{q}'$ pairs, there are six different hadronic decay possibilities, while three different leptonic decays are allowed. Therefore, one third of the top quarks descays leptonically and two third decay hadronically. In $t\bar{t}$ events, the decays of both top quarks need to be considered and they are classified as three different final states:

- In the dilepton channel, both intermediate W bosons decay leptonically. The final state consists of two b quarks, two charged leptons and two neutrinos.

- In the lepton+jets channel (also called semi-leptonic channel), there is one hadronically and one leptonically decaying W boson, leading to two b quarks, two lighter quarks, one charged lepton and one neutrino in the final state.
- In the all-jets channel (also called fully-hadronic channel), both W bosons decay hadronically. The final state is characterized by two b quarks and four lighter quarks.

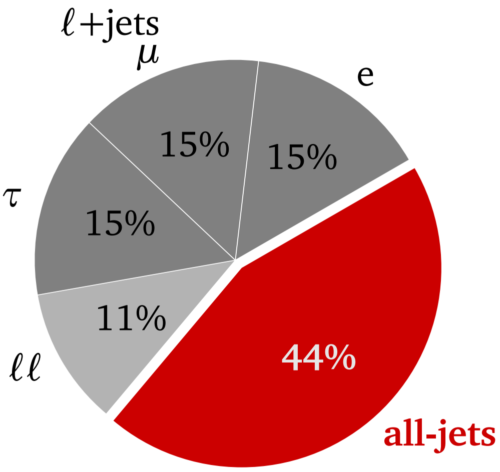

Figure 1.10: Branching ratios of the $t\bar{t}$ decay for the dilepton channel ($\ell\ell$), the lepton+jets channel, and the all-jets channel. For the lepton+jets channel, the separate parts for the three lepton generations are shown.

The relative branching ratios of the $t\bar{t}$ decay are shown in Fig. 1.10. The dilepton channel has the lowest branching fraction and experimentally suffers from the presence of two prompt neutrinos which cannot be detected. The lepton+jets channel and all-jets channel have the same branching ratios, but experimentally often only $\ell = \mathrm{e}$ and μ are used, because τ leptons decay further. This is experimentally more challenging, because there are several decay modes that include at least one neutrino. The lepton+jets channel is often chosen due to its characteristic signature with a single lepton in association with jets, which can be selected with a low background from other processes. Especially final states with muons are easy to reconstruct with modern detectors (cf. Chapter 2). Since only one prompt neutrino is produced, its momentum can be reconstructed from missing transverse momentum in the event, although the resolution is rather poor compared to direct reconstruction of final state particles. In principle the all-jets final state is the best choice, because the branching fraction is the largest and all final state particles can be reconstructed. This is especially beneficial for top quark mass measurements. However, there is huge background from QCD multijet production, making the event selection very demanding. Furthermore, there are many possibilities to assign the reconstructed objects to the $t\bar{t}$ decay products. Both of these issues can be dealt with reasonably well using sophisticated reconstruction techniques, as described in Chapter 4 for the top quark mass measurement in the all-jets final state.

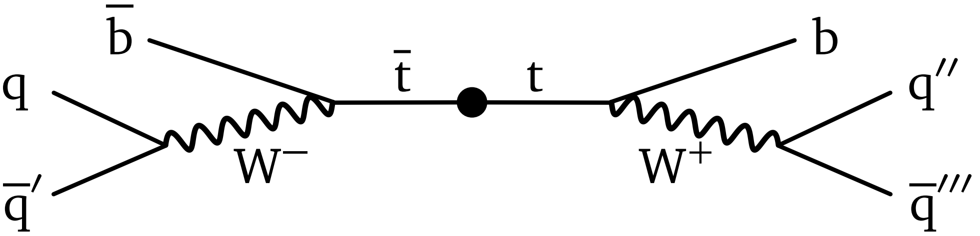

Figure 1.11: Sketch of the decay of the $t\bar{t}$ system in the all-jets final state. The dot marks the interaction point.

Figure 1.11 shows a sketch of the decay of the $t\bar{t}$ system in the all-jets final state. In the $t\bar{t}$ center-of-mass frame, the top quarks have a back-to-back topology, which is distorted by a possible total boost in the laboratory frame. The final state quarks form bunches of hadrons which are reconstructed as jets in the detector, as further described in Chapter 3. Depending on the partonic center-of-mass energy, or equivalently the mass of the $t\bar{t}$ system, the top quarks may have a boost in the center-of-mass system, leading to more collimated decay products. The decay products of both branches thus tend to be separated into two distinct hemispheres. This effect is stronger for higher partonic center-of-mass energies, while lower energies lead to more spherical topologies. In this thesis, only *resolved* topologies are considered, where the jets initiated by the six final state quarks are still reconstructed individually, in contrast to *boosted* topologies, where all decay products of one top quark are reconstructed as a single jet.

The expected topology for resolved $t\bar{t}$ events in the all-jets final state consists of six hardronic jets reconstructed in the detector, as illustrated in Fig. 1.12.

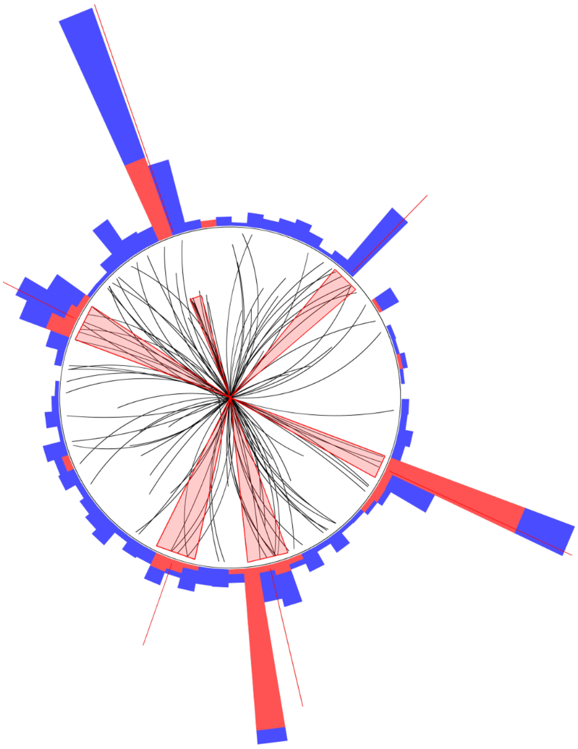

Figure 1.12: Event display of a simulated $t\bar{t}$ event in the all-jets final state. The black lines represent reconstructed tracks in the tracking system, while the blue and red bars show energy entries in the calorimeters. Six jets are found in this event, which are shown as red cones. The event display has been created using the FIREWORKS software [42, 43] and was post processed manually.

1.4 Previous top quark mass measurements at the LHC and the Tevatron

Top quark mass measurements as presented in this thesis in Chapters 4 and 5 are called direct measurements, as they infer the mass from a mass-sensitive distribution of quantities calculated from the top quark decay products. These are calibrated using Monte-Carlo event generators. According to Refs. [44, 45], the top quark mass extracted from direct measurements corresponds to the pole mass, because the decay products in Monte-Carlo generators are distributed according to a Breit-Wigner function. However, there are inaccuracies in the modeling, as with many numerical calculations, which concern the perturbative calculation and the non-perturbative modeling, especially the hadronization. Estimates on the shift of the measured mass with respect to the pole mass reach from a few hundred MeV to "well below 1 GeV" [46–48]. In Ref. [46] it is argued that direct measurements rather correspond to a short distance mass, called MSR mass, evaluated at a small scale, which is close to the pole mass [44]. The MSR mass, defined in Ref. [49], depends on a scale parameter R and interpolates between the pole mass and $\overline{\mathrm{MS}}$ mass [47]. In the $R \to 0$ limit, it is equal to the pole mass.

Previous direct top quark mass measurements in the all-jets final state have been performed by Tevatron and LHC experiments at lower center-of-mass energies [50–54]. The most precise one of these has been obtained by CMS at $\sqrt{s} = 8\,\mathrm{TeV}$ [52], resulting in a mass of

$$m_\mathrm{t} = 172.32 \pm 0.25\,(\mathrm{stat{+}JSF}) \pm 0.59\,(\mathrm{syst})\,\mathrm{GeV}\,.$$

Combining the results of several measurements using different final states at $\sqrt{s} = 7$ and $8\,\mathrm{TeV}$, ATLAS and CMS reported values of $m_\mathrm{t} = 172.69 \pm 0.48\,\mathrm{GeV}$ [55] and $172.44 \pm 0.48\,\mathrm{GeV}$ [52], respectively, while a value of $m_\mathrm{t} = 174.30 \pm 0.65\,\mathrm{GeV}$ was obtained by combining the Tevatron results [56].

A first measurement of the top quark mass at $\sqrt{s} = 13\,\mathrm{TeV}$ was presented using lepton+jets events [57], yielding

$$m_\mathrm{t} = 172.25 \pm 0.08\,(\mathrm{stat{+}JSF}) \pm 0.62\,(\mathrm{syst})\,\mathrm{GeV}\,,$$

where the same pp collision dataset recorded with the CMS detector in 2016 has been used as in this thesis for the measurement in the all-jets channel.

An alternative to direct measurements are top quark mass determinations from $\mathrm{t\bar{t}}$ production cross section measurements. As the cross section depends on the top quark mass, a measurement of the total, or even differential, cross section can be used to determine the top quark mass. Since the used calculation is performed in a well-defined renormalization scheme, these methods do not suffer from the ambiguity present for direct measurements. However, current uncertainties are of the order of a few GeV [58, 59] with multi-differential cross section measurements reaching the sub-GeV level [60].

Approaches using boosted top quarks whose decay products are reconstructed as single jets can also be employed to measure the top quark mass. The jet mass distribution is sensitive to m_t and can be calculated using soft-collinear effective theory [46, 61–70]. Although suffering from a worse statistical precision compared to standard approaches, measurements using boosted top quarks become competitive with rising luminosities, e.g., in Ref. [71] with

$$\begin{aligned} m_{\mathrm{t}} &= 172.6 \pm 0.4\,(\mathrm{stat}) \pm 1.6\,(\mathrm{exp}) \pm 1.5\,(\mathrm{model}) \pm 1.0\,(\mathrm{theo})\,\mathrm{GeV} \\ &= 172.6 \pm 2.5\,\mathrm{GeV}\,. \end{aligned}$$

Although the interpretation of the top quark mass from direct measurements continues to be an actively discussed topic in the theory community, direct measurements still provide the most precise determinations, even when explicitly considering uncertainties due to possible ambiguities in the definition of the extracted mass [44].

2

Experimental setup

Chapter contents

To produce heavy particles, such as the top quark, in the laboratory, high-energy particle colliders are needed. The cleanest collisions are achieved with electron-positron colliders, but circular machines suffer from synchrotron-radiation losses that limit the achievable energy. For higher energies, proton-proton colliders are necessary, the largest and most high-energetic one being the Large Hadron Collider operated at CERN [72].

Very sophisticated detector systems are employed to record particles created in the high-energy collisions. Here, the CMS detector is used [73], which is a general purpose experiment, aiming at a broad physics program reaching from precision measurements to direct searches for new physics. The ATLAS experiment [74] uses different technologies for the sub-detector systems, but is designed to serve the same purposes. This complementarity has been planned to be able to confirm or falsify possible discoveries of one experiment, especially with the search for the Higgs boson in mind. The LHCb experiment [75] is mainly designed to study b-hadron decays. It is a forward spectrometer and therefore operated at lower luminosities. The ALICE detector [76] is used to analyze the collisions of heavy ion nuclei.

2.1 The Large Hadron Collider

The Large Hadron Collider (LHC) [72] is a circular collider ring with a circumference of 26.7 km, located in a tunnel $45 - 170$ m underground at the French-Swiss border at CERN near Geneva. Before the LHC began its operation with Run 1 in 2010, the tunnel had been used for the Large Electron-Positron Collider (LEP), which was decommissioned in 2000. The LHC was originally designed for a proton-proton center-of-mass energy $\sqrt{s}$ of 14 TeV. While it operated at $\sqrt{s} = 7$ and 8 TeV in Run 1, it has been restarted for Run 2 in 2015 at $\sqrt{s} = 13$ TeV.

A pre-accelerator chain is used to reach these high energies. It is composed of previous main accelerators which have been located at CERN. Protons are first accelerated in a linear accelerator (Linac2), which injects the beam into the proton synchrotron booster (PSB) and subsequently into the proton synchrotron (PS). Afterwards, they are further accelerated to a beam energy of 450 GeV in the super proton synchrotron (SPS), from which the beam is finally injected into the LHC. An illustration of the CERN accelerator complex, not only consisting of the LHC pre-accelerator chain, is shown in Fig. 2.1.

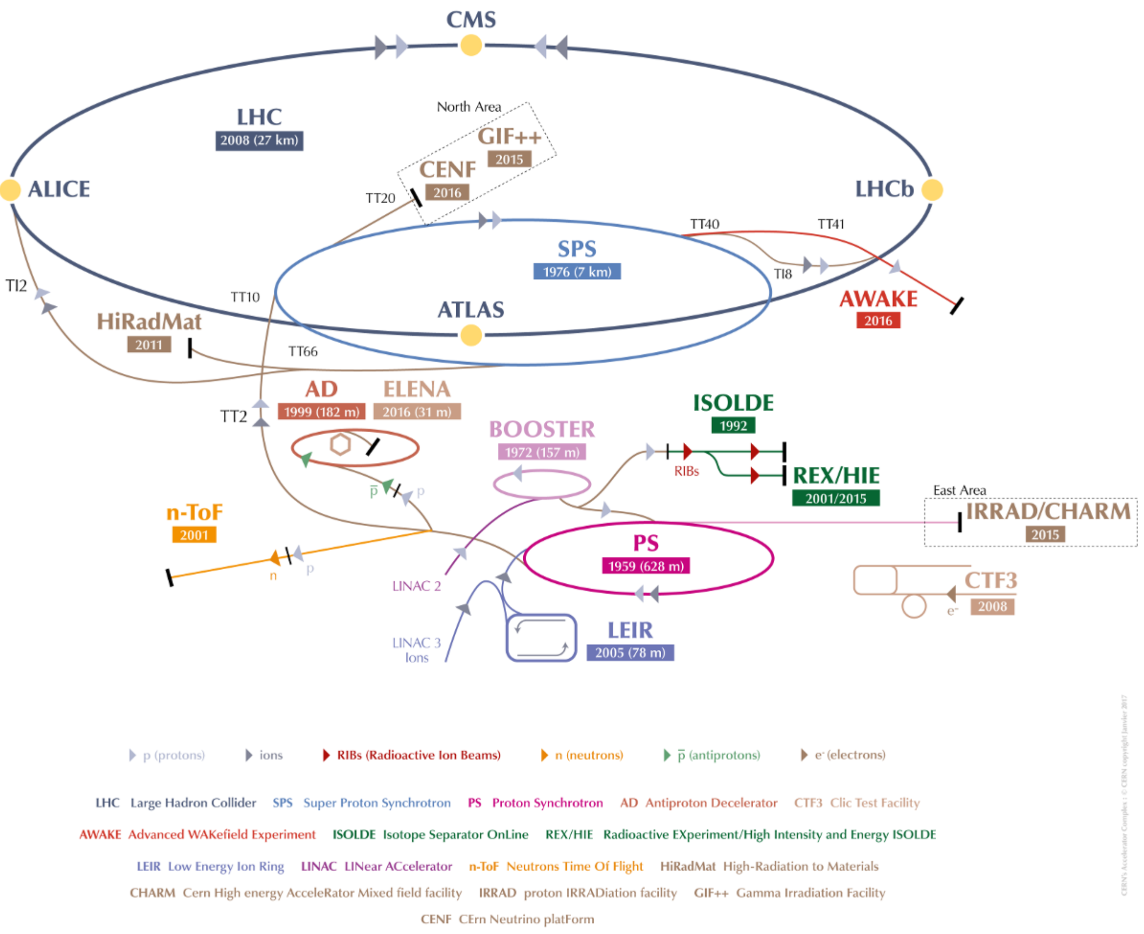

Figure 2.1: The CERN accelerator complex [77].

Figure 2.2 shows the eight sectors of the LHC with the four interaction points, where the beams can intersect. The four detectors are build around these collision points. Sector four hosts the superconducting cavities, accelerating the particles further at an operation frequency of 400 MHz. The protons are forced to circular trajectories using dipole magnets. To focus the beam, quadrupole magnets are installed, as well as higher-order multipoles, most importantly sextupoles, to correct for chromaticity, i.e., energy-dependent tune shifts, and the influence of non-linear fields introduced by magnet irregularities. The superconducting magnets are made of NbTi Rutherford cables and cooled to a temperature below 2 K. Two separate magnetic fields are needed, because the counterrotating beams have same-sign electrical charge, but the coils for both directions are housed in the same mechanical structure [72].

The number of events that can be observed per time unit for a specific scattering process is proportional to the instantaneous luminosity L, which is a characteristic value of the collider. The protons circulate in $n_b = 2808$ bunches in each direction and collide in intervals of 25 ns. For a symmetric collider like the LHC, the instantaneous luminosity

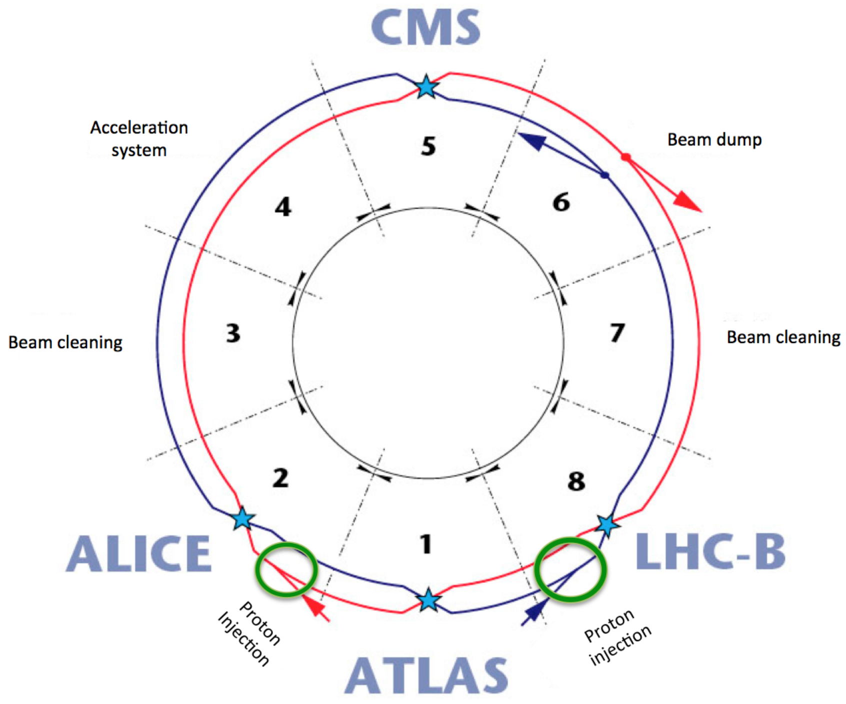

Figure 2.2: The eight sectors of the LHC ring with both beams that are intersecting at four interaction points [78].

is given by

$$L = \frac{N_b^2 n_b f \gamma}{4\pi \varepsilon_n \beta^*} F_{\mathrm{hg}}.$$

The number of protons per bunch is denoted $N_b \approx 10^{11}$, the revolution frequency f, the Lorentz factor γ, the normalized emittance ε_n, and the value of the beta-function at the interaction point β^*. The hourglass factor F_{hg} accounts for the finite crossing angle of both beams. Initially planned to reach instantaneous luminosities of up to $10^{34}\,\mathrm{cm}^{-2}\mathrm{s}^{-1} = 10\,\mathrm{Hz/nb}$, the LHC delivered up to 15.3 Hz/nb in the 2016 run for CMS, as shown in Fig. 2.3, and even more than 20 Hz/nb in 2017 and 2018. For the total number of events produced for a specific process, the integrated luminosity

$$\mathcal{L} = \int L\,\mathrm{d}t$$

is the important quantity. The number of produced events is given by

$$N_{\mathrm{evt}} = \mathcal{L} \cdot \sigma\,,$$

with the cross section σ for a specific process.

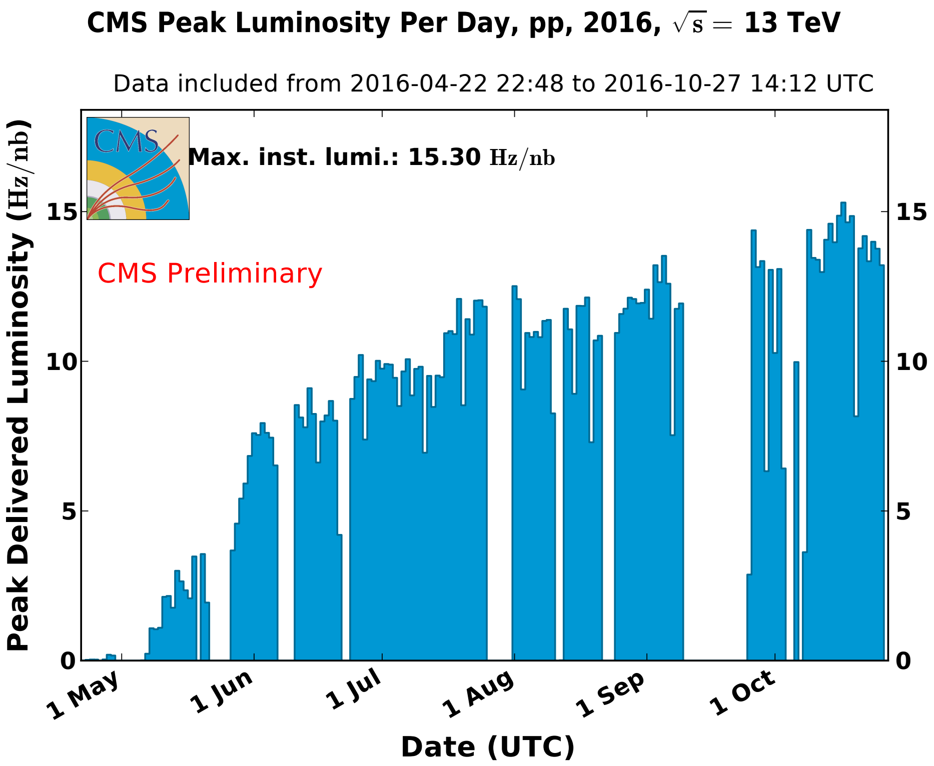

Figure 2.3: Peak instantaneous luminosity on a day-by-day basis for CMS in 2016 [79].

The LHC can also accelerate heavy ions. Heavy ion collisions are analyzed mainly by the ALICE Collaboration, but also used by CMS and ATLAS. Especially, fully stripped lead ions ($^{208}\mathrm{Pb}^{82+}$) can be accelerated to beam energies of up to 2.76 TeV per nucleon, either operating in pPb or PbPb collision mode [72].

In Run 1 the LHC operated at $\sqrt{s} = 7\,\mathrm{TeV}$ (2011) and 8 TeV (2012) for pp collisions, followed by the long shutdown 1, in which measures were taken to increase the energy closer to the design. Run 2 started in 2015 at $\sqrt{s} = 13\,\mathrm{TeV}$ and continued in 2016, 2017, and 2018, where the design luminosity was reached and even exceeded. The long shutdown 2 followed the data taking in 2018 and the restart for Run 3 is foreseen for 2021 with the option to increase the center-of-mass energy to 14 TeV.

2.2 The CMS detector

The data used in this thesis has been collected by the Compact Muon Solenoid (CMS) detector [73], which is located at interaction point 5 of the LHC and operated by the CMS Collaboration. Built around the collision point it spans approximately 20 m in length with a diameter of 15 m. The origin of the coordinate system is placed at the interaction point with the z axis parallel to the beam direction, pointing westwards, the x axis pointing towards center of the LHC, and the y axis pointing upwards. The azimuthal angle $\phi \in [-\pi, \pi]$ is measured from the x axis in the x-y plane and the polar angle $\vartheta \in [0, \pi]$ is usually substituted by the pseudorapidity $\eta = -\ln \tan \frac{\vartheta}{2}$. Distances in the η-ϕ plane are denoted $\Delta R = \sqrt{\Delta\phi^2 + \Delta\eta^2}$. The detector consists of several subcomponents, each specialized to reconstruct different particle types and measure their trajectories, energies, or momenta. The subdetectors are divided into barrel and endcap parts, covering the central (small $|\eta|$) and forward (large $|\eta|$) regions, respectively. The general layout of these can be seen in Fig. 2.4.

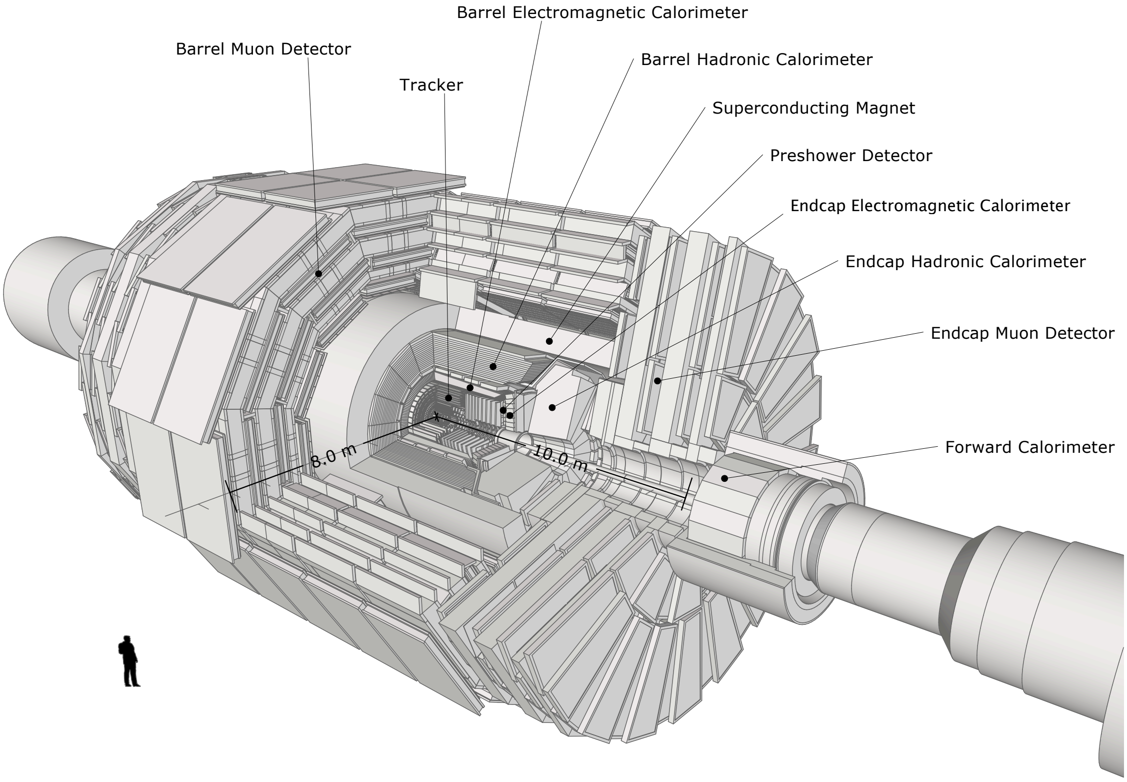

Figure 2.4: Schematic view of the CMS detector [80, 81]. The labels show the barrel and endcap subdetectors.

CMS uses a superconducting solenoid magnet with a diameter of 6 m that weighs 220 t to bend charged particle tracks in the x-y plane in order to determine their transverse momenta. Rutherford cables of NbTi are wound in four layers and carry a current of up to 19 kA. The interior of the magnet, which is occupied by the inner tracking system and the main calorimeters, is provided with a homogeneous 3.8 T magnetic field parallel to the beam direction. The magnetic flux is returned on the outside by an iron yoke, in which the muon system is embedded [73].

The innermost part of the detector is occupied by the silicon-based inner tracking system, built around the beam pipe, with a length of 5.8 m and a diameter of 2.5 m. It is used to reconstruct trajectories of charged particles and to identify primary interaction vertices and secondary vertices, which result for example from b-hadron decays. Closest to the beam pipe, the pixel detector with a fine granularity ensures the ability to precisely determine track origins and vertices. Overall, it consists of 66 million pixels with a cell size of $100 \times 150\,\mu\text{m}^2$. The pixel detector is built in three layers in the barrel and two endcap disks. The innermost layer has a radius of 4.4 cm. Further outward, a silicon strip detector is used, consisting of ten barrel layers and twelve endcap disks with a total of 9.3 million strips. The exact layout, subdivision, and pseudorapidity coverage of the inner tracking system is shown in Fig. 2.5. The total active silicon area of the tracker is approximately $200\,\text{m}^2$ [73].

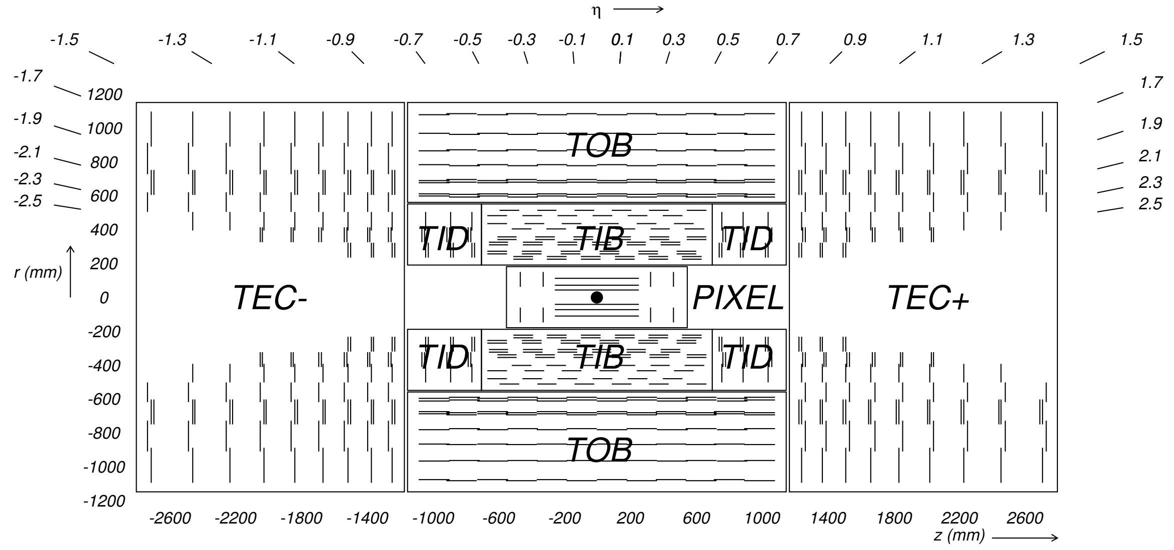

Figure 2.5: Schematic cross section of the CMS inner tracking system. The strip tracker is divided into inner and outer barrel (TIB, TOB), inner disks (TID) and endcaps (TEC). Each line represents a detector module [73].

Around the tracker at an inner radius of 1.3 m, CMS is equipped with a homogeneous electromagnetic calorimeter (ECAL), mainly used to measure electron and photon energies. Lead tungstate ($PbWO_4$) crystals with a radiation length X_0 of 0.89 cm and a Molière radius of 2.2 cm serve as scintillating material. They are directed towards the collision point with a slight tilt to ensure that particles cannot pass gaps between the crystals. In the ECAL barrel (EB), covering $|\eta| < 1.479$, each of the 61200 crystals has a length of $23.0\,\text{cm} \approx 25.8X_0$ and a front area of $22 \times 22\,\text{mm}^2$. The ECAL endcaps (EE) each contain 7324 crystals with a length of $22.0\,\mathrm{cm} \approx 24.7X_0$ and a front cross section of $28.62 \times 28.62\,\mathrm{mm}^2$ that cover $1.479 < |\eta| < 3.0$. For the conversion of scintillation light into electrical signals, avalanche photodiodes are used in the EB and vacuum phototriodes in the EE. The relative energy resolution can be parametrized with respect to the photon or electron energy E as

$$\left(\frac{\sigma}{E}\right)^2 = \left(\frac{2.8\%}{\sqrt{E/\,\mathrm{GeV}}}\right)^2 + \left(\frac{12\%}{E/\,\mathrm{GeV}}\right)^2 + (0.30\%)^2\,,$$

where the numerical parameters have been determined in a beam test [82]. The first term is of stochastic origin, mainly due to the Poissonian distribution of the number of scintillation photons that are counted. The second summand is attributed to noise from electronics and digitization. Other effects like the non-uniformity of the light collection, intercalibration errors, and energy leakage from the rear side of the crystals are contained in the last constant term. In order to identify the decay of neutral mesons to two photons, a preshower detector is placed in front of the ECAL for the region $1.653 < |\eta| < 2.6$. It is realized as a sampling calorimeter with lead and silicon strip layers [73].

Between the ECAL and the magnet, i.e., at a radial distance between 1.77 m and 2.95 m in the barrel, the hadron calorimeter (HCAL) is responsible for measuring the energy of hadrons. It is built as a sampling calorimeter using layers of brass and plastic scintillators, while the front- and back-plates are made of steel. The barrel part ($|\eta| < 1.3$) consists of 36 azimuthal wedges and is segmented into parts covering 0.087×0.087 in $\Delta\eta \times \Delta\phi$. The 17 scintillator layers are read out with the help of photodiodes. In the forward direction the endcaps cover a pseudorapidity of $1.3 < |\eta| < 3.0$. While for $|\eta| < 1.6$ the granularity is the same as in the barrel, it is degraded to $\Delta\eta \times \Delta\phi = 0.17 \times 0.17$ for $|\eta| > 1.6$. A further outer hadronic calorimeter is placed outside of the magnet for the barrel part. Hadrons passing the ECAL and HCAL can be detected using a scintillation detector making use of the stopping power of the magnet coil. A forward calorimeter extends the pseudorapidity coverage up to $|\eta| = 5.2$. It is built of quartz fibres embedded in steel absorbers that detect Cherenkov light emitted by particles passing the detector and is therefore mainly sensitive to the electromagnetic shower component [73].

The muon system is placed outside of the magnet coil. In the barrel ($|\eta| < 1.2$) four stations of drift tube chambers are used to reconstruct muon trajectories. Cathode strip chambers are employed in the endcaps ($0.9 < |\eta| < 2.4$), also arranged in four stations. Additionally, six barrel layers of resistive plate chambers and three disks per endcap are used mainly for triggering purposes [73].

To read out and store the detector signals, a trigger system is needed, because at a collision rate of 40 MHz it is impossible to store the data of all collision events. The selection made by the trigger is designed to accept events in which potentially interesting physics processes occurred and is the first step of the event selection for every analysis. The trigger is designed as a two-tiered system using a level-1 trigger (L1) and a high-level-trigger (HLT). For the L1 trigger simple information from the calorimeters and muon detectors is used. It is a hardware trigger implemented using custom programmable devices and it reduces the event rate from 40 MHz to $\mathcal{O}(100\,\mathrm{kHz})$. A more sophisticated selection with a particle reconstruction closer to that used in the offline analysis is possible with the HLT, which is a software trigger running on computer farms. Different HLT paths exist, targeting different final states. Paths with similar requirements, i.e., selections based on the same objects, are grouped into output streams, which define the primary datasets that are stored. The HLT event output rate of $\mathcal{O}(1\,\mathrm{kHz})$ can be handled and stored to disk [73, 83, 84].

During the 2016 data taking, an integrated luminosity of approximately $38\,\mathrm{fb}^{-1}$ has been recorded with the CMS detector, as shown in Fig. 2.6. Of these, approximately $36\,\mathrm{fb}^{-1}$ have been certified as good for physics analyses. Figure 2.7 shows the delivered luminosity for all years of data taking. While in the years of LHC Run 1 (2010-2012) the integrated luminosity was generally lower than in 2016, the later data taking periods of Run 2 provided slightly more integrated luminosity each year.

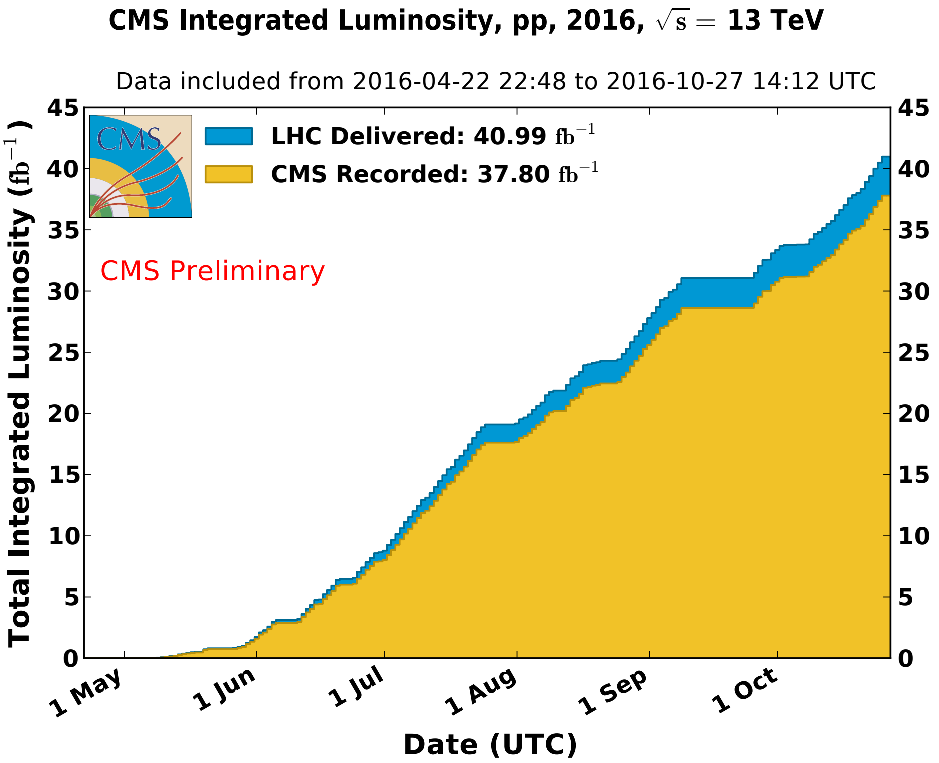

Figure 2.6: Cumulative integrated luminosity for the 2016 data taking delivered to and recorded with the CMS detector. Each bin represents a day [79].

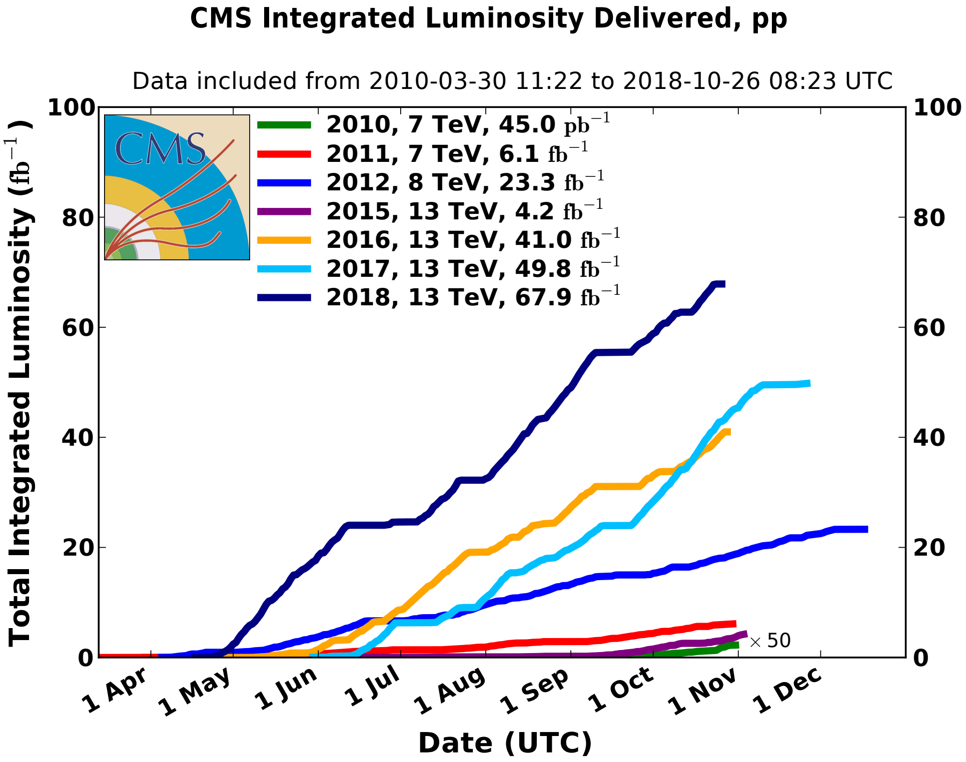

Figure 2.7: Cumulative integrated luminosity for all data taking periods delivered to the CMS detector. The LHC Run 1 spans the years 2010 to 2012 and Run 2 the years 2015 to 2018 [79].

3

Event reconstruction and Monte-Carlo simulation

Chapter contents

Events recorded with the CMS detector are further processed and analyzed within the CMS software framework (CMSSW) which is based on the ROOT data analysis framework and its libraries written in C++ [85, 86]. A reduced version of the Analysis Object Data (AOD) format is used, called MINIAOD [87]. It contains physics objects, such as leptons, photons, jets, and missing transverse momentum.

Starting from MINIAOD input files, all parts of the analysis are performed on the German National Analysis Facility (NAF) infrastructure. For the submission of jobs to the local batch system the `grid-control` submission tool is used [88].

The reconstruction techniques used to obtain the physics objects contained in MINIAOD are described in the following. In addition, the jet energy calibrations and the simulation of physics processes in high-energy collisions are described.

3.1 Event reconstruction

In general, particles traversing the detector need to be identified and distinguished, which is made possible by linking information of different sub-detector signals. Furthermore, directions and energies or momenta of the particles need to be measured. In the assumed high-energy limit, the masses of the reconstructed particles can be neglected and the energy becomes equal to the magnitude of the momentum vector $\vec{p}$,

$$E \approx |\vec{p}|\,.$$

The initial boost along the beam direction (z) is unknown, because the colliding partons (quarks or gluons) only carry a fraction of the proton momentum, as further described in Section 3.2. Accordingly, only the transverse momentum $\vec{p}_\mathrm{T}$ is used for many purposes, which is the projection of $\vec{p}$ onto the x-y plane. Its absolute value is denoted

$p_\mathrm{T} = |\vec{p}_\mathrm{T}| = \sqrt{p_x^2 + p_y^2}$, which is sometimes also called transverse energy E_T. The pseudorapidity

$$\eta = -\ln \tan \frac{\vartheta}{2}$$

depends only on the angle ϑ with respect to the z axis. It becomes equal to the rapidity y relative to the beam axis in the high energy limit, which is given by

$$y = \frac{1}{2} \ln \frac{E + p_z}{E - p_z} \,.$$

Differences in the rapidity, $\Delta y \approx \Delta\eta$, are invariant under Lorentz boosts along the z axis, which is also true for transverse momenta and differences in the azimuthal angle $\Delta\phi$. Distances between objects are therefore also mostly given as Euclidean distances in the η-ϕ plane,

$$\Delta R = \sqrt{\Delta\phi^2 + \Delta\eta^2} \,.$$

The particle-flow (PF) event reconstruction algorithm [89–91] is used, aiming to reconstruct and identify all individual particles. Signals from different detector components are linked, i.e., energy deposit information from the calorimeters and momentum information from the curvature of tracks, as well as direction information. The resulting PF candidates are muons, electrons, photons, charged hadrons, and neutral hadrons. High-level physics objects are constructed from the PF candidates, most importantly leptons, photons, and jets. The reconstruction algorithms, identification criteria, and calibrations are provided centrally by the physics object groups (POGs) for the whole collaboration. In the following, the parts most important for this analysis are described briefly.

Primary vertex:

The reconstructed vertex defined as the primary pp interaction vertex is the one with the largest summed physics-object p_T^2. The physics objects considered here are jets clustered using the anti-k_T jet algorithm [92, 93], described below, only considering the tracks associated with the specific vertex, and the missing transverse momentum $\vec{p}_\mathrm{T}^{\,\text{miss, vertex}}$ calculated as the negative vectorial sum of the transverse momenta of the jets from the vertex

$$\vec{p}_\mathrm{T}^{\,\text{miss, vertex}} := - \sum_{i \in \text{track-jets from vertex}} \vec{p}_\mathrm{T}(i) \,.$$

Further pp collisions may occur within the same bunch crossing or are reconstructed from detector signals of particles originating from adjacent bunch crossings, called pileup. The pileup distribution of the analyzed data with an average of 23 interactions is shown in Fig. 3.1.

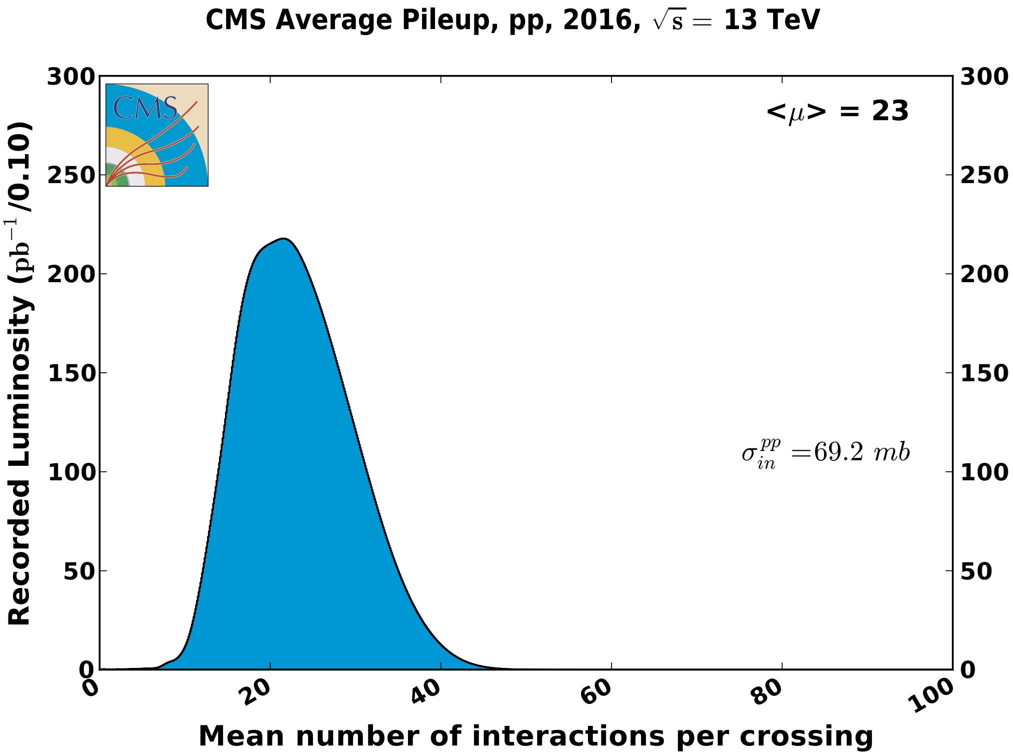

Figure 3.1: Mean number of pp interactions per bunch crossing for the 2016 run at $\sqrt{s} = 13\,\text{TeV}$ [79].

Muons:

Muons are reconstructed using information from the inner tracking system, as well as the dedicated outer muon system. If tracks in both systems can be matched, all hits are combined into a "global muon" fit used by the PF algorithm [94]. Further identification criteria, corresponding to the working points provided by the Muon POG [95], can be applied. These include the χ^2 per number of degrees of freedom (χ^2/N_{df}) of the global muon track fit, the number of used muon chamber hits, the number of muon stations matched to the track, the transverse impact parameter and longitudinal distance with respect to the primary vertex, the number of pixel hits, and the number of tracker layers with hits.

Photons and electrons:

Photons and electrons, summarized as electromagnetic objects, deposit energy in the ECAL. In addition, electron trajectories are reconstructed in the tracking system. Photons can convert to $\mathrm{e}^+\mathrm{e}^-$ pairs before reaching the ECAL. These diverge in ϕ, owing to the magnetic field. Electrons can emit bremsstrahlung photons. All energy deposits need to be associated to the right objects, which is achieved by employing the PF algorithm for a consistent global event description (GED) [96], instead of building ECAL clusters independently and then eventually matching them to tracks [97, 98], as done in Run 1.

Identification criteria, defined by the EGamma POG, are applied to select photons and electrons. For photons, the ratio of the energy deposited in the HCAL and ECAL, shower shape variables, and isolation variables are used [99]. For electrons, in addition to these, angular differences between the track and the ECAL cluster, difference between the ECAL energy and track momentum, impact parameters, the number of missing hits along the trajectory, and a photon conversion veto are utilized [100].

Hadrons and non-isolated photons:

The remaining calorimeter clusters are identified as charged hadrons, neutral hadrons, or non-isolated photons. Non-isolated photons in a hadronic shower result mainly from the decay of neutral mesons like $\pi^0 \to \gamma\gamma$. Clusters in the ECAL without a linked track are identified as non-isolated photons, while HCAL clusters without a linked track are identified as neutral hadrons. The calorimeter clusters with linked tracks are combined to charged hadrons [91].

Jets:

The collimated bunches of hadrons initiated by quarks and gluons are reconstructed as hadronic jets. For this a clustering algorithm is needed.

PF candidates are clustered using the anti-k_t algorithm [92, 93, 101], which is a sequential jet algorithm in contrast to cone algorithms. It is infrared and collinear safe. Initially, each particle is considered as a pseudo-jet. These are merged sequentially until a stop criterion is fulfilled. The distance measure

$$d_{ij} := \min\left\{k_{\mathrm{T}i}^{-2}, k_{\mathrm{T}j}^{-2}\right\} \cdot \frac{\Delta_{ij}^2}{D^2}$$

for a pseudo-jet pair (i, j) is calculated with the transverse momentum k_{T} and the Euclidean distance Δ_{ij} in the y-ϕ space. The pair with the smallest distance d_{ij} is merged and used as a single pseudo jet for the next iteration until the distance $d_{iB} := k_{\mathrm{T}i}^{-2}$ of a pseudo-jet i to the beam axis yields the smallest distance. The pseudo-jet i is a final jet and not further considered in the clustering of the rest of the event. The distance parameter D controls the size of the jets and is set to $D = 0.4$, like it is used for most CMS analyses in Run 2.

To reduce the influence of particles from pileup, charged hadrons which are identified as originating from a different vertex than the primary pp interaction vertex are excluded from the clustering. This procedure is called charged hadron subtraction (CHS).

b tagging:

Jets originating from b quarks (b jets) can be identified using different algorithms. Such a jet most likely contains a B hadron, because the initial b quark becomes part of a bound state in the hadronization. The B hadron decays further with a finite life time, i.e., it travels some distance before decaying. Though it does not reach the tracker, it creates a secondary vertex which can be reconstructed using the tracks originating from the decay. For this analysis, the combined secondary vertex algorithm (CSVv2) [102, 103] is used for b tagging, further discussed in Section 4.1.

Missing transverse momentum:

The missing transverse momentum is the negative vectorial sum of the transverse momenta of all reconstructed particles,

$$\vec{p}_{\mathrm{T}}^{\,\mathrm{miss}} := -\sum_{i\in\mathrm{particles}} \vec{p}_{\mathrm{T}}(i)$$

and its absolute value $p_{\mathrm{T}}^{\mathrm{miss}} = |\vec{p}_{\mathrm{T}}^{\,\mathrm{miss}}|$ is often called missing transverse energy $E_{\mathrm{T}}^{\mathrm{miss}}$. It can arise from particles that cannot be reconstructed, such as neutrinos in the SM or BSM particles, or energy mismeasurements due to the finite object resolutions, especially of jets.

3.1.1 Jet energy scale corrections

Several effects influence the energy of the jets with respect to the energy of the initiating high-momentum particles. First of all, the choice of the jet radius or the distance parameter is a trade-off. To cluster all final state particles originating from one quark or gluon, a large radius is desired, such that no energy is lost (out-of-cone radiation). However, this leads to an increased contribution of particles from different sources, namely pileup and multi-parton interactions (MPI).

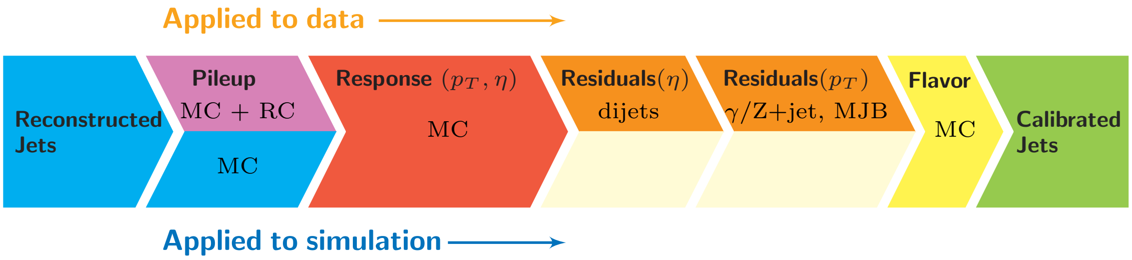

Figure 3.2: Schematic sketch of the CMS jet energy correction stages for data and simulation [104].

A sophisticated correction procedure for the jet energy scale (JES/JEC) is needed, which is performed in several stages in the CMS experiment, as sketched in Fig. 3.2. The first step is an energy offset correction to correct for pileup. This offset is mainly due to contributions from neutral hadrons and photons. On top of that, corrections depending on p_{T} and η are derived from simulated events. Furthermore, p_{T}- and η-dependent residual corrections are applied to data only, which are derived with in situ measurements of the momentum balance in dijet, photon+jet, Z+jet, and multijet events [104], to correct the remaining data/simulation differences. No corrections based on the flavor of the initiating quark or gluon are applied, but uncertainties for the differences are considered, as described in Section 4.6.

3.1.2 Jet energy resolution corrections

The jet energy resolution measured in data is worse than in simulation. Therefore, the simulated jets are modified to correct for the difference [104]. The scaling method is used, multiplying the reconstructed jet four-momentum with the factor

$$c_{\mathrm{JER}} = 1 + (s_{\mathrm{JER}} - 1)\, \frac{p_{\mathrm{T}} - p_{\mathrm{T}}(\mathrm{particle})}{p_{\mathrm{T}}}\,,$$

where p_{T} is the reconstructed transverse momentum, $p_{\mathrm{T}}(\mathrm{particle})$ is the transverse momentum of the jet clustered from generated particles and s_{JER} is the data-to-simulation core resolution scale factor provided by the JetMET group [105]. The η dependent sacle factors s_{JER} and the corresponding uncertainties can be found in Table 4.6.

3.2 Monte-Carlo simulation

Simulations of high-energy collisions are necessary for most analyses for signal events, as well as for background processes. In many cases, backgrounds are estimated from data, in order not to rely on the simulation, but such estimation methods still need to be validated using simulated events. Furthermore, signal events need to be generated in order to design the analysis strategy. This is true for searches, because the processes are potentially hypothetical, as well as for many SM measurements in order not to bias a result by designing the strategy based on data.

In this thesis, simulation is used to validate the background estimation procedure and derive a systematic uncertainty for it, as described in Section 4.4. Furthermore, the signal is simulated with different top quark masses to calibrate the measurement and variations of the simulation parameters are used to obtain systematic uncertainties, as described in Sections 4.5 and 4.6.

Monte-Carlo (MC) methods are used to simulate proton-proton collisions. Several different stages of the scattering process and event evolution have to be simulated, as illustrated in Fig. 3.3.

Simulation of the hard process:

The most interesting part is the hard interaction, i.e., the collision of quarks and gluons, as shown in Fig. 1.7 for $\mathrm{t\bar{t}}$ production, which is calculated with a matrix element (ME) generator, using perturbative calculations. The ME generators used are POWHEG v2 [107–110] and MADGRAPH5_aMC@NLO [111, 112], further described in Section 4.1.

Parton distribution functions:

The calculation of the partonic cross section $\hat{\sigma}_{ij\to X}$ for partons i and j depends on the partonic center-of-mass energy $\hat{s} = x_1 x_2 s$. The momentum fraction x that a parton i carries relative to the total proton momentum is described by parton distribution functions (PDFs) $f_i(x)$, which cannot be calculated perturbatively and are therefore

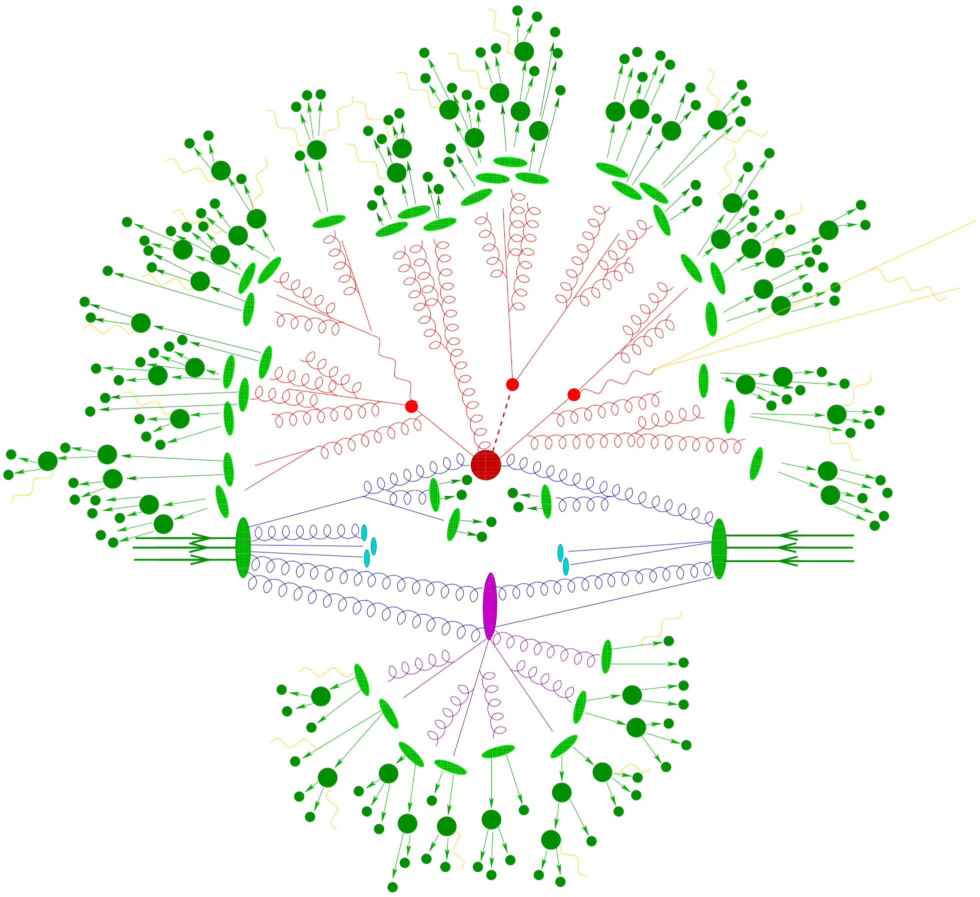

Figure 3.3: Illustration of the different parts of an event as modeled by an event generator. The hard interaction (here, $\mathrm{t\bar{t}H}$ production) is marked as a red blob and followed by the decay of the top quarks and the Higgs boson with additional QCD radiation, all shown in red. The purple process represents multi-parton interactions. The hadronization of final-state partons is shown as light green blobs and the subsequent hadron decays as dark green blobs. Electromagnetic radiation is shown in yellow [106].

extracted by means of a fit using mainly deep-inelastic scattering data. Owing to the factorization theorem, the cross section $\sigma_{\mathrm{pp}\to X}(s)$ at a center-of-mass energy $\sqrt{s}$ can be calculated by separating the perturbative and non-perturbative parts at a factorization scale Q^2,

$$\sigma_{\mathrm{pp}\to X}(s) = \sum_{i,j\in\{\mathrm{q},\bar{\mathrm{q}},\mathrm{g}\}} \int \mathrm{d}x_1 \mathrm{d}x_2 f_i(x_1,Q^2) f_j(x_2,Q^2) \hat{\sigma}_{ij\to X}(x_1 x_2 s, Q^2)\,.$$

The PDF $f_i(x,Q^2)$ is the probability to find a parton i with a momentum fraction x in the proton when probed at a scale Q^2. Different sets of PDFs exist using different parametrizations. Here, the NNPDF3.0 NLO set [113] is used, which is based on neural networks.

Parton shower and hadronization:

Some of the final state products of the hard process will decay further, which needs to be simulated. Since the ME calculation can only be performed to a finite order in perturbation theory, additional QCD radiation is simulated with a parton shower (PS) program, which normally also handles the hadronization of the final state partons. Furthermore, the decay of instable hadrons and electromagnetic radiation are modeled. The remaining partons not involved in the hard interaction may interact, too, which is called multi-parton interactions (MPI) and together with the beam remnants form the underlying event (UE). The PYTHIA 8 [114] PS generator is interfaced to the ME generator to handle all these effects. Different parameters of the PS and hadronization program control the underlying event activity, and need to be tuned using data (UE tunes). The UE tunes employed for the different processes are further listed in Section 4.1.

Color reconnection:

Non-perturbative effects which are poorly modeled, owing to the simplicity of models, can have a severe impact on some observables. Especially relevant for the top quark mass measurement is the color configuration of the final state partons which affects the hadronization.

In the Lund string model implemented in PYTHIA, color is conserved at each parton radiation, leading to a final state in leading color (LC). This may lead to partons close in phase space, but unrelated in color space in LC due to the model, which in nature might be color connected and form a hadron [115].

To achieve a better description, different models for color reconnection (CR) exist that try to implement or approximate effects beyond LC. The default model used in PYTHIA 8 allows a pair of partons to reconnect with a higher reconnection probability for low-p_T pairs. Altering the parameter which is scaling the reconnection probability to assess a systematic uncertainty is generally not believed to cover the space of physical possibilities [115]. Therefore, two different CR models are tested for the results of this thesis to assess a systematic uncertainty.

The “QCD inspired” model can reconnect all pairs of QCD dipoles considering QCD color rules, also allowing junction-like structures, as illustrated in Fig. 3.4. It stochastically samples possibilities beyond LC [115, 116]. In the “gluon move” model, gluons representing kinks in the color strings can be moved from one color string to another one to minimize the string length [117]. It is designed to show rather extreme effects [115].

Also for the cluster hadronization model, as implemented in HERWIG++ 2.4 [118], new models for CR are actively being developed [119].

Pileup:

Additional proton-proton interactions (pileup), as described in Section 3.1, are included in the MC simulation and the events are weighted to match the pileup distribution in data.

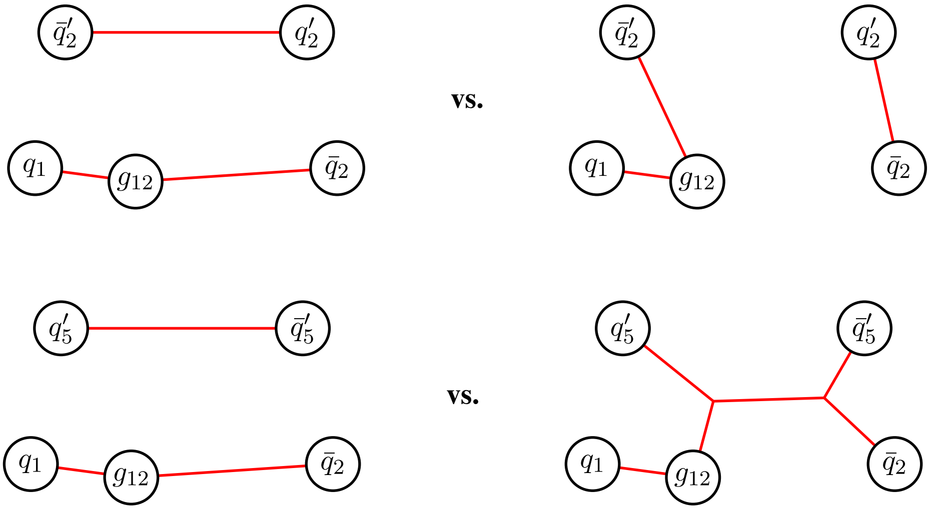

Figure 3.4: Illustration of different color-connection possibilities for a set of quarks (q) and gluons (g) in the “QCD inspired” model. Subscripts label color indices. The left illustrations show original LC string topologies and the right ones alternative connections allowed by the model. Top: The “2” indices match, making a different string connection possible. Bottom: The “2” and “5” indicies match cyclically, resulting in a possible junction-antijunction configuration. Both figures are taken from Ref. [116].

Detector simulation:

To reconstruct the simulated events consistently with data events, a detector simulation is used by means of the GEANT4 program. A description of the full geometry of the CMS experiment is implemented in GEANT4 and it simulates the detector response for all subsystems [120]. The resulting signals are fed to the reconstruction procedure described in Section 3.1 and are processed in the analysis like data. In addition to this reconstruction, generator information can be used for simulated events, e.g., to match reconstructed particles to generated ones.

4

Measurement of the top quark mass in the all-jets final state at $\sqrt{s} = 13\,\mathrm{TeV}$

Chapter contents

In this chapter the measurement of the top quark mass in the all-jets final state at a center-of-mass energy of $\sqrt{s} = 13\,\mathrm{TeV}$ is presented. The data have been taken in 2016 with the CMS detector, with a total integrated luminosity of $35.9\,\mathrm{fb}^{-1}$.

First, the event selection and the used data samples are described, including simulated samples generated using Monte Carlo (MC) event generators. The trigger used to record the events is described and the corrections which are applied to simulated events. A kinematic fit is performed as the next step, allowing for the reduction of the background in the analysis and the improvement of the top quark mass resolution. Next, the background estimation and the validation of the method are described. Following this, the actual mass extraction using the ideogram method is explained, including the pseudo-experiment generation and calibration. Furthermore, different systematic uncertainties are assessed using pseudo-experiments. The result of the measurement using data is presented in the last section of this chapter.

The whole analysis has been prepared in a “blind” way, i.e., using simulated events and pseudo-experiments, in order not to bias any selection or analysis step by evaluating the result on data. Only after taking all decisions on the analysis strategy, the mass extraction has been performed using CMS data.

The top quark mass is determined from the invariant mass distribution of the three jets associated to a top quark decay by fitting signal template distributions determined from simulation to data, i.e., it is a direct measurement as described in Section 1.4. The background distribution template is determined directly from data and the relative normalizations of background and signal are free parameters. It is therefore important to correctly describe the shape of the distributions of kinematic observables of jets with MC simulations, including b-quark-induced jets, while the total normalization is of less importance.

Following the measurement in the all-jets final state, the measurement using both the all-jets and lepton+jets final states simultaneously is presented in Chapter 5.

4.1 Event selection and data samples

An overview of the event selection is presented in this section, designed to select $t\bar{t}$ events in the all-jets final state as described in Section 1.3.

Jets are clustered from particle flow (PF) candidates with the anti-k_t algorithm [92, 93, 101] and a distance parameter of 0.4. Charged hadron subtraction is applied, i.e., charged hadrons are not considered in the clustering if they originate from a primary vertex other than the selected primary proton-proton interaction vertex as defined in Section 3.1. Only jets with $p_T > 30\,\text{GeV}$ reconstructed within $|\eta| < 2.4$ are used in the analysis. Furthermore, the jets have to fulfill the standard loose identification criteria (ID) listed in Table 4.1, which concern the composition of the jets, i.e., multiplicities and energy fractions of the clustered PF candidates.

Table 4.1: Loose jet identification criteria for jets with $|\eta| < 2.4$ [121]. The multiplicities and energy fractions are obtained from the clustered PF candidates.

Neutral Hadron Fraction	< 0.99
Neutral EM Fraction	< 0.99
Number of Constituents	> 1
Charged Hadron Fraction	> 0
Charged Multiplicity	> 0
Charged EM Fraction	< 0.99

The hadronic activity H_T quantifies the total jet energy of an event and is used for the event selection described below. It is defined as the scalar sum of all jet transverse momenta

$$H_T := \sum_{\text{jets}} p_T \,.$$

Jets initiated by b quarks (b jets) can be tagged by identifying secondary vertices stemming from the decay of b hadrons. This is important, because two b quarks are expected in the $\mathrm{t\bar{t}}$ decay, as described in Section 1.3. To be able to reconstruct secondary vertices, the jets need to be reconstructed within the tracker coverage, which is ensured by the η selection requirement. The combined secondary vertex algorithm (CSVv2) b tagger [102, 103] is used with the tight working point (WP), which provides an efficiency of approximately 50% and a mistag probability of approximately 0.1%. This working point is called CSVv2T, and corresponds to a discriminator value of > 0.9535.

An event needs to contain a well reconstructed vertex, i.e., fulfilling $|z_{\mathrm{vtx}}| \leq 24\,\mathrm{cm}$ and $|\rho| = \sqrt{x_{\mathrm{vtx}}^2 + y_{\mathrm{vtx}}^2} \leq 2\,\mathrm{cm}$. Selected events are required to contain at least six jets, at least two of which have to be tagged as b jets. The sixth jet (ordered in p_{T}) needs to have a transverse momentum of $p_{\mathrm{T}}(\mathrm{jet}_6) > 40\,\mathrm{GeV}$ and $H_{\mathrm{T}} > 450\,\mathrm{GeV}$ is required. These requirements closely follow the selection made at the trigger level (see Section 4.2). The two b jets have to be separated in $\Delta R = \sqrt{\Delta\phi^2 + \Delta\eta^2}$ by $\Delta R(\mathrm{b\bar{b}}) > 2.0$. For this requirement, the momenta of the b jets returned by the kinematic fit, described in Section 4.3, are used. This requirement is necessary for the background estimation to work, as described in Section 4.4.

Signal events are triggered with a six-jet-trigger, requiring at least one b tag. More details, especially concerning the trigger efficiency correction are described in Section 4.2. Only certified runs are used and this data sample[1] corresponds to an integrated luminosity of $35.9\,\mathrm{fb}^{-1}$. The integrated luminosities for the seven individual run eras (B-H) of the 2016 CMS data taking are shown in Fig. 4.1.

4.1.1 Simulated samples

Monte Carlo (MC) event generators are employed to simulate physics processes of interest, as described in Section 3.2. Signal $\mathrm{t\bar{t}}$ events are simulated in next-to-leading order (NLO) perturbative QCD using POWHEG v2 [107–110] interfaced with PYTHIA 8.219 [114] for parton shower and hadronization. The tune CUETP8M2T4 is used [122, 123]. For the parton distribution functions (PDFs), the NNPDF3.0 NLO set [113] is used with the strong coupling constant value of $\alpha_S = 0.118$. GEANT4 is used to simulate the response of the CMS detector [120]. A reference top quark mass of $m_{\mathrm{t}} = 172.5\,\mathrm{GeV}$ is assumed and the sample is normalized to the next-to-next-to-leading order (NNLO) cross section of $\sigma_{\mathrm{t\bar{t}}} = 831.76\,\mathrm{pb}$, calculated with the TOP++ program [39]. For this default sample, $N_{\mathrm{gen}} = 77\,229\,341$ events are simulated. To normalize the simulated sample to the recorded integrated luminosity $\mathcal{L}$, events are

---

[1] The `JetHT` primary dataset (PD) is used with the `03Feb2017` reconstruction in the `MINIAOD` data format and all runs from `Run2016B` to `Run2016H` are included. The exact PD paths are listed in Appendix A, Table A.1, in the dataset bookkeeping service (DBS) format. Only certified runs included in `Cert_271036-284044_13TeV_23Sep2016ReReco_Collisions16_JSON.txt` are analyzed. The global tag `80X_dataRun2_2016SeptRepro_v7` is used for the processing of data, except for Run2016H, for which `80X_dataRun2_Prompt_v16` is used. The global tag identifies a unique set of calibration parameters contained in the CMS corrections database.

Processing of all MC events, described in Section 4.1.1, is performed using the `80X_mcRun2_asymptotic_2016_TrancheIV_v8` global tag.

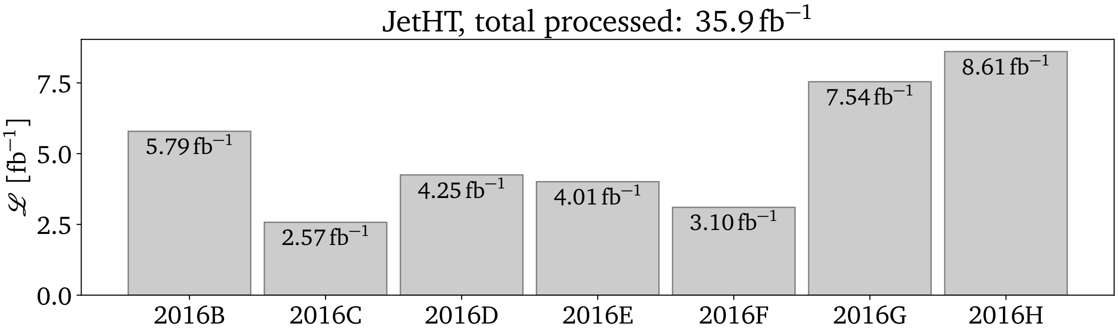

Figure 4.1: Run eras of the 2016 CMS data taking, divided into seven periods (B-H). The processed integrated luminosity for each period is shown, adding up to a total of $35.9\,\mathrm{fb}^{-1}$.

weighted with a factor $\mathcal{L} \cdot \sigma / N_{\mathrm{gen}}$. In addition, the event weights returned by the generator are applied. The name of the sample as contained in the CMS database is listed in Appendix A.2. For alternative masses, the cross section is rescaled following the parametrization [124, 125]

$$\sigma_{\mathrm{t\bar{t}}}(m_{\mathrm{t}}) = \sigma_{\mathrm{t\bar{t}}}(m_{\mathrm{t,\,ref}}) \left(\frac{m_{\mathrm{t,\,ref}}}{m_{\mathrm{t}}}\right)^4 \left[1 + a_1 \left(\frac{m_{\mathrm{t}} - m_{\mathrm{t,\,ref}}}{m_{\mathrm{t,\,ref}}}\right) + a_2 \left(\frac{m_{\mathrm{t}} - m_{\mathrm{t,\,ref}}}{m_{\mathrm{t,\,ref}}}\right)^2\right], \qquad (4.1)$$

using the default mass of 172.5 GeV as reference mass $m_{\mathrm{t,\,ref}}$ and the according cross section as $\sigma_{\mathrm{t\bar{t}}}(m_{\mathrm{t,\,ref}})$. The parameters have been determined in a common effort by the CMS and ATLAS Collaborations in order to provide a consistent prescription for the LHC experiments and can be found in Ref. [125]. Six other samples are utilized with generated top quark masses of 166.5, 169.5, 171.5, 173.5, 175.5, and 178.5 GeV. The corresponding cross sections, obtained from Eq. (4.1), and the numbers of generated events for these samples are listed in Table 4.2. Since the normalization is a free parameter in the final measurement, the assumed signal cross section for different generated masses does not influence the extracted top quark mass. In Appendix A the corresponding database paths are listed.

QCD multijet samples are generated in different bins of generator-level H_{T} utilizing leading order MADGRAPH with the MLM matching scheme [111, 112] for the matrix-element generation and PYTHIA 8 with the CUETP8M1 tune for the fragmentation and hadronization. The database names of the QCD multijet simulation samples[2] are listed in Appendix A.5. The numbers of generated events and the cross sections are listed in Table 4.3.

Further signal samples are used for which some parameters of the simulation are altered to assess different systematic uncertainties, as described in detail in Section 4.6. A list of the database paths of the alternative $\mathrm{t\bar{t}}$ samples for the systematic uncertainties can be found in Appendix A.

---

[2] For some H_{T} bins there are extension samples, labeled “ext”, which have been produced at a later point in time. The numbers of generated events split for the initial and the extension samples can be found in Table A.2 in Appendix A.

Table 4.2: The used generated top quark masses and their cross sections and numbers of generated events. The cross sections are calculated using Eq. (4.1), starting from the reference cross section of the default sample with $m_t^{gen} = 172.5\,\text{GeV}$.

m_t^{gen} [GeV]	$\sigma_{t\bar{t}}$ [pb]	N_{gen}
166.5	983.27	19380254
169.5	903.82	29369560
171.5	855.01	19578812
172.5	831.76	77229341
173.5	809.24	19419050
175.5	766.30	59384660
178.5	706.75	16377176

Table 4.3: Cross sections (σ) and numbers of generated events (N_{gen}) for the QCD samples, divided into different generator-level H_T bins.

H_T [GeV]	σ [pb]	N_{gen}
100— 200	27990000	80684349
200— 300	1712000	57580393
300— 500	347700	54537903
500— 700	32100	62271343
700—1000	6831	45412780
1000—1500	1207	15127293
1500—2000	119.9	11826702
2000— ∞	25.24	6039005

Additional proton-proton interactions (pileup) are included in the simulated samples and they are weighted to match the actual pileup distribution of the data, explained and shown in Section 3.1.

To correct for a difference of the b-tagging efficiency between data and simulation, simulated events are weighted by scale factors provided centrally by the CMS b-tagging working group [126, 127]. The uncertainties of these corrections only have a minor impact on the final measurement, as shown in Section 4.6.

Jet energy corrections (JEC), as described in Section 3.1.1, are applied to remove the influence of pileup (L1) and to correct the jet response compared to particle level jets (L2L3). For data, a further correction is applied to account for the different response observed in data and MC (L2L3Residual). The jet energy resolutions (JER) of the simulated events are smeared to match those observed in data according to the CMS recommendation [105], as described in Section 3.1.2.

4.2 Trigger

The High Level Trigger (HLT) path (`HLT_PFHT450_SixJet40_BTagCSV_p056`) used to record signal events requires the presence of at least six PF jets with $p_{\mathrm{T}} > 40\,\mathrm{GeV}$ and $|\eta| < 2.6$, and $H_{\mathrm{T}} > 450\,\mathrm{GeV}$. Additionally, one jet is required to be b tagged. It is thus specifically designed for the $\mathrm{t\bar{t}} \to 6$ jets topology. For the MC simulated samples, an HLT emulation is used. In addition, an efficiency correction for the difference between data and simulation needs to be determined. Since a total normalization difference does not change the result of the top quark mass extraction, it is only important to correct for efficiency differences which are a function of kinematic observables. For this, the efficiency with respect to a base trigger, requiring only H_{T} with a lower threshold, is calculated in the following and a correction scale factor is derived for the simulation. To exclude a possible bias due to the choice of the base trigger, which is also based on an H_{T}-selection, a cross check using a muon base trigger is performed, which is completely independent of the signal trigger. The correction scale factor obtained with this cross check is used to evaluate an additional systematic uncertainty, described below.

First, the efficiency of the signal trigger is calculated with respect to a base trigger. Here, a trigger requiring $H_{\mathrm{T}} > 350\,\mathrm{GeV}$, is used (`HLT_PFHT350`). The efficiency is calculated using the number of events passing the base trigger ($\#\,\{\mathrm{base}\}$) and the number of events passing both the signal and base trigger ($\#\,\{\mathrm{signal} \wedge \mathrm{base}\}$). The efficiency

$$\varepsilon = \frac{\#\,\{\mathrm{signal} \wedge \mathrm{base}\}}{\#\,\{\mathrm{base}\}}$$

is evaluated for events containing at least six jets with $|\eta| < 2.4$ in the offline selection, where one of the leading six jets needs to be b tagged (the nominal tight working point denoted CSVv2T). The ratio can be calculated in bins of different kinematic variables. It is shown as a function of the transverse momentum of the sixth jet (offline reconstruction) in Fig. 4.2. The trigger turn-on can be observed around the nominal threshold value of $p_{\mathrm{T}}(\mathrm{jet}_6) = 40\,\mathrm{GeV}$. It is smeared due to the differences of the HLT and offline jet reconstruction. In the plateau region, values of $> 95\%$ are reached.

Figure 4.3 (left) shows the same $p_{\mathrm{T}}(\mathrm{jet}_6)$ dependence of the efficiency for the medium and tight b tagging working points (CSVv2L and CSVv2M) in addition to the one shown before (CSVv2T). As expected, the efficiency is generally lower for looser working points (WPs). In addition, the trigger efficiency measurement is shown for the different run periods in Fig. 4.3 (right) to exclude possible inefficiencies that could be present in different periods. No dependence on the chosen run period is observed.

To determine a trigger efficiency correction for MC, the efficiency measurement is repeated for $\mathrm{t\bar{t}}$ simulation and compared to data. Figure 4.4 shows both, the data and MC efficiencies, as a function of $p_{\mathrm{T}}(\mathrm{jet}_6)$. Good agreement is observed in the plateau region, while the deviations become visible in the turn-on region and large for low p_{T}.

To account for this difference, a scale factor for the simulation is determined as a function of $p_{\mathrm{T}}(\mathrm{jet}_6)$ and H_{T}, because these are the kinematic variables used for the trigger. A two-dimensional sigmoid function

$$E(p_{\mathrm{T}}, H_{\mathrm{T}}) = e(p_{\mathrm{T}}; P, S_1, T_1) \cdot e(H_{\mathrm{T}}; 1, S_2, T_2) \tag{4.2}$$

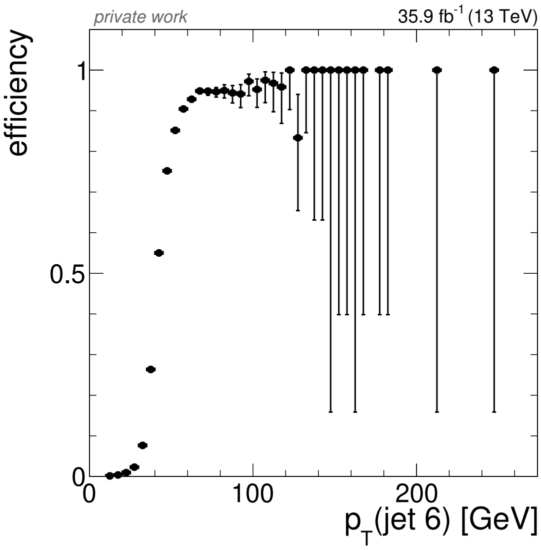

Figure 4.2: The efficiency of the signal trigger with respect to the base trigger in bins of $p_T(\mathrm{jet}_6)$ (offline reconstruction) in data. The error bars correspond to 68% CL Clopper-Pearson intervals.

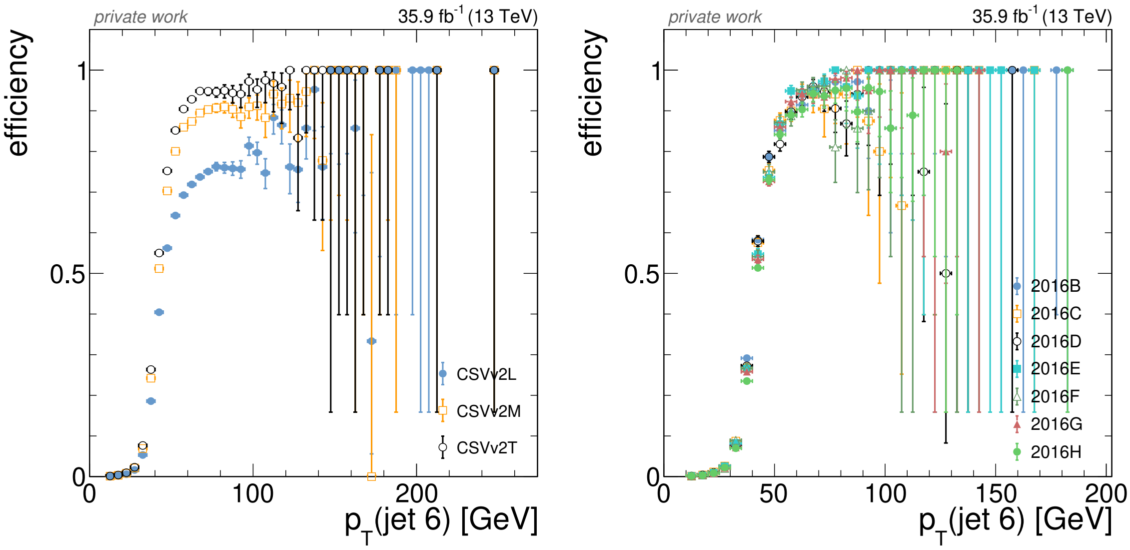

Figure 4.3: The efficiency of the signal trigger with respect to the base trigger in bins of $p_T(\mathrm{jet}_6)$ (offline reconstruction) in data. Left: For different b tagging working points. Right: For different run periods.

with

$$p_T \equiv p_T(\text{jet } 6)$$

and

$$e(x; P, S, T) = \frac{P}{1 + \exp\{-S \cdot (x - T)\}}$$

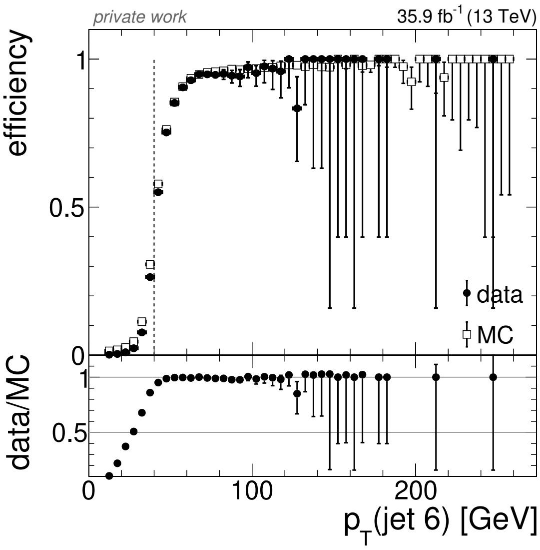

Figure 4.4: Comparison of the trigger efficiency in data and $\mathrm{t\bar{t}}$ MC simulation as a function of $p_\mathrm{T}(\mathrm{jet}_6)$.

is used to separately fit the data and MC efficiencies. Only one plateau parameter P is free, while the other one is set to unity, because it does not add a further degree of freedom. All measured quantities are used in units of GeV, i.e., the fit parameters are dimensionless. The ratio

$$\mathrm{SF}(p_\mathrm{T}, H_\mathrm{T}) = \frac{E_\mathrm{data}(p_\mathrm{T}, H_\mathrm{T})}{E_\mathrm{MC}(p_\mathrm{T}, H_\mathrm{T})} \tag{4.3}$$

is used as a scale factor to correct the simulation. For data, the fitted parameters are

$$\begin{aligned} P &= 0.957 \pm 0.057, \\ S_1 &= 0.28 \pm 0.11, \\ T_1 &= 40.7 \pm 1.7, \\ S_2 &= 0.028 \pm 0.025, \\ T_2 &= 466 \pm 30, \end{aligned}$$

and for the simulation the fit yields

$$\begin{aligned} P &= 0.970 \pm 0.045, \\ S_1 &= 0.25 \pm 0.11, \\ T_1 &= 39.4 \pm 1.8, \\ S_2 &= 0.024 \pm 0.018, \\ T_2 &= 455 \pm 29\,. \end{aligned}$$

The scale factor is applied to the simulated $\mathrm{t\bar{t}}$ events on an event-by-event basis as a function of the transverse momentum of the sixth jet and H_T. An uncertainty of 100% of the correction is assumed, i.e., the total effect of the correction.

Figure 4.5 shows the efficiency as functions of both observables for data and the corrected MC. Good agreement is observed as well as for the comparisons in η and ϕ of the sixth jet shown in Fig. 4.6 and the p_{T} of first and fifth jets (ordered in p_{T}) in Fig. 4.7.

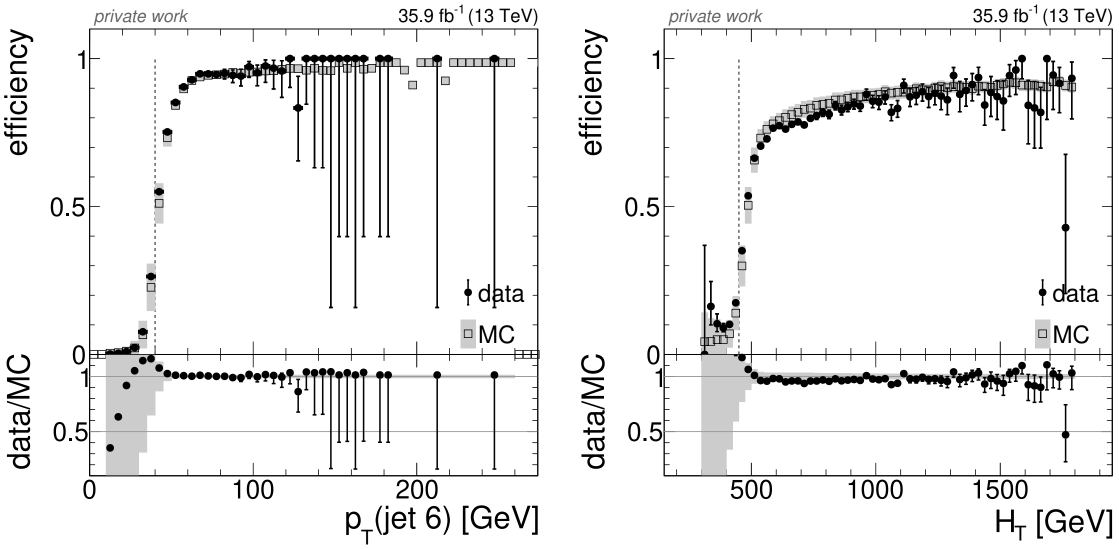

Figure 4.5: Comparison of the trigger efficiency in data and $t\bar{t}$ MC simulation as a function of $p_{\mathrm{T}}(\mathrm{jet}_6)$ (left) and H_{T} (right). The MC events are already corrected with the scale factor described by Eq. (4.3). The uncertainty band corresponds to 100% of the correction.

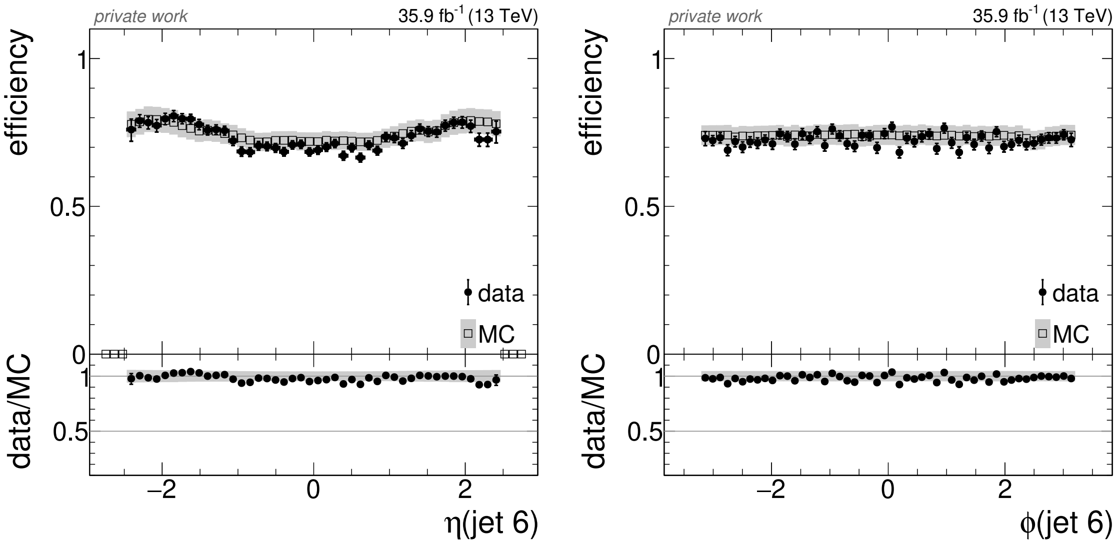

Figure 4.6: Comparison of the trigger efficiency in data and $t\bar{t}$ MC simulation as a function of η (left) and ϕ of the sixth jet. The MC events are already corrected with the scale factor described by Eq. (4.3). The uncertainty band corresponds to 100% of the correction.

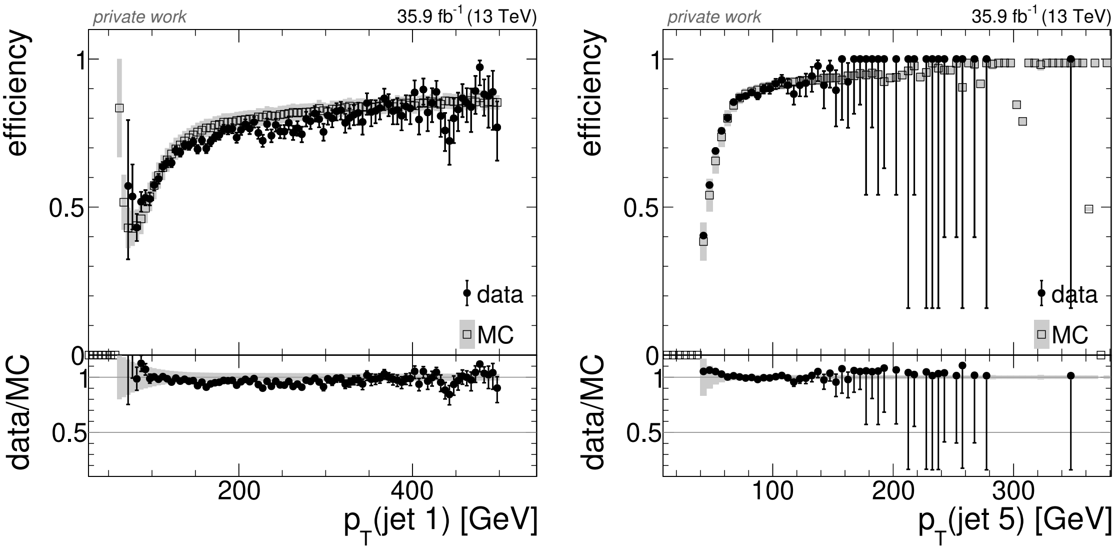

Figure 4.7: Comparison of the trigger efficiency in data and $t\bar{t}$ MC simulation as a function of p_T for the first jet (left) and the fifth jet (right), ordered in p_T. The MC events are already corrected with the scale factor described by Eq. (4.3). The uncertainty band corresponds to 100% of the correction.

Since the base trigger contains an H_T requirement, as the signal trigger does, a cross check using a different base trigger is performed, to exclude any bias. The single-muon trigger `HLT_IsoMu24` is used, requiring the presence of at least one isolated muon with $p_T > 24\,\text{GeV}$. The same efficiency measurement is performed using this base trigger, where the nominal correction derived before (Eq. (4.3)) is applied already. The result shown in Fig. 4.8 shows reasonable closure for the $p_T(\text{jet}_6)$ and H_T distributions.

An absolute difference of the efficiency is not of interest for the analysis, because the normalization is a free parameter. To be sure that any shape difference is covered by the uncertainty, an additional trigger uncertainty component is derived, as described in the following.

In addition to the nominal scale factor derived using the H_T base trigger, an alternative scale factor is derived using the single-muon base trigger. The same parametrization described by Eq. (4.2) is used, resulting in the following fit parameters for data

$$\begin{aligned} P &= 0.770 \pm 0.076, \\ S_1 &= 0.22 \pm 0.13, \\ T_1 &= 43.3 \pm 3.4, \\ S_2 &= 0.011 \pm 0.006, \\ T_2 &= 565 \pm 83, \end{aligned}$$

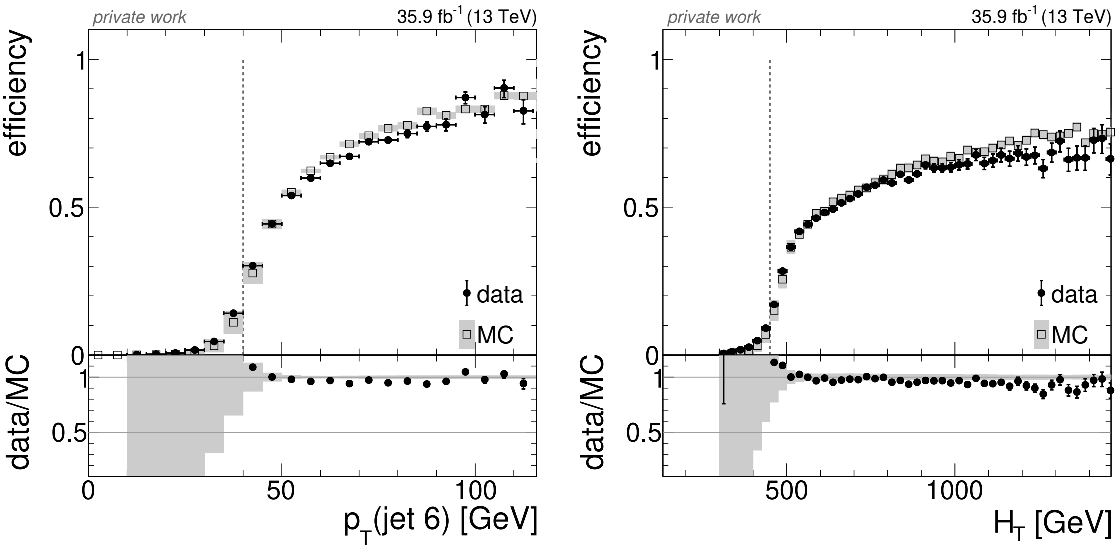

Figure 4.8: Comparison of the trigger efficiency in data and $t\bar{t}$ MC simulation as a function of $p_{\mathrm{T}}(\mathrm{jet}_6)$ (left) and H_{T} (right) using the single-muon base trigger. The MC events are already corrected with the nominal scale factor described by Eq. (4.3) derived using the H_{T} base trigger. The uncertainty band corresponds to 100% of the correction.

and these for simulation

$$\begin{aligned} P &= 0.856 \pm 0.072, \\ S_1 &= 0.19 \pm 0.10, \\ T_1 &= 43.1 \pm 3.3, \\ S_2 &= 0.011 \pm 0.006, \\ T_2 &= 573 \pm 73. \end{aligned}$$

The efficiencies after this version of the correction are show in Fig. 4.9 for $p_{\mathrm{T}}(\mathrm{jet}_6)$ and H_{T}, where good agreement can be observed.

For the total systematic uncertainty related to the trigger, two components are considered, finally. An 100% uncertainty of the nominal scale factor, differential in $p_{\mathrm{T}}(\mathrm{jet}_6)$ and H_{T}, is assumed, as described above. In addition, the scale factor derived using the single-muon base trigger is used instead of the nominal one and the difference with respect to the nominal result is quoted. For the result of the final measurement the larger effect of these two is used as the systematic uncertainty.

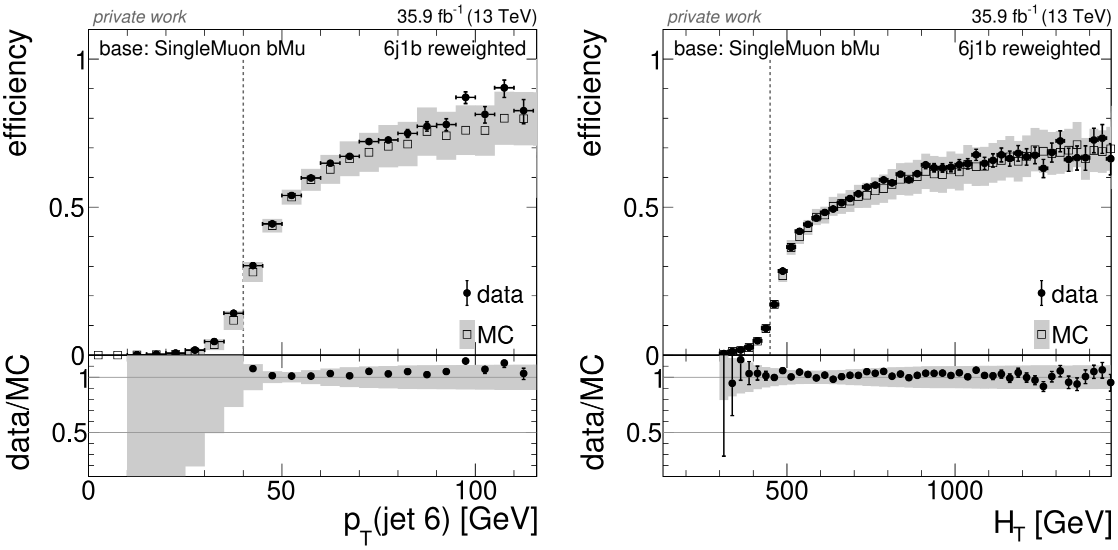

Figure 4.9: Comparison of the trigger efficiency in data and $\mathrm{t\bar{t}}$ MC simulation as a function of $p_\mathrm{T}(\mathrm{jet}_6)$ (left) and H_T (right) using the single-muon base trigger. The MC events are corrected with the alternative scale factor described by Eq. (4.3) derived using the single-muon base trigger. The uncertainty band corresponds to 100% of the correction.

4.3 Kinematic fit

To improve the resolution of the top quark mass, a kinematic fit is applied using the KinFit package [128] as implemented in the CMS software[3]. The idea is that the jet momenta are fitted to match the hypothesis of a $\mathrm{t\bar{t}}$ event. Using a selection criterion based on the goodness of the fit, background from multijet events can be reduced and the fraction of correct jet-parton assignments can be increased. The fit exploits the known topology of the signal events, i.e., pair production of a heavy particle and antiparticle, each decaying to Wb with $\mathrm{W} \to \mathrm{q\bar{q}'}$. The three-momenta, given by $(p_\mathrm{T}, \eta, \phi)$, of the jets are varied and the minimum of

$$\chi^2 = \sum_{j\in\mathrm{jets}} \left[\frac{\left(p_{\mathrm{T}j}^{\mathrm{reco}} - p_{\mathrm{T}j}^{\mathrm{fit}}\right)^2}{\sigma^2_{p_{\mathrm{T}j}}} + \frac{\left(\eta_j^{\mathrm{reco}} - \eta_j^{\mathrm{fit}}\right)^2}{\sigma^2_{\eta_j}} + \frac{\left(\phi_j^{\mathrm{reco}} - \phi_j^{\mathrm{fit}}\right)^2}{\sigma^2_{\phi_j}} \right]$$

is determined with the three constraints $m_{\mathrm{W}^+} = m_{\mathrm{W}^-} = 80.4\,\mathrm{GeV}$ and $m_\mathrm{t} = m_{\bar{\mathrm{t}}}$. This means that the jet momenta are varied to enforce the kinematic requirements belonging to the $\mathrm{t\bar{t}}$ topology in a way that least modifies the originally reconstructed jets. All quantities labeled “reco” refer to the originally reconstructed jets, while those labeled “fit” are varied in this minimization procedure. The resolutions in p_T, η, and ϕ for jet j are labeled σ_{Xj}. Compared to the object resolutions used in the analyses at

---

[3] The CMS software module `TopQuarkAnalysis/TopKinFitter` is used.

$\sqrt{s} = 8\,\text{TeV}$ [129], the noise term of the resolution has been increased[4] by quadratically adding 3 GeV, because of the higher pileup at $\sqrt{s} = 13\,\text{TeV}$.

Technically, the kinematic fit is a minimization of a function subject to contraints, solved using the method of Lagrange multipliers. The function to minimize is $\chi^2(\{\vec{p}_j^{\,\text{fit}}\})$, which depends on the jet momenta. The contraints g_c are introduced in a form such that $g_c(\{\vec{p}_j^{\,\text{fit}}\}) = 0$. In this case the three constraints are

$$\begin{aligned} g_1 &= m_{\text{W1}}^{\text{fit}} - 80.4\,\text{GeV}, \\ g_2 &= m_{\text{W2}}^{\text{fit}} - 80.4\,\text{GeV}, \\ g_3 &= m_{\text{t1}}^{\text{fit}} - m_{\text{t1}}^{\text{fit}}. \end{aligned}$$

These are incorporated into the Lagrange function $\mathcal{L}$ as summands to the actual function to minimize with the Lagrange multipliers λ_c as scalar factors,

$$\mathcal{L}(\{\vec{p}_j^{\,\text{fit}}\}, \{\lambda_c\}) = \chi^2(\{\vec{p}_j^{\,\text{fit}}\}) + \sum_c \lambda_c g_c(\{\vec{p}_j^{\,\text{fit}}\}).$$

Now the solution is obtained by finding the jet momenta $\{\vec{p}_j^{\,\text{fit}}\}$ and Lagrange multipliers $\{\lambda_c\}$ that solve

$$\vec{\nabla}_{\{\vec{p}_j^{\,\text{fit}}\},\{\lambda_c\}} \mathcal{L}(\{\vec{p}_j^{\,\text{fit}}\}, \{\lambda_c\}) = 0.$$

All possible parton-jet assignments are tested, but only b-tagged jets are used as b candidates and only non-b-tagged jets as light quark candidates. Equivalent choices (e.g., swapping the two jets originating from one W boson) are not considered separately. Of the remaining 12 possibilities only the assignment yielding the smallest χ^2 is used in the following. All quantities labeld “fit” in the following correspond to this solution at the minimum.

The χ^2 value can be used as a goodness-of-fit (gof) measure. It can be translated to a p-value using the general χ^2 probability density $f_n(\chi^2)$ with n degrees of freedom,

$$p_n(\chi^2) = \int_{\chi^2}^{\infty} f_n(x)\,\mathrm{d}x.$$

For n degrees of freedom, the probability density is given by

$$f_n(x) = \frac{1}{2^{n/2}\Gamma\left(\frac{n}{2}\right)} x^{n/2-1} \mathrm{e}^{-x/2}$$

for $x > 0$ and $f_n(x) = 0$ for $x \leq 0$. The argument is denoted x instead of χ^2 for better readability and Γ is the gamma function.

---

[4] It is worth noting that in principle anything reasonable could be assumed for the resolution, because the same algorithm is applied to data and simulated events. The latter have already been corrected to match the jet energy resolutions of data. Therefore, any scaling of the resolutions used in the kinematic fit will alter the χ^2 distribution for data and simulation in the same way. Such a change could be compensated by altering the selection made using the χ^2 value.

For the all-jets channel, there are $3 \times 6 = 18$ fit parameters and all 18 momentum components are measured. Together with the three constraints, $n = 18 - (18 - 3) = 3$ degrees of freedom remain[5]. For three degrees of freedom the probability density function reads

$$f_3(\chi^2) = \sqrt{\frac{\chi^2}{2\pi}} \mathrm{e}^{-\chi^2/2}$$

and the corresponding p-value is given by

$$p_3(\chi^2) = \int_{\chi^2}^{\infty} f_3(x)\,\mathrm{d}x = 1 - \mathrm{erf}\left(\sqrt{\frac{\chi^2}{2}}\right) + \sqrt{\frac{2\chi^2}{\pi}} \mathrm{e}^{-\chi^2/2},$$

where

$$\mathrm{erf}(x) := \frac{1}{\sqrt{\pi}} \int_{-x}^{x} e^{-t^2}\,\mathrm{d}t$$

is the Gauss error function. In the following, this “goodness-of-fit probability” is denoted $P_{\mathrm{gof}} := p_3(\chi^2)$.

In simulation, event generator information can be used to validate the correct assignment of the reconstructed jets to the top quark decay products. Events are classified accordingly as *correct* or *wrong* permutations. A parton-jet assignment is considered correct if the jets can be matched unambiguously to the right partons within $\Delta R < 0.3$. Wrong permutations can occur, because a wrong parton-jet assignment yields a smaller χ^2 than the correct one or a jet from the $\mathrm{t\bar{t}}$ system is out of acceptance, not reconstructed, or failing the identification requirements.

Figure 4.10 shows the χ^2 distribution of $\mathrm{t\bar{t}}$ events, separately for correct and wrong permutations. The correct permutations peak at low values of χ^2, indicating a good fit result, because the reconstructed jet momenta only have to be varied little with respect to the resolutions to fit the $\mathrm{t\bar{t}}$ hypothesis. Events with wrong assignments tend to large values of χ^2, because momenta of one or more jets are forced far off their reconstructed values.

Events are required to fulfill $P_{\mathrm{gof}} > 0.1$ for the best assignment. This is equivalent to a selection of $\chi^2 < 6.3$, which is fulfilled for 62% of the correctly assigned events, while 96% of the wrongly assigned events are removed. Requiring $P_{\mathrm{gof}} > 0.1$ increases the fraction of correct permutations from 6.4% to 50.8%.

Figure 4.11 shows the P_{gof} distribution of $\mathrm{t\bar{t}}$ events for $P_{\mathrm{gof}} > 0.1$. The rather flat P_{gof} distribution for the correct permutations shows that the assumed jet energy resolutions are reasonably well-suited, although a small residual slope is present. In general, the p-value of any fit of a correct model is uniformly distributed. The rise towards small values of P_{gof} can be mainly attributed to a non-perfect description of the jet resolutions used in the kinematic fit. The wrong assignments show a clear peak at low P_{gof}, corresponding to large χ^2 values as described above.

---

[5] In contrast, for the lepton+jets channel there are $n = 2$ degrees of freedom, because the neutrino z component cannot be measured and only the x and y components are obtained from the missing transverse momentum.

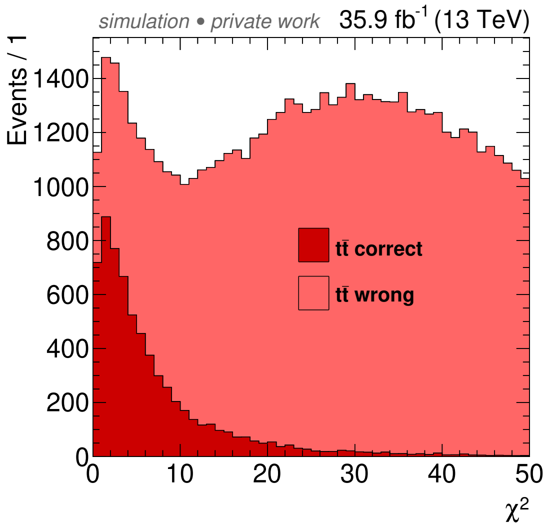

Figure 4.10: Kinematic fit χ^2 distribution distribution for correct and wrong tt̄ permutations for the best assignment selected by the kinematic fit, using simulated tt̄ events only.

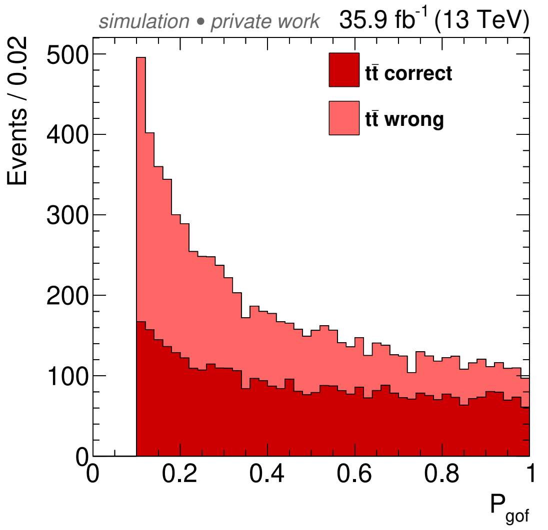

Figure 4.11: Kinematic fit P_{gof} distribution for correct and wrong tt̄ permutations for the best assignment selected by the kinematic fit, using simulated tt̄ events only. The $P_{\text{gof}} > 0.1$ selection is already applied for purposes of presentation.

Figure 4.12 shows the top quark mass distributions for the assignment chosen by the fit for the reconstructed ($m_{\text{t}}^{\text{reco}}$) and fitted ($m_{\text{t}}^{\text{fit}}$) jets. For $m_{\text{t}}^{\text{reco}}$, the top quark is used which has the associated b jet with the larger p_{T}. The top plot displays $m_{\text{t}}^{\text{reco}}$ before the P_{gof} requirement, while the bottom plots show $m_{\text{t}}^{\text{reco}}$ and $m_{\text{t}}^{\text{fit}}$ for $P_{\text{gof}} > 0.1$. In all cases the correct permutations form a peak approximately around the assumed top quark mass of 172.5 GeV, while the wrong permutations show a broad and more flat distribution reaching to higher masses. This high-mass peak is greatly reduced by the

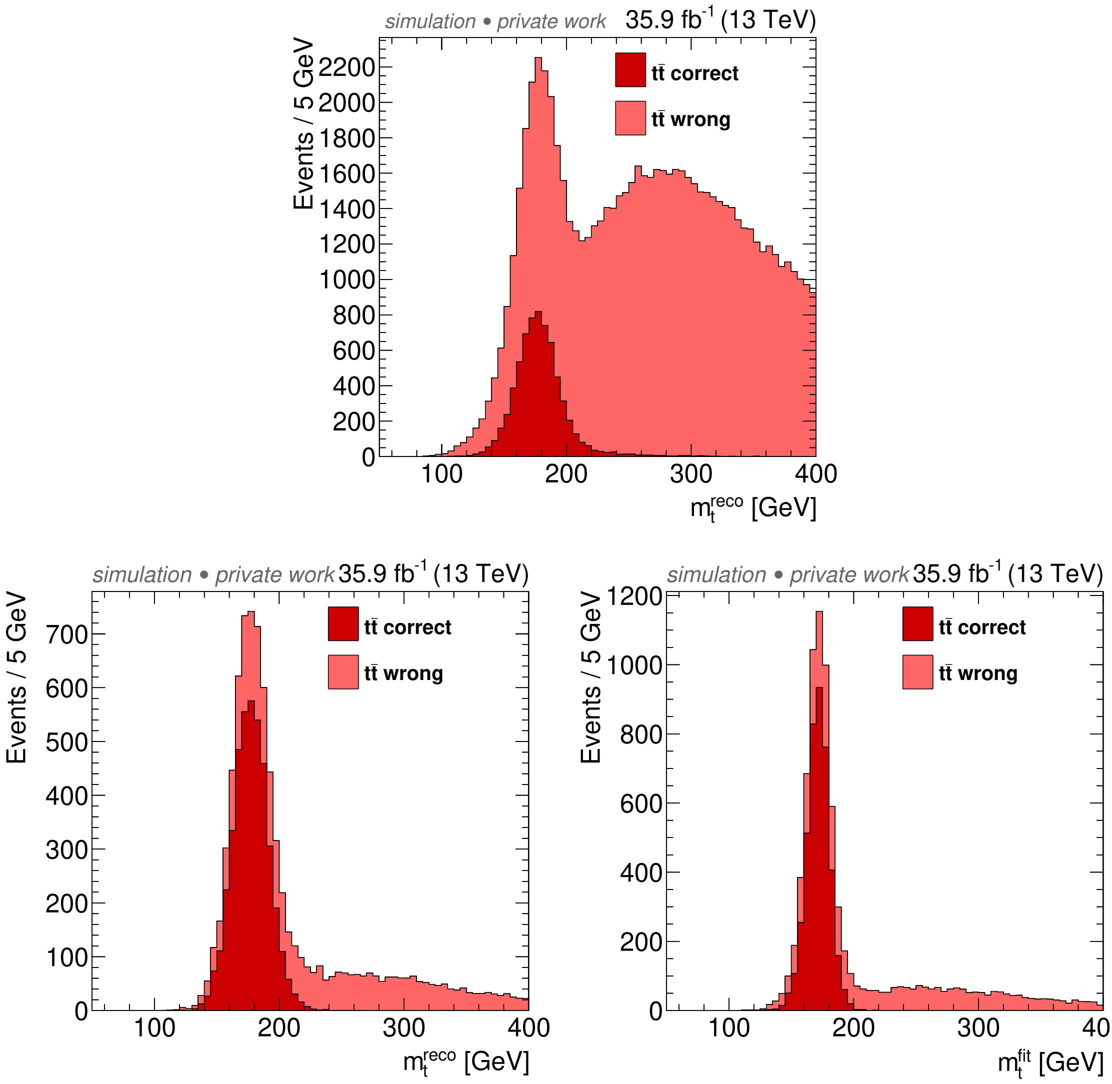

Figure 4.12: Top quark mass distributions calculated from the originally reconstructed jets (top and bottom left) and from the fitted jets (bottom right). The top plot displays $m_\mathrm{t}^\mathrm{reco}$ before the P_gof requirement, while the bottom plots show $m_\mathrm{t}^\mathrm{reco}$ and $m_\mathrm{t}^\mathrm{fit}$ for $P_\mathrm{gof} > 0.1$. For $m_\mathrm{t}^\mathrm{reco}$, the top quark is used which has the associated b jet with the larger p_T. A similar distribution is obtained for the other top quark, which is not shown here.

P_{gof} selection and the overall ratio of correct to wrong assignments is improved, in total resulting in a sharp top quark mass peak with a flat tail towards higher masses. The fit improves the mass resolution from 14.0 GeV to 8.8 GeV for the correct permutations, both evaluated after the $P_{\text{gof}} > 0.1$ requirement. Figure 4.13 shows the reconstructed W boson mass before and after the P_{gof} selection. The average of the masses of both W bosons in the event is used. Similar to $m_{\text{t}}^{\text{reco}}$, the correct permutations for $m_{\text{W}}^{\text{reco}}$ form a peak around the W boson mass, while for the wrong assignments there is a large tail at higher masses, which is drastically reduced by the kinematic fit selection. The fitted W boson mass is not shown, because it has exactly the same value for all events, as enforced by the kinematic fit.

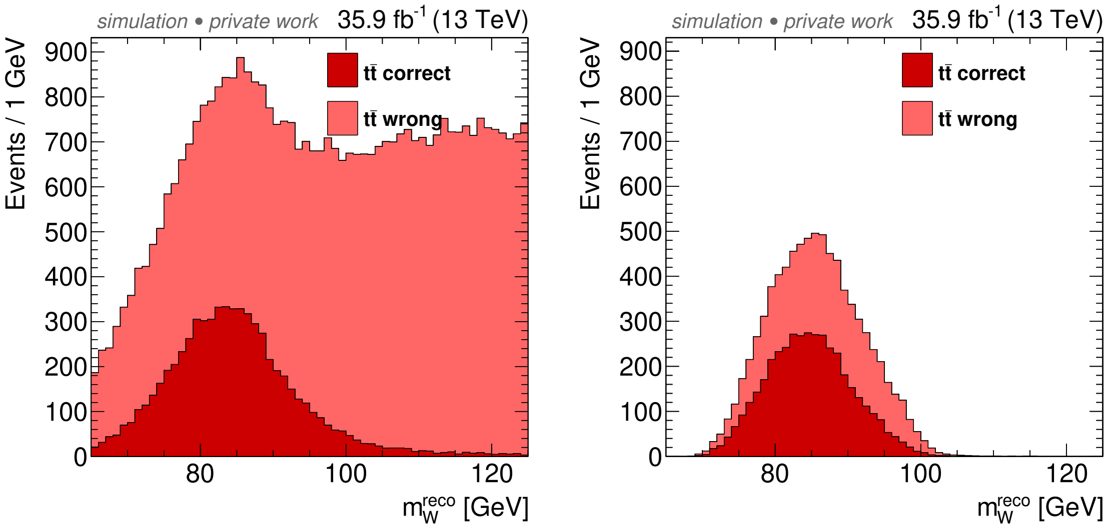

Figure 4.13: W boson mass distributions before and after the P_{gof} selection calculated from the originally reconstructed jets. The average of the masses of both W bosons in the event is used. The left plot displays $m_{\text{W}}^{\text{reco}}$ before the P_{gof} requirement, while the right plot shows $m_{\text{W}}^{\text{reco}}$ for $P_{\text{gof}} > 0.1$. The fitted W boson mass is not shown, because it has exactly the same value for all events, as enforced by the kinematic fit.

A cut flow is listed in Table 4.4, showing the number of selected data and signal events after different selection stages. Additionally, the purity of the selected sample is given after each selection step, i.e., the ratio of expected $\text{t}\bar{\text{t}}$ signal events to selected data events. After the final selection, 10 799 data events remain, of which 8 126 are expected to be $\text{t}\bar{\text{t}}$ events. Thus, only approximately 25% of the selected events are background stemming from non-$\text{t}\bar{\text{t}}$ multijet production.

Table 4.4: Cut flow showing the number of selected data and signal events after different selection stages. The purity is the ratio of expected $\mathrm{t\bar{t}}$ events to selected data events.

Selection step	data	$\mathrm{t\bar{t}}$	purity
Trigger, 6 jets, 2 b tags	1392670	237126	17.0%
$H_\mathrm{T} > 450\,\mathrm{GeV}$	1342630	232498	17.3%
$p_\mathrm{T}(\mathrm{jet}_6) > 40\,\mathrm{GeV}$	1130714	212697	18.8%
$\Delta R(\mathrm{b\bar{b}}) > 2.0$	359456	103882	28.9%
$P_\mathrm{gof} > 0.1$	10799	8126	75.2%

4.4 Background estimation

Events from non-$\mathrm{t\bar{t}}$ multijet production can still pass the selection criteria and provide a substantial background due to the huge production cross section. Therefore, an estimate of this purely combinatorial background is needed. Because the multijet background is hard to simulate and not perfectly modeled, the background is predicted from data, as described in the following.

Background multijet events are selected, because they either contain jets originating from b quarks or light jets mistagged as b jets. A fraction of these events is fulfilling the goodness-of-fit criterion due to combinatorial chance, but not due to an underlying decay topology. Therefore, it is assumed that b jets can be exchanged with light-flavor jets for the background estimation, which is purely data driven. This is possible, because the probability for mimicking the signal topology does not depend on whether events contain light-flavor jets only or include b jets, as depicted in Fig. 4.14. The $\Delta R(\mathrm{b\bar{b}}) > 2.0$ selection described before is important for the background prediction, because it breaks down for small values of $\Delta R(\mathrm{b\bar{b}})$. This is due to gluons splittings to two b quarks ($\mathrm{g} \rightarrow \mathrm{b\bar{b}}$), which tend to be collimated, such that the opening angle of the resulting b jets is small. This correlated production of two jets cannot be reproduced by the background estimation method, as shown in Section 4.4.1, because it is based on the assumption of purely combinatorial constellations.

For the background estimation, the same selection is applied as described above, but instead of requiring two b-tagged jets, events with exactly zero b tags are used. For this veto a very loose b tagging working point of CSVv2 > 0.2 is used in order to exclude signal contamination of $\mathrm{t\bar{t}}$ events in this QCD-multijet-enriched sample. For this selection only 0.2% of the events are $\mathrm{t\bar{t}}$ events, as determined using $\mathrm{t\bar{t}}$ and QCD simulation samples. A trigger similar to the signal trigger is used for this selection, which is not requiring the presence of b jets, namely `HLT_PFHT450_SixJet40`. This trigger is prescaled, i.e., only a certain fraction of events that would be selected are actually recorded. The prescale value varied during the data taking. Its effective total value is not important, as long as enough events are recorded to perform the background estimation with enough statistical precision, which is verified in the following.

The kinematic fit is applied as before, but here any of the six light jets can be assigned to the partons originating from the W decays, as well as those serving as b quarks. This leads to 90 possible permutations per event that have to be evaluated, which is

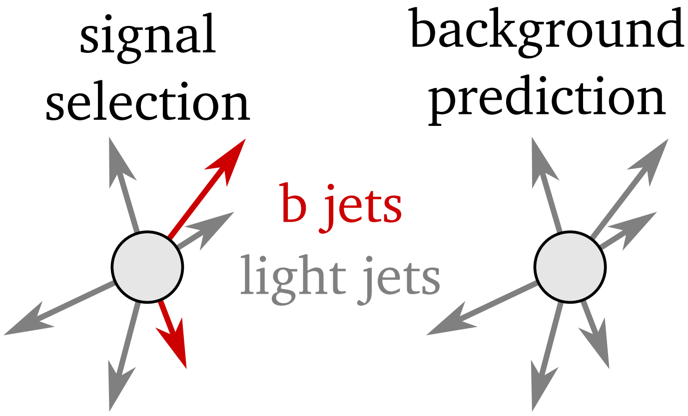

Figure 4.14: Left: Sketch of the event topology of the signal selection, requiring b tagged jets. Right: Sketch of the event topology of the selection used for the background prediction, containing zero b tagged jets. Kinematically, both can mimic the $t\bar{t}$ event topology with the same probability.

still computable within a reasonable run time. This method allows to determine the kinematic shapes of the background, but the normalization is unknown. The relative normalization of signal and background is a free parameter in the final measurement, so the knowledge of the background shape is sufficient. In the following plots, the background is simply normalized to the difference of the integrals of the data and expected signal distributions (#background events = #data events − #expected signal events). This background estimation sample contains approximately five times the number of background events expected from direct QCD multijet background simulation, so it provides a good statistical precision.

4.4.1 Validation using simulation

To validate the background estimation method, the procedure described above is applied to simulated QCD multijet events. The result is compared to the corresponding distributions obtained by simply applying the signal selection (i.e., two b tags) to the QCD multijet simulation, referred to as *direct simulation*.

Figure 4.15 shows the fitted top quark mass and reconstructed W boson mass distributions, which are of importance in the mass extraction procedure. The histograms are normalized to unity, because the prediction has to be scaled to fit the total number of events selected for the direct simulation. This is also reflected in the smaller error bars of the prediction with respect to the direct simulation. The lower panels show the ratio between direct simulation and prediction. In both cases the prediction agrees well with the direct simulation within the statistical precision.

As described above, the $\Delta R(b\bar{b}) > 2.0$ selection is important for the background prediction, because it breaks down for small values of $\Delta R(b\bar{b})$, as shown in Fig. 4.16. Here, the $\Delta R(b\bar{b})$ selection is omitted to show the region of $\Delta R(b\bar{b}) < 2.0$. The histograms are normalized in the $\Delta R(b\bar{b}) > 2.0$ region, where good agreement is observed. For $\Delta R(b\bar{b}) < 2.0$, the prediction shows a flat behavior, while the direct simulation is en-

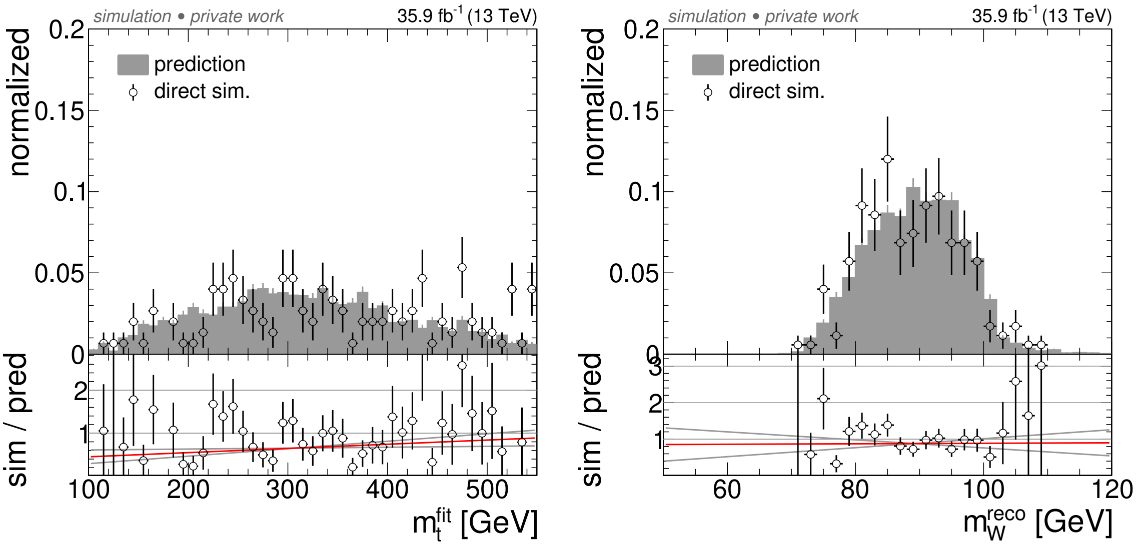

Figure 4.15: Test of the background prediction. Comparison of the background prediction as obtained with the method later applied to data to the direct simulation (both on QCD multijet simulation) for the fitted top quark mass (left) and reconstructed W boson mass (right) distributions. Both histograms are normalized to unity. In the ratio plot the best least squares straight line fit is shown in red and the ±1σ variations of the slope parameter in gray.

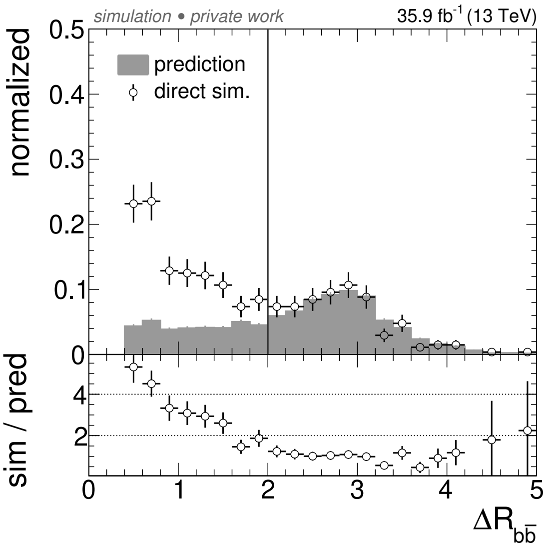

Figure 4.16: Comparison of the background prediction as obtained with the method later applied to data to the direct simulation (both on QCD multijet simulation) for the $\Delta R(b\bar{b})$ distribution. Both histograms are normalized to unity in the region of $\Delta R(b\bar{b}) > 2.0$, indicated by the vertical line. In the lower panel, the ratio between direct simulation and prediction is shown.

hanced at low values, owing to collimated g → $\mathrm{b\bar{b}}$ splittings. Therefore the $\Delta R(\mathrm{b\bar{b}})$ selection is applied, enabling the background prediction and at the same time reducing the overall background contribution.

The only important observables which have to be described properly are $m_{\mathrm{t}}^{\mathrm{fit}}$ and $m_{\mathrm{W}}^{\mathrm{reco}}$, shown in Fig. 4.15. Further distributions for the leading six jets are shown in Figs. 4.17 and 4.18, namely the p_{T} and η distributions. No plots are shown for ϕ, because they are flat within the statistical precision, as the detector is symmetric in ϕ. The kinematic distributions for all six jets show reasonable agreement.

To estimate the systematic uncertainty introduced by the background prediction method, the ratio shown in Fig. 4.15 is used and a straight line fit is applied using the least squares method. Because the normalization of the background is free in the measurement, only the uncertainty of the slope parameter, i.e., the shape, is of interest. Because the slope parameter m would be correlated to the offset b in the simple fit equation

$$y = mx + b,$$

a fit with decorrelated parameters is performed instead. For this, the center of gravity

$$x_0 = \sum_{i=1}^{N} \frac{x_i}{\sigma_i^2} \Bigg/ \sum_{i=1}^{N} \frac{1}{\sigma_i^2}$$

is determined and the fit equation is modified to

$$y = m(x - x_0) + b.$$

For the $m_{\mathrm{t}}^{\mathrm{fit}}$ distribution, the fit of the slope parameter yields $0.00097 \pm 0.00076\,\mathrm{GeV}^{-1}$ and for the $m_{\mathrm{W}}^{\mathrm{reco}}$ distribution $0.00067 \pm 0.01163\,\mathrm{GeV}^{-1}$. These are compatible with zero within 1.3 and 0.06 standard deviations, respectively. Therefore, no correction is applied, but the variations are used to determine the systematic uncertainty. In addition to the best fit result (red line), the result using the $\pm 1\sigma$ variations of the slope parameter are shown (gray lines) in Fig. 4.15. These variations are used to reweight the predicted distribution and by means of this determine the shape uncertainty of the background distribution (see Sections 4.5.1 and 4.6.1).

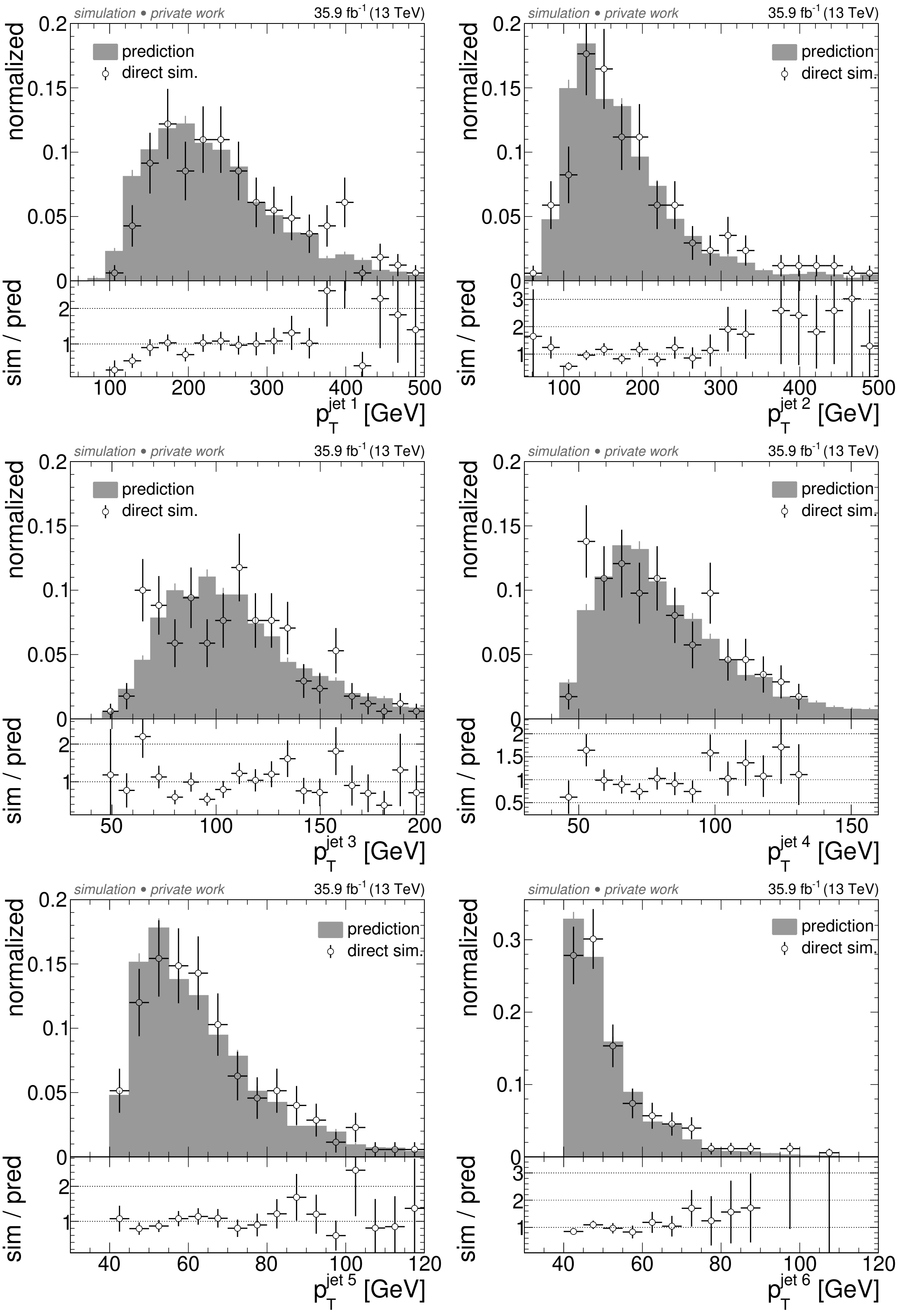

Figure 4.17: Comparison of the background prediction as obtained with the method later applied to data to the direct simulation (both on QCD multijet simulation) for the p_{T} distributions of the six leading jets. Both histograms are normalized to unity. In the lower panel, the ratio between direct simulation and prediction is shown.

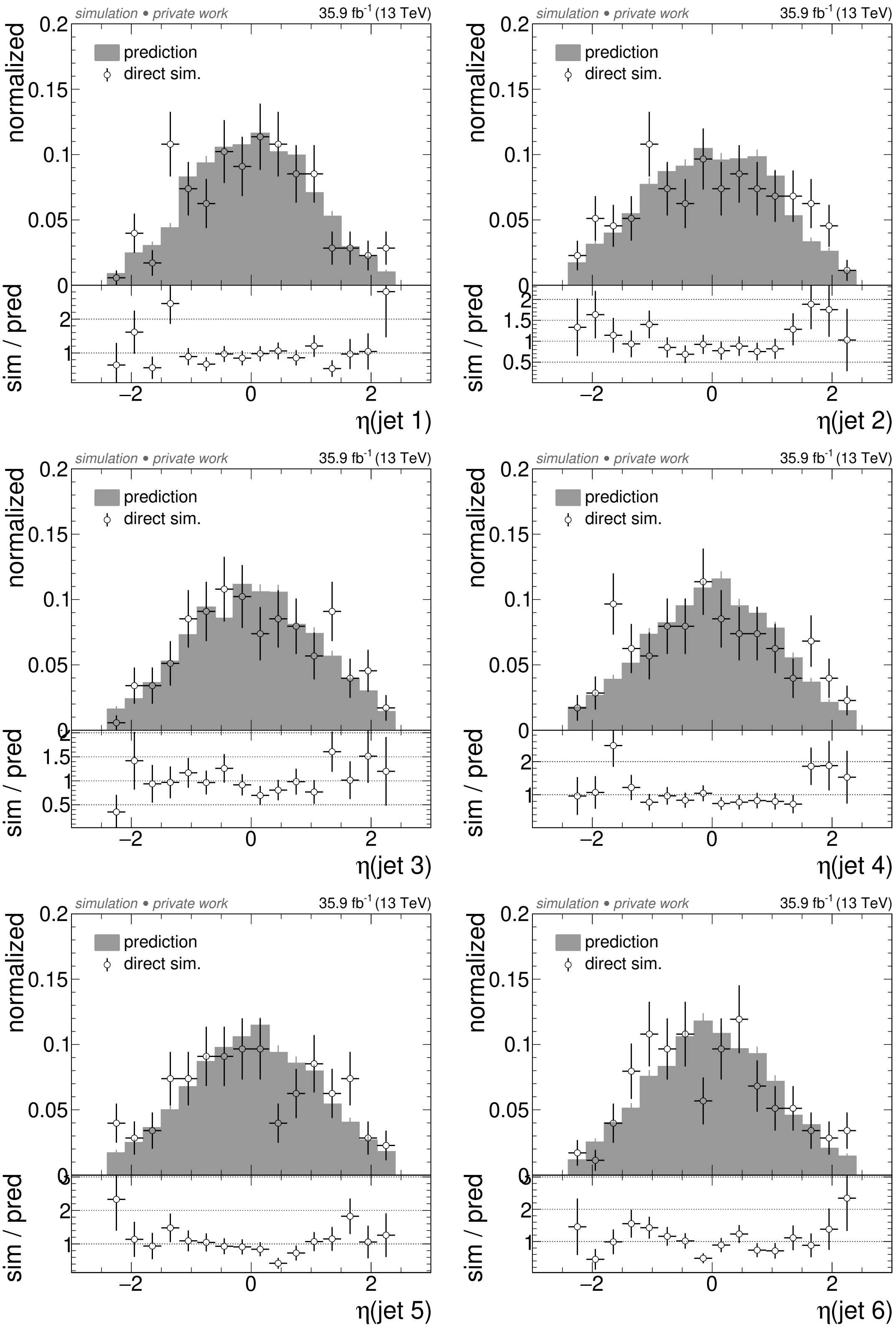

Figure 4.18: Comparison of the background prediction as obtained with the method later applied to data to the direct simulation (both on QCD multijet simulation) for the η distributions of the six leading jets. Both histograms are normalized to unity. In the lower panel, the ratio between direct simulation and prediction is shown.

4.4.2 Application to data

The background estimation method has only been applied to simulation in Section 4.4.1 to validate the performance. For the actual measurement, it is applied to data in order not to rely on the modeling of the background in simulation. Figure 4.19 shows the $m_{\mathrm{t}}^{\mathrm{fit}}$ and $m_{\mathrm{W}}^{\mathrm{reco}}$ distributions already shown in Section 4.4.1 for the direct QCD multijet simulation and the background estimate obtained from simulation. Here, also the actual prediction using data is shown, which is used in the following. The general shapes of the prediction from data are similar to those expected from simulation for both distributions and the method provides a good statistical precision. The prediction from data shows a softer spectrum, though, i.e., the distributions tend to lower mass scales compared to the simulated ones. This shows that it is useful to use a background estimate from data, because the multijet background is hard to simulate and not perfectly modeled.

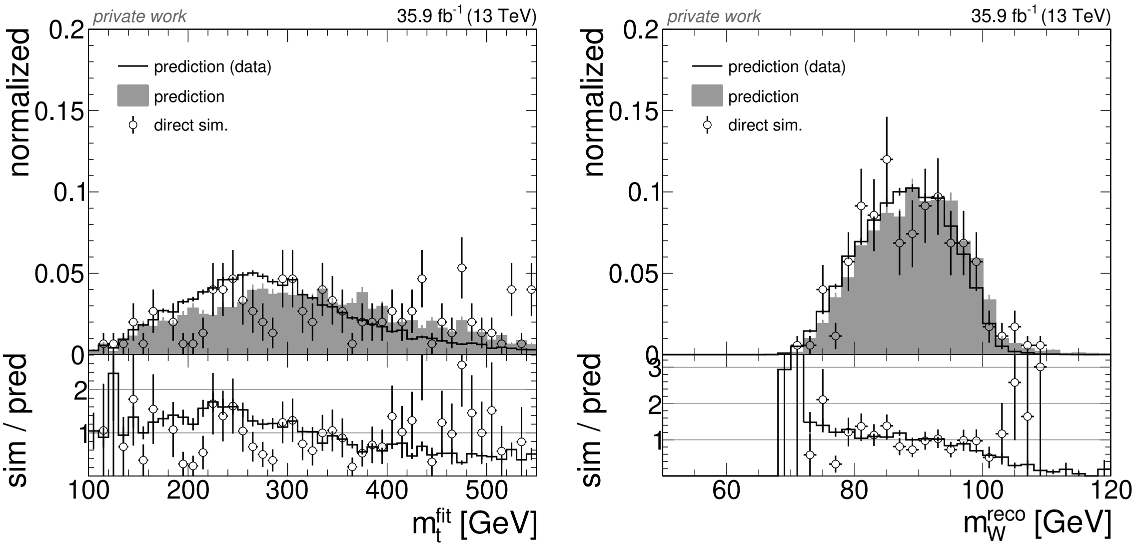

Figure 4.19: Comparison of the background prediction applied to QCD multijet simulation (gray histogram) to the direct simulation (open circles) for the fitted top quark mass (left) and reconstructed W boson mass (right) distributions, as already shown in Fig. 4.15. In addition to Fig. 4.15, the actual background prediction obtained from data is shown (black histogram). All histograms are normalized to unity. The lower panel shows the ratio to the prediction obtained from simulation. The error bars represent the respective statistical uncertainties of the histogram bins.

Figures 4.20, 4.21, and 4.22 show comparisons of data to $\mathrm{t\bar{t}}$ signal simulation with the multijet background prediction applied. Systematic uncertainties are included as hashed bands in the plots. These are described in Section 4.6. The P_{gof}, $\Delta R(\mathrm{b\bar{b}})$, and H_{T} distributions, shown in Fig. 4.20, are described well. These observables are of special importance, because they are used for the event selection. The reconstructed top quark mass distribution, i.e., the invariant mass calculated using the jets before the kinematic fit, is also shown. Because in general both top quarks in the event have different invariant masses before the kinematic fit, the average of both is shown for $m_{\mathrm{t}}^{\mathrm{reco}}$. In addition, the p_{T} and η distributions of the first six jets, ordered in p_{T}, are shown in Figs. 4.21 and 4.22, also showing a reasonable agreement between data and prediction within the quoted uncertainties. No plots are shown for ϕ, because they are flat within the statistical precision, as the detector is symmetric in ϕ.

Figure 4.23 shows the final distributions of fitted top quark mass and reconstructed W boson mass values. The average of the masses of both W bosons in the event is used. These are the two observables that are used in the final measurement. The $m_{\mathrm{t}}^{\mathrm{fit}}$ peak is dominated by correct assignments. The multijet background contribution in this final selections is less than 25%, as described above, and it is mainly distributed towards larger masses compared to the $\mathrm{t\bar{t}}$ events with correct assignments. In the $\mathrm{t\bar{t}}$ peak region, which is the most relevant for the measurement, the background contribution is very small.

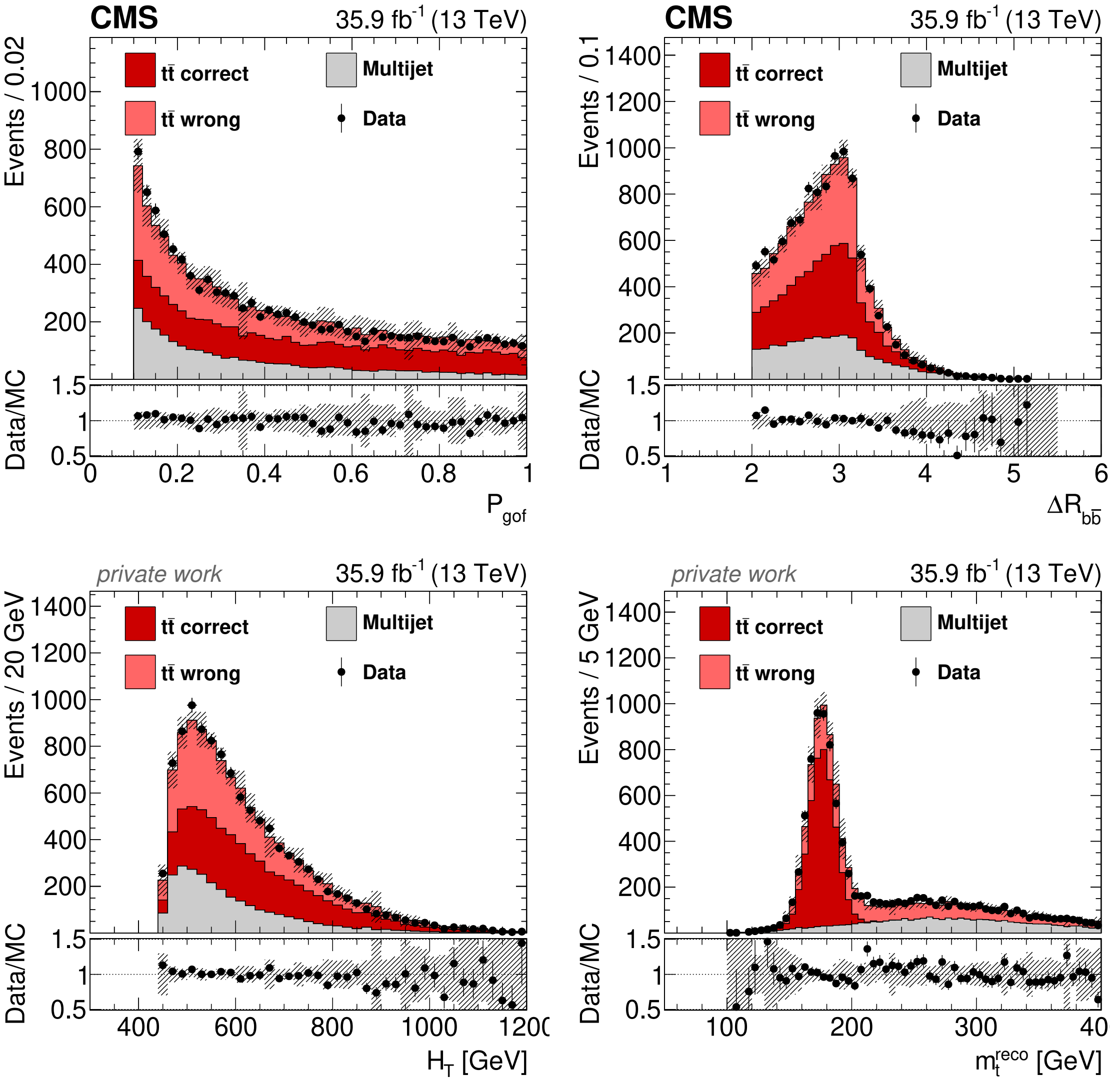

Figure 4.20: The P_{gof}, $\Delta R(\text{b}\bar{\text{b}})$ [1], H_{T}, and $m_{\text{t}}^{\text{reco}}$ distributions of data compared to signal MC and the multijet background estimate. Because in general both top quarks in the event have different invariant masses before the kinematic fit, the average of both is shown for the reconstructed top quark mass $m_{\text{t}}^{\text{reco}}$. The hashed bands represent the uncertainty of the prediction, as described in Section 4.6.

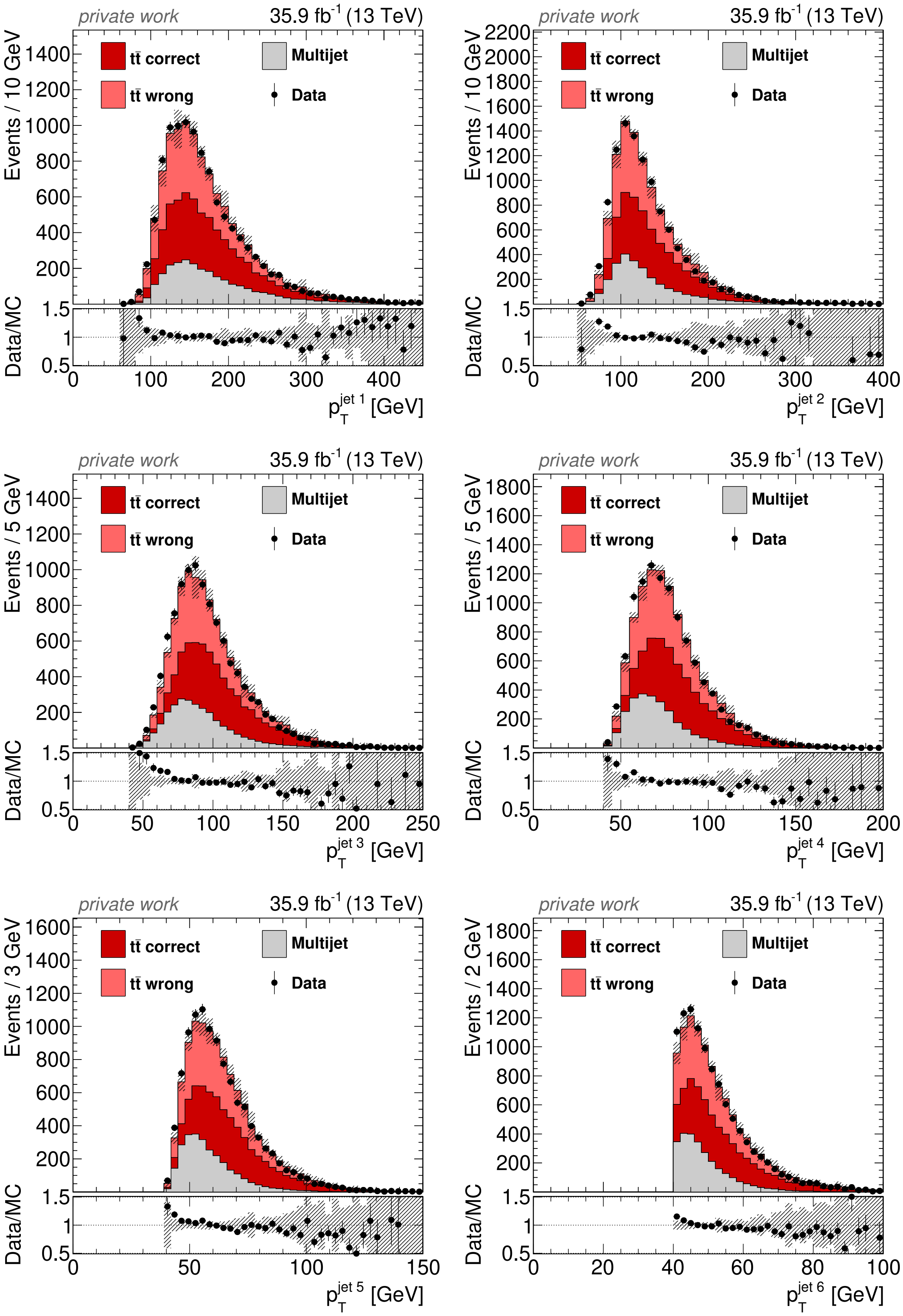

Figure 4.21: The p_T distributions of data compared to signal MC and the multijet background estimate for the six leading jets. The hashed bands represent the uncertainty of the prediction, as described in Section 4.6.

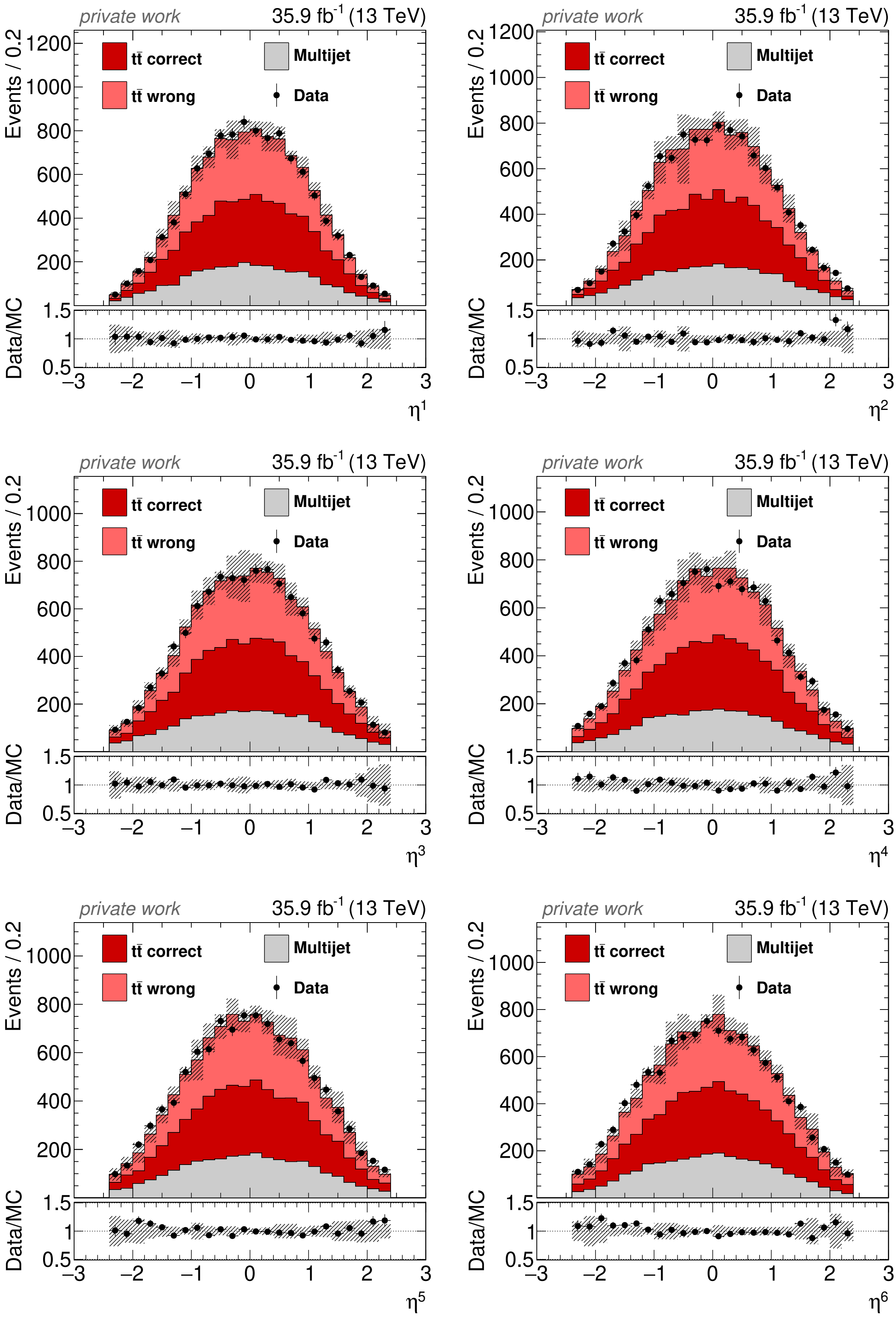

Figure 4.22: The η distributions of data compared to signal MC and the multijet background estimate for the six leading jets. The hashed bands represent the uncertainty of the prediction, as described in Section 4.6.

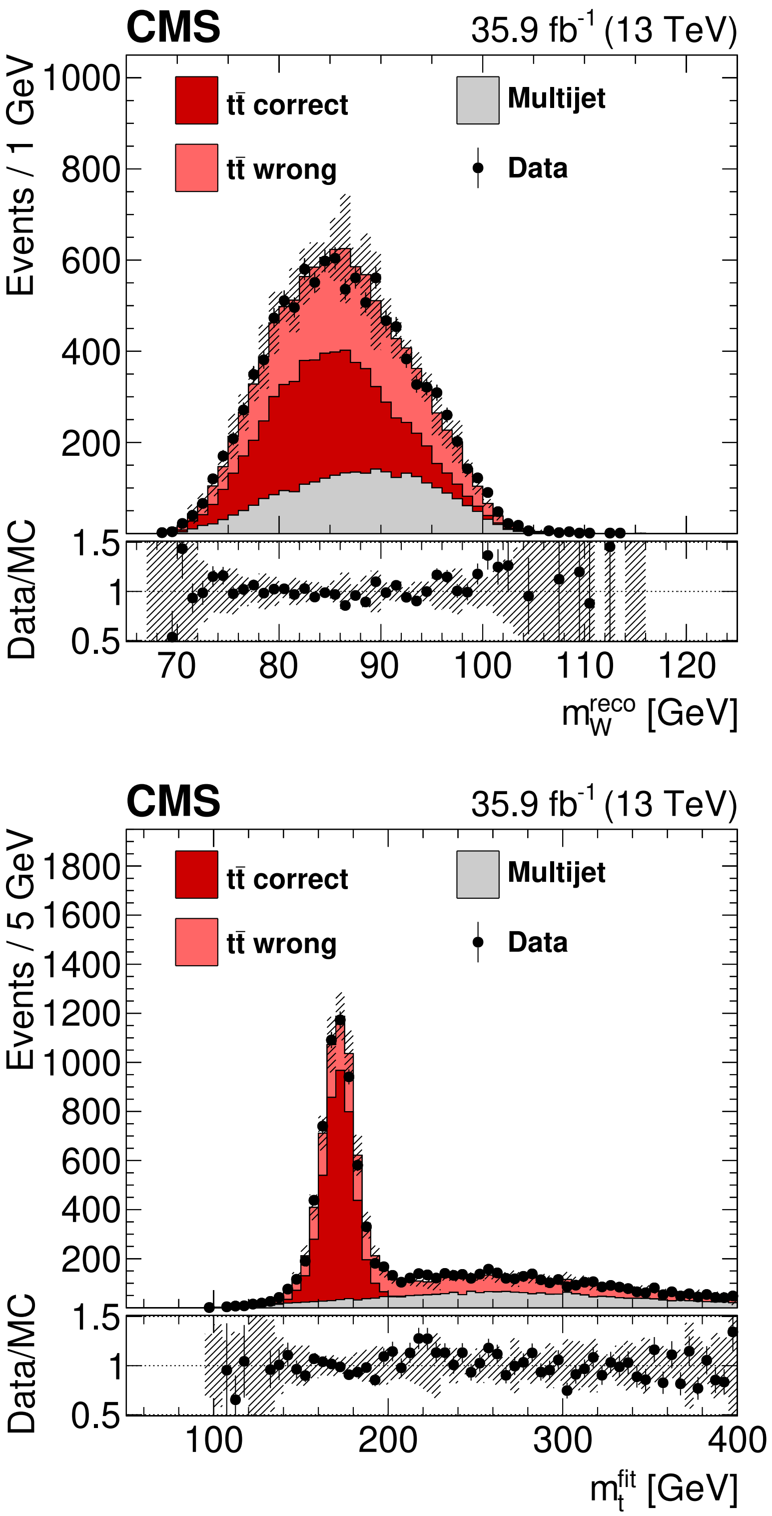

Figure 4.23: Distributions of the reconstructed W boson mass (top) and the fitted top quark mass (bottom) values of data compared to signal MC and the multijet background estimate. The shown reconstructed W boson mass is the average of both W bosons in the event. The hashed bands represent the uncertainty of the prediction, as described in Section 4.6. Published in Ref. [1].

4.5 Ideogram method

The ideogram method is used to extract the top quark mass. It has been used for the measurement of the W boson mass at LEP with the DELPHI experiment [130]. At the Tevatron $p\overline{p}$ collider it has been applied to measure the top quark mass with the D0 and CDF experiments [131, 132] in different final states and finally has been employed by several top quark mass measurements using the CMS detector at $\sqrt{s} = 7$ and 8 TeV [51, 52, 133–136], as well as for the lepton+jets final state at $\sqrt{s} = 13$ TeV [57, 137, 138].

A maximum likelihood fit is performed using probability density functions, which are analytic functions of the parameters of interest. These templates are created using simulated events.

The distribution of $m_{\mathrm{t}}^{\mathrm{fit}}$ is used, which is sensitive to the top quark mass m_{t}. In addition to m_{t}, a global jet energy scale factor (JSF) is introduced as a fit parameter. This factor is applied to all jet momenta after the standard jet energy corrections described in Section 3.1.1, which depend on p_{T} and η, have been applied. As a second observable for the fit, the reconstructed W boson mass $m_{\mathrm{W}}^{\mathrm{reco}}$ is introduced, where the average of the masses of the two W bosons in the event is used. It is sensitive to the jet energies and can therefore be used to constrain the JSF fit parameter. This is sketched in Fig. 4.24. Using this procedure, systematic uncertainties that affect jet energies can be reduced for the m_{t} measurement.

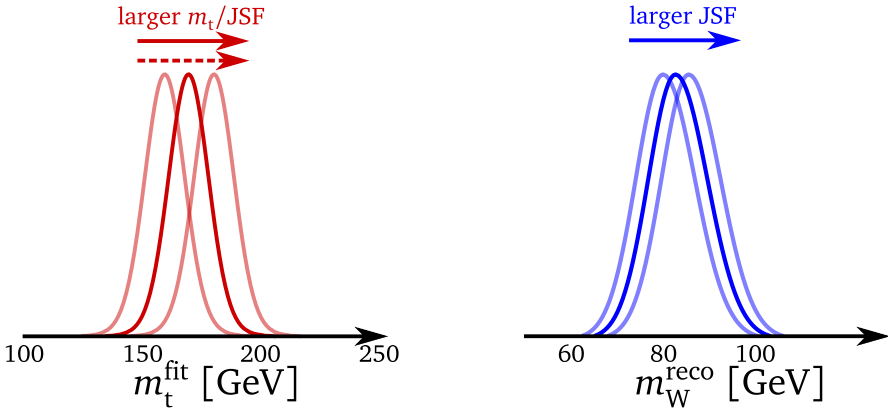

Figure 4.24: Sketch of the dependence of $m_{\mathrm{t}}^{\mathrm{fit}}$ (left) and $m_{\mathrm{W}}^{\mathrm{reco}}$ (right) on the fit parameters for the mass extraction. A larger m_{t} as well as a larger JSF leads to an average increase of $m_{\mathrm{t}}^{\mathrm{fit}}$. Similarly, increasing the JSF will on average increase $m_{\mathrm{W}}^{\mathrm{reco}}$, which can therefore be used to constrain the JSF.

Mathematically, the likelihood $\mathcal{L}\left(m_{\mathrm{t}}, \mathrm{JSF}\right)$ is a function of the parameters of interest m_{t} and JSF, which is the probability $P\left(\mathrm{sample} | m_{\mathrm{t}}, \mathrm{JSF}\right)$ of observing the measured data sample given some values for these parameters. This sample likelihood is given by the product of the probabilities of all events,

$$\begin{aligned}\mathcal{L}(m_{\mathrm{t}}, \mathrm{JSF}) &= P(\mathrm{sample}|m_{\mathrm{t}}, \mathrm{JSF}) \\ &= \prod_{\mathrm{events}} P(\mathrm{event}|m_{\mathrm{t}}, \mathrm{JSF}) \\ &= \prod_{\mathrm{events}} P\left(m_{\mathrm{t}}^{\mathrm{fit}}, m_{\mathrm{W}}^{\mathrm{reco}}|m_{\mathrm{t}}, \mathrm{JSF}\right),\end{aligned} \tag{4.4}$$

where for each event the observables $m_{\mathrm{t}}^{\mathrm{fit}}$ and $m_{\mathrm{W}}^{\mathrm{reco}}$ are used. This likelihood is maximized, yielding the best fit values for m_{t} and JSF. A prior probability for the JSF can be assumed, incorporating the prior knowledge of the jet energy scale, i.e., in general

$$P(\mathrm{JSF})P(\mathrm{sample}|m_{\mathrm{t}}, \mathrm{JSF}) \tag{4.5}$$

is maximized instead. As verified using simulated events, $m_{\mathrm{t}}^{\mathrm{fit}}$ and $m_{\mathrm{W}}^{\mathrm{reco}}$ can be treated as uncorrelated to very good approximation, such that the event probability $P\left(m_{\mathrm{t}}^{\mathrm{fit}}, m_{\mathrm{W}}^{\mathrm{reco}}|m_{\mathrm{t}}, \mathrm{JSF}\right)$ factorizes into

$$\begin{aligned}P\left(m_{\mathrm{t}}^{\mathrm{fit}}, m_{\mathrm{W}}^{\mathrm{reco}}|m_{\mathrm{t}}, \mathrm{JSF}\right) &= f_{\mathrm{sig}} P\left(m_{\mathrm{t}}^{\mathrm{fit}}, m_{\mathrm{W}}^{\mathrm{reco}}|m_{\mathrm{t}}, \mathrm{JSF}\right) \\ &\quad + \left(1 - f_{\mathrm{sig}}\right) P_{\mathrm{bkg}}\left(m_{\mathrm{t}}^{\mathrm{fit}}, m_{\mathrm{W}}^{\mathrm{reco}}\right) \\ &= f_{\mathrm{sig}} \sum_{j} f_j P_j\left(m_{\mathrm{t}}^{\mathrm{fit}}|m_{\mathrm{t}}, \mathrm{JSF}\right) P_j\left(m_{\mathrm{W}}^{\mathrm{reco}}|m_{\mathrm{t}}, \mathrm{JSF}\right) \\ &\quad + \left(1 - f_{\mathrm{sig}}\right) P_{\mathrm{bkg}}\left(m_{\mathrm{t}}^{\mathrm{fit}}\right) P_{\mathrm{bkg}}\left(m_{\mathrm{W}}^{\mathrm{reco}}\right).\end{aligned} \tag{4.6}$$

Here, the f_j specify the fractions of the different permutation cases for $j \in \{\mathrm{correct}, \mathrm{wrong}\}$, i.e., the fractions of correctly and wrongly assigned jets to the $\mathrm{t\bar{t}}$ system decay. The fraction of signal events is denoted f_{sig}.

For the probability densities $P_j\left(m_{\mathrm{t}}^{\mathrm{fit}}|m_{\mathrm{t}}, \mathrm{JSF}\right)$ and $P_j\left(m_{\mathrm{W}}^{\mathrm{reco}}|m_{\mathrm{t}}, \mathrm{JSF}\right)$, analytical functions depending on m_{t} and JSF are determined, as described in Section 4.5.1, for $j \in \{\mathrm{correct}, \mathrm{wrong}\}$. The probability densities for the background, $P_{\mathrm{bkg}}\left(m_{\mathrm{t}}^{\mathrm{fit}}\right)$ and $P_{\mathrm{bkg}}\left(m_{\mathrm{W}}^{\mathrm{reco}}\right)$, are independent of the fit parameters and therefore not altered in the fit. Only the signal fraction f_{sig}, and therefore the background fraction $f_{\mathrm{bkg}} = 1 - f_{\mathrm{sig}}$, is a free fit parameter which will change the normalization of the background template. In addition, the correct permutation fraction $f_{\mathrm{correct}} = 1 - f_{\mathrm{wrong}}$ is also floating in the fit.

Three different variations of a maximum likelihood fit are performed to extract the top quark mass.

- In the 1D analysis, the JSF is fixed to unity, corresponding to a Dirac delta function for the prior probability $P(\mathrm{JSF}) \propto \delta(1)$, i.e., the standard CMS jet energy calibration.

- For the 2D analysis the JSF is completely free in the maximum likelihood fit, which can be be described by a flat prior probability $P(\mathrm{JSF}) = \mathrm{const}$. This method allows for a partial compensation of some systematic uncertainties.

- The hybrid method is a weighted combination of both approaches, corresponding to a Gaussian constraint of the JSF around unity, $P(\mathrm{JSF}) = \mathcal{N}(1, \sigma_c^2)$. The width of the Gaussian is denoted σ_c.

The signal fraction and correct permutation fraction are free parameters in all three versions of the fit.

For the hybrid method, one can in principle choose the width σ_c of the prior probability, which can be translated to a "hybrid weight"

$$w_{\mathrm{hyb}} = \frac{\sigma_{\mathrm{2D}}^2}{\sigma_{\mathrm{2D}}^2 + \sigma_{\mathrm{c}}^2},$$

where σ_{2D} is the statistical uncertainty of the JSF obtained in the 2D fit. This weight is used to interpolate between the 1D and 2D methods and specifies the importance of the 1D method with respect to 2D method. It is evident that the 2D and 1D methods can be recovered in the limits of $w_{\mathrm{hyb}} = 0$ and 1:

$$\begin{array}{llll} \text{“flat” prior:} & \sigma_{\mathrm{c}} \to \infty: & w_{\mathrm{hyb}} \to 0 & \text{(2D method)} \\ \text{“}\delta\text{” prior:} & \sigma_{\mathrm{c}} \to 0: & w_{\mathrm{hyb}} \to 1 & \text{(1D method)} \end{array}$$

This interpolation is sketched in Fig. 4.25. Accordingly, the width of the prior probability can be specified in terms of the weight,

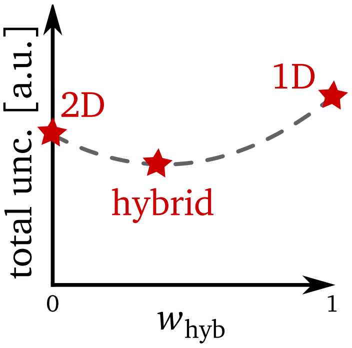

Figure 4.25: Sketch of the interpolation between the 2D and 1D methods using the hybrid weight w_{hyb} for the hybrid method. The 2D and 1D methods are recovered in the limits of $w_{\mathrm{hyb}} = 0$ and 1.

$$\sigma_{\mathrm{c}} = \sigma_{\mathrm{2D}}\sqrt{1/w_{\mathrm{hyb}} - 1}. \tag{4.7}$$

Any weight $w_{\mathrm{hyb}} \in [0,1]$ can be chosen, which is translated into a width σ_c for the JSF prior probability in Eq. (4.5), with which the mass extraction is performed. The weight w_{hyb} can therefore be scanned and the fit can be performed using the according σ_c to optimize the total uncertainty of the top quark mass measurement. A hybrid weight of $w_{\mathrm{hyb}} = 0.3$ has been shown to be optimal in this analysis and is used in the following, as further discussed in Section 4.7.

4.5.1 Templates

To describe the probability density functions, analytic templates are built for the fitted top quark and reconstructed W boson masses. These are constructed separately for $\mathrm{t\bar{t}}$ correct, $\mathrm{t\bar{t}}$ wrong and the background. Any possible non-perfect description is compensated by a calibration step, described in Section 4.5.2, before the mass extraction is performed.

Background templates

Since the background is independent of the signal hypothesis, a simple spline interpolation is used to describe the functional form. It is shown in Fig. 4.26 for both distributions used in the ideogram method. The black histograms show the background estimate, obtained as described in Section 4.4 and the red curves are the spline interpolations, used as $P_{\mathrm{bkg}}\left(m_{\mathrm{t}}^{\mathrm{fit}}\right)$ and $P_{\mathrm{bkg}}\left(m_{\mathrm{W}}^{\mathrm{reco}}\right)$. The gray histograms show the background estimate reweighted according to the slope variations within the uncertainty, as described in Section 4.4.1. The dashed lines show the corresponding parametrizations of these variations. These are used as the variations to determine the systematic background uncertainty described in Section 4.6.1. For the $m_{\mathrm{t}}^{\mathrm{fit}}$ distribution, both slope variations are positive, where one variation is very close to a slope of zero, as discussed before. Therefore, both dashed lines in Fig. 4.26 (left) tend to vary into the same direction with respect to the default parametrization, but one line is almost identical to the default one. Since the systematic uncertainties are symmetrized in the end, i.e., the maximum of the up- and down-variations is used, this treatment can be considered conservative, which is acceptable, since the systematic uncertainty of the background is small with respect to other uncertainty sources, as described in Section 4.6.

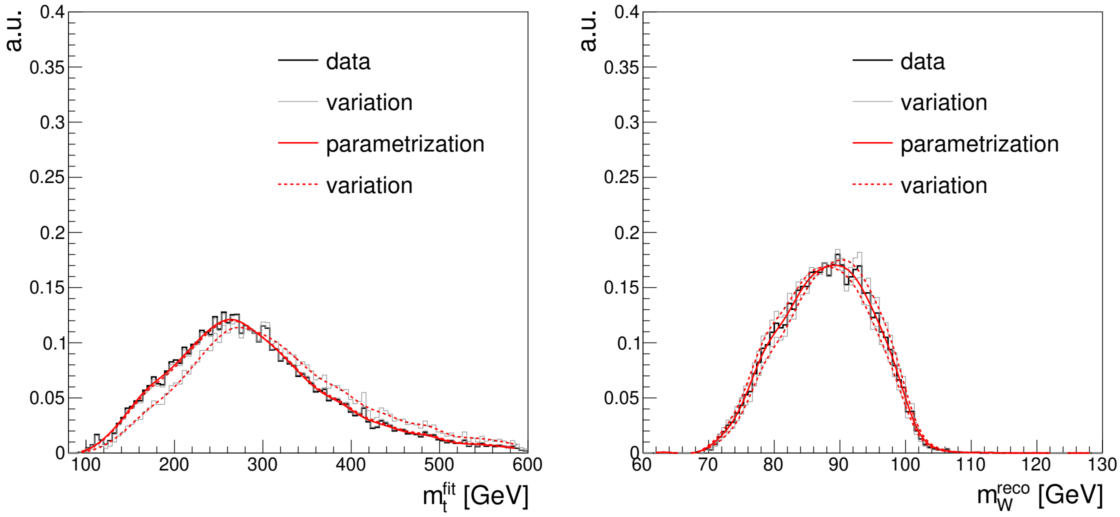

Figure 4.26: Background templates (red lines) parameterizing the background estimated from data (black histograms), i.e., $P_{\mathrm{bkg}}\left(m_{\mathrm{t}}^{\mathrm{fit}}\right)$ and $P_{\mathrm{bkg}}\left(m_{\mathrm{W}}^{\mathrm{reco}}\right)$ in Eq. (4.6). The systematic variations of the data (gray histograms) are also shown together with the corresponding templates (dashed red lines).

$\mathrm{t\bar{t}}$ signal templates

The distributions of $\mathrm{t\bar{t}}$ events are all fitted by analytic probability density functions described in the following. To capture the dependence of all shapes on the top quark mass m_{t} and the JSF, the original parameters of the probability density functions are themselves parameterized as a function of m_{t}, JSF, and the product of both, $m_{\mathrm{t}} \cdot \mathrm{JSF}$. Then, a simultaneous fit of these meta-parameters is performed, using all seven different top quark mass samples at once. For each, three values for JSF of 0.98, 1.00, and 1.02 are used, resulting in a total of 21 signal datasets. The functions described in the following correspond to the implementations in the RooFit package [139] and all probability density functions are normalized.

The $m_{\mathrm{t}}^{\mathrm{fit}}$ distribution for correct permutations, $P_{\mathrm{correct}}\left(m_{\mathrm{t}}^{\mathrm{fit}}|m_{\mathrm{t}},\mathrm{JSF}\right)$, is described by a Breit-Wigner convoluted with a Gaussian probability density function,

$$P_{\mathrm{correct}}\left(m_{\mathrm{t}}^{\mathrm{fit}}|m_{\mathrm{t}},\mathrm{JSF}\right)=\mathrm{BW}\left(m_{\mathrm{t}}^{\mathrm{fit}}\middle|M(m_{\mathrm{t}},\mathrm{JSF}),\Gamma(m_{\mathrm{t}},\mathrm{JSF})\right)*\mathcal{N}\left(m_{\mathrm{t}}^{\mathrm{fit}}\middle|\mu=0,\sigma(m_{\mathrm{t}},\mathrm{JSF})\right).$$

The parameters M, Γ, and σ are functions of m_{t} and JSF. The distributions are shown in Fig. 4.27 (top) for different generated top quark masses and jet scale factors. As expected, the distribution shifts with changes in generated m_{t} and JSF.

For the wrong permutations, the sum of a Landau function and a Gaussian is used for the $m_{\mathrm{t}}^{\mathrm{fit}}$ distribution

$$\begin{aligned}P_{\mathrm{wrong}}\left(m_{\mathrm{t}}^{\mathrm{fit}}|m_{\mathrm{t}},\mathrm{JSF}\right)=&A\cdot\mathrm{Landau}\left(m_{\mathrm{t}}^{\mathrm{fit}}\middle|\mu_{\mathrm{L}}(m_{\mathrm{t}},\mathrm{JSF}),\sigma_{\mathrm{L}}(m_{\mathrm{t}},\mathrm{JSF})\right)\\&+B\cdot\mathcal{N}\left(m_{\mathrm{t}}^{\mathrm{fit}}\middle|\mu(m_{\mathrm{t}},\mathrm{JSF}),\sigma(m_{\mathrm{t}},\mathrm{JSF})\right),\end{aligned}$$

with the four parameters μ_{L}, σ_{L}, μ, and σ being functions of m_{t} and JSF. These are also shown in Fig. 4.27 (bottom) for different generated top quark masses and jet scale factors. There are two components visible in this distribution. The broader peak at high masses is mainly of combinatorial nature, similar to the background, while for some events at least one top quark can be correctly reconstructed, resulting in a peak similar to that for correct assignments, which is sensitive to the chosen top quark mass.

The $m_{\mathrm{W}}^{\mathrm{reco}}$ distribution for correct permutations $P_{\mathrm{correct}}\left(m_{\mathrm{W}}^{\mathrm{reco}}|m_{\mathrm{t}},\mathrm{JSF}\right)$ is described by an asymmetric Gaussian probability density function (also called bifurcated Gaussian distribution or split normal distribution),

$$P_{\mathrm{correct}}\left(m_{\mathrm{W}}^{\mathrm{reco}}|m_{\mathrm{t}},\mathrm{JSF}\right)=\mathcal{AN}\left(m_{\mathrm{W}}^{\mathrm{reco}}\middle|\mu(m_{\mathrm{t}},\mathrm{JSF}),\sigma_{\mathrm{L}}(m_{\mathrm{t}},\mathrm{JSF}),\sigma_{\mathrm{R}}(m_{\mathrm{t}},\mathrm{JSF})\right),$$

with two different widths σ_{L} and σ_{R} for the left ($< \mu$) and right sides ($> \mu$). Again, the parameters μ, σ_{L}, and σ_{R} are functions of m_{t} and JSF.

Likewise, the distribution of $m_{\mathrm{W}}^{\mathrm{reco}}$ is modeled as an asymmetric Gaussian function for wrong permutations,

$$P_{\mathrm{wrong}}\left(m_{\mathrm{W}}^{\mathrm{reco}}|m_{\mathrm{t}},\mathrm{JSF}\right)=\mathcal{AN}\left(m_{\mathrm{W}}^{\mathrm{reco}}\middle|\mu(m_{\mathrm{t}},\mathrm{JSF}),\sigma_{\mathrm{L}}(m_{\mathrm{t}},\mathrm{JSF}),\sigma_{\mathrm{R}}(m_{\mathrm{t}},\mathrm{JSF})\right).$$

The parametrizations of the $m_{\mathrm{W}}^{\mathrm{reco}}$ distributions are shown in Fig. 4.28 for correct and wrong permutations for different generated top quark masses and jet scale factors. Especially for the correct assignments, the shift of the distribution with varying values for JSF is visible.

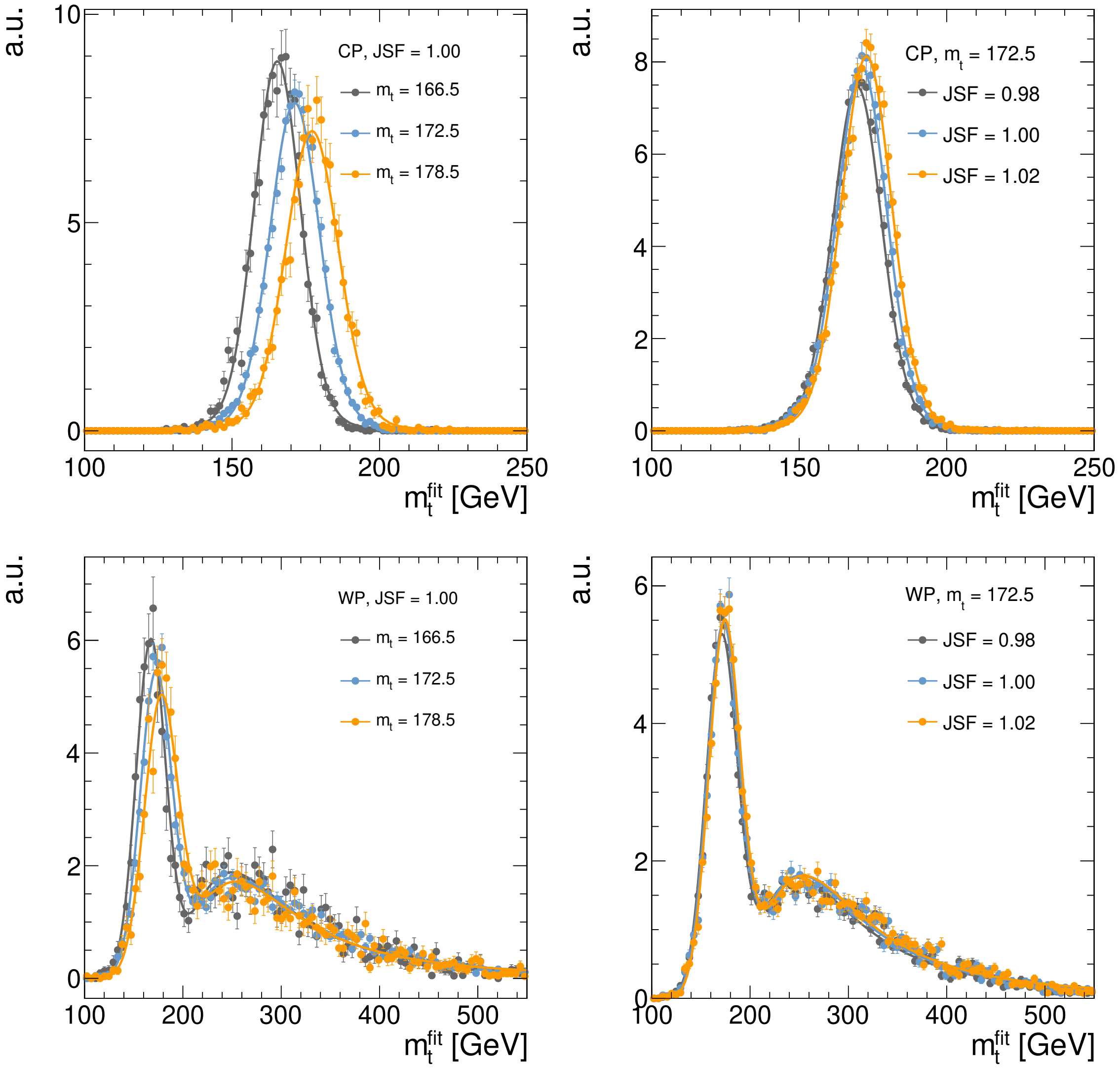

Figure 4.27: The fitted templates for the m_t^{fit} distribution for different generated top quark masses and jet scale factors. The upper plots show the templates for the correct permutations, $P_{\text{correct}}\left(m_t^{\text{fit}}|m_t, \text{JSF}\right)$, the lower plots for wrong permutations, $P_{\text{wrong}}\left(m_t^{\text{fit}}|m_t, \text{JSF}\right)$. The JSF is fixed to the default value on the left side and different values of m_t are displayed. On the right side, m_t is fixed to the default value and different values of JSF are used.

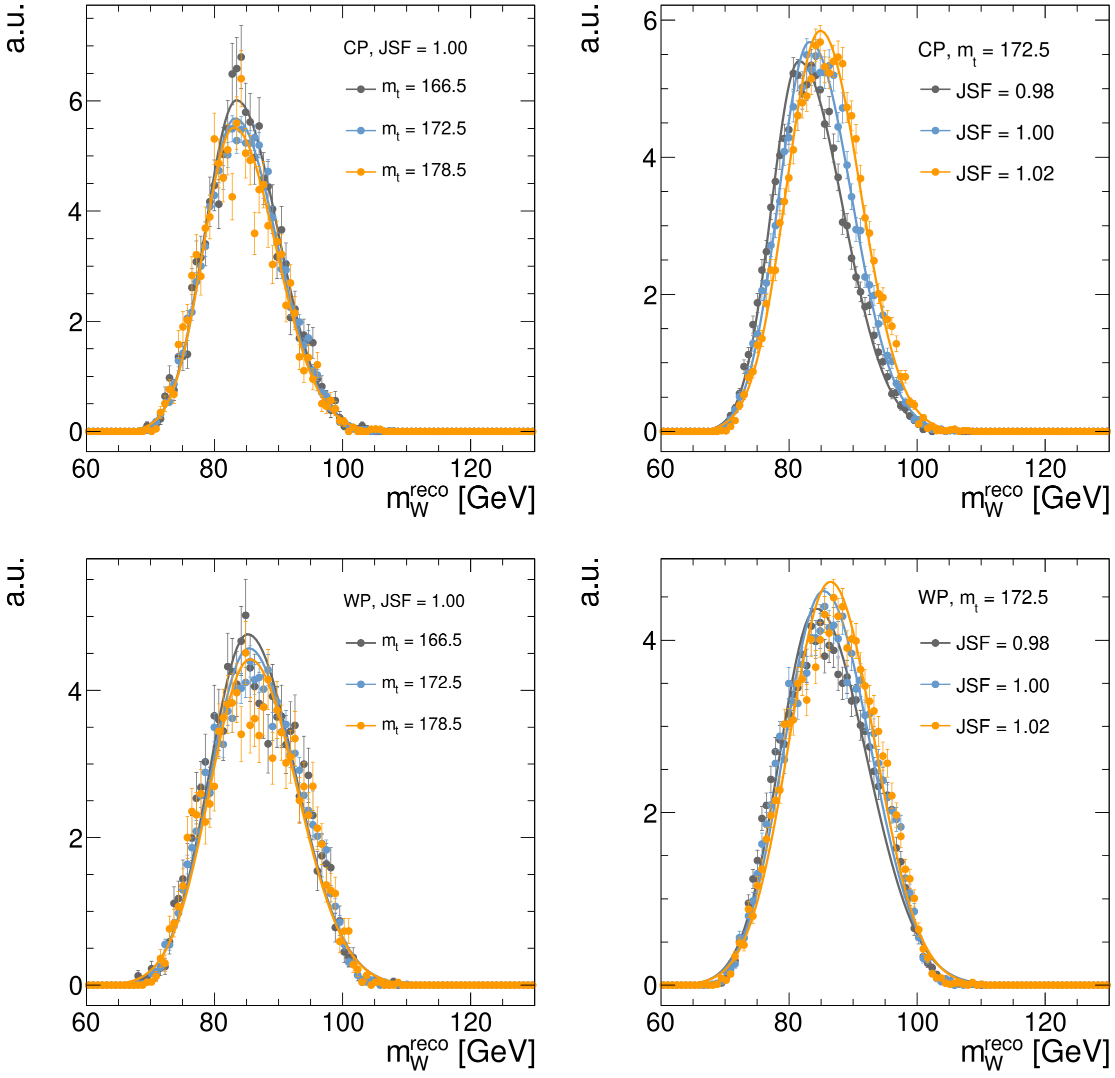

Figure 4.28: The fitted templates for the $m_{\mathrm{W}}^{\mathrm{reco}}$ distribution for different generated top quark masses and jet scale factors. The upper plots show the templates for the correct permutations, $P_{\mathrm{correct}}\left(m_{\mathrm{W}}^{\mathrm{reco}}|m_{\mathrm{t}},\mathrm{JSF}\right)$, the lower plots for wrong permutations, $P_{\mathrm{wrong}}\left(m_{\mathrm{W}}^{\mathrm{reco}}|m_{\mathrm{t}},\mathrm{JSF}\right)$. The JSF is fixed to the default value on the left side and different values of m_{t} are displayed. On the right side, m_{t} is fixed to the default value and different values of JSF are used.

4.5.2 Pseudo-experiments and calibration

For the calibration of the method and the evaluation of systematic uncertainties, pseudo-experiments are performed using simulated signal samples and the background prediction. Events are drawn randomly from the pools of simulated signal events and background events using the expected proportions given by the signal fraction calculated from the number of selected signal events and the total data event yield. The total number of events utilized for a pseudo-experiment is determined by drawing from a Poisson distribution $\mathrm{Pois}(\lambda)$ with a mean λ given by the number of selected data events. For the signal events, all event weights described above are used to weight the probability for an event to be picked.

Each time, pseudo-experiments are used in the following, a few thousand pseudo-experiments are generated to yield statistically significant results.

Before the mass extraction is performed, a calibration step is applied to correct for possible biases introduced by the choice of the functional forms of the templates described in Section 4.5.1. To calibrate the mass extraction method, pseudo-experiments are performed for seven different generated values of $m_\mathrm{t}^\mathrm{gen}$ and three input JSF values. The average extracted values are compared to the input values,

$$\begin{aligned}\text{mass bias} &= \left\langle m_\mathrm{t,extr} - m_\mathrm{t}^\mathrm{gen}\right\rangle ,\\ \text{JSF bias} &= \langle \mathrm{JSF}_\mathrm{extr} - \mathrm{JSF}\rangle ,\end{aligned}$$

where the index “extr” denotes the extracted value of the pseudo-experiment.

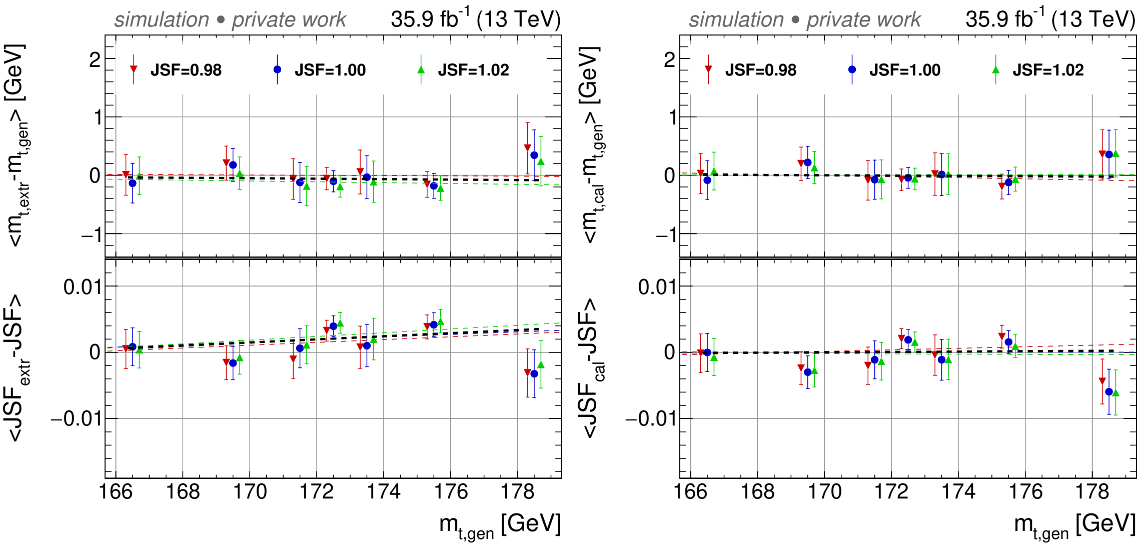

Figure 4.29: Difference of extracted and generated top quark masses and JSFs for different input masses and JSFs before (left) and after (right) the calibration. A linear fit is performed for each input JSF separately and shown as dashed line.

Figure 4.29 (left) shows these as a function of $m_\mathrm{t}^\mathrm{gen}$ for the different JSF values. A linear fit in $m_\mathrm{t}^\mathrm{gen}$ is performed for each input JSF separately and shown. For the calibration of the extracted top quark mass and the JSF, both are fitted with two-dimensional functions of the form

$$a_0 + a_1(m_{\mathrm{t,extr}} - 172.5) + a_2(\mathrm{JSF}_{\mathrm{extr}} - 1) + a_3(m_{\mathrm{t,extr}} - 172.5)(\mathrm{JSF}_{\mathrm{extr}} - 1),$$

which are used to obtain the calibrated the top quark mass $m_{\mathrm{t,cal}}$ and the calibrated jet scale factor $\mathrm{JSF}_{\mathrm{cal}}$. The calibration therefore depends linearly on the extracted values of top quark mass, JSF, and the product of both. Pseudo-experiments using the calibrated extraction show that this bias correction works, which can be seen in Fig. 4.29 (right).

Using the calibrated pseudo-experiments, the pulls

$$\mathrm{pull} = \frac{m_{\mathrm{t,cal}} - m_{\mathrm{t,gen}}}{\sigma\left(m_{\mathrm{t,cal}}\right)}$$

are calculated and a Gaussian fit to the pull distribution is performed. The mean widths are shown in Fig. 4.30 as a function of the generated mass for different JSF values. The values are close to unity, as expected.

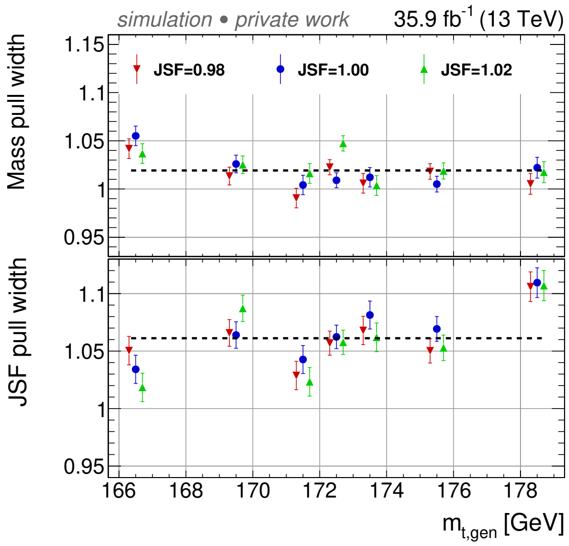

Figure 4.30: The mean mass and JSF pull widths as a function of the generated mass for different JSF values.

The expected statistical uncertainty for the 1D mass measurement derived from the pseudo-experiments is shown in Fig. 4.31. Its expected value of approximately 0.16 GeV is improved with respect to the value of 0.23 GeV measured at $\sqrt{s} = 8$ TeV [52], due to the higher number of selected events.

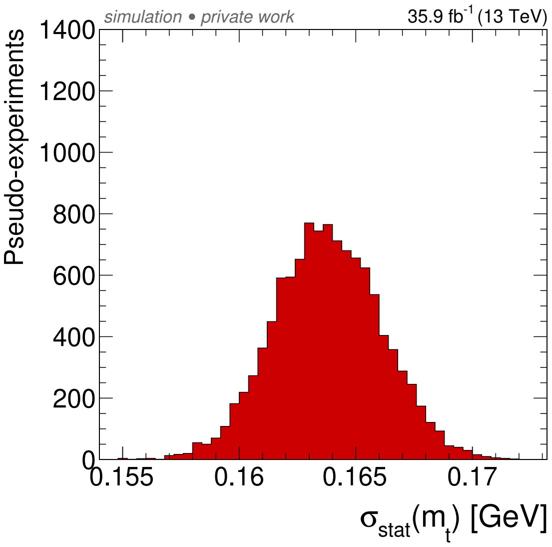

Figure 4.31: Expected statistical uncertainty distribution for the 1D mass measurement derived from pseudo-experiments.

4.6 Systematic uncertainties

Different sources of systematic uncertainties are considered for the measurement. The individual contributions are evaluated using simulation-based pseudo-experiments, as described before. To determine the contribution of an uncertainty source, pseudo-experiments are generated using an alternative MC signal sample for which the uncertainty source (e.g. jet energy resolution) is varied. The shift

$$\delta x_i = x_{\text{variation, }i} - x_{\text{nominal}}$$

of the resulting measurement with respect to the nominal measurement determines the contribution of the uncertainty source i. Here, x denotes m_{t} or JSF for the different extraction methods.

The contributions from the different sources of systematic uncertainties are shown in Table 4.5. These are described in more detail in the following. In most cases, the systematic uncertainty sources are varied by ±1 standard deviations ("two-sided uncertainties"), and the absolute values of the largest observed shifts in m_{t} and JSF are quoted as the uncertainties for the final measurement. For some uncertainty sources, only one variation is considered, e.g. a comparison to an alternative model ("single-sided uncertainties").

For uncertainties which are evaluated using an independently generated MC sample, the shifts in the table are displayed with a statistical uncertainty ($\delta x = \delta x_0 \pm \delta x_s$). Uncertainty sources which are varied by reweighting the default MC signal sample have a negligible statistical uncertainty for the shift, because the samples are correlated.

The total systematic uncertainty $\sigma_{\text{syst., total}}$ for a measurement is obtained by summing all individual systematic uncertainties in quadrature

$$\sigma^2_{\text{syst., total}} = \sum_i (\delta x_i)^2.$$

Table 4.5: List of systematic uncertainties for the all-jets channel. The signs of the shifts ($\delta x = x_{\mathrm{variation}} - x_{\mathrm{nominal}}$) correspond to the $+1$ standard deviation variation of the systematic uncertainty source. For linear sums of the uncertainty groups, the relative signs have been considered. Shifts determined using dedicated samples for the systematic variation are displayed with the corresponding statistical uncertainty [1].

	2D		1D	hybrid	
	$\delta m_{\mathrm{t}}^{\mathrm{2D}}$ [GeV]	$\delta\mathrm{JSF}^{\mathrm{2D}}$ [%]	$\delta m_{\mathrm{t}}^{\mathrm{1D}}$ [GeV]	$\delta m_{\mathrm{t}}^{\mathrm{hyb}}$ [GeV]	$\delta\mathrm{JSF}^{\mathrm{hyb}}$ [%]
Experimental uncertainties					
Method calibration	0.06	0.2	0.06	0.06	0.2
JEC (quad. sum)	0.18	0.3	0.73	0.15	0.2
– Intercalibration	−0.04	−0.1	+0.12	−0.04	−0.1
– MPFInSitu	−0.03	0.0	+0.22	+0.08	+0.1
– Uncorrelated	−0.17	−0.3	+0.69	+0.12	+0.2
Jet energy resolution	−0.09	+0.2	+0.09	−0.04	+0.1
b tagging	0.02	0.0	0.01	0.02	0.0
Pileup	−0.06	+0.1	0.00	−0.04	+0.1
Background	0.10	0.1	0.03	0.07	0.1
Trigger	+0.04	−0.1	−0.04	+0.02	−0.1
Modeling uncertainties					
JEC flavor (linear sum)	−0.35	+0.1	−0.31	−0.34	0.0
– light quarks (uds)	+0.10	−0.1	−0.01	+0.07	−0.1
– charm	+0.03	0.0	−0.01	+0.02	0.0
– bottom	−0.29	0.0	−0.29	−0.29	0.0
– gluon	−0.19	+0.2	+0.03	−0.13	+0.2
b jet modeling (quad. sum)	0.09	0.0	0.09	0.09	0.0
– b frag. Bowler–Lund	−0.07	0.0	−0.07	−0.07	0.0
– b frag. Peterson	−0.05	0.0	−0.04	−0.05	0.0
– semileptonic b hadron decays	−0.03	0.0	−0.03	−0.03	0.0
PDF	0.01	0.0	0.01	0.01	0.0
Ren. and fact. scales	0.05	0.0	0.04	0.04	0.0
ME/PS matching	+0.32±0.20	−0.3	−0.05±0.14	+0.24±0.18	−0.2
ISR PS scale	+0.17±0.17	−0.2	+0.13±0.12	+0.12±0.14	−0.1
FSR PS scale	+0.22±0.12	−0.2	+0.11±0.08	+0.18±0.11	−0.1
Top quark p_{T}	+0.03	0.0	+0.02	+0.03	0.0
Underlying event	+0.16±0.19	−0.3	−0.07±0.14	+0.10±0.17	−0.2
Early resonance decays	+0.02±0.28	+0.4	+0.38±0.19	+0.13±0.24	+0.3
CR modeling (max. shift)	+0.41±0.29	−0.4	−0.43±0.20	−0.36±0.25	−0.3
– “gluon move” (ERD on)	+0.41±0.29	−0.4	+0.10±0.20	+0.32±0.25	−0.3
– “QCD inspired” (ERD on)	−0.32±0.29	−0.1	−0.43±0.20	−0.36±0.25	−0.1
Total systematic	**0.81**	**0.9**	**1.03**	**0.70**	**0.7**
Statistical (expected)	0.21	0.2	0.16	0.20	0.1
Total (expected)	**0.83**	**0.9**	**1.04**	**0.72**	**0.7**

For sources with a statistical uncertainty larger than the observed shift itself ($\delta x_s > \delta x_0$), the size of the statistical uncertainty δx_s is used as δx_i, instead. This is a conservative estimate, as further discussed in Section 4.6.3. The total uncertainty σ_{total} is calculated as the quadratic sum of the total systematic uncertainty and the statistical uncertainty of the measurement,

$$\sigma_{\text{total}}^2 = \sigma_{\text{syst., total}}^2 + \sigma_{\text{stat}}^2.$$

The systematic uncertainties considered as relevant for this measurement and the methods used to evaluate them, are described below. They are grouped into *experimental uncertainties* and *modeling uncertainties*.

4.6.1 Experimental uncertainties

The experimental uncertainties originating from the employed experimental methods and calibrations are described in the following.

Fit calibration:

The uncertainty of the mass extraction method is given by the residual uncertainty of the fit calibration. The quadratic sum of statistical uncertainty and residual bias after the calibration (Fig. 4.29 (right)) is quoted as the systematic uncertainty.

p_{T}- and η-dependent JEC:

The jet energy scale factor applied in the mass extraction is applied to all jet energies, independent of p_{T} and η. On the other hand, the standard CMS jet energy corrections (JECs) depend on p_{T} and η and therefore, the corresponding uncertainties cannot be fully compensated. To assess the JEC uncertainty, the jet energies are scaled up and down according to their individual data/MC uncertainties using the default CMS prescription [104, 140]. The 23 individual sources are grouped into the three groups Intercalibration, MPFInSitu, and Uncorrelated, as suggested by the LHCtopWG to ease combination efforts. These recommendations are documented in Refs. [140, 141].

Jet energy resolution:

The jet energy resolution in simulation is modified to match the worse resolutions measured in data [104]. To account for the resolution uncertainty, the jet energy resolution in the simulation is modified by ±1 standard deviations with respect to the degraded resolution. The resolution scale factors, used as described in Ref. [105] and Section 3.1.2, and uncertainties for this analysis have been provided by the CMS JetMET group [142]. The values can be found in Table 4.6.

b tagging:

The events are weighted to account for the p_{T}-dependent uncertainty of the b tag efficiencies and misidentification rates of the CSVv2 b tagger [102, 103].

Table 4.6: Jet energy resolution scale factors and uncertainties for the different η bins [142], used as described in Ref. [105].

η bin	scale factor	uncertainty
0.000 − 0.522	1.109	0.0322
0.522 − 0.783	1.138	0.0337
0.783 − 1.131	1.114	0.0299
1.131 − 1.305	1.123	0.0379
1.305 − 1.740	1.084	0.0268
1.740 − 1.930	1.082	0.0554
1.930 − 2.043	1.140	0.0965
2.043 − 2.322	1.067	0.0511
2.322 − 2.5	1.177	0.1568
2.5 − 2.853	1.364	0.1095
2.853 − 2.964	1.857	0.2007
2.964 − 3.139	1.328	0.1244
3.139 − 5.191	1.160	0.1488

Pileup:

To estimate the uncertainty in the determination of the number of pileup events and the reweighting procedure, the inelastic proton-proton cross section [143] used in the determination is varied by ±4.6%.

Background:

The systematic variations of the background templates, as described in Section 4.5.1 and shown in Fig. 4.26, are used and the results are compared to the default. These variations result from the shape reweighting described in Section 4.4.1 and shown in Fig. 4.15.

Trigger:

To estimate the uncertainty of the trigger selection, the data/simulation scale factor described in Section 4.2 is omitted. Additionally a base trigger requiring the presence of one muon is used to derive the correction factor. The maximum of the observed shifts with respect to the nominal correction is quoted as uncertainty.

4.6.2 Modeling uncertainties

Systematic uncertainties arise from the used theory models. Most models have parameters which are determined using measurements or other considerations, which are partly ad-hoc. Variations of these parameters, typically within their uncertainties, lead to different results, i.e., modeling uncertainties. In some cases, even different models are available, which are compared to assess an uncertainty.

Flavor-dependent JEC:

The fragmentation implemented in PYTHIA 6.422 [144] uses the Lund string model, in contrast to the cluster fragmentation model used in HERWIG++ 2.4 [118]. Both depend on a number of tuning parameters, which can influence the individual fragmentation of jets of different flavors, i.e., jets initiated by gluons, light quarks, and b quarks. Therefore, the difference in jet energy response between PYTHIA 6.422 and HERWIG++ 2.4 is determined for each jet flavor [104]. Since the JSF is measured from light quarks (with gluon contamination), flavor uncertainties for jets from light quarks, gluons, and b quarks are evaluated separately and added linearly, in order to take into account differences between the energy responses of different jet flavors.

b jet modeling:

The uncertainty regarding the fragmentation of b quarks is split into three components.

- The fragmentation into b hadrons is varied in simulation within the uncertainties of the Bowler–Lund fragmentation function tuned to data measured by the ALEPH [145] and DELPHI [146] collaborations.
- Instead of the Bowler–Lund fragmentation function, the Peterson fragmentation function is used and the difference between the two approaches is quoted as an uncertainty.
- Lastly, the uncertainty from the semileptonic b hadron branching fraction is obtained by varying it by −0.45% and +0.77%, which is the range of the measurements from B^0/B^+decays and their uncertainties [147].

The resulting effects are added in quadrature for the quoted b jet modeling uncertainty.

Parton distribution function (PDF):

The 100 PDF replicas of the NNPDF3.0 NLO ($\alpha_s = 0.118$) set are used to repeat the analysis [113]. The variance of the results is used as the PDF uncertainty. In addition, α_s is scaled to 0.117 and 0.119. The maximum of the replica variance and the α_s variations is quoted as the PDF uncertainty.

Renormalization and factorization scales:

In the matrix-element calculation, the renormalization and factorization scales, μ_R and μ_F, are varied. The simulated events are weighted to match the shapes of events generated with the alternative values for the renormalization and factorization scales. The nominal values of μ_R and μ_F are scaled independently from each other and simultaneously by factors of 0.5 and 2, i.e., only variations where both are scaled in the same direction are omitted. The quoted uncertainty corresponds to the envelope of the resulting shifts, i.e., the variation with the largest absolute shift.

ME/PS matching:

The model parameter $h_{\text{damp}} = 1.58^{+0.66}_{-0.59}$ [123] used in POWHEG that controls the matching of the matrix element (ME) to the PYTHIA parton shower (PS) is varied within its uncertainties.

ISR PS scale:

The parton shower scale value used for the simulation of initial-state radiation in PYTHIA is scaled up by 2 and down by 0.5 in dedicated signal samples.

FSR PS scale:

The parton shower scale value used for the simulation of final-state radiation in PYTHIA is scaled up by $\sqrt{2}$ and down by $1/\sqrt{2}$ [122] in dedicated samples, affecting the fragmentation and hadronization, as well as additional jet emission. For the FSR variation samples, a shift of the jet energy response for light quarks is observed compared to the default sample. This would be removed by corresponding residual jet energy corrections derived in γ/Z+jet events, if the corresponding FSR PS scale choice would be used in the default sample for which the standard corrections are derived. To correct for the difference, the jet momenta in the FSR variation samples are scaled to reproduce the light-jet energy response of the default sample.

Top quark p_{T}:

Next-to-next-to-leading-order effects are shown to influence the top quark p_{T} spectrum [148]. To take this into account, the transverse momentum spectrum of the top quark in simulation is weighted to describe the distribution measured by the CMS Collaboration [149, 150]. This correction is not applied for the default measurement, but the impact of this variation on the measurement is quoted as a systematic uncertainty.

Underlying event:

Measurements of the underlying event have been used to tune PYTHIA parameters describing nonperturbative QCD effects [122, 123]. The parameters of the tune are varied within their uncertainties.

Early resonance decays:

Modeling of color reconnection (CR) introduces systematic uncertainties which are estimated by comparing different CR models and settings. In the default sample, the top quark decay products are not included in the CR process. This setting is compared to the case of including the decay products by enabling early resonance decays (ERD) in PYTHIA 8.

Color reconnection modeling:

In addition to the default model used in PYTHIA 8, two alternative color reconnection (CR) models are used, namely a model with string formation beyond leading color ("QCD inspired") [116] and a model allowing the gluons to be moved to another string ("gluon move") [117]. Underlying event measurements are used to tune the parameters of all models [122, 123]. The largest shifts induced by the variations are assigned as the CR uncertainty.

This approach to determine the CR uncertainty, as well as the early resonance decay variation, is new relative to the Run 1 results at $\sqrt{s} = 7$ and 8 TeV, because these CR models have become only recently available in PYTHIA 8. The new models were first used to evaluate the m_t uncertainty due to CR in Ref. [57]. Like in this analysis, the same increase in systematic uncertainty with respect to the Run 1 result has been observed.

4.6.3 Summary and comparison of the uncertainties

The systematic uncertainties are listed in Table 4.5 for all three mass extraction methods. The signs of the shifts correspond to the +1 standard deviation variation of the systematic uncertainty source. All shifts resulting from the up and down variations of the uncertainty sources can be found in Appendix B.1. A graphical representation of the uncertainties is shown in Fig. 4.32.

The uncertainty due to the JEC is greatly reduced for the 2D and hybrid methods with respect to the 1D method. In general, the 2D uncertainty is smaller than the 1D uncertainty, because parts of the systematic uncertainties can be absorbed by the fit of the JSF. By construction, the hybrid method provides the smallest uncertainty, as already mentioned in Section 4.5 and further specified in Section 4.7.

The total systematic uncertainty for the hybrid method, which provides the main result of the measurement, is dominated by uncertainties related to the flavor-dependent jet energy corrections, mainly stemming from the b quark part, and the modeling of color reconnection, including the choice of early resonance decays.

It is worth noting, that for a number of uncertainties, the statistical uncertainty of the shift is very large, i.e., that the shift is not significant. This is due to the tight signal selection, mainly dictated by the trigger requirements, which reject a great part of the signal, such that the remaining MC events only provide low statistical precision. Also, the choice to take the maximum of the shift and its statistical uncertainty can be considered conservative. It has been discussed to not assign uncertainties for insignificant shifts, or take the quadratic difference of the shift and the uncertainty, which can even lead to negative contributions to the total uncertainty (see for example Chapter 6.3.2 of Ref. [151]). Such options might be considered for future measurements. Furthermore, larger signal samples for the systematic variations should be generated, to increase the significance of the shifts. This might require generator-level cuts, to be able to generate more events in the phase space of the hard selection required for the all-jets channel. Another option is to implement more systematic variations, for which currently independent samples are used, using weighting of the default sample, instead. This is currently investigated for analyses using the full Run 2 data for the ISR, FSR and ME/PS matching uncertainties.

In Ref. [57], an additional matrix-element generator uncertainty has been considered for the lepton+jets final state: Instead of using POWHEG v2 as ME generator, the MADGRAPH5_aMC@NLO 2.2.2 generator with the FxFx matching scheme is used [111, 152]. In the case of this analysis, the difference between the results obtained with the two generators is found to be $\delta m_{\mathrm{t}}^{\mathrm{hyb}} = +0.31 \pm 0.52$ for the hybrid method in the all-jets channel. However, this is not significant because of the insufficient statistical precision of the available MADGRAPH5_aMC@NLO sample. Since the radiation after the top quark decay is described by PYTHIA, no significant impact of the ME generator choice is expected beyond the variation of the PS scales and matching. Therefore, no ME generator uncertainty is considered in the total uncertainty of the measurement, but the number is just quoted here as a cross-check.

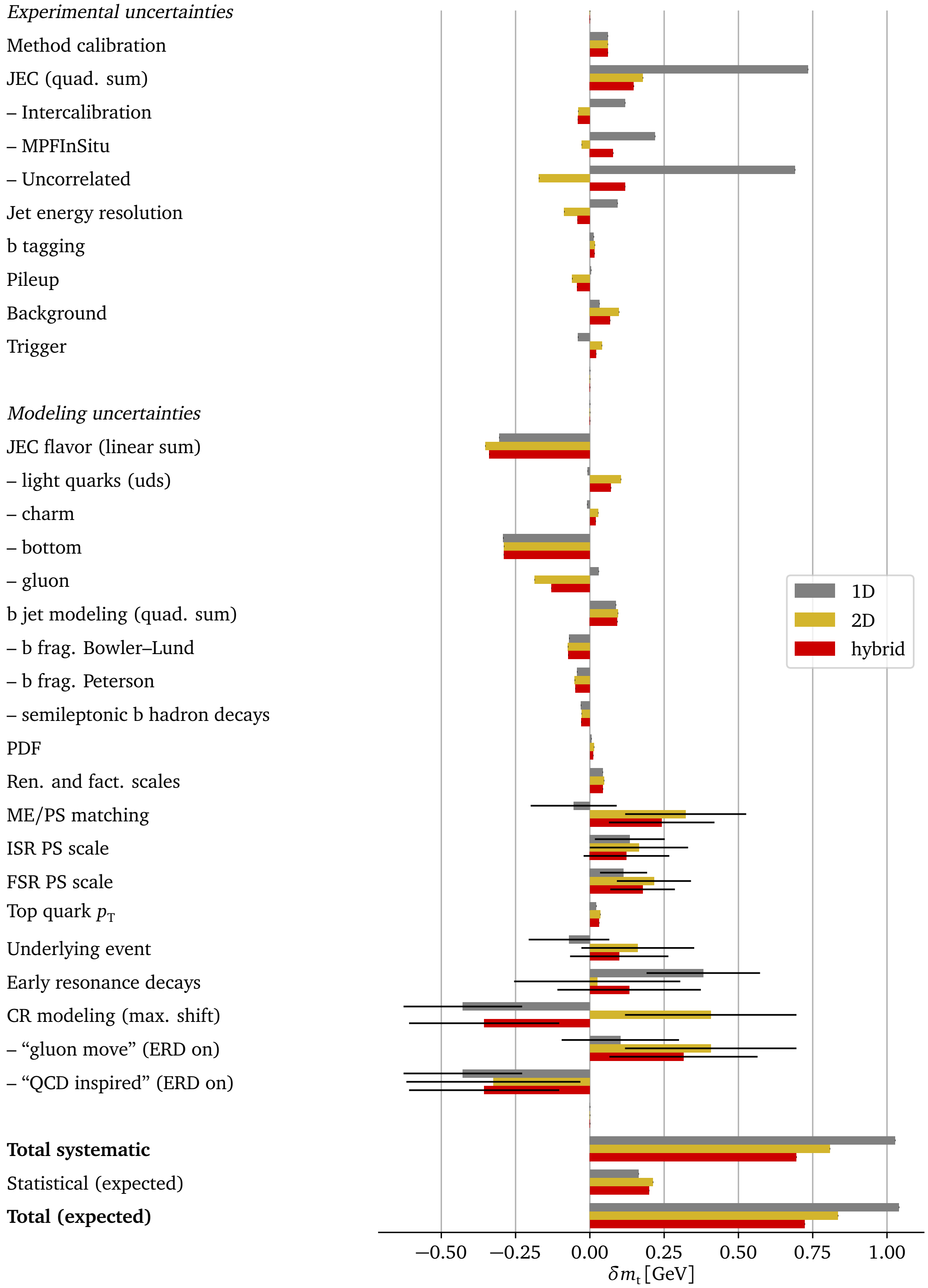

Figure 4.32: The sizes of the uncertainty components for the all-jets channel. The three bars for each component represent the 1D, 2D, and hybrid methods. For two-sided uncertainties, the largest of the two shifts is shown, using the sign of the up-variation. Shifts that have an associated statistical uncertainty are presented with the corresponding error bars.

4.7 Hybrid weight scan

The width of the JSF prior probability, or equivalently the hybrid weight w_{hyb} can be chosen freely, as described in Section 4.5. It is optimized to obtain the smallest uncertainty for the measurement. For this, specific values for w_{hyb} are chosen and translated to a prior probability width according to Eq. (4.7). The mass extraction using pseudo-experiments is repeated for each w_{hyb} and the most important uncertainties are calculated as before. These include the jet energy corrections, jet energy resolutions, final and initial state radiation, underlying event, ME/PS matching, flavor-dependent JEC, early resonance decays, and color reconnection modeling. The results for six different choices of w_{hyb} are shown in Fig. 4.33 (left). Figure 4.33 (right) also includes the 2D and 1D results at $w_{\mathrm{hyb}} = 0$ and 1.

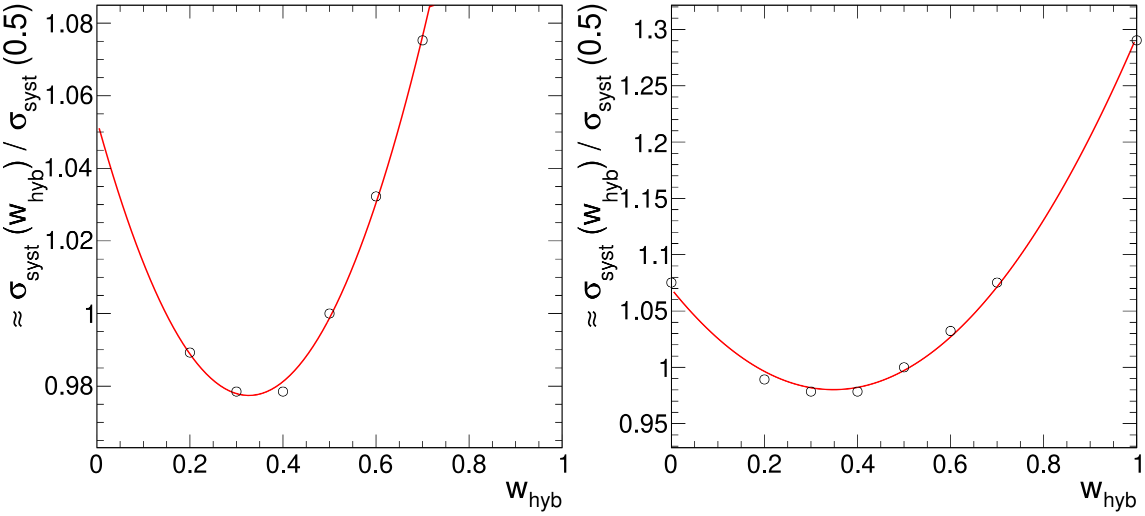

Figure 4.33: Left: The systematic uncertainties obtained for six different choices for w_{hyb}, normalized to the value for $w_{\mathrm{hyb}} = 0.5$. Right: In addition, the values for the 2D and 1D results are also inserted at $w_{\mathrm{hyb}} = 0$ and 1. The red lines are parabolic fits to the points shown in a plot. The approximately equal sign (≈) indicates that only the largest uncertainty components have been considered.

The shown systematic uncertainty $\sigma_{\mathrm{syst}}(w_{\mathrm{hyb}})$ is normalized to the value $\sigma_{\mathrm{syst}}(0.5)$ obtained with $w_{\mathrm{hyb}} = 0.5$, which was the weight used at the beginning. This was also the value used in the $\sqrt{s} = 8\,\mathrm{TeV}$ analysis. A parabolic function is fit to the points and in both cases a minimum is found at about $w_{\mathrm{hyb}} = 0.3$. The function is rather flat, i.e., a small variation of the weight around the minimum does not alter the result much. The overall improvement with respect to the start value is approximately 2%. If the statistical uncertainty is included in the uncertainty determination for the hybrid weight scan, the same optimal value and improvement are observed, because the systematic uncertainty is dominant.

To demonstrate that the hybrid mass extraction can indeed be seen as a weighted combination of the 1D and 2D results, it is explicitly constructed. The “reconstructed” hybrid mass for a hybrid weight w_{hyb} is constructed as

$$m^{\mathrm{hyb}*} = w_{\mathrm{hyb}} m^{\mathrm{1D}} + (1 - w_{\mathrm{hyb}}) m^{\mathrm{2D}}.$$

Correspondingly, for each uncertainty component i, the "reconstructed" shift for the hybrid method is given by

$$\delta m_i^{\mathrm{hyb}*} = w_{\mathrm{hyb}} \delta m_i^{\mathrm{1D}} + (1 - w_{\mathrm{hyb}}) \delta m_i^{\mathrm{2D}}.$$

With these reconstructed shifts, the total uncertainty is calculated as before. It is shown in Fig. 4.34 for different values of w_{hyb}. Here, also the actual values for the 1D and 2D methods are shown, as well as the actual hybrid result at $w_{\mathrm{hyb}} = 0.3$. The same parabolic behavior is observed as for the real hybrid measurements. Especially the reconstructed uncertainty value for the final choice of $w_{\mathrm{hyb}} = 0.3$ can be reproduced. Also in this case, a flat minimum is reached around 0.3. It should be noted that in this reconstruction all uncertainty components are considered.

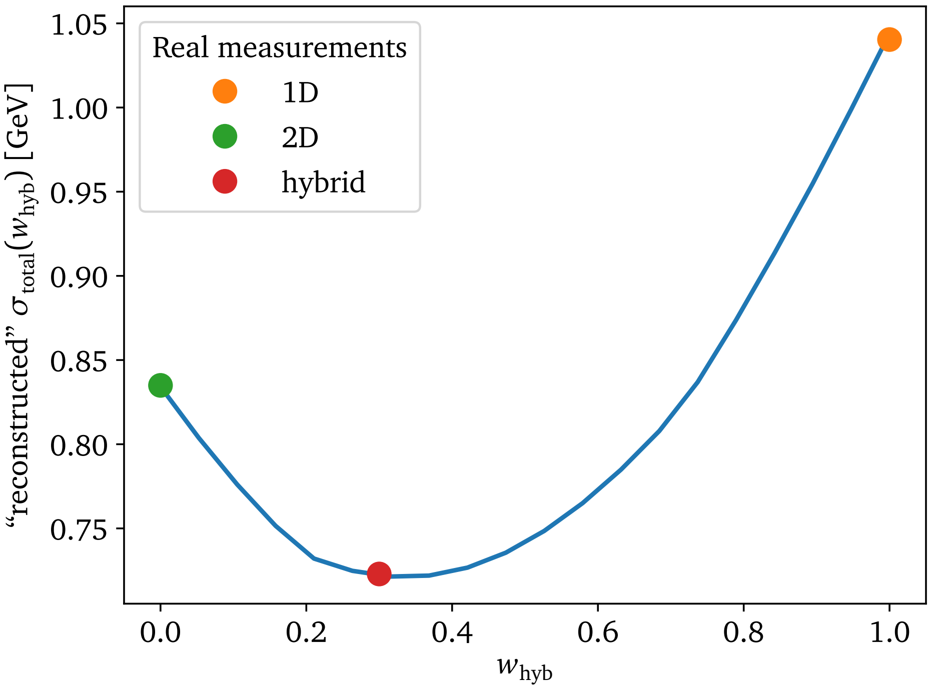

Figure 4.34: "Reconstructed" total uncertainties obtained from a weighted combination of the 1D and 2D methods as a function of the hybrid weight w_{hyb} (blue line). The dots show the 1D and 2D results, as well as the actual hybrid result at $w_{\mathrm{hyb}} = 0.3$.

4.8 Result

Finally, the measurement is performed with data. For the 2D fit using the 10 799 $\mathrm{t\bar{t}}$ all-jets candidate events, the extracted parameters are

$$\begin{aligned} m_{\mathrm{t}}^{\mathrm{2D}} &= 172.43 \pm 0.22\,(\text{stat+JSF}) \pm 0.81\,(\text{syst})\,\text{GeV and} \\ \mathrm{JSF}^{\mathrm{2D}} &= 0.996 \pm 0.002\,(\text{stat}) \pm 0.009\,(\text{syst}). \end{aligned}$$

The corresponding 1D and hybrid fits yield

$$\begin{aligned} m_{\mathrm{t}}^{\mathrm{1D}} &= 172.13 \pm 0.17\,(\text{stat}) \pm 1.03\,(\text{syst})\,\text{GeV}, \\ m_{\mathrm{t}}^{\mathrm{hyb}} &= 172.34 \pm 0.20\,(\text{stat+JSF}) \pm 0.70\,(\text{syst})\,\text{GeV, and} \\ \mathrm{JSF}^{\mathrm{hyb}} &= 0.997 \pm 0.002\,(\text{stat}) \pm 0.007\,(\text{syst}). \end{aligned}$$

Figure 4.35 shows the likelihood contours for $-2\Delta\ln\mathcal{L} = 2.3$ in the m_{t}-JSF plane for the 2D and hybrid methods. These ellipses correspond to 68% confidence level, i.e., represent the statistical uncertainty. In addition, the 1D measurement is shown with its error bar and the likelihood profiles for the top quark mass are shown in the lower panel for all three methods. The hybrid measurement is the main result of this analysis, since it is constructed to provide the lowest uncertainty. Due to the larger data sample used in this analysis, the statistical uncertainty is reduced with respect to the result of $m_{\mathrm{t}} = 172.32 \pm 0.25\,(\text{stat+JSF}) \pm 0.59\,(\text{syst})\,\text{GeV}$ obtained at $\sqrt{s} = 8\,\text{TeV}$. The result is in good agreement with the previous measurement, for which a leading order generator has been used for the $\mathrm{t\bar{t}}$ simulation, employed for the calibration, whereas in this analysis, an NLO simulation was used.

The systematic uncertainty is increased with respect to the Run 1 result, mainly because of the availability of more sophisticated color-reconnection model variations in PYTHIA 8, such that a broader set of CR models could be compared. These new models have first been used to evaluate the m_{t} uncertainty due to color reconnection in Ref. [57], where the same increase in systematic uncertainty with respect to the Run 1 result is observed. This is displayed in Fig. 4.36, which also shows the good compatibility of all measurements.

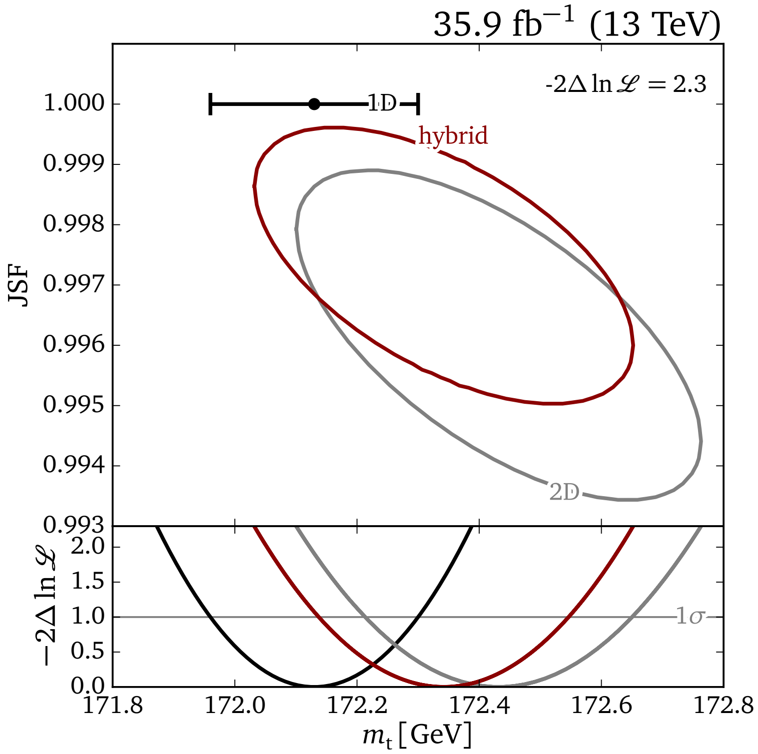

Figure 4.35: Upper panel: Likelihood contours for $-2\Delta\ln\mathcal{L} = 2.3$, representing 68% confidence level, in the m_t-JSF plane for the 2D and hybrid methods using the all-jets channel. The 1D result is shown with an error bar, corresponding to $-2\Delta\ln\mathcal{L} = 1$. Lower panel: The likelihood profiles for the top quark mass for all three methods. The level corresponding to one standard deviation (σ) is shown.

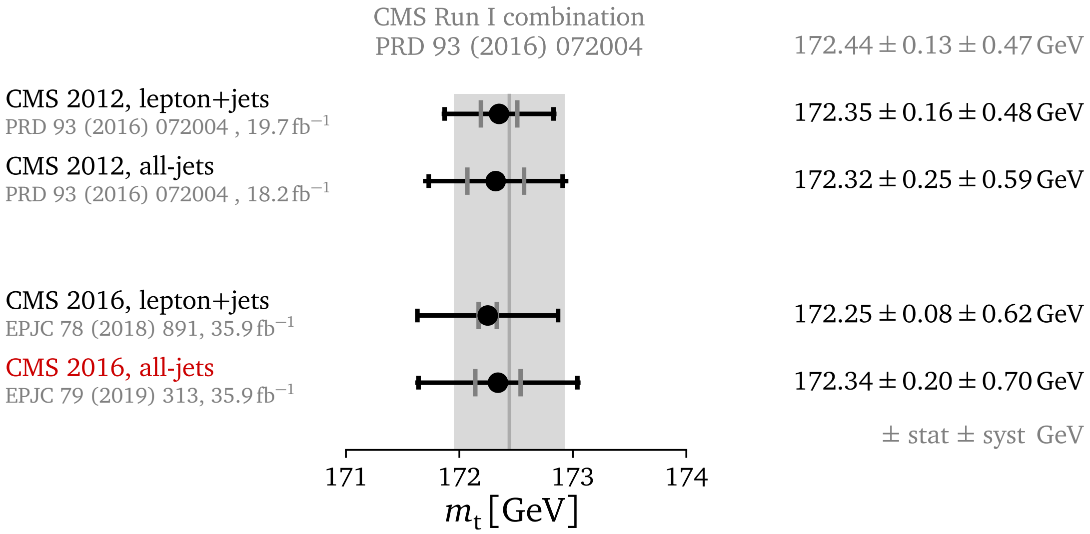

Figure 4.36: Comparison of the top quark mass measurement in the all-jets channel (red), presented in this thesis, to the result in the lepton+jets channel using the same dataset from 2016 and to the equivalent results at $\sqrt{s} = 8\,\text{TeV}$ using data collected in 2012. For all values the results of the hybrid method are displayed. The lines of the error bars show the total uncertainty, while the gray caps mark the statistical component and the black caps mark the systematic component. The gray line and area in the background represent the result of the combination of several CMS Run 1 results.

5

Combination with the lepton+jets channel

Chapter contents

A combined measurement of the top quark mass in the lepton+jets and all-jets final states is presented. The dataset taken in 2016 at $\sqrt{s} = 13\,\text{TeV}$ is used, corresponding to an integrated luminosity of $35.9\,\text{fb}^{-1}$.

The documentation of the lepton+jets analysis can be found in Refs. [57, 138, 153, 154], while the analysis of the all-jets final state has been presented in Refs. [1, 4, 155] and in Chapter 4 of this thesis. All aspects of the event selections and analysis strategies are kept unchanged. For the mass extraction, the ideogram method is used with a combined likelihood function described in Section 5.2, yielding single values for m_t and JSF. For this approach, no estimation of correlations for different uncertainty sources is needed, unlike for common combination attempts which use the results of several measurements and estimated correlations, like the best linear unbiased estimator (BLUE) method. In Section 5.3 a combination with the BLUE method is presented for comparison.

5.1 Measurement using the lepton+jets channel

The measurement of the top quark mass in the lepton+jets channel is described in Refs. [57, 138, 153, 154]. Since the event reconstruction and final mass extraction use very similar methods to those presented in this thesis, only a short overview of the lepton+jets analysis is given here.

Events are triggered using a single-muon or single-electron trigger. For muons, a minimum p_T of 24 GeV is required, while the threshold for electrons is 32 GeV. In both cases, the leptons need to be isolated from other energy deposits in the detector.

In the offline selection, events containing exactly one isolated lepton are used. Muons are required to be reconstructed within $|\eta| < 2.4$ with $p_\mathrm{T} > 26\,\mathrm{GeV}$ and for electrons, $|\eta| < 2.1$ and $p_\mathrm{T} > 34\,\mathrm{GeV}$ is required. Tau leptons are not explicitly considered in the selection, because the reconstruction is more complicated owing to the several decay modes of tau leptons and the presence of neutrinos from the decay. Tau leptons can still enter the signal selection due to decays to muons or electrons.

Jets are clustered using the anti-k_t algorithm as described in Section 4.1. Events are required to contain at least four jets with $p_\mathrm{T} > 30\,\mathrm{GeV}$ and $|\eta| < 2.4$. Among the leading four jets, exactly two need to be tagged as b jets. For this, the same CSVv2 algorithm is used as described in Section 4.1, but instead of the tight working point, the medium working point is used, corresponding to an efficiency of approximately 70% with a mistag rate of approximately 1%.

Like for the all-jets channel, $\mathrm{t\bar{t}}$ signal events are divided into different assignment classes. In addition to the correct permutations (cp) and wrong permutations (wp), unmatched permutations (un) are considered for the lepton+jets channel, which are included in the wrong permutations in the all-jets analysis. Wrong permutations correspond to those, where the right jets are selected, but the assignment to the partons is wrong, while in the case of unmatched permutations, at least one parton from the $\mathrm{t\bar{t}}$ decay cannot be matched to one of the selected jets.

Also in this channel, a kinematic fit is performed similar to that described in Section 4.3, but using the HitFit package [156]. The inputs to the fit are the momenta of the four jets, similar to the all-jets channel, the lepton momentum and the missing transverse momentum. The constraints are again the invariant mass of the W boson candidates (80.4 GeV) and the equality of the masses of the top quark and top antiquark candidates. Since only the two b tagged jets can be used as b quark candidates, the other two jets unambiguously form the W boson candidate. This leaves only two possible permutations in exchanging the b jets. In addition, for each of these, two solutions are considered for the longitudinal component of the neutrino momentum. Thus, a total of four permutations is available for the lepton+jets channel, in contrast to the 12 possible assignments for the all-jets channel. In the lepton+jets channel, all four permutations are used. The handling in the mass extraction is further discussed in Section 5.2.1. Since one component of the neutrino momentum cannot be measured, because only the missing transverse momentum $\vec{p}_\mathrm{T}^\mathrm{miss}$ can be used for the x and y momentum components, the number of degrees of freedom for the kinematic fit is reduced by one with respect to the all-jets channel. For $n = 2$ degrees of freedom the probability density function is

$$f_2(\chi^2) = \frac{1}{2} e^{-\chi^2/2}$$

and the corresponding p-value is

$$p_2(\chi^2) = \int_{\chi^2}^{\infty} f_2(x)\,dx = e^{-\chi^2/2}.$$

Events need to fulfill $P_{\mathrm{gof}} := p_2(\chi^2) > 0.2$ to be selected after the kinematic fit. This final selection contains 101 992 muon+jets events and 59 504 electron+jets events. Non-$\mathrm{t\bar{t}}$ background is determined using simulated samples and consists mainly of single top quark events, with minor contributions from W/Z +jets, QCD multijet, and diboson events. It amounts to a total of 4.3% after the final selection.

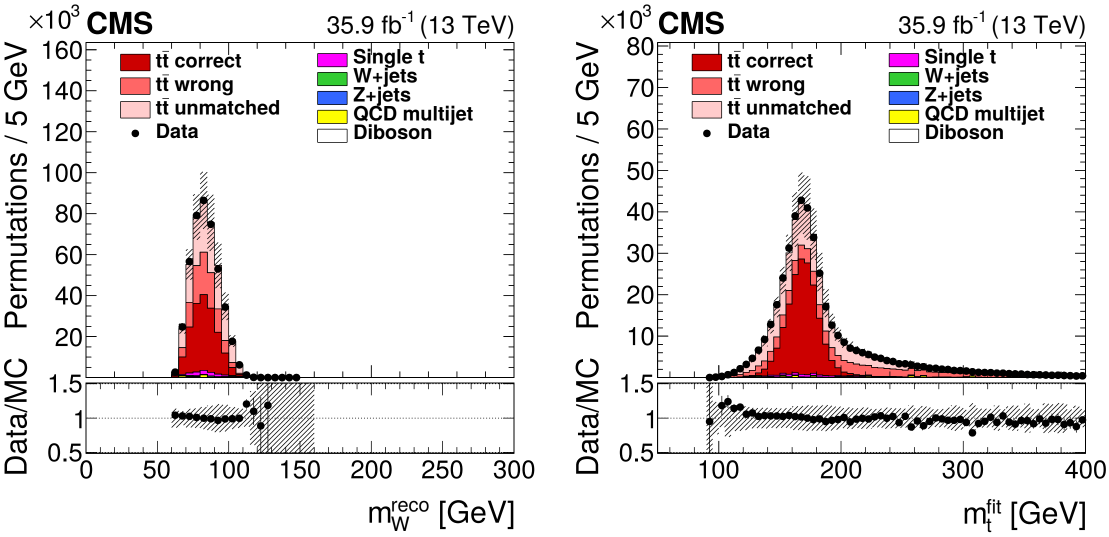

Figure 5.1: Reconstructed W boson masses $m_{\mathrm{W}}^{\mathrm{reco}}$ (left) and fitted top quark masses $m_{\mathrm{t}}^{\mathrm{fit}}$ (right) in the lepton+jets channel using the final selection [57]. The hashed bands represent the uncertainty of the prediction. The simulated processes are normalized to the recorded integrated luminosity.

The final distributions of $m_{\mathrm{W}}^{\mathrm{reco}}$ and $m_{\mathrm{t}}^{\mathrm{fit}}$, used for the mass extraction, are shown in Fig. 5.1. The resolution of the fitted top quark mass of 11 GeV is worse than for the all-jets channel, because of the worse missing transverse momentum resolution compared to the jet momentum resolution.

For the mass extraction, the ideogram method is employed, also using a 1D, 2D, and hybrid version. All four permutations are considered, as further described in Section 5.2.1. The 2D measurement in the lepton+jets channel [57] yields

$$\begin{aligned} m_{\mathrm{t}}^{\mathrm{2D}} &= 172.40 \pm 0.09\,(\mathrm{stat{+}JSF}) \pm 0.75\,(\mathrm{syst})\,\mathrm{GeV}, \\ \mathrm{JSF}^{\mathrm{2D}} &= 0.994 \pm 0.001\,(\mathrm{stat}) \pm 0.011\,(\mathrm{syst}). \end{aligned}$$

and the 1D and the hybrid fits result in

$$\begin{aligned} m_\mathrm{t}^{\mathrm{1D}} &= 171.93 \pm 0.06\,(\mathrm{stat}) \pm 1.10\,(\mathrm{syst})\,\mathrm{GeV}, \\ m_\mathrm{t}^{\mathrm{hyb}} &= 172.25 \pm 0.08\,(\mathrm{stat{+}JSF}) \pm 0.62\,(\mathrm{syst})\,\mathrm{GeV}, \\ \mathrm{JSF}^{\mathrm{hyb}} &= 0.996 \pm 0.001\,(\mathrm{stat}) \pm 0.008\,(\mathrm{syst}). \end{aligned}$$

5.2 Combined measurement

The events selected in the all-jets channel and those selected in the lepton+jets final state are used now simultaneously to determine the top quark mass. All selections are kept unchanged, resulting in a total of 172 295 events available for the mass extraction. Of these, 97 events are contained in both, the all-jets and the lepton+jets selections, which is possible, because no explicit lepton veto is applied in the all-jets analysis. Since these are only less than 0.1% of the events, no attempt is made to orthogonalize the selections. This could easily be achieved by a lepton veto for the all-jets final states, but would in principle require the derivation of new templates and introduce uncertainties related to the lepton identification and isolation criteria for the all-jets final state.

As for the single-channel measurements, the ideogram method is used to extract the top quark mass m_t and an additional jet scale factor JSF from the data sample. Also here, the 1D, 2D, and hybrid methods are used for the extraction and all three results are reported.

5.2.1 Total likelihood

To perform the mass extraction, a combined likelihood function is needed, including both, the lepton+jets and all-jets channels. It is given by the product likelihood,

$$\mathcal{L}(m_\mathrm{t}, \mathrm{JSF}) = \mathcal{L}_{\text{all-jets}}(m_\mathrm{t}, \mathrm{JSF}) \cdot \mathcal{L}_{\ell\text{+jets}}(m_\mathrm{t}, \mathrm{JSF}), \tag{5.1}$$

with the single-channel likelihoods $\mathcal{L}_{\text{all-jets}}(m_\mathrm{t}, \mathrm{JSF})$ and $\mathcal{L}_{\ell\text{+jets}}(m_\mathrm{t}, \mathrm{JSF})$ for the all-jets and lepton+jets channels, respectively. It is worth noting that the likelihood for the lepton+jets channel itself is already constructed similarly from the electron+jets and muon+jets channels,

$$\mathcal{L}_{\ell\text{+jets}}(m_\mathrm{t}, \mathrm{JSF}) = \mathcal{L}_{\text{e+jets}}(m_\mathrm{t}, \mathrm{JSF}) \cdot \mathcal{L}_{\mu\text{+jets}}(m_\mathrm{t}, \mathrm{JSF}).$$

Since $N_\mathrm{perm} = 4$ permutations per event are used for the lepton+jets channel, the likelihood per event is constructed as the sum of the likelihoods for all permutations, each weighted by the respective value of P_gof. In addition, each event is weighted by

$$w_\mathrm{evt} = c \sum_{i=1}^{N_\mathrm{perm}} P_\mathrm{gof}(i)$$

to give more emphasis to events that are more likely to contain a correct assignment. The normalization constant c is chosen such that the average of w_evt yields 1. Therefore, the lepton+jets likelihood reads

$$\mathcal{L}_{\ell+\text{jets}}\left(\text{sample}|m_\text{t},\text{JSF}\right)=\prod_{\text{events}}\left(\sum_{i=1}^{N_\text{perm}}P_\text{gof}(i)\cdot P\left(m_\text{t}^\text{fit},m_\text{W}^\text{reco}\middle|m_\text{t},\text{JSF}\right)\right)^{w_\text{evt}}.$$

The all-jets part of the likelihood, $\mathcal{L}_\text{all-jets}$, is given by Eq. (4.4). For all likelihood components used in Eq. (5.1), the same analytic functions are used as for the single-channel mass extractions. These are described in Section 4.5.1 for the all-jets channel and can be found in Refs. [138, 153] for the lepton+jets channel.

The total likelihood function given by Eq. (5.1) is maximized, yielding single values for m_t and JSF. For this measurement using both final states simultaneously in a single likelihood function, no estimation of correlations for different uncertainty sources is needed, unlike for common combination attempts which use the results of several measurements and estimated correlations. This is further discussed in Section 5.3.

5.2.2 Calibration validation

As for the single-channel measurements, pseudo-experiments are generated and the mass extraction is performed using these. For the single-channel measurements, these are used to calibrate the measurement with different generated values for m_t and JSF. Furthermore, pseudo-experiments with systematic variations are used to evaluate the systematic uncertainties for the combined measurement.

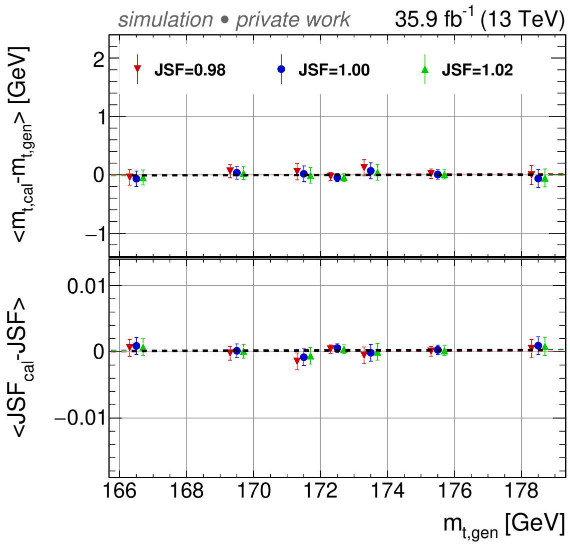

Figure 5.2: Difference of extracted and generated top quark masses and JSFs for different input masses and JSFs after the single-channel calibrations for the combined measurement.

No calibration is performed for the combined mass extraction, though, but the single-channel calibrations are used and only a validation is performed, ensuring that the combined measurement yields a reliable result. This validation is shown in Fig. 5.2 for different generated top quark masses and jet scale factors. No residual dependence is observed, showing that the calibrations for the individual channels still work when used in the combined likelihood and that the mass extraction can be performed on data.

The systematic uncertainties evaluated using pseudo-experiments for the combined measurement are discussed in Section 5.2.3.

5.2.3 Systematic uncertainties

The systematic uncertainty sources for the combined measurement are mainly those described in Section 4.6 and most of them are identical for the lepton+jets final state [57, 138, 153].

For the pseudo-experiments, the systematic uncertainty sources are varied simultaneously. For example, the ISR parton-shower scale is shifted upwards for both channels in the pseudo-experiments and the measurement is repeated to evaluate the effect on the extracted top quark mass. This procedure does not require the estimation of correlations, in contrast to combination methods like BLUE (see Section 5.3), which depends on the precision to which this correlation can be determined, which in many cases cannot be exact.

A special case are uncertainties which only affect a single channel. For example, the variation of the multijet background in the all-jets channel does not influence the lepton+jets part of the likelihood. Thus, such uncertainty sources are only varied for the corresponding channel. For the all-jets channel these are the background and trigger uncertainties. In addition, uncertainties specific to the lepton+jets channel are introduced, including the background and trigger uncertainties, as well as uncertainties arising from the lepton isolation and identification criteria, and are described in Refs. [57, 138, 153].

Table 5.1 lists all systematic uncertainties for the 1D, 2D and hybrid method of the combined measurement. In addition, a graphical representation can be found in Fig. 5.3.

Like for the all-jets result, the uncertainty due to the JEC is reduced for the 2D and hybrid methods with respect to the 1D method and the 2D uncertainty is smaller than the 1D uncertainty, because parts of the systematic uncertainties can be absorbed by the fit of the JSF. Also here, the hybrid method provides the smallest uncertainty.

For the main result, provided by the hybrid method, the total uncertainty is also dominated by uncertainties related to the flavor-dependent jet energy corrections and the modeling of color reconnection.

Due to the larger selected samples, some shifts are more significant than for the all-jets channel, i.e., the cases where the uncertainty of the shift is larger than the shift itself are more rare. Thus, the conservative treatment of taking the maximum of both does not have a strong impact in the combined measurement.

Table 5.1: List of systematic uncertainties for the combined mass extraction. The signs of the shifts ($\delta x = x_{\text{variation}} - x_{\text{nominal}}$) correspond to the +1 standard deviation variation of the systematic uncertainty source. For linear sums of the uncertainty groups, the relative signs have been considered. Shifts determined using dedicated samples for the systematic variation are displayed with the corresponding statistical uncertainty [1].

	2D		1D	hybrid	
	$\delta m_{\mathrm{t}}^{\mathrm{2D}}$ [GeV]	$\delta \mathrm{JSF}^{\mathrm{2D}}$ [%]	$\delta m_{\mathrm{t}}^{\mathrm{1D}}$ [GeV]	$\delta m_{\mathrm{t}}^{\mathrm{hyb}}$ [GeV]	$\delta \mathrm{JSF}^{\mathrm{hyb}}$ [%]
Experimental uncertainties					
Method calibration	0.03	0.0	0.03	0.03	0.0
JEC (quad. sum)	0.12	0.2	0.82	0.17	0.3
– Intercalibration	−0.01	0.0	+0.16	+0.04	+0.1
– MPFInSitu	−0.01	0.0	+0.23	+0.07	+0.1
– Uncorrelated	−0.12	−0.2	+0.77	+0.15	+0.3
Jet energy resolution	−0.18	+0.3	+0.09	−0.10	+0.2
b tagging	0.03	0.0	0.01	0.02	0.0
Pileup	−0.07	+0.1	+0.02	−0.05	+0.1
All-jets background	0.01	0.0	0.00	0.01	0.0
All-jets trigger	+0.01	0.0	0.00	+0.01	0.0
ℓ+jets Background	−0.02	0.0	+0.01	−0.01	0.0
ℓ+jets Trigger	0.00	0.0	0.00	0.00	0.0
Lepton isolation	0.00	0.0	0.00	0.00	0.0
Lepton identification	0.00	0.0	0.00	0.00	0.0
Modeling uncertainties					
JEC flavor (linear sum)	−0.39	+0.1	−0.31	−0.37	+0.1
– light quarks (uds)	+0.11	−0.1	−0.01	+0.07	−0.1
– charm	+0.03	0.0	−0.01	+0.02	0.0
– bottom	−0.31	0.0	−0.31	−0.31	0.0
– gluon	−0.22	+0.3	+0.02	−0.15	+0.2
b jet modeling (quad. sum)	0.08	0.1	0.04	0.06	0.1
– b frag. Bowler–Lund	−0.06	+0.1	−0.01	−0.05	0.0
– b frag. Peterson	−0.03	0.0	0.00	−0.02	0.0
– semileptonic b hadron decays	−0.04	0.0	−0.04	−0.04	0.0
PDF	0.01	0.0	0.01	0.01	0.0
Ren. and fact. scales	0.01	0.0	0.02	0.01	0.0
ME/PS matching	−0.10±0.08	+0.1	+0.02±0.05	+0.07±0.07	+0.1
ME generator	+0.16±0.21	+0.2	+0.32±0.13	+0.21±0.18	+0.1
ISR PS scale	+0.07±0.08	+0.1	+0.10±0.05	+0.07±0.07	0.1
FSR PS scale	+0.23±0.07	−0.4	−0.19±0.04	+0.12±0.06	−0.3
Top quark p_{T}	+0.01	−0.1	−0.06	−0.01	−0.1
Underlying event	−0.06±0.07	+0.1	+0.00±0.05	−0.04±0.06	+0.1
Early resonance decays	−0.20±0.08	+0.7	+0.42±0.05	−0.01±0.07	+0.5
CR modeling (max. shift)	+0.37±0.09	−0.2	+0.22±0.06	+0.33±0.07	−0.1
– “gluon move” (ERD on)	+0.37±0.09	−0.2	+0.22±0.06	+0.33±0.07	−0.1
– “QCD inspired” (ERD on)	−0.11±0.09	−0.1	−0.21±0.06	−0.14±0.07	−0.1
Total systematic	**0.71**	**1.0**	**1.07**	**0.61**	**0.7**
Statistical (expected)	0.08	0.1	0.05	0.07	0.1
Total (expected)	**0.72**	**1.0**	**1.08**	**0.61**	**0.7**

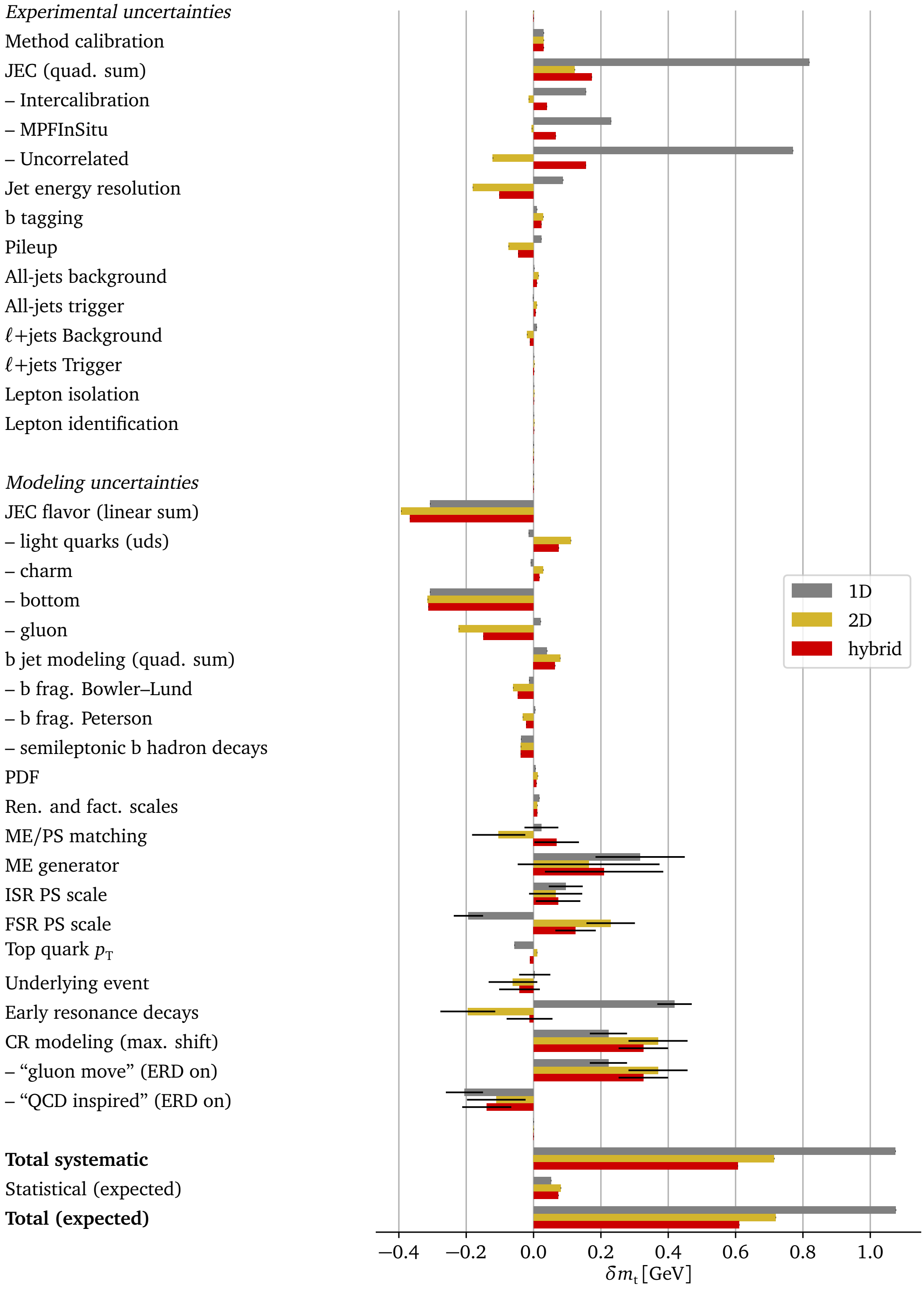

Figure 5.3: The sizes of the uncertainty components for the combined all-jets and lepton+jets channels. The three bars for each component represent the 1D, 2D, and hybrid methods. For two-sided uncertainties, the largest of the two shifts is shown, using the sign of the up-variation. Shifts that have an associated statistical uncertainty are presented with the corresponding error bars.

Comparison to the single-channel uncertainties

The expected total uncertainty of 0.61 GeV for the combined measurement is lower than the uncertainty for the all-jets channel. It is also improved with respect to the lepton+jets result with a total uncertainty of 0.63 GeV.

A comparison of the uncertainties of the hybrid mass extraction can be found in Table 5.2 for the all-jets and lepton+jets channels and the combined measurement. Figure 5.4 shows a graphical representation of this comparison. The corresponding figures for the 1D and 2D approaches can be found in Appendix B.3.

In general, most uncertainties for the combined measurement are similar to those for the lepton+jets channel, because the combination is dominated by that channel. For almost all components, the shift for the combined measurement is slightly smaller than that for the lepton+jets channel. Unfortunately, the shifts for the dominating uncertainties have the same sign for the all-jets and lepton+jets channels, such that the combination cannot profit much from cancellation effects. An example for such a partial cancellation is the underlying event uncertainty, which is not a dominant one, though. Other dominating uncertainties, like the flavor-dependent JECs, have the same sign and a similar amplitude for the single channels, such that the overall improvement is small.

Table 5.2: Comparison of the hybrid mass uncertainties for the all-jets and lepton+jets [57] channels, as well as the combination. The signs of the shifts follow the convention of Tables 4.5 and 5.1 [1].

	$\delta m_{\mathrm{t}}^{\mathrm{hyb}}$ [GeV]		
	all-jets	ℓ+jets	combination
Experimental uncertainties			
Method calibration	0.06	0.05	0.03
JEC (quad. sum)	0.15	0.18	0.17
– Intercalibration	−0.04	+0.04	+0.04
– MPFInSitu	+0.08	+0.07	+0.07
– Uncorrelated	+0.12	+0.16	+0.15
Jet energy resolution	−0.04	−0.12	−0.10
b tagging	0.02	0.03	0.02
Pileup	−0.04	−0.05	−0.05
All-jets background	0.07	—	0.01
All-jets trigger	+0.02	—	+0.01
ℓ+jets background	—	+0.02	−0.01
Modeling uncertainties			
JEC flavor (linear sum)	−0.34	−0.39	−0.37
– light quarks (uds)	+0.07	+0.06	+0.07
– charm	+0.02	+0.01	+0.02
– bottom	−0.29	−0.32	−0.31
– gluon	−0.13	−0.15	−0.15
b jet modeling (quad. sum)	0.09	0.12	0.06
– b frag. Bowler–Lund	−0.07	−0.05	−0.05
– b frag. Peterson	−0.05	+0.04	−0.02
– semileptonic b hadron decays	−0.03	+0.10	−0.04
PDF	0.01	0.02	0.01
Ren. and fact. scales	0.04	0.01	0.01
ME/PS matching	+0.24	−0.07	+0.07
ME generator	—	+0.20	+0.21
ISR PS scale	+0.14	+0.07	+0.07
FSR PS scale	+0.18	+0.13	+0.12
Top quark p_{T}	+0.03	−0.01	−0.01
Underlying event	+0.17	−0.07	−0.06
Early resonance decays	+0.24	−0.07	−0.07
CR modeling (max. shift)	−0.36	+0.31	+0.33
– “gluon move” (ERD on)	+0.32	+0.31	+0.33
– “QCD inspired” (ERD on)	−0.36	−0.13	−0.14
Total systematic	**0.70**	**0.62**	**0.61**
Statistical (expected)	0.20	0.08	0.07
Total (expected)	**0.72**	**0.63**	**0.61**

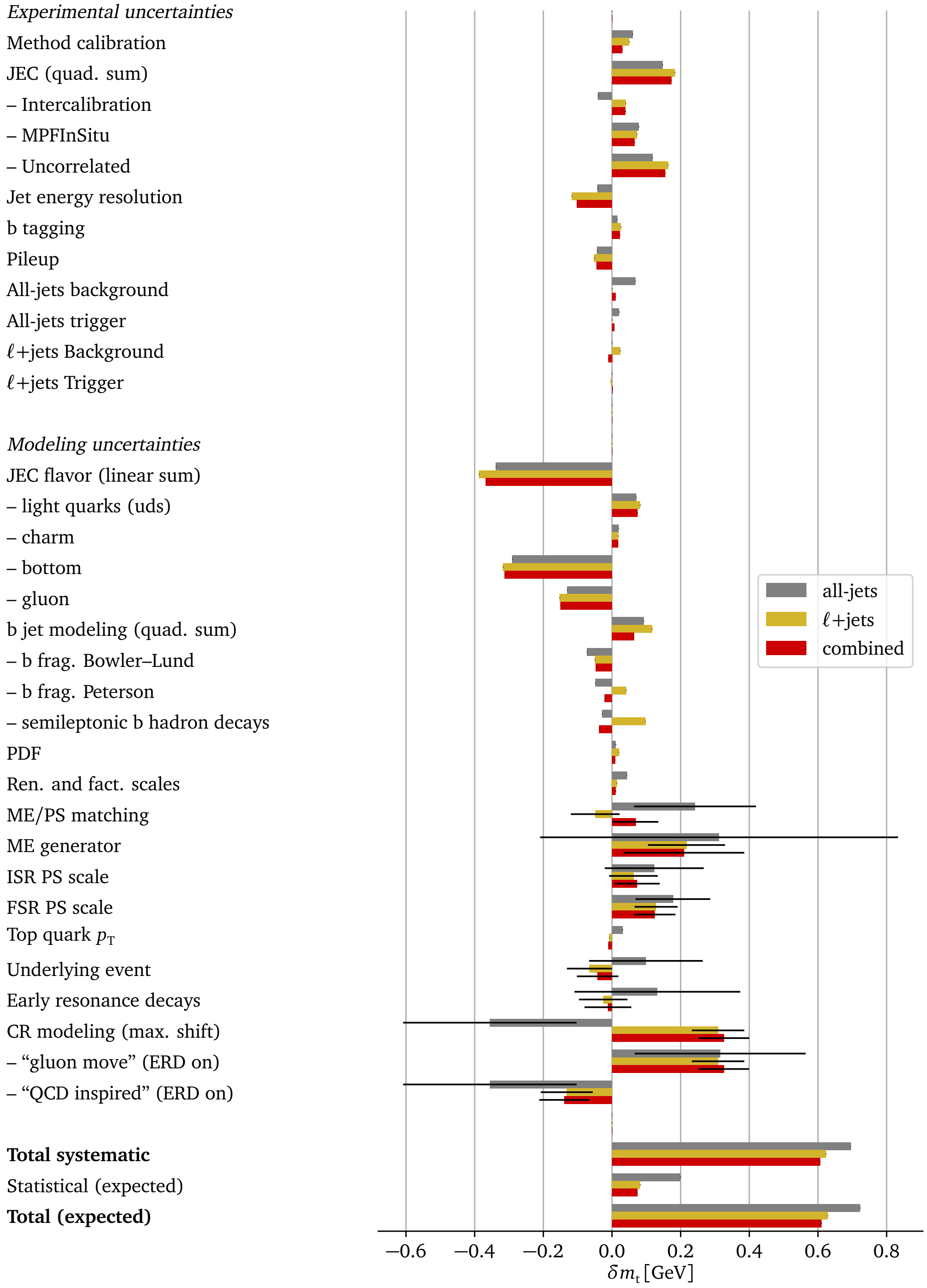

Figure 5.4: The sizes of the uncertainty components for the hybrid top quark mass measurement. The three bars for each component represent the measurements using the all-jets channel, the lepton+jets channel, and combined measurent. For two-sided uncertainties, the largest of the two shifts is shown, using the sign of the up-variation. Shifts that have an associated statistical uncertainty are presented with the corresponding error bars.

5.2.4 Weighted combination

The result is dominated by the lepton+jets part, because the number $N_\mathrm{L} = 161\,496$ of selected events in the lepton+jets channel is significantly larger than the corresponding number $N_\mathrm{A} = 10\,799$ for the all-jets channel. This way, only the statistical precision is considered for the relative importance of the channels in the likelihood for the combined measurement.

Since the total uncertainties of both separate results are dominated by the systematic uncertainties, those could be considered as well, i.e., the likelihoods could be weighted taking into account the total uncertainties. To achieve this, two steps are used to modify the approach described by Eq. (5.1). First, the lepton+jets likelihood is scaled to match the statistical precision of the all-jets selection. Second, relative weights w_L and w_A are introduced considering the total uncertainties $\sigma_{\ell\text{+jets}}$ and $\sigma_\text{all-jets}$ of the single-channel results.

Since the logarithmic likelihoods are proportional to the number of events,

$$\ln \mathcal{L}_i \propto N_i \,,$$

the lepton+jets likelihood is rescaled by the relative events counts

$$\ln \mathcal{L}_{\ell\text{+jets}} \rightarrow \frac{N_\mathrm{A}}{N_\mathrm{L}} \ln \mathcal{L}_{\ell\text{+jets}} \,. \tag{5.2}$$

This artificially leads to an increased statistical uncertainty, which is acceptable, because the measurements are dominated by systematic uncertainties.

To take into account the weights for the second step, the total likelihood is modified to be

$$\mathcal{L} = \left(\mathcal{L}_\text{all-jets}\right)^{w_\mathrm{A}} \cdot \left(\mathcal{L}_{\ell\text{+jets}}\right)^{w_\mathrm{L}} \,,$$

with the weights w_A and w_L for the all-jets and lepton+jets channels, respectively. Consequently, the logarithmic likelihood becomes a weighted sum

$$\ln \mathcal{L} = w_\mathrm{A} \ln \mathcal{L}_\text{all-jets} + w_\mathrm{L} \ln \mathcal{L}_{\ell\text{+jets}} \,.$$

The weights are given by

$$w_i = \frac{1/\sigma_i^2}{\sum_{i=\mathrm{L,\,A}} 1/\sigma_i^2} \,,$$

where the total uncertainties are $\sigma_{\ell\text{+jets}} = 0.63\,\mathrm{GeV}$ and $\sigma_\text{all-jets} = 0.72\,\mathrm{GeV}$. Assuming the lepton+jets likelihood to be rescaled already, the relative weights are

$$w'_\mathrm{A} = \frac{1/\sigma^2_\text{all-jets}}{1/\sigma^2_\text{all-jets} + 1/\sigma^2_{\ell\text{+jets}}} = \frac{\sigma^2_{\ell\text{+jets}}}{\sigma^2_{\ell\text{+jets}} + \sigma^2_\text{all-jets}} = 0.43$$

$$\text{and} \quad w'_\mathrm{L} = 0.57 \,.$$

Because $\mathcal{L}_{\ell\text{+jets}}$ has to be scaled anyway, there is no need to also downscale $\mathcal{L}_{\text{all-jets}}$. Instead, the appropriate relative weight of $w'_{\text{L}}/w'_{\text{A}}$ is only considered for $\mathcal{L}_{\ell\text{+jets}}$. Incorporating the scaling described by Eq. (5.2) into the weights, one finally obtains

$$\begin{aligned} & w_{\text{A}} = 1 \\ \text{and} \quad & w_{\text{L}} = \frac{N_{\text{A}}}{N_{\text{L}}} \cdot \frac{w'_{\text{L}}}{w'_{\text{A}}} = 0.089\,. \end{aligned}$$

Instead of fixing the value, different values for the combination weight w_{L} can be assumed to test if the overall precision of the measurement can be improved at all. This combination weight scan is performed in the same way as the hybrid weight scan described in Section 4.7 for the all-jets channel. The result of the scan is presented in Fig. 5.5 relative to the unweighted combination.

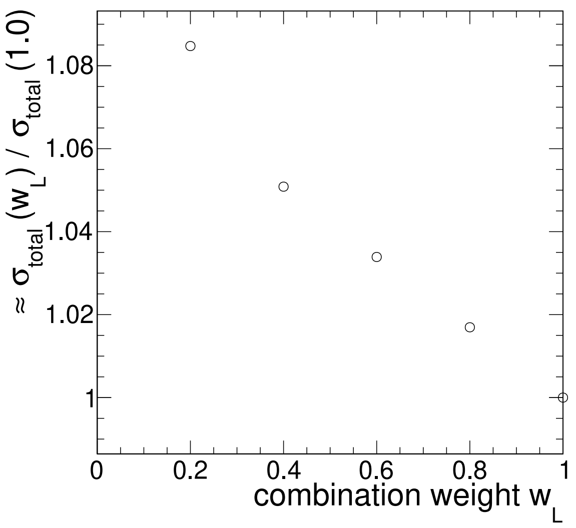

Figure 5.5: The systematic uncertainties obtained for six different choices for the combination weight w_{L} normalized to the result for the unweighted combination, corresponding to $w_{\text{L}} = 1$.

For all tested values of $w_{\text{L}} < 1$, the total uncertainty is larger than the total uncertainty for the unweighted combined measurement, but only increased in the range of a few percent. The uncertainty grows monotonically towards $w_{\text{L}} \to 0$, i.e., no precision is gained for weights in the range $w_{\text{L}} \in (0, 1)$. Therefore, the simple unweighted likelihood as used before is utilized for the combined measurement and the main result of this thesis, presented in Section 5.2.6.

5.2.5 Validation of the hybrid weight choice

The hybrid weight w_{hyb}, controlling the strength of the JSF prior constraint for the hybrid measurement, had the same value of 0.3 for the all-jets and lepton+jets channels. To validate that this choice is also optimal for the combined measurement, a hybrid weight scan is performed, exactly as described in Section 4.7 for the all-jets channel.

The result is shown in Fig. 5.6 and also here a minimal uncertainty is reached at around $w_{\mathrm{hyb}} = 0.3$, justifying that this value is also used for the combination.

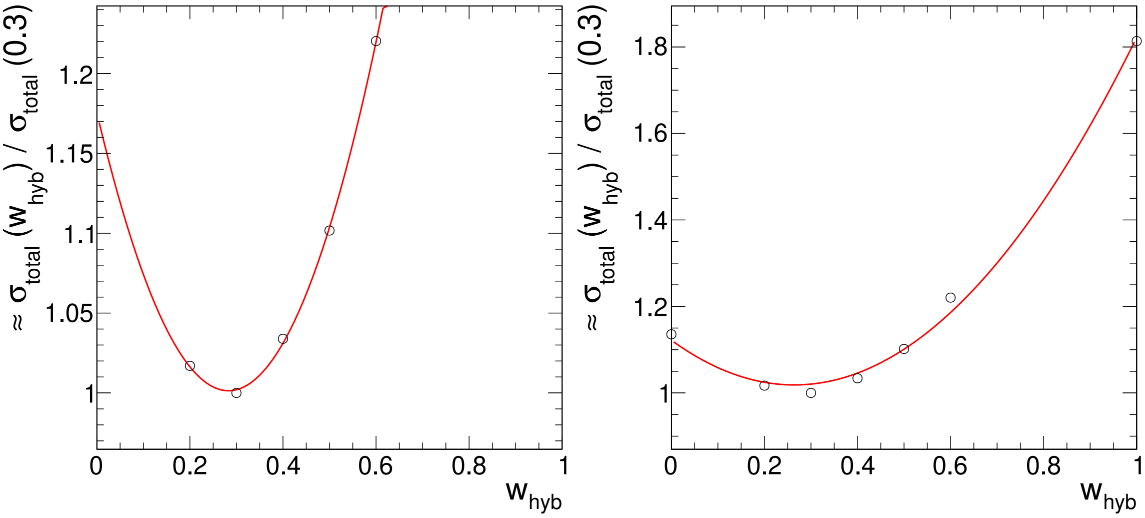

Figure 5.6: Hybrid weight scan for the combined top quark mass measurement. Left: The total uncertainties obtained for six different choices for w_{hyb}, normalized to the value for $w_{\mathrm{hyb}} = 0.3$. Right: In addition, the values for the 2D and 1D results are inserted manually at $w_{\mathrm{hyb}} = 0$ and 1. The red lines are parabolic fits to the points. The approximately equal sign (≈) indicates that only the largest uncertainty components have been considered.

In addition, also the “reconstructed” hybrid mass uncertainty, as described on page 85, is scanned for different values of w_{hyb}. The shift for the uncertainty source i is obtained by combining the 1D and 2D values,

$$\delta m_i^{\mathrm{hyb}*} = w_{\mathrm{hyb}} \delta m_i^{\mathrm{1D}} + (1 - w_{\mathrm{hyb}}) \delta m_i^{\mathrm{2D}} .$$

The result for the total uncertainty is shown in Fig. 5.7 as a function of w_{hyb}, again verifying a minimum at $w_{\mathrm{hyb}} \approx 0.3$. Also for the combined measurement, this method reconstructs the total uncertainty of the actual hybrid measurement very well.

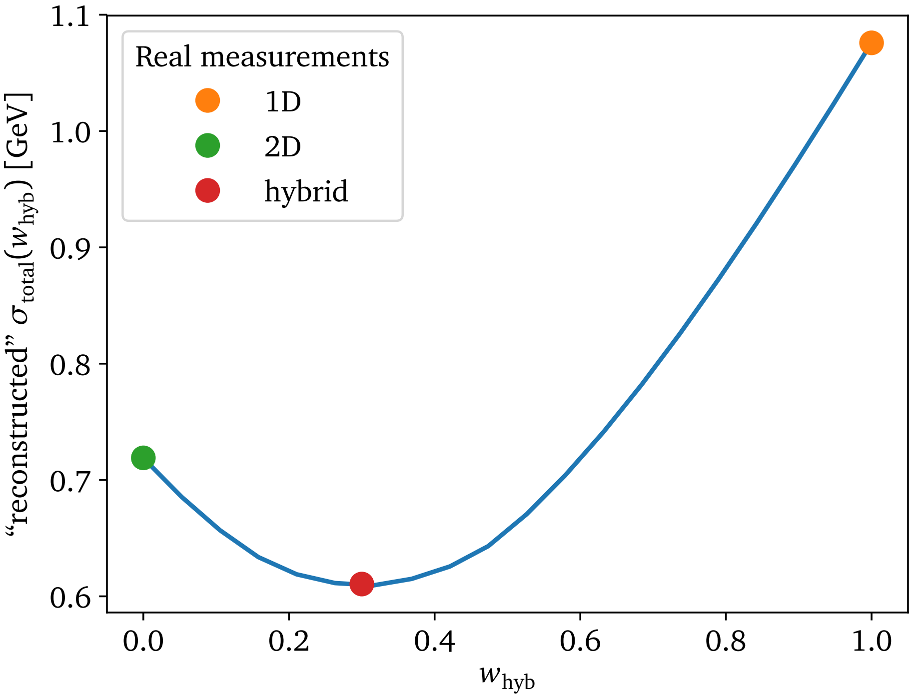

Figure 5.7: "Reconstructed" total uncertainties obtained from a weighted combination of the 1D and 2D methods as a function of the hybrid weight w_{hyb} (blue line) for the combined top quark mass measurement. The dots show the 1D and 2D results, as well as the actual hybrid result at $w_{\text{hyb}} = 0.3$.

5.2.6 Result

The combined measurement is performed using the all-jets and lepton+jets data and yields

$$\begin{aligned} m_{\mathrm{t}}^{\mathrm{2D}} &= 172.39 \pm 0.08\,(\text{stat+JSF}) \pm 0.70\,(\text{syst})\,\text{GeV and} \\ \text{JSF}^{\mathrm{2D}} &= 0.995 \pm 0.001\,(\text{stat}) \pm 0.010\,(\text{syst}) \end{aligned}$$

for the 2D method. The 1D and hybrid fits result in

$$\begin{aligned} m_{\mathrm{t}}^{\mathrm{1D}} &= 171.94 \pm 0.05\,(\text{stat}) \pm 1.07\,(\text{syst})\,\text{GeV}, \\ m_{\mathrm{t}}^{\mathrm{hyb}} &= 172.26 \pm 0.07\,(\text{stat+JSF}) \pm 0.61\,(\text{syst})\,\text{GeV, and} \\ \text{JSF}^{\mathrm{hyb}} &= 0.996 \pm 0.001\,(\text{stat}) \pm 0.007\,(\text{syst})\,. \end{aligned}$$

Like for the single-channel results, the hybrid measurement is considered the main result. This is the first top quark mass measurement using the combined $\mathrm{t\bar{t}}$ lepton+jets and all-jets final states.

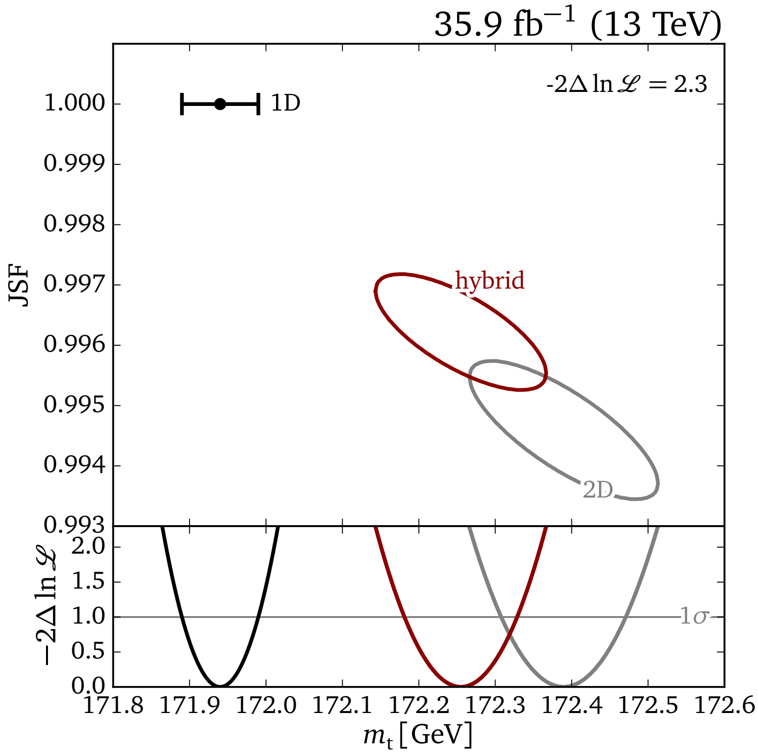

Figure 5.8: Upper panel: Likelihood contours for $-2\Delta\ln\mathcal{L} = 2.3$, representing 68% confidence level, in the m_{t}-JSF plane for the 2D and hybrid methods using the combined measurement. The 1D result is shown with an error bar, corresponding to $-2\Delta\ln\mathcal{L} = 1$. Lower panel: The likelihood profiles for the top quark mass for all three methods. The level corresponding to one standard deviation (σ) is shown.

Figure 5.8 shows the likelihood contours for $-2\Delta\ln\mathcal{L} = 2.3$ in the m_{t}-JSF plane for the 2D and hybrid methods, corresponding to 68% confidence level. In addition, the 1D measurement is shown with its error bar and the likelihood profiles for the top quark mass are shown in the lower panel for all three methods. Like for the all-jets channel, the hybrid measurement is the main result of this analysis, since it is constructed to provide the lowest uncertainty. The statistical uncertainty is reduced with respect to the all-jets result, because of the significantly increased number of selected events in the combined data sample.

The likelihood contours for $-2\Delta\ln\mathcal{L} = 2.3$ in the m_t-JSF plane are shown in Fig. 5.9 for the hybrid measurement results for the all-jets and lepton+jets channels, as well as for the combination. Additionally, the likelihood profiles for the top quark mass are shown. Both channels are in statistical agreement with each other. The result of the combination is closer to the lepton+jets channel, as expected.

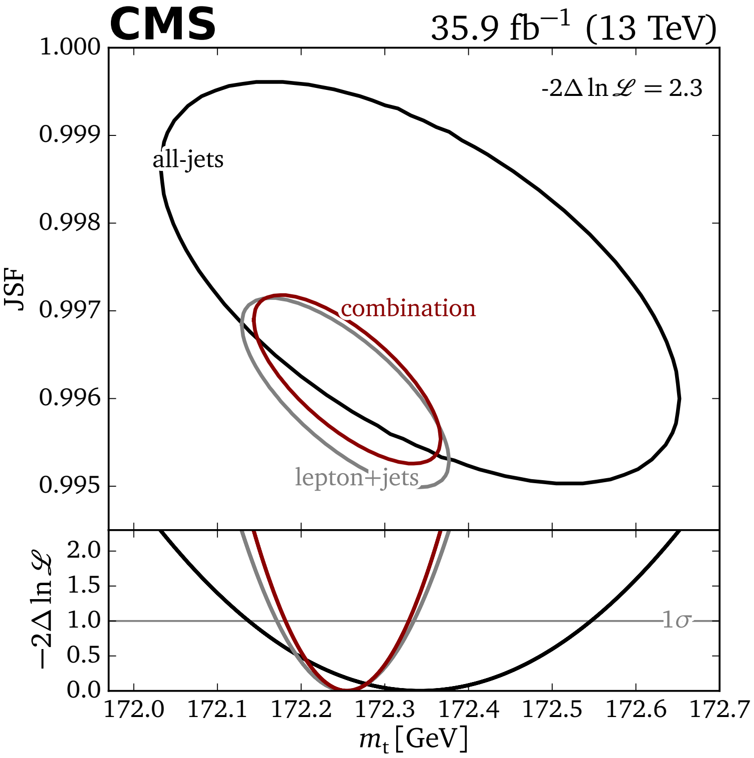

Figure 5.9: Likelihood contours for $-2\Delta\ln\mathcal{L} = 2.3$ in the m_t-JSF plane (upper panel) and the likelihood profiles for the top quark mass (lower panel). The hybrid measurement results for the all-jets and lepton+jets channels, as well as for the combination, are shown [1].

The systematic uncertainty is still larger than that for the most precise Run 1 results, for the same reasons discussed for the single channel results, i.e., mainly the availability of more color-reconnection model variations in PYTHIA 8. This is displayed in Fig. 5.10, showing the result of the combined measurement compared to the single-channel results, including the systematic uncertainties, and the Run 1 combination. Also here, good compatibility of the measurements can be observed.

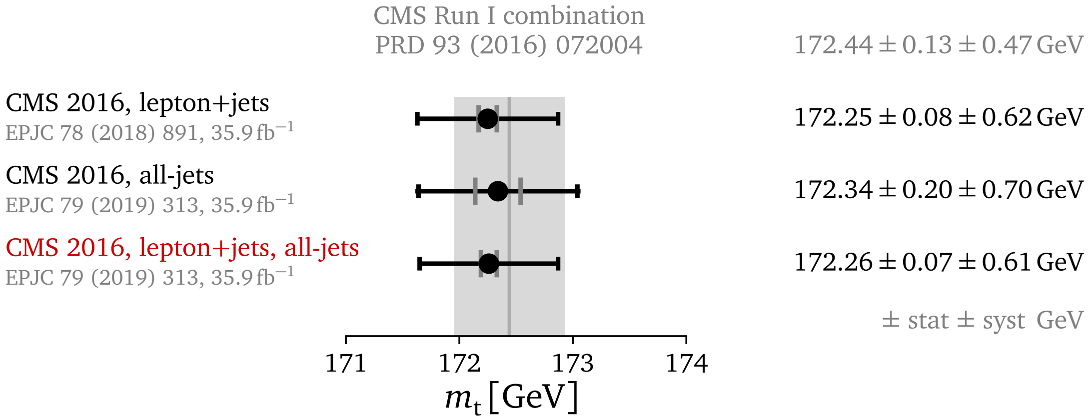

Figure 5.10: Comparison of the top quark mass measurement in the combined all-jets and lepton+jets channels (red), presented in this thesis, to the single-channel results using the same dataset from 2016. For all values the results of the hybrid method are displayed. The lines of the error bars show the total uncertainty, while the gray caps mark the statistical component and the black caps mark the systematic component. The gray line and area in the background represent the result of the combination of several CMS Run 1 results.

5.3 BLUE combination

An alternative approach to a combined measurement is the combination of separate results. This strategy is often chosen when a combined measurement is technically impossible or too complicated. The usual procedure used in particle physics is the best linear unbiased estimator (BLUE) method [157, 158]. An example with relevance to this measurement is the top quark mass world combination [159]. To take into account the systematic uncertainties, the correlations between the measurements for all uncertainty components have to be estimated, though, which cannot be done precisely in many cases. Therefore, assumptions have to be made, which often lead to the choice of 100 or 0% correlation for the single components.

5.3.1 Method description

The BLUE method is used to combine n measurements of a quantity y, denoted

$$y_1, \dots, y_n,$$

together with the corresponding uncertainties σ_i. For the method to be exact, the precise knowledge of all correlations is required, i.e., the full $n \times n$ covariance matrix E has to be known. The estimator $\hat{y}$ constructed with the BLUE method is subject to three requirements.

Linear: The estimator $\hat{y}$ is a linear combination of the measurement values $y_1, \dots, y_n$,

$$\hat{y} = \sum_{i=1}^{n} \alpha_i y_i, \tag{5.3}$$

where each measurement y_i is weighted with a factor of $\alpha_i \in \mathbb{R}$. The values $\alpha_1, \dots, \alpha_n$ are summarized in a $\mathbb{R}^n$ vector

$$\alpha = \begin{bmatrix} \alpha_1 \\ \vdots \\ \alpha_n \end{bmatrix}.$$

Unbiased: For the estimator $\hat{y}$ to be unbiased, the weights α_i need to sum up to unity,

$$\sum_{i=1}^{n} \alpha_i = 1\,.$$

Best: The set of $\{\alpha_i\}$ is chosen that minimizes the variance σ^2 of $\hat{y}$,

$$\sigma^2 = \alpha^{\mathrm{T}} E \alpha = \sum_{i=1}^{n} \sum_{j=1}^{n} E_{ij} \alpha_i \alpha_j. \tag{5.4}$$

Negative weights, and therefore also weights larger than unity, are explicitly allowed and to be expected in certain cases.

The method thus consists in finding the α providing the minimal σ^2. An algebraic solution is given by

$$\alpha = E^{-1}U/(U^{\mathrm{T}}E^{-1}U),$$

where a n-component design vector

$$U = \begin{bmatrix} 1 \\ \vdots \\ 1 \end{bmatrix}$$

is used. The estimator $\hat{y}$ is then given by Eq. (5.3). The algebraic solution is equivalent to a χ^2 minimization considering correlations, i.e., directly finding the $\hat{y}$ minimizing

$$\chi^2 = \sum_{i=1}^{n}\sum_{j=1}^{n}(\hat{y} - y_i)(\hat{y} - y_j)(E^{-1})_{ij} .$$

For completely uncorrelated measurements, E is a diagonal matrix and the BLUE method becomes a simple $1/\sigma_i^2$-weighted mean with weights given by

$$\alpha_i = (E^{-1}U)_i/(U^{\mathrm{T}}E^{-1}U) = \frac{1}{\sigma_i^2}\Bigg/\sum_{j=1}^{n}\frac{1}{\sigma_j^2} .$$

5.3.2 Reduced correlations

If the correlations of the input to BLUE become strong, the weights assigned to some measurements may become negative [157]. This is expected and correct if the covariance matrix is really exact. In most applications, the covariance matrix is estimated, though, and negative weights are often considered as a sign that the correlations are overestimated. To overcome this, a commonly used option for BLUE is that of “reduced correlations”. For two measurements X and Y the correlation of an uncertainty component is given by

$$\rho_{XY} = \mathrm{Cov}_{XY}/(\sigma_X\sigma_Y) .$$

Choosing the labeling such that $\sigma_X \leq \sigma_Y$, a reduced correlation ρ_{XY}^{red} is introduced by first splitting σ_Y into $(\sigma_X) + (\sigma_Y - \sigma_X)$. Only the (σ_X) part is assumed to be fully correlated with X, while the remaining $(\sigma_Y - \sigma_X)$ part is treated as uncorrelated. The reduced covariance then reads

$$\mathrm{Cov}_{XY}^{\mathrm{red}} = \rho_{XX}\sigma_X\sigma_X = \sigma_X^2$$

and the corresponding reduced correlation is given by

$$\rho_{XY}^{\mathrm{red}} = \mathrm{Cov}_{XY}^{\mathrm{red}}/(\sigma_X\sigma_Y) = \sigma_X^2/(\sigma_X\sigma_Y) = \sigma_X/\sigma_Y .$$

Neither the estimation of the correlations, nor the method of reduced correlations are statistically exact methods or based on first principles. Thus, in practice, the total correlation ρ is often varied around the estimated (reduced) correlation value to verify that correlation assumptions do not alter the result much.

5.3.3 Implementation and results

As the input for the lepton+jets channel, $m_{\mathrm{t}} = 172.25 \pm 0.63$ GeV is used, corresponding to the result presented in Ref. [57], and for the all-jets channel 172.34 ± 0.72 GeV. Table 5.3 lists the assumed correlations of the individual uncertainty components between the all-jets and lepton+jets channels. These are set to either 0 or 100% and follow the correlation assumptions of the latest world combination as close as possible [159].

Table 5.3: Correlations of the individual uncertainty components assumed in the BLUE combination of the all-jets and lepton+jets channels for the hybrid mass measurement.

Source	Correlation
Method calibration	0%
JEC Intercalibration	100%
JEC MPFInSitu	100%
JEC Uncorrelated	100%
Jet energy resolution	100%
b tagging	100%
Pileup	100%
Background	0%
Trigger	0%
JEC flavor	100%
b jet modeling	100%
PDF	100%
Ren. and fact. scales	100%
ME/PS matching	100%
ME generator	100%
ISR PS scale	100%
FSR PS scale	100%
Top quark p_{T}	100%
Underlying event	100%
Early resonance decays	100%
CR modeling	100%
Stat.	0%

For completely uncorrelated components, the choices are rather clear. For example, the background estimations for both channels are derived using completely independent methods, the used triggers are unrelated, and the method calibration and statistical uncertainties are of purely statistical origin. Most systematic uncertainty sources are correlated, because they are derived using the same variation of a calibration or comparing different models. While the sources may be 100% correlated, the resulting shifts might not. It is even possible that the resulting shifts have a different sign and assuming a negative correlation would be appropriate. The situation is further complicated for shifts with a statistical uncertainty. For insignificant shifts, assuming a sign for the correlation is not easy to justify. Thus, it is not expected that a completely exact result can be obtained using a BLUE combination. The correlations listed in Table 5.3 are used for a first attempt and a more general consideration of the total correlation is presented in Section 5.3.4.

The covariance matrix for a single source i is constructed using the uncertainty components σ^i_{L} and σ^i_{A} of both analyses and their correlation coefficient ρ^i,

$$E^i = \begin{bmatrix} \left(\sigma^i_{\mathrm{L}}\right)^2 & \rho^i\sigma^i_{\mathrm{L}}\sigma^i_{\mathrm{A}} \\ \rho^i\sigma^i_{\mathrm{L}}\sigma^i_{\mathrm{A}} & \left(\sigma^i_{\mathrm{A}}\right)^2 \end{bmatrix}.$$

The sum of all E^i yields the total covariance matrix

$$E = \sum_i E^i$$

used for the BLUE combination.

An own PYTHON implementation of the BLUE method, provided as `blue_combine` package [160], is used, which has been cross-checked with an existing FORTRAN code. The script defining the exact input, including the construction of the covariance matrix can be found in Appendix C.1, Listing C.1.

The covariance matrix constructed using the assumptions listed in Table 5.3 is

$$E[\mathrm{GeV}^2] = \begin{bmatrix} 0.3989 & 0.3684 \\ 0.3684 & 0.5269 \end{bmatrix},$$

corresponding to an overall correlation coefficient of 80%. The BLUE combination of the all-jets and lepton+jets channels yields

weight ℓ+jets	0.839
weight all-jets	0.161

$m_{\mathrm{t}} = 172.265 \pm 0.628\,\mathrm{GeV}$

with a p-value of 0.836 for the χ^2 with one degree of freedom. The weight for the lepton+jets channel is larger, because the uncertainty is smaller. Thus, the result is dominated by this channel, similar to the likelihood-based combination.

For comparison, the method of reduced correlations is applied, yielding a covariance matrix of

$$E[\mathrm{GeV}^2] = \begin{bmatrix} 0.3989 & 0.2811 \\ 0.2811 & 0.5269 \end{bmatrix},$$

i.e., a lower correlation coefficient of 61%. With this covariance matrix, the result becomes

weight ℓ+jets	0.676
weight all-jets	0.324

$m_{\mathrm{t}} = 172.279 \pm 0.601\,\mathrm{GeV}$

with a χ^2 p-value of 0.881. The reduced correlation leads to a slightly increased importance of the all-jets channel, but the lepton+jets channel is still dominating the combination. The uncertainty is reduced by more than 20 MeV.

Following Eq. (5.4), the individual uncertainty components i of the BLUE combination result can be calculated using

$$\sigma_i^2 = \alpha^{\mathrm{T}} E_i \alpha \, .$$

These uncertainties for the different sources are listed in Table 5.4 for the default BLUE combination and for the case using reduced correlations. Since the two values for each source are obtained by a weighted combination of the single-channel uncertainty components and the weights are not altered much, most values are very similar. Because in both cases the weights are positive, the combinations result in a value between the single-channel results, as displayed in Fig. 5.11. The central value for the default BLUE combination is closer to the measurement using both final states simultaneously, while the combination with reduced correlations is shifted upwards by 20 MeV. Similar total uncertainties are obtained with the BLUE combinations compared to the likelihood-

Table 5.4: Uncertainty components for the BLUE combination results using the correlation assumptions listed in Table 5.3 and for reduced correlations.

	Uncertainty [GeV]	
Source	default	red. cor.
Method calibration	0.04	0.04
JEC Intercalibration	0.04	0.04
JEC MPFInSitu	0.07	0.07
JEC Uncorrelated	0.15	0.14
Jet energy resolution	0.11	0.09
b tagging	0.03	0.03
Pileup	0.05	0.04
Background	0.02	0.03
Trigger	0.00	0.01
JEC flavor	0.38	0.36
b jet modeling	0.12	0.10
PDF	0.02	0.02
Ren. and fact. scales	0.01	0.02
ME/PS matching	0.10	0.10
ME generator	0.17	0.14
ISR PS scale	0.08	0.08
FSR PS scale	0.14	0.14
Top quark p_{T}	0.01	0.01
Underlying event	0.09	0.09
Early resonance decays	0.10	0.10
CR modeling	0.32	0.32
Stat.	0.07	0.08

based combination. For the default BLUE combination it is 20 MeV larger and for the reduced correlations it is 10 MeV smaller.

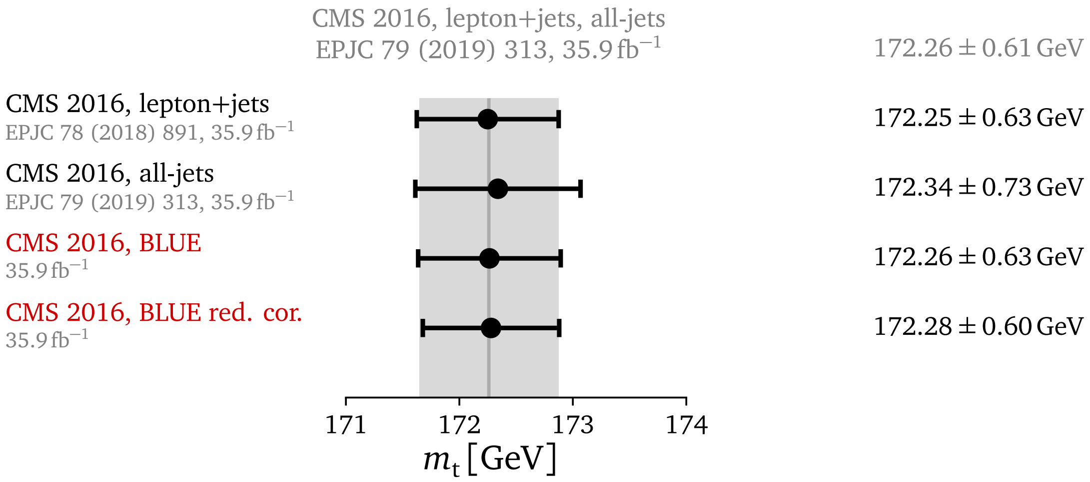

Figure 5.11: Comparison of the BLUE combinations (red) to the single channel results. The first BLUE result corresponds to the correlation assumptions listed in Table 5.3, and for the second one, reduced correlations have been used. The single-channel values correspond to the hybrid results, which are also used for the BLUE combinations. The error bars show the total uncertainties and the gray line and area in the background represent the result of the likelihood-based combination (hybrid result).

The BLUE combination results are just provided as a sanity-check, because correlation assumptions have to be made, which is not necessary for the actual measurement using the combined likelihood presented in Section 5.2.

5.3.4 Correlation scan

Any assumptions that are made concerning the correlations for individual uncertainty sources (e.g., Table 5.3) will only alter the total correlation ρ, because the diagonal elements of the covariance matrix are fixed and given by the variances of the two measurements, σ_L^2 and σ_A^2. Thus, only the off-diagonal elements are changed. Therefore, it is possible to simply scan the only degree of freedom ρ between 0 and 100%. Negative correlations are not considered, because this case is not relevant for this example. The covariance matrix for a given value of ρ is

$$E = \begin{bmatrix} \sigma_L^2 & \rho\sigma_L\sigma_A \\ \rho\sigma_L\sigma_A & \sigma_A^2 \end{bmatrix}.$$

Figure 5.12 shows the resulting weights (red lines) as a function of ρ for both channels. The weight for the lepton+jets channel is always larger than the all-jets weight, which becomes negative at approximately 87%. The black line in Fig. 5.12 shows the resulting uncertainty of the combination result as a function of ρ. As expected, the

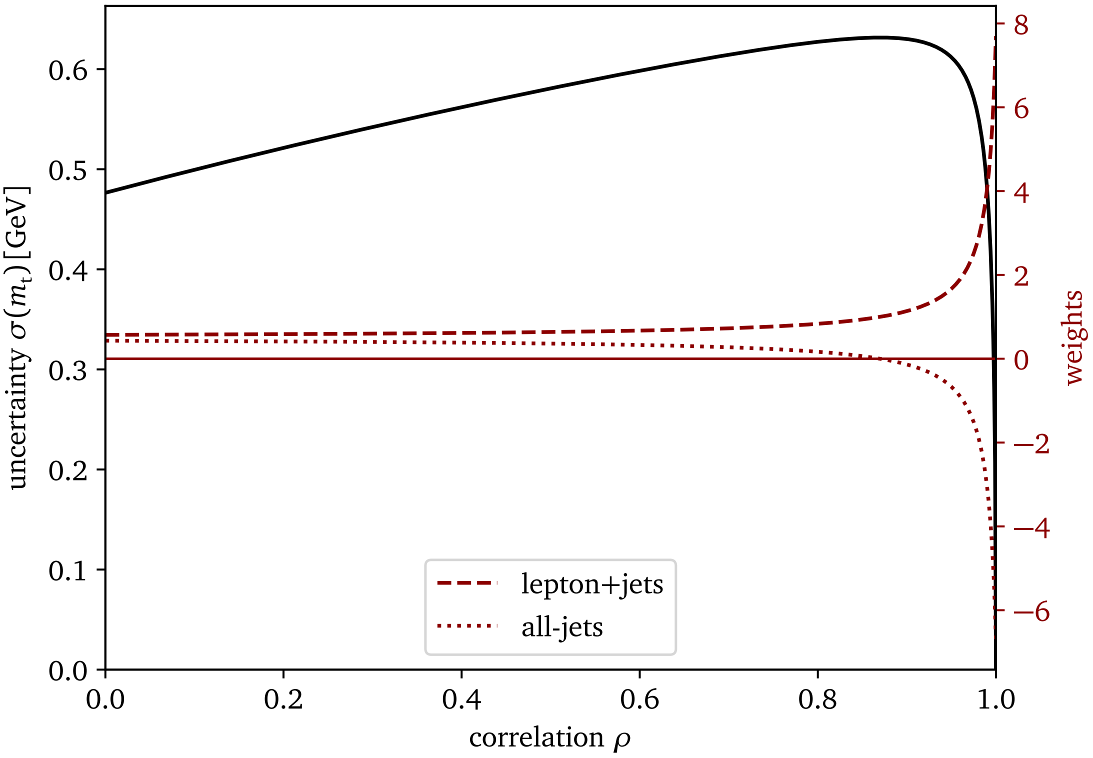

Figure 5.12: Correlation scan for the BLUE combination. The uncertainty of the combined result (left scale, black line) is shown as a function of the total correlation ρ and the weights α_i assigned to both channels (right scale, red lines).

uncertainty first rises with increasing correlation. For correlation coefficients close to 100%, the uncertainty rapidly drops to zero, as discussed and explained in Ref. [157], which indicates an overestimation of ρ.

In Fig. 5.13, the uncertainties for the BLUE combination using the correlation assumptions listed in Table 5.3 are shown, as well as for the reduced correlations, on top of the correlation scan values. Both are placed in a correlation region before the artificial uncertainty drop at high correlations. In addition, the total uncertainty of the likelihood-based combination, presented in Section 5.2, is shown. Its value lies between the two BLUE variants, indicating that both do not perfectly represent the truth, while they are not far off.

Figure 5.14 shows the actual value of the BLUE combination as a function of ρ, also including the values using the default correlation assumptions and the reduced correlations. The measurement using the combined likelihood of both channels is shown for comparison. As mentioned before, the default BLUE combination results in a value close to the likelihood-based combination, while the reduced correlations give a slightly larger result. While for small correlation coefficients the dependence of the result on ρ is moderate, it gets stronger for large values of ρ. The combination value drops to 171.65 GeV for $\rho = 100\%$, which is outside of the range of the input measurements,

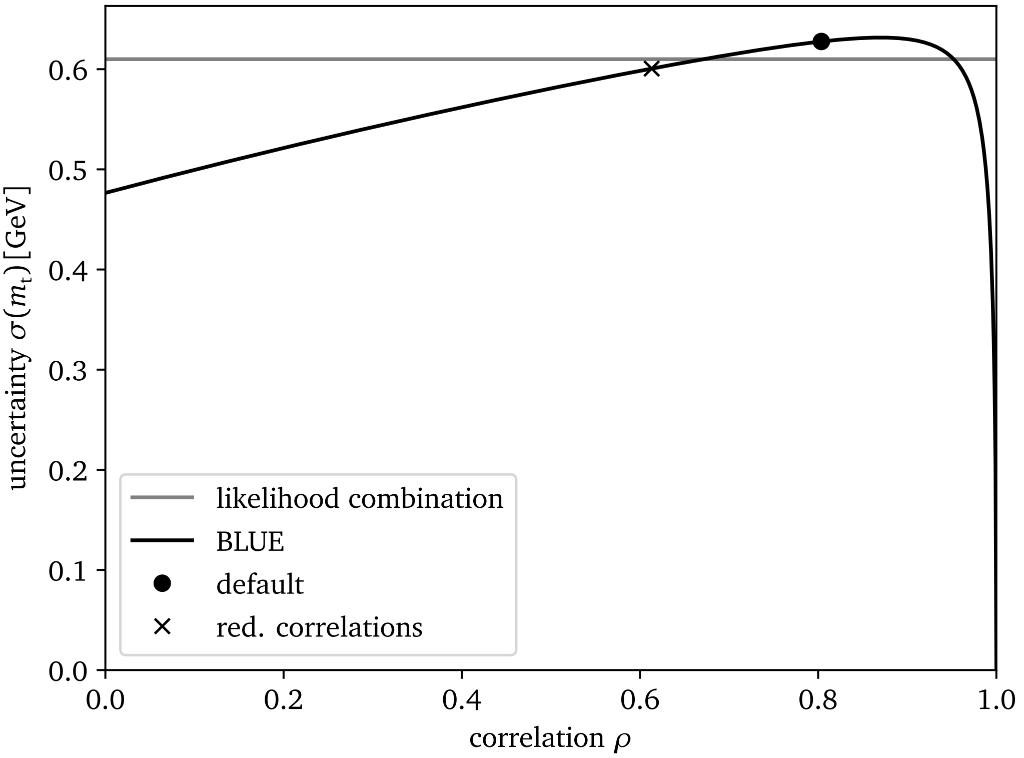

Figure 5.13: Correlation scan for the BLUE combination. The uncertainty of the combined result (black line) is shown as a function of the total correlation ρ. For comparison, the uncertainty using the default correlation assumptions listed in Table 5.3 is shown, as well as the uncertainty using reduced correlations. The total uncertainty of the likelihood-based combination (gray line), presented in Section 5.2, is shown as well.

owing to the negative weight for one measurement. This kind of extrapolation is expected for strong positive correlations [157].

It is worth noting that no correlation coefficient recovers the likelihood-based combination. While Fig. 5.13 suggests a value of $\rho \approx 67\%$ to yield approximately the right uncertainty, $\rho \approx 83\%$ would be required to recover the measured top quark mass value according to Fig. 5.14. A general problem are uncertainty components which are estimated from non-significant shifts, i.e., shifts with a statistical uncertainty larger than the shift itself. These cannot be included in a completely reliable fashion for the BLUE method, again justifying the usage of the likelihood-based combination presented in Section 5.2.

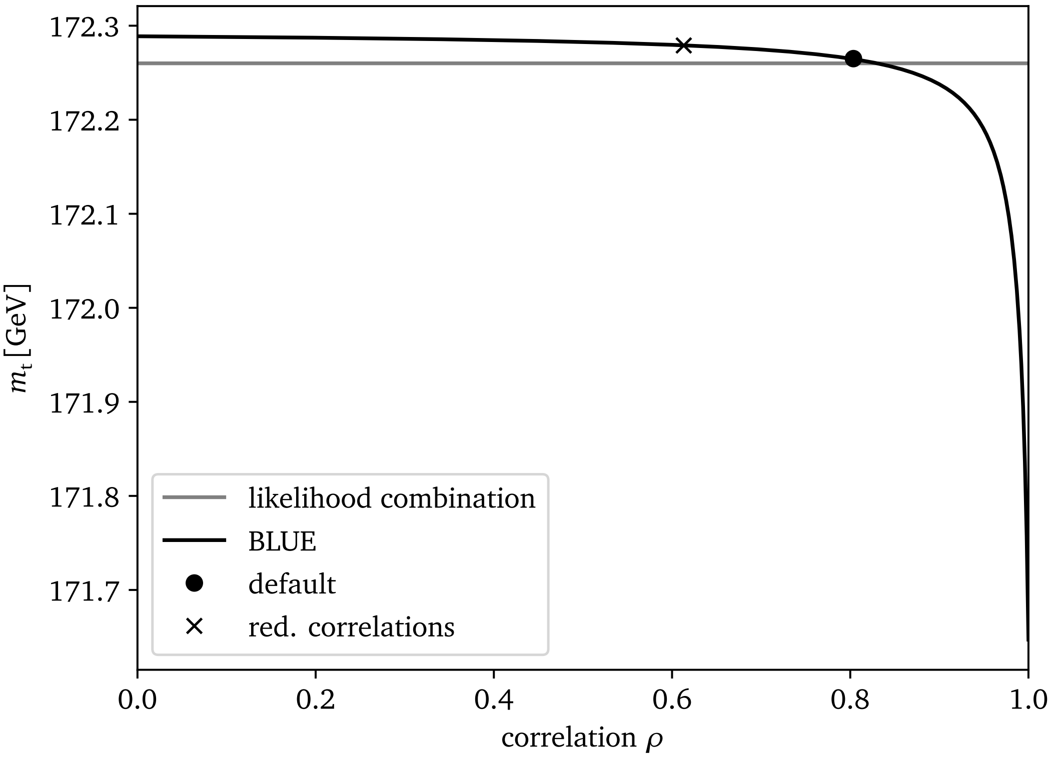

Figure 5.14: Correlation scan for the BLUE combination. The value of the BLUE combination (black line) is shown as a function of the total correlation ρ. For comparison, the result using the default correlation assumptions listed in Table 5.3 is shown, as well as the value using reduced correlations. The measurement using the combined likelihood of both channels (gray line), presented in Section 5.2, is shown as well.

6

Global electroweak fit

Chapter contents

The measurement result for the top quark mass is interpreted in the context of a fit of the standard model parameters in the electroweak sector, as described in Refs. [31–34] and already discussed in Section 1.2. The GFITTER 2.2 software is utilized with a setup[1] corresponding to the one employed for the latest update by the Gfitter Group [38]. All input values follow those in Ref. [38], also listed in Table D.1 in Appendix D, except for the top quark mass[2], for which the result of $m_{\mathrm{t}} = 172.26 \pm 0.07\,(\mathrm{stat{+}JSF}) \pm 0.61\,(\mathrm{syst})$ GeV presented in Chapter 5 is used. An additional theoretical uncertainty of 0.5 GeV is added quadratically to the uncertainty of m_{t}, as routinely done by the Gfitter group, to account for the ambiguity of the top quark mass definition and non-perturbative effects, discussed in Section 1.4.

6.1 Results

The global fit results in a χ^2 of 18.8 for 15 degrees of freedom, which translates to a p-value of 0.22 and is comparable to the result presented in Ref. [38] with $\chi^2/N_{\mathrm{df}} = 18.6/15$ and a p-value of 0.23. In Ref. [38], a value of $m_{\mathrm{t}} = 172.47 \pm 0.46\,(\mathrm{meas.}) \pm 0.5\,(\mathrm{theo.\ ambig.})\,\mathrm{GeV} = 172.47 \pm 0.68\,\mathrm{GeV}$ has been used for the top quark mass, which is a conservative combination of several LHC measurements by the Gfitter group.

By means of the fit, parameters of the SM can be determined indirectly by removing the corresponding direct measurement value from the fit and perform a χ^2 scan and find the minimum. This is illustrated in Fig. 6.1 for the top quark mass where the best fit value and the intervals of one and two standard deviations (1σ and 2σ) can be read off the $\Delta\chi^2 = \chi^2 - {\chi^2}_{\mathrm{min}}$ curve, where ${\chi^2}_{\mathrm{min}}$ is the minimal value of χ^2. The indirect determination of m_{t} yields a larger value than the direct measurement with a deviation of approximately 2σ, as already observed before [38], and the uncertainty of the indirect determination is much larger. Furthermore, $\Delta\chi^2$ curves for fits excluding

---

[1] Many thanks to Roman Kogler, who is part of the Gfitter group, for providing the necessary initial input data card, advice concerning the performed fits, and useful discussions about the results.

[2] The top quark pole mass, i.e., the mass in the on-shell renormalization scheme described in Section 1.1, is used in the parametrizations implemented in GFITTER.

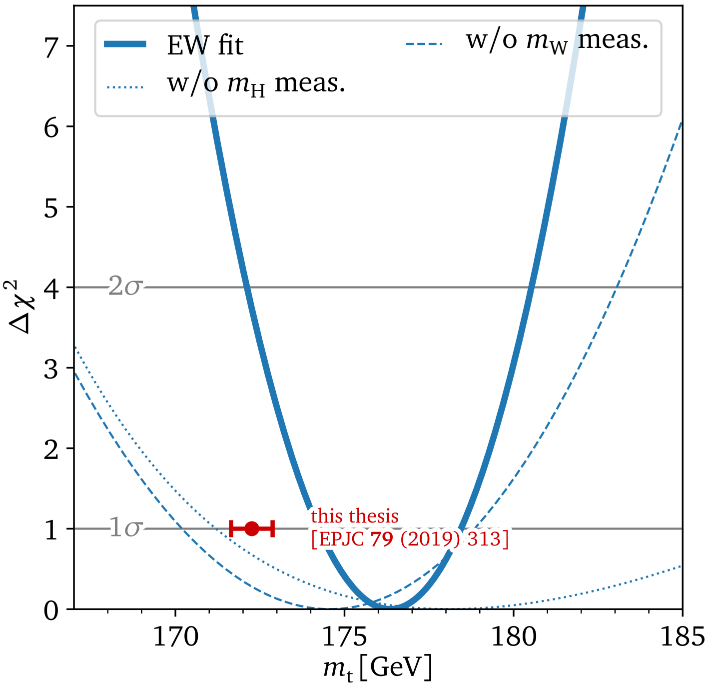

Figure 6.1: $\Delta\chi^2$ as a function of the top quark mass (m_t). The solid line represents a scan of m_t, i.e., the m_t measurement is not used as a fit input. The dashed and dotted lines represent scans in which also the Higgs boson mass and W boson mass measurements are excluded from the fit, respectively. The red dot shows the direct measurement presented in this thesis.

also the Higgs boson mass and W boson mass measurements[3] are shown, which provide a larger uncertainty, illustrating the importance of those measurements for the fit to be able to constrain the top quark mass parameter.

More interestingly, the W boson mass can be determined indirectly using the top quark mass measurement as one of the inputs to the global fit. It yields $m_W = 80.352 \pm 0.007$ GeV and the $\Delta\chi^2$ curve is shown in Fig. 6.2. The uncertainty is lower than those of available direct measurements [161–163]. In addition, fits excluding also the m_t and m_H measurements, respectively, are shown, for which the uncertainty of the indirect determination is increased. Furthermore, a version of the fit is presented for which the uncertainty of the m_t measurement is artificially set to zero, keeping the central value unchanged. Only little gain with respect to the uncertainty of the indirect m_W determination is observed, i.e., a perfect top quark mass measurement alone would not improve this SM consistency test much.

Figure 6.2 also shows the $\Delta\chi^2$ curve for the Higgs boson mass. Here, the indirect determination of m_H is far less accurate than the direct measurement [8]. However, the exclusion of the m_W and especially the m_t measurement from the fit results in much

---

[3] Technically, some parameters are allowed to vary within a finite range, which is especially important for the top quark mass, as used in other plots. This is described in more detail in Appendix D.

larger uncertainties, showing the importance of these measurements. Also for this scan, setting the m_{t} uncertainty to zero does not improve the result much, whereas setting the m_{W} uncertainty to zero[4] shows a more significant improvement.

Figure 6.3 shows two-dimensional parameter scans of the global fit. The contours for $\Delta\chi^2 = 2.3$ and 5.99, corresponding to 68% and 95% confidence level (CL), respectively, are shown. In the top plot, the scanned parameters are m_{W} and m_{H} and the red ellipse shows the fit contours. This is compared to the direct measurements, showing the same small tensions as already observed in the 1-dimensional scans. For the gray contours, the m_{t} measurement is excluded from the fit. Here, the constraining power of the fit is drastically reduced. The bottom plot of Fig. 6.3 shows the two-dimensional scan of m_{W} and m_{t}, which is typically shown to illustrate the potential of the electroweak fit as an SM consistency test. Since m_{t} is scanned, the measurement is not included in the fit and thus the contours are the same as shown in Ref. [38]. Only the direct measurement of m_{t} shown in the plot is different and corresponds to the result presented in this thesis.

All in all, the global fit shows that the current measurements indicate a consistent electroweak sector in the standard model. To be able to see more significant tensions, the precision of the top quark mass measurement and especially of the W boson mass have to be increased further.

---

[4] For technical reasons, the uncertainty of the W boson mass measurement is set to 0.001 MeV.

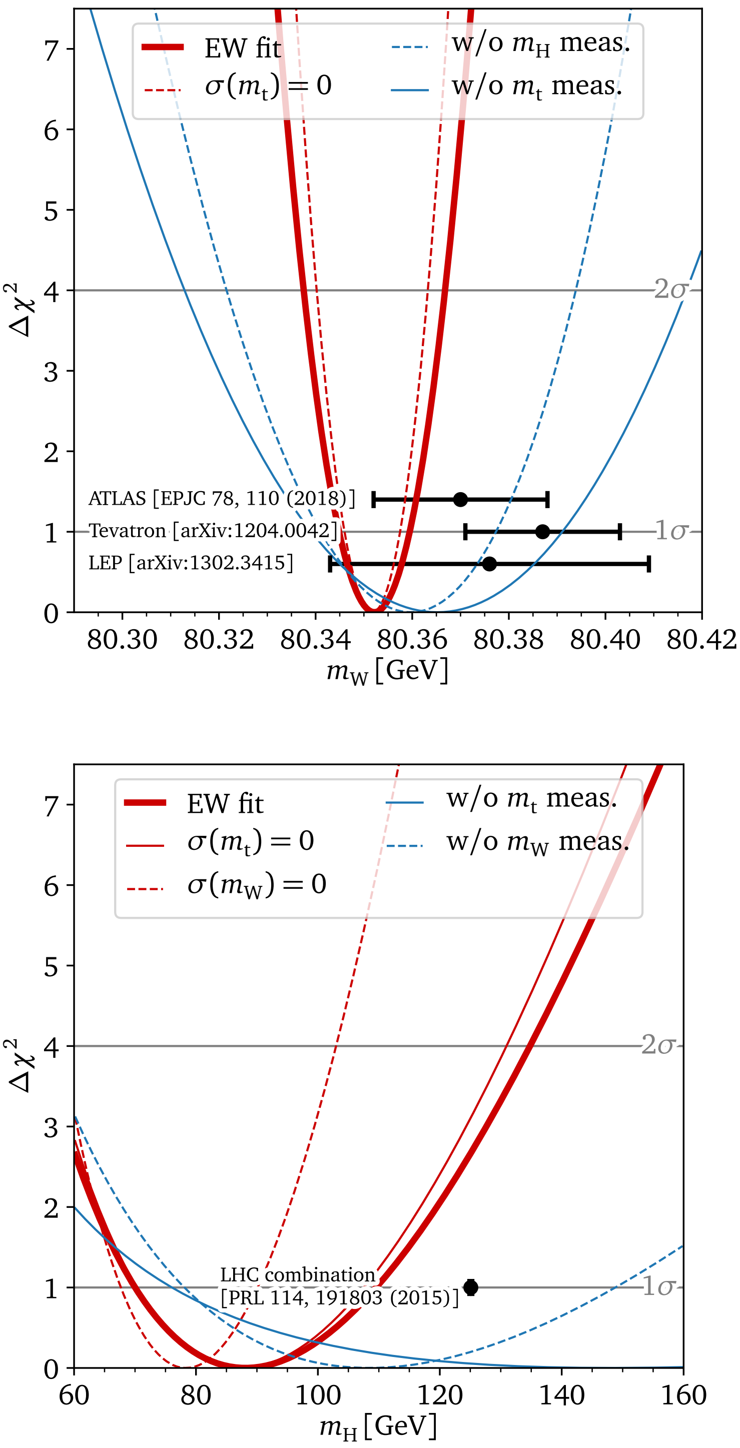

Figure 6.2: $\Delta\chi^2$ as a function of the W boson mass (m_{W}, top) and of the Higgs boson mass (m_{H}, bottom). The thick solid line represents scans of m_{W} and m_{H}, respectively, i.e., the corresponding measurement is not used as a fit input. The other red lines show scans in which the uncertainty of specific input measurements are artificially set to zero. The blue lines show scans for which individual measurements are excluded from the fit. The dots show direct measurements of m_{W} [161–163] and m_{H} [8] for comparison.

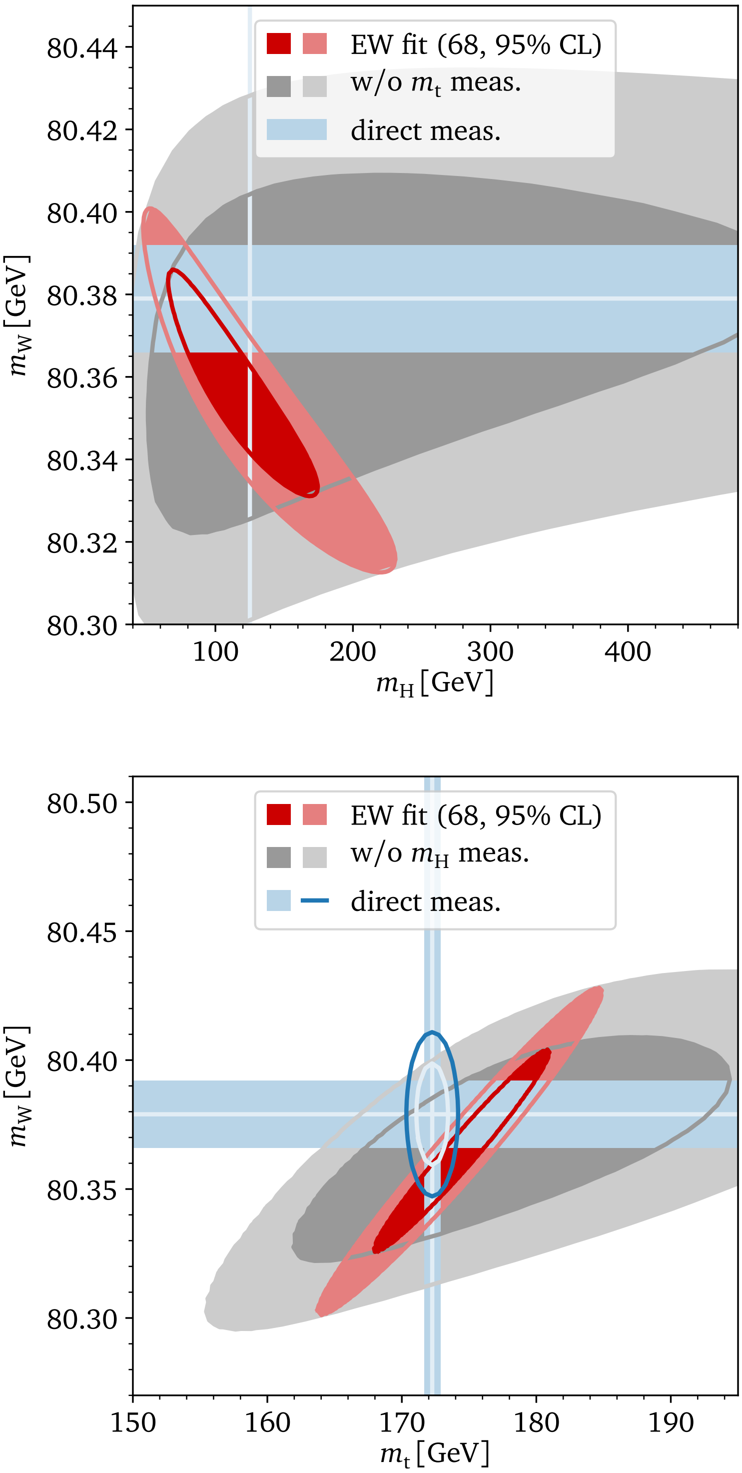

Figure 6.3: Two-dimensional parameter scans of the global fit. Top: Scan of the m_W and m_H parameters. Bottom: Scan of the m_W and m_t parameters. Two concentric contours are shown for $\Delta\chi^2 = 2.3$ and 5.99, corresponding to 68% and 95% CL, respectively. For the gray contours, the m_t (top) or m_H (bottom) measurements are excluded from the fit. The lines and error bands represent the direct measurements.

7

Summary and outlook

Chapter contents

In this chapter the results of the top quark mass measurements, described in detail in Chapters 4 and 5, are summarized and compared to other measurements performed at the LHC using different $\mathrm{t\bar{t}}$ final states. In the end, an outlook is given for possible future versions of the measurement.

7.1 Summary

As described in Chapter 4, the top quark mass is measured using $\mathrm{t\bar{t}}$ events recorded at the LHC with the CMS experiment. Proton-proton collisions at $\sqrt{s} = 13\,\mathrm{TeV}$ are analyzed, corresponding to an integrated luminosity of $35.9\,\mathrm{fb}^{-1}$ collected in 2016. The $\mathrm{t\bar{t}}$ all-jets final state is used, i.e., events with six jets reconstructed in the detector are selected. A kinematic fit is utilized to reconstruct the full $\mathrm{t\bar{t}}$ system and improve the top quark mass resolution. In addition, a goodness-of-fit criterion is applied to decrease the background stemming from QCD multijet production. The remaining background contribution is estimated from data.

By means of the ideogram method, the top quark mass (m_t) and an additional jet energy scale factor (JSF) are measured using analytic likelihood functions. The main result, exploiting prior knowledge of the JSF, is

$$m_\mathrm{t} = 172.34 \pm 0.20\,(\text{stat+JSF}) \pm 0.70\,(\text{syst})\,\mathrm{GeV}.$$

As discussed in Section 1.4, the value of m_t measured using this extraction method can be interpreted as a top quark mass close to the pole mass.

Furthermore, a combined measurement using the $\mathrm{t\bar{t}}$ all-jets and lepton+jets final states simultaneously is presented, as described in Chapter 5. The lepton+jets analysis has been presented in Refs. [57, 138, 153, 154] and is used in this combined measurement by taking the likelihood, incorporating all selected lepton+jets events. For the measurement using both final states, a combined likelihood is constructed, involving all four observables utilized in the separate analyses. A single measurement for m_t and JSF is then performed employing the same method as for the single channels, resulting in

$$m_t = 172.26 \pm 0.07\,(\text{stat+JSF}) \pm 0.61\,(\text{syst})\,\text{GeV}.$$

This is the first measurement using both final states in a single likelihood function for the mass extraction, which allows to evaluate all systematic uncertainties simultaneously. It is compared to BLUE combinations with different correlation assumptions, which provide similar results, but cannot reproduce the exact value and uncertainty.

The results are in good agreement with previous CMS and ATLAS measurements obtained at $\sqrt{s} = 7$, 8, and 13 TeV. For the measurements at lower center-of-mass energies, leading-order $t\bar{t}$ simulation has been employed for the calibration of the measurement, whereas an NLO simulation has been utilized here. The modeling uncertainties are larger than in the previous measurements at lower center-of-mass energies because of the use of new alternative color reconnection models that were not previously available. The measurements are compared to a number of LHC top quark mass measurements using $t\bar{t}$ events with different final states in Fig. 7.1. Overall, good agreement between the other LHC measurements at different center-of-mass energies and the measurements presented here is observed. No world combination is shown, because the latest one is rather outdated and does not include the most precise LHC measurements [159]. Furthermore, the result of the D0 experiment in the lepton+jets final state [164] included in the world combination is believed to be flawed by some people, being checked by an independent group [165]. A combination of the most precise CMS and ATLAS results is still in preparation in the context of the LHCtopWG.

Direct measurements aiming to reconstruct the full top quark decays still provide the most precise top quark mass determinations, while alternative methods still have larger uncertainties. Examples of these are measurements using the invariant mass of the lepton and the b jet only, or a secondary vertex, J/ψ, or muon of the b-hadron decay [166–169]. As explained in Section 1.4, mass extractions from cross section measurements in a well-defined renormalization scheme, as well as the utilization of boosted top quarks provide alternatives that might become competitive in the future.

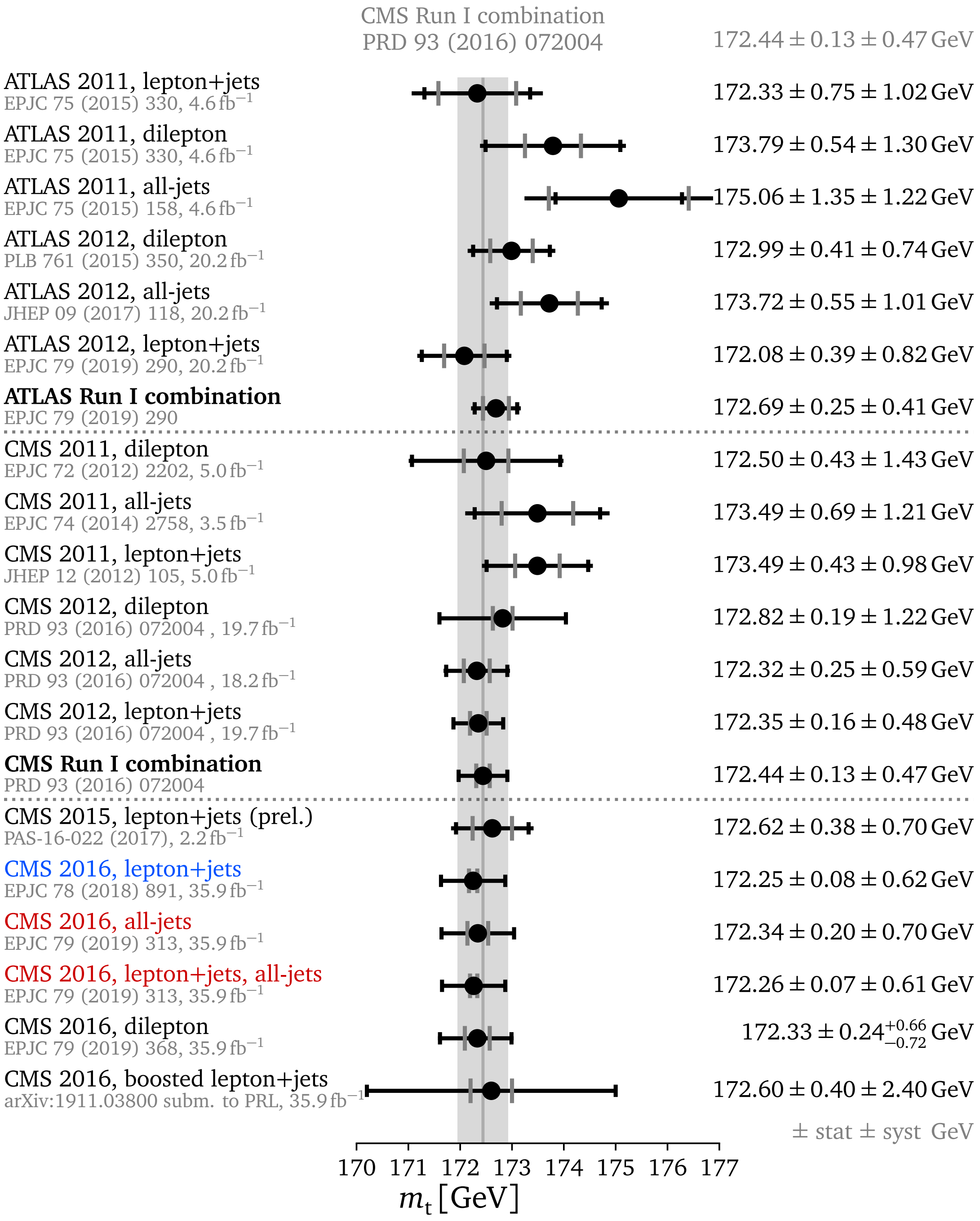

Figure 7.1: Comparison of top quark mass measurements performed at the LHC using $t\bar{t}$ events with different final states and different center-of-mass energies. The red entries correspond to the measurements presented in this thesis, the blue entry is the measurement using the lepton+jets final state only. The lines of the error bars show the total uncertainty, while the gray caps mark the statistical component and the black caps mark the systematic component. The gray line and area in the background represent the result of the combination of several CMS Run 1 results.

7.2 Outlook

Measurements of the top quark mass in the $\mathrm{t\bar{t}}$ all-jets final state are competitive with those using the lepton+jets and dilepton channel. Although the branching fraction for this final state is the largest, less events are contained in the final selection. This is due to the tight selection requirements imposed by the trigger, which is designed in a way to keep the rate moderate for the large cross section for hadronic final states at hadron colliders. This is not a problem concerning the statistical precision of the dataset, because the measurements are dominated by systematic uncertainties. The mass resolution is even better than for the lepton+jets final state, because all decay products are reconstructed. However, the tight selection also leads to a low selection efficiency for the simulated events in this very hard kinematic region. Already in this analysis, the size of the generated MC samples for systematic variations becomes a dominating effect. For future analyses, even harder selection criteria will have to be applied to cope with increasing instantaneous luminosity and pileup. It might therefore not be feasible to simply generate more MC evens, of which the largest part is rejected, but it might be worth applying generator cuts for the systematic variation samples, for example by requiring large final-state-quark momenta or generated H_T, to only simulate events in the hard kinematic region. Maybe a reconstruction of the $\mathrm{t\bar{t}}$ system at the trigger level, e.g., using a simplified version of the kinematic fit, could be used to loosen the kinematic selection criteria that need to be applied. Furthermore, variations can be implemented as event weights to the nominal sample, rather than generating statistically independent samples, like it is already done for the renormalization and factorization scale variations. This is currently being investigated for full Run 2 analyses for FSR, ISR, and ME/PS matching variations [170, 171], e.g., for the m_t measurement in the lepton+jets final state [172, 173]. Furthermore, the choice to take the maximum of the shift and its statistical uncertainty as the systematic uncertainty for a variation should be revisited, as discussed in Section 4.6.3.

With a better statistical precision of the MC samples, even harder selections could be used to further reduce the QCD multijet background and increase the fraction of correct assignments for $\mathrm{t\bar{t}}$ events. However, the uncertainty stemming from the background is not a problem in this analysis, and studies have shown that increasing the number of correct assignments does not necessarily improve the overall uncertainty of top quark mass measurements [174].

If the statistical precision of the simulated samples is sufficient, increased statistical precision of the data could be beneficial to perform differential top quark mass measurements, i.e., measurements in bins of different kinematic observables, as already shown for the lepton+jets final state in Refs. [57, 138]. This might be especially useful to constrain color reconnection strength parameters or exclude some color reconnection models. In general, more dedicated studies concerning color reconnection will be necessary, and top quark physics might be a good tool for such investigations.

Also, profile likelihood fits including all systematic uncertainties as nuisance parameters will become more important in the future. Taking into account additional fit variables, for example the b-jet energy scale could be constrained, which is a leading uncertainty for both measurements presented here. If distributions can be identified, which are sensitive to the used color reconnection model and strength, these could be included to constrain the color reconnection uncertainties or even exclude some of the models. For these nuisance parameter fits, more data will help and better handling of the statistical uncertainties for the systematic variations will be especially useful for these new approaches [58, 172, 173, 175]. The increasing instantaneous luminosities that will be provided to the LHC experiments in the future will ensure the collection of much larger datasets, such that the full power of profile likelihood fits to constrain nuisance parameters can be exploited.

With these expected improvements, the experimental uncertainty of future top quark mass measurements will probably shrink to values significantly below 0.5 GeV.

Appendix A

Database paths of data and MC samples

A.1 2016 data samples

Table A.1: DBS paths of the used primary datasets. The `JetHT` primary dataset is used, which contains the events passing the relevant triggers.

/JetHT/Run2016B-03Feb2017_ver2-v2/MINIAOD
/JetHT/Run2016C-03Feb2017-v1/MINIAOD
/JetHT/Run2016D-03Feb2017-v1/MINIAOD
/JetHT/Run2016E-03Feb2017-v1/MINIAOD
/JetHT/Run2016F-03Feb2017-v1/MINIAOD
/JetHT/Run2016G-03Feb2017-v1/MINIAOD
/JetHT/Run2016H-03Feb2017_ver2-v1/MINIAOD
/JetHT/Run2016H-03Feb2017_ver3-v1/MINIAOD

A.2 Simulated signal samples

/TT_TuneCUETP8M2T4_13TeV-powheg-pythia8/RunIISummer16MiniAODv2-PUMoriond17_80X_mcRun2_asymptotic_2016_TrancheIV_v6-v1/MINIAODSIM

A.3 Alternative masses

/TT_TuneCUETP8M2T4_mtop1665_13TeV-powheg-pythia8/RunIISummer16MiniAODv2-PUMoriond17_80X_mcRun2_asymptotic_2016_TrancheIV_v6-v1/MINIAODSIM

/TT_TuneCUETP8M2T4_mtop1695_13TeV-powheg-pythia8/RunIISummer16MiniAODv2-PUMoriond17_80X_mcRun2_asymptotic_2016_TrancheIV_v6_ext1-v1/MINIAODSIM

/TT_TuneCUETP8M2T4_mtop1695_13TeV-powheg-pythia8/RunIISummer16MiniAODv2-PUMoriond17_80X_mcRun2_asymptotic_2016_TrancheIV_v6_ext2-v1/MINIAODSIM

/TT_TuneCUETP8M2T4_mtop1715_13TeV-powheg-pythia8/RunIISummer16MiniAODv2-PUMoriond17_80X_mcRun2_asymptotic_2016_TrancheIV_v6-v1/MINIAODSIM

/TT_TuneCUETP8M2T4_mtop1735_13TeV-powheg-pythia8/RunIISummer16MiniAODv2-

PUMoriond17_80X_mcRun2_asymptotic_2016_TrancheIV_v6-v1/MINIAODSIM

/TT_TuneCUETP8M2T4_mtop1755_13TeV-powheg-pythia8/RunIISummer16MiniAODv2-PUMoriond17_80X_mcRun2_asymptotic_2016_TrancheIV_v6-v1/MINIAODSIM

/TT_TuneCUETP8M2T4_mtop1755_13TeV-powheg-pythia8/RunIISummer16MiniAODv2-PUMoriond17_80X_mcRun2_asymptotic_2016_TrancheIV_v6_ext1-v1/MINIAODSIM

/TT_TuneCUETP8M2T4_mtop1755_13TeV-powheg-pythia8/RunIISummer16MiniAODv2-PUMoriond17_80X_mcRun2_asymptotic_2016_TrancheIV_v6_ext2-v1/MINIAODSIM

/TT_TuneCUETP8M2T4_mtop1785_13TeV-powheg-pythia8/RunIISummer16MiniAODv2-PUMoriond17_80X_mcRun2_asymptotic_2016_TrancheIV_v6-v1/MINIAODSIM

A.4 Systematic variations

/TT_TuneCUETP8M2T4down_13TeV-powheg-pythia8/RunIISummer16MiniAODv2-PUMoriond17_80X_mcRun2_asymptotic_2016_TrancheIV_v6-v1/MINIAODSIM

/TT_TuneCUETP8M2T4down_13TeV-powheg-pythia8/RunIISummer16MiniAODv2-PUMoriond17_80X_mcRun2_asymptotic_2016_TrancheIV_v6_ext1-v1/MINIAODSIM

/TT_TuneCUETP8M2T4up_13TeV-powheg-pythia8/RunIISummer16MiniAODv2-PUMoriond17_80X_mcRun2_asymptotic_2016_TrancheIV_v6-v1/MINIAODSIM

/TT_TuneCUETP8M2T4up_13TeV-powheg-pythia8/RunIISummer16MiniAODv2-PUMoriond17_80X_mcRun2_asymptotic_2016_TrancheIV_v6_ext1-v1/MINIAODSIM

/TT_TuneCUETP8M2T4_13TeV-powheg-pythia8-evtgen/RunIISummer16MiniAODv2-PUMoriond17_80X_mcRun2_asymptotic_2016_TrancheIV_v6-v1/MINIAODSIM

/TT_TuneCUETP8M2T4_13TeV-powheg-fsrdown-pythia8/RunIISummer16MiniAODv2-PUMoriond17_80X_mcRun2_asymptotic_2016_TrancheIV_v6-v1/MINIAODSIM

/TT_TuneCUETP8M2T4_13TeV-powheg-fsrdown-pythia8/RunIISummer16MiniAODv2-PUMoriond17_80X_mcRun2_asymptotic_2016_TrancheIV_v6_ext1-v1/MINIAODSIM

/TT_TuneCUETP8M2T4_13TeV-powheg-fsrdown-pythia8/RunIISummer16MiniAODv2-PUMoriond17_80X_mcRun2_asymptotic_2016_TrancheIV_v6_ext2-v1/MINIAODSIM

/TT_TuneCUETP8M2T4_13TeV-powheg-fsrup-pythia8/RunIISummer16MiniAODv2-PUMoriond17_80X_mcRun2_asymptotic_2016_TrancheIV_v6-v1/MINIAODSIM

/TT_TuneCUETP8M2T4_13TeV-powheg-fsrup-pythia8/RunIISummer16MiniAODv2-PUMoriond17_80X_mcRun2_asymptotic_2016_TrancheIV_v6_ext1-v1/MINIAODSIM

/TT_TuneCUETP8M2T4_13TeV-powheg-fsrup-pythia8/RunIISummer16MiniAODv2-PUMoriond17_80X_mcRun2_asymptotic_2016_TrancheIV_v6_ext2-v1/MINIAODSIM

/TT_TuneCUETP8M2T4_13TeV-powheg-isrdown-pythia8/RunIISummer16MiniAODv2-PUMoriond17_80X_mcRun2_asymptotic_2016_TrancheIV_v6-v1/MINIAODSIM

/TT_TuneCUETP8M2T4_13TeV-powheg-isrdown-pythia8/RunIISummer16MiniAODv2-PUMoriond17_80X_mcRun2_asymptotic_2016_TrancheIV_v6_ext1-v1/MINIAODSIM

/TT_TuneCUETP8M2T4_13TeV-powheg-isrdown-pythia8/RunIISummer16MiniAODv2-PUMoriond17_80X_mcRun2_asymptotic_2016_TrancheIV_v6_ext2-v1/MINIAODSIM

/TT_TuneCUETP8M2T4_13TeV-powheg-isrup-pythia8/RunIISummer16MiniAODv2-PUMoriond17_80X_mcRun2_asymptotic_2016_TrancheIV_v6_ext1-v1/MINIAODSIM

/TT_TuneCUETP8M2T4_13TeV-powheg-isrup-pythia8/RunIISummer16MiniAODv2-PUMoriond17_80X_mcRun2_asymptotic_2016_TrancheIV_v6_ext2-v1/MINIAODSIM

/TT_hdampDOWN_TuneCUETP8M2T4_13TeV-powheg-pythia8/RunIISummer16MiniAODv2-PUMoriond17_80X_mcRun2_asymptotic_2016_TrancheIV_v6-v1/MINIAODSIM

/TT_hdampDOWN_TuneCUETP8M2T4_13TeV-powheg-pythia8/RunIISummer16MiniAODv2-PUMoriond17_80X_mcRun2_asymptotic_2016_TrancheIV_v6_ext1-v1/MINIAODSIM

/TT_hdampUP_TuneCUETP8M2T4_13TeV-powheg-pythia8/RunIISummer16MiniAODv2-PUMoriond17_80X_mcRun2_asymptotic_2016_TrancheIV_v6-v1/MINIAODSIM

/TT_hdampUP_TuneCUETP8M2T4_13TeV-powheg-pythia8/RunIISummer16MiniAODv2-PUMoriond17_80X_mcRun2_asymptotic_2016_TrancheIV_v6_ext1-v1/MINIAODSIM

/TT_TuneCUETP8M2T4_QCDbasedCRTune_erdON_13TeV-powheg-pythia8/RunIISummer16MiniAODv2-PUMoriond17_80X_mcRun2_asymptotic_2016_TrancheIV_v6-v1/MINIAODSIM

/TT_TuneCUETP8M2T4_QCDbasedCRTune_erdON_13TeV-powheg-pythia8/RunIISummer16MiniAODv2-PUMoriond17_80X_mcRun2_asymptotic_2016_TrancheIV_v6_ext1-v1/MINIAODSIM

/TT_TuneCUETP8M2T4_GluonMoveCRTune_13TeV-powheg-pythia8/RunIISummer16MiniAODv2-PUMoriond17_80X_mcRun2_asymptotic_2016_TrancheIV_v6-v1/MINIAODSIM

/TT_TuneCUETP8M2T4_GluonMoveCRTune_erdON_13TeV-powheg-pythia8/RunIISummer16MiniAODv2-PUMoriond17_80X_mcRun2_asymptotic_2016_TrancheIV_v6-v1/MINIAODSIM

/TT_TuneCUETP8M2T4_erdON_13TeV-powheg-pythia8/RunIISummer16MiniAODv2-PUMoriond17_80X_mcRun2_asymptotic_2016_TrancheIV_v6-v1/MINIAODSIM

/TT_TuneCUETP8M2T4_erdON_13TeV-powheg-pythia8/RunIISummer16MiniAODv2-PUMoriond17_80X_mcRun2_asymptotic_2016_TrancheIV_v6_ext1-v1/MINIAODSIM

/TTJets_TuneCUETP8M2T4_13TeV-amcatnloFXFX-pythia8/RunIISummer16MiniAODv2

-PUMoriond17_backup_80X_mcRun2_asymptotic_2016_TrancheIV_v6-v1/MINIAODSIM

/TT_TuneEE5C_13TeV-powheg-herwigpp/RunIISummer16MiniAODv2-PUMoriond17_80X_mcRun2_asymptotic_2016_TrancheIV_v6-v1/MINIAODSIM

/TT_TuneEE5C_13TeV-powheg-herwigpp/RunIISummer16MiniAODv2-PUMoriond17_80X_mcRun2_asymptotic_2016_TrancheIV_v6_ext2-v1/MINIAODSIM

/TT_TuneEE5C_13TeV-powheg-herwigpp/RunIISummer16MiniAODv2-PUMoriond17_80X_mcRun2_asymptotic_2016_TrancheIV_v6_ext3-v1/MINIAODSIM

/TTJets_TuneCUETP8M1_13TeV-madgraphMLM-pythia8/RunIISummer16MiniAODv2-PUMoriond17_80X_mcRun2_asymptotic_2016_TrancheIV_v6-v1/MINIAODSIM

A.5 Simulated QCD background samples

/QCD_HT100to200_TuneCUETP8M1_13TeV-madgraphMLM-pythia8/RunIISummer16MiniAODv2-PUMoriond17_80X_mcRun2_asymptotic_2016_TrancheIV_v6-v1/MINIAODSIM

/QCD_HT200to300_TuneCUETP8M1_13TeV-madgraphMLM-pythia8/RunIISummer16MiniAODv2-PUMoriond17_80X_mcRun2_asymptotic_2016_TrancheIV_v6-v1/MINIAODSIM

/QCD_HT300to500_TuneCUETP8M1_13TeV-madgraphMLM-pythia8/RunIISummer16MiniAODv2-PUMoriond17_80X_mcRun2_asymptotic_2016_TrancheIV_v6-v1/MINIAODSIM

/QCD_HT500to700_TuneCUETP8M1_13TeV-madgraphMLM-pythia8/RunIISummer16MiniAODv2-PUMoriond17_80X_mcRun2_asymptotic_2016_TrancheIV_v6-v1/MINIAODSIM

/QCD_HT700to1000_TuneCUETP8M1_13TeV-madgraphMLM-pythia8/RunIISummer16MiniAODv2-PUMoriond17_80X_mcRun2_asymptotic_2016_TrancheIV_v6-v1/MINIAODSIM

/QCD_HT1000to1500_TuneCUETP8M1_13TeV-madgraphMLM-pythia8/RunIISummer16MiniAODv2-PUMoriond17_80X_mcRun2_asymptotic_2016_TrancheIV_v6-v1/MINIAODSIM

/QCD_HT1500to2000_TuneCUETP8M1_13TeV-madgraphMLM-pythia8/RunIISummer16MiniAODv2-PUMoriond17_80X_mcRun2_asymptotic_2016_TrancheIV_v6-v1/MINIAODSIM

/QCD_HT2000toInf_TuneCUETP8M1_13TeV-madgraphMLM-pythia8/RunIISummer16MiniAODv2-PUMoriond17_80X_mcRun2_asymptotic_2016_TrancheIV_v6-v1/MINIAODSIM

/QCD_HT200to300_TuneCUETP8M1_13TeV-madgraphMLM-pythia8/RunIISummer16MiniAODv2-PUMoriond17_80X_mcRun2_asymptotic_2016_TrancheIV_v6_ext1-v1/MINIAODSIM

/QCD_HT300to500_TuneCUETP8M1_13TeV-madgraphMLM-pythia8/RunIISummer16MiniAODv2-PUMoriond17_80X_mcRun2_asymptotic_2016_TrancheIV_v6_ext1-v1/MINIAODSIM

`/QCD_HT500to700_TuneCUETP8M1_13TeV-madgraphMLM-pythia8/RunIISummer16MiniAODv2-PUMoriond17_80X_mcRun2_asymptotic_2016_TrancheIV_v6_ext1-v2/MINIAODSIM`

`/QCD_HT700to1000_TuneCUETP8M1_13TeV-madgraphMLM-pythia8/RunIISummer16MiniAODv2-PUMoriond17_80X_mcRun2_asymptotic_2016_TrancheIV_v6_ext1-v1/MINIAODSIM`

`/QCD_HT1000to1500_TuneCUETP8M1_13TeV-madgraphMLM-pythia8/RunIISummer16MiniAODv2-PUMoriond17_80X_mcRun2_asymptotic_2016_TrancheIV_v6_ext1-v1/MINIAODSIM`

`/QCD_HT1500to2000_TuneCUETP8M1_13TeV-madgraphMLM-pythia8/RunIISummer16MiniAODv2-PUMoriond17_80X_mcRun2_asymptotic_2016_TrancheIV_v6_ext1-v1/MINIAODSIM`

`/QCD_HT2000toInf_TuneCUETP8M1_13TeV-madgraphMLM-pythia8/RunIISummer16MiniAODv2-PUMoriond17_80X_mcRun2_asymptotic_2016_TrancheIV_v6_ext1-v1/MINIAODSIM`

Table A.2: Cross sections (σ) and numbers of generated events (N_gen) for the QCD samples, divided into different generator-level H_T bins. The numbers of generated events are separated for the basic samples and the extensions (ext).

H_T [GeV]	σ [pb]	N_gen+	ext
100— 200	27990000	80684349+	0
200— 300	1712000	18722416+	38857977
300— 500	347700	17035891+	37502012
500— 700	32100	18929951+	43341392
700—1000	6831	15629253+	29783527
1000—1500	1207	4767100+	10360193
1500—2000	119.9	3970819+	7855883
2000— ∞	25.24	1991645+	4047360

Appendix B

Systematic uncertainty shifts

B.1 All-jets channel

```
== Defined ensembles:
  CR_QCDbasedCRTune_erdON: m2D=172.16±0.16 jsf2D=1.005±0.001 m1D=172.56±0.11 mHyb=172.28±0.14 jsfHyb=1.004±0.001
                 CR_erdON: m2D=172.48±0.25 jsf2D=1.006±0.002 m1D=172.98±0.17 mHyb=172.63±0.21 jsfHyb=1.004±0.001
                GluonMove: m2D=172.60±0.15 jsf2D=1.000±0.001 m1D=172.61±0.11 mHyb=172.60±0.14 jsfHyb=1.000±0.001
          GluonMove erdON: m2D=172.89±0.15 jsf2D=1.003±0.001 m1D=173.09±0.11 mHyb=172.95±0.13 jsfHyb=1.002±0.001
                 JER down: m2D=172.48±0.13 jsf2D=1.001±0.001 m1D=172.56±0.09 mHyb=172.50±0.12 jsfHyb=1.001±0.001
JER re +sys expV2 HS comb down: m2D=172.50±0.13 jsf2D=1.000±0.001 m1D=172.51±0.09 mHyb=172.50±0.12 jsfHyb=1.000±0.001
JER re +sys expV2 HS comb up: m2D=172.37±0.14 jsf2D=1.004±0.001 m1D=172.66±0.10 mHyb=172.46±0.12 jsfHyb=1.003±0.001
JER re +sys expV2 newCentrVal central: m2D=172.37±0.14 jsf2D=1.004±0.001 m1D=172.69±0.10 mHyb=172.46±0.12 jsfHyb=1.003±0.001
JER re +sys expV2 newCentrVal down: m2D=172.44±0.13 jsf2D=1.002±0.001 m1D=172.59±0.10 mHyb=172.48±0.12 jsfHyb=1.001±0.001
JER re +sys expV2 newCentrVal up: m2D=172.31±0.14 jsf2D=1.006±0.001 m1D=172.78±0.10 mHyb=172.45±0.13 jsfHyb=1.004±0.001
            JER syst down: m2D=172.55±0.13 jsf2D=0.998±0.001 m1D=172.42±0.09 mHyb=172.51±0.11 jsfHyb=0.999±0.001
              JER syst up: m2D=172.33±0.14 jsf2D=1.006±0.001 m1D=172.77±0.10 mHyb=172.47±0.12 jsfHyb=1.004±0.001
                   JER up: m2D=172.41±0.13 jsf2D=1.003±0.001 m1D=172.63±0.10 mHyb=172.47±0.12 jsfHyb=1.002±0.001
    LHEscaleWeightID_1001: m2D=172.45±0.14 jsf2D=1.002±0.001 m1D=172.60±0.10 mHyb=172.50±0.12 jsfHyb=1.001±0.001
    LHEscaleWeightID_1002: m2D=172.46±0.14 jsf2D=1.002±0.001 m1D=172.59±0.10 mHyb=172.50±0.12 jsfHyb=1.001±0.001
    LHEscaleWeightID_1003: m2D=172.45±0.13 jsf2D=1.002±0.001 m1D=172.62±0.09 mHyb=172.50±0.12 jsfHyb=1.001±0.001
    LHEscaleWeightID_1004: m2D=172.41±0.14 jsf2D=1.002±0.001 m1D=172.58±0.10 mHyb=172.46±0.12 jsfHyb=1.002±0.001
    LHEscaleWeightID_1005: m2D=172.41±0.15 jsf2D=1.002±0.001 m1D=172.56±0.10 mHyb=172.46±0.13 jsfHyb=1.001±0.001
```

```
    LHEscaleWeightID_1006: m2D=172.41±0.14 jsf2D=1.002±0.001 m1D=172.59±0.10 mHyb=172.47±0.12 jsfHyb=1.002±0.001
    LHEscaleWeightID_1007: m2D=172.49±0.13 jsf2D=1.002±0.001 m1D=172.63±0.09 mHyb=172.53±0.11 jsfHyb=1.001±0.001
    LHEscaleWeightID_1008: m2D=172.50±0.13 jsf2D=1.001±0.001 m1D=172.61±0.09 mHyb=172.53±0.11 jsfHyb=1.001±0.001
    LHEscaleWeightID_1009: m2D=172.48±0.13 jsf2D=1.002±0.001 m1D=172.64±0.09 mHyb=172.53±0.11 jsfHyb=1.001±0.001
             amcatnloFXFX: m2D=172.75±0.59 jsf2D=1.003±0.005 m1D=172.96±0.41 mHyb=172.81±0.51 jsfHyb=1.002±0.004
     amcatnloFXFX no fneg: m2D=171.71±0.73 jsf2D=1.014±0.006 m1D=172.87±0.49 mHyb=172.06±0.63 jsfHyb=1.010±0.004
   bJESWeight_centralFrag: m2D=172.44±0.14 jsf2D=1.002±0.001 m1D=172.59±0.10 mHyb=172.48±0.12 jsfHyb=1.001±0.001
      bJESWeight_downFrag: m2D=172.50±0.14 jsf2D=1.002±0.001 m1D=172.64±0.10 mHyb=172.54±0.12 jsfHyb=1.001±0.001
  bJESWeight_petersonFrag: m2D=172.40±0.14 jsf2D=1.002±0.001 m1D=172.56±0.10 mHyb=172.45±0.12 jsfHyb=1.001±0.001
 bJESWeight_semilepbrDown: m2D=172.48±0.13 jsf2D=1.002±0.001 m1D=172.63±0.10 mHyb=172.53±0.12 jsfHyb=1.001±0.001
   bJESWeight_semilepbrUp: m2D=172.45±0.14 jsf2D=1.002±0.001 m1D=172.59±0.10 mHyb=172.49±0.12 jsfHyb=1.001±0.001
        bJESWeight_upFrag: m2D=172.37±0.14 jsf2D=1.002±0.001 m1D=172.52±0.10 mHyb=172.41±0.12 jsfHyb=1.001±0.001
bTagWeight_bTagCjetSFDown: m2D=172.46±0.14 jsf2D=1.002±0.001 m1D=172.61±0.10 mHyb=172.50±0.12 jsfHyb=1.001±0.001
  bTagWeight_bTagCjetSFUp: m2D=172.45±0.14 jsf2D=1.002±0.001 m1D=172.60±0.10 mHyb=172.50±0.12 jsfHyb=1.001±0.001
    bTagWeight_bTagSFDown: m2D=172.45±0.14 jsf2D=1.002±0.001 m1D=172.60±0.10 mHyb=172.49±0.12 jsfHyb=1.001±0.001
      bTagWeight_bTagSFUp: m2D=172.47±0.13 jsf2D=1.002±0.001 m1D=172.61±0.09 mHyb=172.51±0.11 jsfHyb=1.001±0.001
  bTagWeight_misTagSFDown: m2D=172.46±0.14 jsf2D=1.002±0.001 m1D=172.61±0.10 mHyb=172.50±0.12 jsfHyb=1.001±0.001
    bTagWeight_misTagSFUp: m2D=172.45±0.13 jsf2D=1.002±0.001 m1D=172.60±0.10 mHyb=172.49±0.12 jsfHyb=1.001±0.001
              bkg mW down: m2D=172.36±0.13 jsf2D=1.003±0.001 m1D=172.61±0.10 mHyb=172.44±0.12 jsfHyb=1.002±0.001
                bkg mW up: m2D=172.55±0.14 jsf2D=1.000±0.001 m1D=172.58±0.10 mHyb=172.56±0.12 jsfHyb=1.000±0.001
              bkg mt down: m2D=172.45±0.13 jsf2D=1.002±0.001 m1D=172.60±0.10 mHyb=172.50±0.12 jsfHyb=1.001±0.001
                bkg mt up: m2D=172.43±0.13 jsf2D=1.002±0.001 m1D=172.58±0.10 mHyb=172.48±0.12 jsfHyb=1.001±0.001
                  default: m2D=172.46±0.13 jsf2D=1.002±0.001 m1D=172.60±0.10 mHyb=172.50±0.12 jsfHyb=1.001±0.001
      flavor:down bottom: m2D=172.74±0.13 jsf2D=1.002±0.001 m1D=172.89±0.10 mHyb=172.79±0.12 jsfHyb=1.001±0.001
       flavor:down charm: m2D=172.43±0.14 jsf2D=1.002±0.001 m1D=172.60±0.10 mHyb=172.48±0.12 jsfHyb=1.002±0.001
       flavor:down gluon: m2D=172.59±0.14 jsf2D=1.000±0.001 m1D=172.57±0.10 mHyb=172.58±0.12 jsfHyb=1.000±0.001
       flavor:down light: m2D=172.35±0.13 jsf2D=1.003±0.001 m1D=172.61±0.10 mHyb=172.43±0.12 jsfHyb=1.002±0.001
        flavor:up bottom: m2D=172.17±0.13 jsf2D=1.002±0.001 m1D=172.31±0.10 mHyb=172.21±0.12 jsfHyb=1.001±0.001
         flavor:up charm: m2D=172.48±0.13 jsf2D=1.001±0.001 m1D=172.59±0.10 mHyb=172.51±0.12 jsfHyb=1.001±0.001
         flavor:up gluon: m2D=172.27±0.13 jsf2D=1.004±0.001 m1D=172.60±0.10 mHyb=172.37±0.12 jsfHyb=1.003±0.001
         flavor:up light: m2D=172.55±0.13 jsf2D=1.001±0.001 m1D=172.60±0.09 mHyb=172.57±0.12 jsfHyb=1.000±0.001
```

```
       loose amcatnloFXFX: m2D=173.40±0.27 jsf2D=0.975±0.002 m1D=171.40±0.17 mHyb=172.79±0.23 jsfHyb=0.982±0.002
            loose default: m2D=172.89±0.07 jsf2D=0.975±0.001 m1D=170.94±0.05 mHyb=172.30±0.06 jsfHyb=0.983±0.000
           loose mtop1715: m2D=171.88±0.07 jsf2D=0.975±0.001 m1D=169.92±0.04 mHyb=171.28±0.06 jsfHyb=0.982±0.000
           loose mtop1735: m2D=173.58±0.07 jsf2D=0.978±0.001 m1D=171.82±0.05 mHyb=173.04±0.06 jsfHyb=0.984±0.000
loose onlyCP amcatnloFXFX: m2D=173.40±0.27 jsf2D=0.975±0.002 m1D=171.40±0.17 mHyb=172.79±0.23 jsfHyb=0.982±0.002
     loose onlyCP default: m2D=172.89±0.07 jsf2D=0.975±0.001 m1D=170.95±0.05 mHyb=172.30±0.06 jsfHyb=0.983±0.000
loose onlyCPWP amcatnloFXFX: m2D=173.34±0.44 jsf2D=0.967±0.004 m1D=170.85±0.28 mHyb=172.60±0.37 jsfHyb=0.977±0.003
   loose onlyCPWP default: m2D=172.89±0.10 jsf2D=0.968±0.001 m1D=170.47±0.07 mHyb=172.17±0.09 jsfHyb=0.978±0.001
loose onlyWP amcatnloFXFX: m2D=174.90±0.97 jsf2D=0.919±0.011 m1D=169.33±0.71 mHyb=173.32±0.87 jsfHyb=0.949±0.045
     loose onlyWP default: m2D=174.63±0.22 jsf2D=0.922±0.003 m1D=169.14±0.16 mHyb=173.05±0.19 jsfHyb=0.946±0.002
loose-calib loose-templates onlyCPWP amcatnloFXFX: m2D=173.63±0.54 jsf2D=0.998±0.005 m1D=173.47±0.35 mHyb=173.59±0.45 jsfHyb=0.999±0.004
loose-calib loose-templates onlyCPWP default: m2D=173.00±0.12 jsf2D=1.000±0.001 m1D=173.02±0.08 mHyb=173.01±0.11 jsfHyb=1.000±0.001
loose-calib onlyCPWP amcatnloFXFX: m2D=173.36±0.47 jsf2D=0.999±0.005 m1D=173.30±0.33 mHyb=173.34±0.41 jsfHyb=0.999±0.003
loose-calib onlyCPWP default: m2D=172.86±0.11 jsf2D=1.000±0.001 m1D=172.85±0.08 mHyb=172.86±0.10 jsfHyb=1.000±0.001
              madgraphMLM: m2D=173.07±0.38 jsf2D=1.003±0.003 m1D=173.34±0.26 mHyb=173.16±0.33 jsfHyb=1.002±0.002
      onlyCP amcatnloFXFX: m2D=172.72±0.54 jsf2D=1.004±0.005 m1D=173.02±0.37 mHyb=172.81±0.47 jsfHyb=1.003±0.003
           onlyCP default: m2D=172.49±0.12 jsf2D=1.000±0.001 m1D=172.47±0.09 mHyb=172.49±0.11 jsfHyb=1.000±0.001
      onlyWP amcatnloFXFX: m2D=173.84±2.31 jsf2D=0.981±0.018 m1D=172.37±1.85 mHyb=173.40±2.11 jsfHyb=0.987±0.012
           onlyWP default: m2D=172.99±0.39 jsf2D=1.002±0.003 m1D=173.14±0.32 mHyb=173.04±0.36 jsfHyb=1.001±0.002
              pdf_as_down: m2D=172.45±0.13 jsf2D=1.002±0.001 m1D=172.60±0.10 mHyb=172.50±0.12 jsfHyb=1.001±0.001
                pdf_as_up: m2D=172.46±0.14 jsf2D=1.002±0.001 m1D=172.60±0.10 mHyb=172.50±0.12 jsfHyb=1.001±0.001
   powheg-fsrdown-pythia8: m2D=172.42±0.08 jsf2D=1.000±0.001 m1D=172.44±0.06 mHyb=172.43±0.07 jsfHyb=1.000±0.000
     powheg-fsrup-pythia8: m2D=172.76±0.11 jsf2D=1.000±0.001 m1D=172.73±0.08 mHyb=172.75±0.10 jsfHyb=1.000±0.001
 powheg-hdampDOWN-pythia8: m2D=172.78±0.15 jsf2D=0.998±0.001 m1D=172.66±0.11 mHyb=172.74±0.13 jsfHyb=0.999±0.001
   powheg-hdampUP-pythia8: m2D=172.61±0.16 jsf2D=1.000±0.001 m1D=172.57±0.11 mHyb=172.60±0.14 jsfHyb=1.000±0.001
   powheg-isrdown-pythia8: m2D=172.45±0.10 jsf2D=1.000±0.001 m1D=172.47±0.07 mHyb=172.46±0.08 jsfHyb=1.000±0.001
     powheg-isrup-pythia8: m2D=172.62±0.10 jsf2D=1.000±0.001 m1D=172.63±0.07 mHyb=172.62±0.08 jsfHyb=1.000±0.001
    powheg-pythia8-evtgen: m2D=173.53±0.36 jsf2D=0.994±0.003 m1D=173.06±0.25 mHyb=173.38±0.31 jsfHyb=0.996±0.002
          powheg_herwigpp: m2D=168.54±0.42 jsf2D=1.012±0.004 m1D=169.47±0.30 mHyb=168.82±0.36 jsfHyb=1.008±0.002
                   puDown: m2D=172.52±0.13 jsf2D=1.001±0.001 m1D=172.61±0.10 mHyb=172.54±0.12 jsfHyb=1.001±0.001
                     puUp: m2D=172.40±0.14 jsf2D=1.003±0.001 m1D=172.60±0.10 mHyb=172.46±0.12 jsfHyb=1.002±0.001
```

```
                scaleDown: m2D=172.60±0.14 jsf2D=0.999±0.001 m1D=172.53±0.10 mHyb=172.58±0.12 jsfHyb=0.999±0.001
                  scaleUp: m2D=172.62±0.13 jsf2D=0.999±0.001 m1D=172.55±0.09 mHyb=172.60±0.12 jsfHyb=0.999±0.001
source:down_CorrelationGroupIntercalibration: m2D=172.45±0.14 jsf2D=1.000±0.001 m1D=172.48±0.10 mHyb=172.46±0.12 jsfHyb=1.000±0.001
source:down_CorrelationGroupMPFInSitu: m2D=172.44±0.14 jsf2D=0.999±0.001 m1D=172.38±0.10 mHyb=172.42±0.12 jsfHyb=1.000±0.001
source:down_CorrelationGroupUncorrelated: m2D=172.58±0.14 jsf2D=0.991±0.001 m1D=171.91±0.10 mHyb=172.38±0.12 jsfHyb=0.994±0.001
source:down_SubTotalPileUp: m2D=172.55±0.14 jsf2D=0.997±0.001 m1D=172.36±0.10 mHyb=172.49±0.12 jsfHyb=0.998±0.001
source:down_TotalNoFlavorNoTime: m2D=172.56±0.14 jsf2D=0.991±0.001 m1D=171.85±0.10 mHyb=172.35±0.12 jsfHyb=0.994±0.001
source:up_CorrelationGroupIntercalibration: m2D=172.42±0.14 jsf2D=1.003±0.001 m1D=172.68±0.10 mHyb=172.50±0.12 jsfHyb=1.002±0.001
source:up_CorrelationGroupMPFInSitu: m2D=172.43±0.13 jsf2D=1.005±0.001 m1D=172.80±0.09 mHyb=172.54±0.12 jsfHyb=1.003±0.001
source:up_CorrelationGroupUncorrelated: m2D=172.28±0.13 jsf2D=1.013±0.001 m1D=173.27±0.09 mHyb=172.58±0.11 jsfHyb=1.009±0.001
 source:up_SubTotalPileUp: m2D=172.34±0.13 jsf2D=1.006±0.001 m1D=172.84±0.09 mHyb=172.49±0.12 jsfHyb=1.004±0.001
source:up_TotalNoFlavorNoTime: m2D=172.30±0.13 jsf2D=1.013±0.001 m1D=173.32±0.09 mHyb=172.60±0.12 jsfHyb=1.009±0.001
                    topPt: m2D=172.49±0.14 jsf2D=1.002±0.001 m1D=172.62±0.10 mHyb=172.53±0.12 jsfHyb=1.001±0.001
          trigger mu base: m2D=172.49±0.14 jsf2D=1.001±0.001 m1D=172.56±0.10 mHyb=172.51±0.12 jsfHyb=1.001±0.001
              trigger off: m2D=172.50±0.13 jsf2D=1.001±0.001 m1D=172.58±0.09 mHyb=172.52±0.12 jsfHyb=1.001±0.001

== Defined comparisons:
                       CR: m2D= 0.41      jsf2D=-0.004       m1D=-0.43      mHyb=-0.36      jsfHyb=-0.003
       CR def to CR erdON: m2D=+0.02±0.28 jsf2D=+0.004±0.002 m1D=+0.38±0.19 mHyb=+0.13±0.24 jsfHyb=+0.003±0.002
      CR def to GM erdOFF: m2D=+0.14±0.20 jsf2D=-0.002±0.002 m1D=+0.01±0.15 mHyb=+0.10±0.18 jsfHyb=-0.001±0.001
       CR def to GM erdON: m2D=+0.43±0.20 jsf2D=+0.001±0.002 m1D=+0.48±0.14 mHyb=+0.45±0.18 jsfHyb=+0.000±0.001
     CR erdON to GM erdON: m2D=+0.41±0.29 jsf2D=-0.004±0.002 m1D=+0.10±0.20 mHyb=+0.32±0.25 jsfHyb=-0.003±0.002
CR erdON to QCDinsp erdON: m2D=-0.32±0.29 jsf2D=-0.001±0.003 m1D=-0.43±0.20 mHyb=-0.36±0.25 jsfHyb=-0.001±0.002
                   CR+ERD: m2D= 0.49      jsf2D= 0.006       m1D= 0.57      mHyb= 0.43      jsfHyb= 0.004
                 FSR var.: m2D=+0.22±0.12 jsf2D=-0.002±0.001 m1D=+0.09±0.09 mHyb=+0.18±0.11 jsfHyb=-0.001±0.001
                           m2D=-0.02±0.11 jsf2D=-0.001±0.001 m1D=-0.11±0.08 mHyb=-0.05±0.10 jsfHyb=-0.001±0.001
                 ISR var.: m2D=+0.17±0.17 jsf2D=-0.002±0.001 m1D=+0.03±0.12 mHyb=+0.12±0.14 jsfHyb=-0.001±0.001
                           m2D=-0.00±0.17 jsf2D=-0.002±0.001 m1D=-0.13±0.12 mHyb=-0.04±0.14 jsfHyb=-0.001±0.001
          JEC (quad. sum): m2D= 0.18      jsf2D= 0.011       m1D= 0.73      mHyb= 0.15      jsfHyb= 0.008
 JEC: Flavor (linear sum): m2D=-0.35±0.00 jsf2D=+0.001±0.000 m1D=-0.31±0.00 mHyb=-0.34±0.00 jsfHyb=+0.000±0.000
                           m2D=+0.29±0.00 jsf2D=-0.000±0.000 m1D=+0.27±0.00 mHyb=+0.28±0.00 jsfHyb=-0.000±0.000
```

```
    JEC: Intercalibration: m2D=-0.04±0.00 jsf2D=+0.002±0.000 m1D=+0.08±0.00 mHyb=-0.00±0.00 jsfHyb=+0.001±0.000
                           m2D=-0.01±0.00 jsf2D=-0.001±0.000 m1D=-0.12±0.00 mHyb=-0.04±0.00 jsfHyb=-0.001±0.000
           JEC: MPFInSitu: m2D=-0.03±0.00 jsf2D=+0.003±0.000 m1D=+0.20±0.00 mHyb=+0.04±0.00 jsfHyb=+0.002±0.000
                           m2D=-0.02±0.00 jsf2D=-0.003±0.000 m1D=-0.22±0.00 mHyb=-0.08±0.00 jsfHyb=-0.002±0.000
              JEC: PileUp: m2D=-0.11±0.00 jsf2D=+0.005±0.000 m1D=+0.24±0.00 mHyb=-0.01±0.00 jsfHyb=+0.003±0.000
                           m2D=+0.10±0.00 jsf2D=-0.004±0.000 m1D=-0.24±0.00 mHyb=-0.01±0.00 jsfHyb=-0.003±0.000
 JEC: TotalNoFlavorNoTime: m2D=-0.16±0.00 jsf2D=+0.011±0.000 m1D=+0.72±0.00 mHyb=+0.11±0.00 jsfHyb=+0.008±0.000
                           m2D=+0.10±0.00 jsf2D=-0.011±0.000 m1D=-0.76±0.00 mHyb=-0.15±0.00 jsfHyb=-0.008±0.000
        JEC: Uncorrelated: m2D=-0.17±0.00 jsf2D=+0.011±0.000 m1D=+0.67±0.00 mHyb=+0.08±0.00 jsfHyb=+0.008±0.000
                           m2D=+0.13±0.00 jsf2D=-0.010±0.000 m1D=-0.69±0.00 mHyb=-0.12±0.00 jsfHyb=-0.007±0.000
                      JER: m2D=-0.05±0.00 jsf2D=+0.001±0.000 m1D=+0.03±0.00 mHyb=-0.03±0.00 jsfHyb=+0.001±0.000
                           m2D=+0.02±0.00 jsf2D=-0.001±0.000 m1D=-0.04±0.00 mHyb=+0.00±0.00 jsfHyb=-0.001±0.000
JER re +sys expV2 HS comb: m2D=-0.09±0.00 jsf2D=+0.002±0.000 m1D=+0.06±0.00 mHyb=-0.04±0.00 jsfHyb=+0.001±0.000
                           m2D=+0.04±0.00 jsf2D=-0.002±0.000 m1D=-0.09±0.00 mHyb=+0.00±0.00 jsfHyb=-0.001±0.000
JER re +sys expV2 newCentrVal: m2D=-0.14±0.00 jsf2D=+0.004±0.000 m1D=+0.17±0.00 mHyb=-0.05±0.00 jsfHyb=+0.003±0.000
                               m2D=-0.02±0.00 jsf2D=+0.000±0.000 m1D=-0.01±0.00 mHyb=-0.01±0.00 jsfHyb=+0.000±0.000
JER re +sys expV2 newCentrVal centr_shift: m2D=-0.09±0.00 jsf2D=+0.002±0.000 m1D=+0.08±0.00 mHyb=-0.04±0.00 jsfHyb=+0.002±0.000
JER re +sys expV2 newCentrVal wrt new centr: m2D=-0.05±0.00 jsf2D=+0.002±0.000 m1D=+0.09±0.00 mHyb=-0.01±0.00 jsfHyb=+0.001±0.000
                                             m2D=+0.07±0.00 jsf2D=-0.002±0.000 m1D=-0.09±0.00 mHyb=+0.02±0.00 jsfHyb=-0.002±0.000
                 JER syst: m2D=-0.12±0.00 jsf2D=+0.004±0.000 m1D=+0.17±0.00 mHyb=-0.03±0.00 jsfHyb=+0.003±0.000
                           m2D=+0.10±0.00 jsf2D=-0.004±0.000 m1D=-0.18±0.00 mHyb=+0.01±0.00 jsfHyb=-0.002±0.000
                  PDF RMS: m2D= 0.01      jsf2D= 0.000       m1D= 0.01      mHyb= 0.01      jsfHyb= 0.000
                   PDF as: m2D=-0.00±0.00 jsf2D=-0.000±0.000 m1D=-0.00±0.00 mHyb=-0.00±0.00 jsfHyb=-0.000±0.000
                           m2D=+0.00±0.00 jsf2D=+0.000±0.000 m1D=+0.00±0.00 mHyb=+0.00±0.00 jsfHyb=+0.000±0.000
             PDF envelope: m2D= 0.04      jsf2D= 0.000       m1D= 0.02      mHyb= 0.03      jsfHyb= 0.000
                PDF total: m2D= 0.01      jsf2D= 0.000       m1D= 0.01      mHyb= 0.01      jsfHyb= 0.000
                   Pileup: m2D=-0.05±0.00 jsf2D=+0.001±0.000 m1D=+0.00±0.00 mHyb=-0.04±0.00 jsfHyb=+0.001±0.000
                           m2D=+0.06±0.00 jsf2D=-0.001±0.000 m1D=+0.00±0.00 mHyb=+0.04±0.00 jsfHyb=-0.001±0.000
                  Trigger: m2D= 0.04      jsf2D=-0.001       m1D=-0.04      mHyb= 0.02      jsfHyb=-0.001
               Trigger mu: m2D=+0.03±0.00 jsf2D=-0.001±0.000 m1D=-0.04±0.00 mHyb=+0.01±0.00 jsfHyb=-0.001±0.000
              Trigger off: m2D=+0.04±0.00 jsf2D=-0.001±0.000 m1D=-0.02±0.00 mHyb=+0.02±0.00 jsfHyb=-0.001±0.000
```

```
          Tune var.: m2D=+0.16±0.19 jsf2D=-0.003±0.002 m1D=-0.05±0.13 mHyb=+0.10±0.17 jsfHyb=-0.002±0.001
                     m2D=+0.14±0.19 jsf2D=-0.003±0.002 m1D=-0.07±0.14 mHyb=+0.08±0.17 jsfHyb=-0.002±0.001
        aMCatNLOFXFX: m2D=+0.29±0.60 jsf2D=+0.001±0.005 m1D=+0.36±0.42 mHyb=+0.31±0.52 jsfHyb=+0.001±0.004
              b Tag: m2D=+0.01±0.00 jsf2D=-0.000±0.000 m1D=+0.01±0.00 mHyb=+0.01±0.00 jsfHyb=-0.000±0.000
                     m2D=-0.01±0.00 jsf2D=+0.000±0.000 m1D=-0.01±0.00 mHyb=-0.01±0.00 jsfHyb=+0.000±0.000
        b Tag Cjets: m2D=-0.00±0.00 jsf2D=-0.000±0.000 m1D=-0.00±0.00 mHyb=-0.00±0.00 jsfHyb=-0.000±0.000
                     m2D=+0.00±0.00 jsf2D=+0.000±0.000 m1D=+0.01±0.00 mHyb=+0.01±0.00 jsfHyb=+0.000±0.000
b frag Bowler-Lund: m2D=-0.07±0.00 jsf2D=+0.000±0.000 m1D=-0.07±0.00 mHyb=-0.07±0.00 jsfHyb=+0.000±0.000
                     m2D=+0.06±0.00 jsf2D=-0.000±0.000 m1D=+0.06±0.00 mHyb=+0.06±0.00 jsfHyb=-0.000±0.000
   b frag Peterson: m2D=-0.05±0.00 jsf2D=+0.000±0.000 m1D=-0.04±0.00 mHyb=-0.05±0.00 jsfHyb=+0.000±0.000
    b jet modeling: m2D= 0.09      jsf2D= 0.000       m1D= 0.09      mHyb= 0.09      jsfHyb= 0.000
          b misTag: m2D=-0.01±0.00 jsf2D=+0.000±0.000 m1D=-0.00±0.00 mHyb=-0.00±0.00 jsfHyb=+0.000±0.000
                     m2D=+0.00±0.00 jsf2D=-0.000±0.000 m1D=+0.00±0.00 mHyb=+0.00±0.00 jsfHyb=-0.000±0.000
      b semilep br: m2D=-0.01±0.00 jsf2D=-0.000±0.000 m1D=-0.01±0.00 mHyb=-0.01±0.00 jsfHyb=-0.000±0.000
                     m2D=+0.03±0.00 jsf2D=+0.000±0.000 m1D=+0.03±0.00 mHyb=+0.03±0.00 jsfHyb=+0.000±0.000
         b tagging: m2D= 0.02      jsf2D= 0.000       m1D= 0.01      mHyb= 0.02      jsfHyb= 0.000
        background: m2D= 0.10      jsf2D= 0.001       m1D= 0.03      mHyb= 0.07      jsfHyb= 0.001
     background mW: m2D=+0.10±0.00 jsf2D=-0.001±0.000 m1D=-0.02±0.00 mHyb=+0.06±0.00 jsfHyb=-0.001±0.000
                     m2D=-0.10±0.00 jsf2D=+0.001±0.000 m1D=+0.01±0.00 mHyb=-0.06±0.00 jsfHyb=+0.001±0.000
     background mt: m2D=-0.02±0.00 jsf2D=-0.000±0.000 m1D=-0.03±0.00 mHyb=-0.02±0.00 jsfHyb=-0.000±0.000
                     m2D=-0.00±0.00 jsf2D=-0.000±0.000 m1D=-0.00±0.00 mHyb=-0.00±0.00 jsfHyb=-0.000±0.000
       calibration: m2D=+0.06±0.00 jsf2D=+0.002±0.000 m1D=+0.06±0.00 mHyb=+0.06±0.00 jsfHyb=+0.002±0.000
            evtgen: m2D=+1.07±0.00 jsf2D=-0.008±0.000 m1D=+0.45±0.00 mHyb=+0.89±0.00 jsfHyb=-0.006±0.000
     flavor bottom: m2D=-0.29±0.00 jsf2D=-0.000±0.000 m1D=-0.29±0.00 mHyb=-0.29±0.00 jsfHyb=-0.000±0.000
                     m2D=+0.29±0.00 jsf2D=+0.000±0.000 m1D=+0.29±0.00 mHyb=+0.29±0.00 jsfHyb=+0.000±0.000
      flavor charm: m2D=+0.02±0.00 jsf2D=-0.000±0.000 m1D=-0.01±0.00 mHyb=+0.01±0.00 jsfHyb=-0.000±0.000
                     m2D=-0.03±0.00 jsf2D=+0.000±0.000 m1D=+0.00±0.00 mHyb=-0.02±0.00 jsfHyb=+0.000±0.000
      flavor gluon: m2D=-0.19±0.00 jsf2D=+0.002±0.000 m1D=+0.00±0.00 mHyb=-0.13±0.00 jsfHyb=+0.002±0.000
                     m2D=+0.13±0.00 jsf2D=-0.002±0.000 m1D=-0.03±0.00 mHyb=+0.08±0.00 jsfHyb=-0.001±0.000
      flavor light: m2D=+0.10±0.00 jsf2D=-0.001±0.000 m1D=-0.01±0.00 mHyb=+0.07±0.00 jsfHyb=-0.001±0.000
                     m2D=-0.10±0.00 jsf2D=+0.001±0.000 m1D=+0.01±0.00 mHyb=-0.07±0.00 jsfHyb=+0.001±0.000
```

```
                   h_damp: m2D=+0.16±0.21 jsf2D=-0.002±0.002 m1D=-0.03±0.15 mHyb=+0.10±0.18 jsfHyb=-0.002±0.001
                           m2D=+0.32±0.20 jsf2D=-0.003±0.002 m1D=+0.05±0.14 mHyb=+0.24±0.18 jsfHyb=-0.002±0.001
       loose aMCatNLOFXFX: m2D=+0.51±0.28 jsf2D=-0.001±0.003 m1D=+0.46±0.18 mHyb=+0.49±0.23 jsfHyb=-0.000±0.002
loose onlyCP amcatnloFXFX: m2D=+0.51±0.28 jsf2D=-0.001±0.003 m1D=+0.46±0.18 mHyb=+0.49±0.23 jsfHyb=-0.000±0.002
loose onlyCPWP amcatnloFXFX: m2D=+0.45±0.46 jsf2D=-0.001±0.005 m1D=+0.38±0.29 mHyb=+0.43±0.38 jsfHyb=-0.001±0.003
loose onlyWP amcatnloFXFX: m2D=+0.27±1.00 jsf2D=-0.003±0.011 m1D=+0.18±0.73 mHyb=+0.27±0.89 jsfHyb=+0.003±0.045
              loose shift: m2D=+0.43±0.15 jsf2D=-0.027±0.001 m1D=-1.66±0.11 mHyb=-0.20±0.13 jsfHyb=-0.019±0.001
       loose shift onlyCP: m2D=+0.40±0.14 jsf2D=-0.025±0.001 m1D=-1.52±0.10 mHyb=-0.19±0.12 jsfHyb=-0.017±0.001
       loose shift onlyWP: m2D=+1.64±0.45 jsf2D=-0.080±0.004 m1D=-4.00±0.36 mHyb=+0.01±0.40 jsfHyb=-0.055±0.003
loose-calib loose-templates onlyCPWP aMCatNLOFXFX: m2D=+0.63±0.55 jsf2D=-0.002±0.006 m1D=+0.45±0.35 mHyb=+0.58±0.46 jsfHyb=-0.002±0.004
loose-calib onlyCPWP aMCatNLOFXFX: m2D=+0.51±0.49 jsf2D=-0.001±0.005 m1D=+0.45±0.34 mHyb=+0.49±0.42 jsfHyb=-0.001±0.003
      madgraphMLM pythia8: m2D=+0.62±0.41 jsf2D=+0.002±0.003 m1D=+0.74±0.28 mHyb=+0.66±0.35 jsfHyb=+0.001±0.002
                      muF: m2D=+0.00±0.00 jsf2D=-0.000±0.000 m1D=-0.01±0.00 mHyb=-0.00±0.00 jsfHyb=-0.000±0.000
                           m2D=-0.00±0.00 jsf2D=+0.000±0.000 m1D=+0.02±0.00 mHyb=+0.01±0.00 jsfHyb=+0.000±0.000
                      muR: m2D=-0.05±0.00 jsf2D=+0.000±0.000 m1D=-0.03±0.00 mHyb=-0.04±0.00 jsfHyb=+0.000±0.000
                           m2D=+0.04±0.00 jsf2D=-0.000±0.000 m1D=+0.03±0.00 mHyb=+0.03±0.00 jsfHyb=-0.000±0.000
                  muR muF: m2D=-0.05±0.00 jsf2D=+0.000±0.000 m1D=-0.04±0.00 mHyb=-0.04±0.00 jsfHyb=+0.000±0.000
                           m2D=+0.03±0.00 jsf2D=+0.000±0.000 m1D=+0.04±0.00 mHyb=+0.03±0.00 jsfHyb=+0.000±0.000
muR muF anti (not recomm): m2D=-0.04±0.00 jsf2D=+0.000±0.000 m1D=-0.01±0.00 mHyb=-0.03±0.00 jsfHyb=+0.000±0.000
                           m2D=+0.04±0.00 jsf2D=-0.000±0.000 m1D=+0.01±0.00 mHyb=+0.03±0.00 jsfHyb=-0.000±0.000
                    muR/F: m2D= 0.05      jsf2D= 0.000       m1D= 0.04      mHyb= 0.04      jsfHyb= 0.000
      onlyCP amcatnloFXFX: m2D=+0.23±0.55 jsf2D=+0.004±0.005 m1D=+0.55±0.38 mHyb=+0.32±0.48 jsfHyb=+0.003±0.003
      onlyWP amcatnloFXFX: m2D=+0.84±2.35 jsf2D=-0.021±0.018 m1D=-0.77±1.88 mHyb=+0.36±2.14 jsfHyb=-0.014±0.012
          powheg herwigpp: m2D=-3.92±0.44 jsf2D=+0.010±0.004 m1D=-3.13±0.31 mHyb=-3.68±0.38 jsfHyb=+0.007±0.003
                     stat: m2D=+0.21±0.00 jsf2D=+0.002±0.000 m1D=+0.16±0.00 mHyb=+0.20±0.00 jsfHyb=+0.001±0.000
                   top pt: m2D=+0.03±0.00 jsf2D=-0.000±0.000 m1D=+0.02±0.00 mHyb=+0.03±0.00 jsfHyb=-0.000±0.000
```

B.2 Combined all-jets and lepton+jets channels

```
== Defined ensembles:
  CR_QCDbasedCRTune_erdON: m2D=172.15±0.06 jsf2D=1.007±0.001 m1D=172.71±0.04 mHyb=172.32±0.05 jsfHyb=1.005±0.000
                 CR_erdON: m2D=172.26±0.06 jsf2D=1.008±0.001 m1D=172.92±0.04 mHyb=172.46±0.05 jsfHyb=1.006±0.000
                GluonMove: m2D=172.37±0.06 jsf2D=1.001±0.001 m1D=172.44±0.04 mHyb=172.39±0.05 jsfHyb=1.001±0.000
          GluonMove erdON: m2D=172.63±0.06 jsf2D=1.006±0.001 m1D=173.14±0.04 mHyb=172.78±0.05 jsfHyb=1.004±0.000
       JER both syst down: m2D=172.84±0.05 jsf2D=0.994±0.000 m1D=172.34±0.03 mHyb=172.69±0.04 jsfHyb=0.996±0.000
         JER both syst up: m2D=172.12±0.05 jsf2D=1.007±0.000 m1D=172.67±0.03 mHyb=172.28±0.04 jsfHyb=1.005±0.000
                 JER down: m2D=172.52±0.05 jsf2D=0.999±0.000 m1D=172.47±0.03 mHyb=172.51±0.04 jsfHyb=0.999±0.000
JER re +sys expV2 HS comb down: m2D=172.63±0.05 jsf2D=0.997±0.000 m1D=172.42±0.03 mHyb=172.57±0.04 jsfHyb=0.998±0.000
JER re +sys expV2 HS comb up: m2D=172.30±0.05 jsf2D=1.004±0.000 m1D=172.59±0.03 mHyb=172.38±0.04 jsfHyb=1.002±0.000
JER re +sys expV2 newCentrVal central: m2D=172.25±0.05 jsf2D=1.004±0.000 m1D=172.59±0.03 mHyb=172.35±0.04 jsfHyb=1.003±0.000
JER re +sys expV2 newCentrVal down: m2D=172.46±0.05 jsf2D=1.000±0.000 m1D=172.48±0.03 mHyb=172.47±0.04 jsfHyb=1.000±0.000
JER re +sys expV2 newCentrVal up: m2D=172.07±0.05 jsf2D=1.008±0.000 m1D=172.69±0.04 mHyb=172.26±0.05 jsfHyb=1.005±0.000
                   JER up: m2D=172.40±0.05 jsf2D=1.002±0.000 m1D=172.54±0.03 mHyb=172.44±0.04 jsfHyb=1.001±0.000
    LHEscaleWeightID_1001: m2D=172.45±0.05 jsf2D=1.001±0.000 m1D=172.50±0.03 mHyb=172.47±0.04 jsfHyb=1.000±0.000
    LHEscaleWeightID_1002: m2D=172.45±0.05 jsf2D=1.000±0.000 m1D=172.48±0.03 mHyb=172.46±0.04 jsfHyb=1.000±0.000
    LHEscaleWeightID_1003: m2D=172.46±0.05 jsf2D=1.001±0.000 m1D=172.52±0.03 mHyb=172.48±0.04 jsfHyb=1.000±0.000
    LHEscaleWeightID_1004: m2D=172.46±0.05 jsf2D=1.001±0.000 m1D=172.51±0.03 mHyb=172.48±0.04 jsfHyb=1.000±0.000
    LHEscaleWeightID_1005: m2D=172.46±0.05 jsf2D=1.000±0.000 m1D=172.49±0.03 mHyb=172.47±0.04 jsfHyb=1.000±0.000
    LHEscaleWeightID_1006: m2D=172.47±0.05 jsf2D=1.001±0.000 m1D=172.53±0.03 mHyb=172.48±0.04 jsfHyb=1.001±0.000
    LHEscaleWeightID_1007: m2D=172.44±0.05 jsf2D=1.001±0.000 m1D=172.49±0.03 mHyb=172.46±0.04 jsfHyb=1.000±0.000
    LHEscaleWeightID_1008: m2D=172.44±0.05 jsf2D=1.000±0.000 m1D=172.48±0.03 mHyb=172.45±0.04 jsfHyb=1.000±0.000
    LHEscaleWeightID_1009: m2D=172.45±0.05 jsf2D=1.001±0.000 m1D=172.51±0.03 mHyb=172.47±0.04 jsfHyb=1.000±0.000
             amcatnloFXFX: m2D=172.62±0.20 jsf2D=1.002±0.002 m1D=172.82±0.13 mHyb=172.68±0.17 jsfHyb=1.002±0.001
     amcatnloFXFX no fNeg: m2D=172.62±0.11 jsf2D=1.002±0.001 m1D=172.82±0.07 mHyb=172.68±0.09 jsfHyb=1.002±0.001
   bJESWeight_centralFrag: m2D=172.44±0.05 jsf2D=1.001±0.000 m1D=172.50±0.03 mHyb=172.46±0.04 jsfHyb=1.000±0.000
      bJESWeight_downFrag: m2D=172.49±0.05 jsf2D=1.000±0.000 m1D=172.51±0.03 mHyb=172.50±0.04 jsfHyb=1.000±0.000
  bJESWeight_petersonFrag: m2D=172.42±0.05 jsf2D=1.001±0.000 m1D=172.50±0.03 mHyb=172.45±0.04 jsfHyb=1.001±0.000
 bJESWeight_semilepbrDown: m2D=172.49±0.05 jsf2D=1.001±0.000 m1D=172.54±0.03 mHyb=172.51±0.04 jsfHyb=1.000±0.000
```

```
   bJESWeight_semilepbrUp: m2D=172.44±0.05 jsf2D=1.001±0.000 m1D=172.48±0.03 mHyb=172.45±0.04 jsfHyb=1.000±0.000
        bJESWeight_upFrag: m2D=172.38±0.05 jsf2D=1.001±0.000 m1D=172.49±0.03 mHyb=172.41±0.04 jsfHyb=1.001±0.000
bTagWeight_bTagCjetSFDown: m2D=172.47±0.05 jsf2D=1.000±0.000 m1D=172.50±0.03 mHyb=172.48±0.04 jsfHyb=1.000±0.000
  bTagWeight_bTagCjetSFUp: m2D=172.44±0.05 jsf2D=1.001±0.000 m1D=172.50±0.03 mHyb=172.46±0.04 jsfHyb=1.000±0.000
    bTagWeight_bTagSFDown: m2D=172.43±0.05 jsf2D=1.001±0.000 m1D=172.49±0.03 mHyb=172.45±0.04 jsfHyb=1.000±0.000
      bTagWeight_bTagSFUp: m2D=172.48±0.05 jsf2D=1.000±0.000 m1D=172.51±0.03 mHyb=172.49±0.04 jsfHyb=1.000±0.000
  bTagWeight_misTagSFDown: m2D=172.46±0.05 jsf2D=1.000±0.000 m1D=172.50±0.03 mHyb=172.47±0.04 jsfHyb=1.000±0.000
    bTagWeight_misTagSFUp: m2D=172.45±0.05 jsf2D=1.001±0.000 m1D=172.50±0.03 mHyb=172.47±0.04 jsfHyb=1.000±0.000
                bkg down: m2D=172.44±0.05 jsf2D=1.001±0.000 m1D=172.51±0.03 mHyb=172.46±0.04 jsfHyb=1.001±0.000
             bkg mW down: m2D=172.44±0.05 jsf2D=1.001±0.000 m1D=172.50±0.03 mHyb=172.46±0.04 jsfHyb=1.000±0.000
               bkg mW up: m2D=172.47±0.05 jsf2D=1.000±0.000 m1D=172.50±0.03 mHyb=172.48±0.04 jsfHyb=1.000±0.000
             bkg mt down: m2D=172.46±0.05 jsf2D=1.001±0.000 m1D=172.50±0.03 mHyb=172.47±0.04 jsfHyb=1.000±0.000
               bkg mt up: m2D=172.45±0.05 jsf2D=1.001±0.000 m1D=172.50±0.03 mHyb=172.47±0.04 jsfHyb=1.000±0.000
                  bkg up: m2D=172.43±0.05 jsf2D=1.001±0.000 m1D=172.51±0.03 mHyb=172.46±0.04 jsfHyb=1.001±0.000
                 default: m2D=172.45±0.05 jsf2D=1.001±0.000 m1D=172.50±0.03 mHyb=172.47±0.04 jsfHyb=1.000±0.000
      flavor:down bottom: m2D=172.77±0.05 jsf2D=1.000±0.000 m1D=172.81±0.03 mHyb=172.78±0.04 jsfHyb=1.000±0.000
       flavor:down charm: m2D=172.43±0.05 jsf2D=1.001±0.000 m1D=172.51±0.03 mHyb=172.45±0.04 jsfHyb=1.001±0.000
       flavor:down gluon: m2D=172.66±0.05 jsf2D=0.998±0.000 m1D=172.48±0.03 mHyb=172.61±0.04 jsfHyb=0.998±0.000
       flavor:down light: m2D=172.35±0.05 jsf2D=1.002±0.000 m1D=172.51±0.03 mHyb=172.40±0.04 jsfHyb=1.001±0.000
        flavor:up bottom: m2D=172.15±0.05 jsf2D=1.001±0.000 m1D=172.19±0.03 mHyb=172.16±0.04 jsfHyb=1.000±0.000
         flavor:up charm: m2D=172.48±0.05 jsf2D=1.000±0.000 m1D=172.49±0.03 mHyb=172.49±0.04 jsfHyb=1.000±0.000
         flavor:up gluon: m2D=172.23±0.05 jsf2D=1.004±0.000 m1D=172.52±0.03 mHyb=172.32±0.04 jsfHyb=1.002±0.000
         flavor:up light: m2D=172.56±0.05 jsf2D=0.999±0.000 m1D=172.49±0.03 mHyb=172.54±0.04 jsfHyb=0.999±0.000
            iso wgt down: m2D=172.46±0.05 jsf2D=1.001±0.000 m1D=172.50±0.03 mHyb=172.47±0.04 jsfHyb=1.000±0.000
              iso wgt up: m2D=172.45±0.05 jsf2D=1.001±0.000 m1D=172.50±0.03 mHyb=172.47±0.04 jsfHyb=1.000±0.000
          lepID wgt down: m2D=172.46±0.05 jsf2D=1.001±0.000 m1D=172.50±0.03 mHyb=172.47±0.04 jsfHyb=1.000±0.000
            lepID wgt up: m2D=172.46±0.05 jsf2D=1.001±0.000 m1D=172.50±0.03 mHyb=172.47±0.04 jsfHyb=1.000±0.000
             madgraphMLM: m2D=173.25±0.14 jsf2D=1.001±0.001 m1D=173.30±0.09 mHyb=173.26±0.12 jsfHyb=1.000±0.001
             pdf_as_down: m2D=172.46±0.05 jsf2D=1.001±0.000 m1D=172.50±0.03 mHyb=172.47±0.04 jsfHyb=1.000±0.000
               pdf_as_up: m2D=172.45±0.05 jsf2D=1.001±0.000 m1D=172.50±0.03 mHyb=172.47±0.04 jsfHyb=1.000±0.000
  powheg-fsrdown-pythia8: m2D=172.35±0.08 jsf2D=1.005±0.001 m1D=172.77±0.05 mHyb=172.48±0.07 jsfHyb=1.004±0.001
```

```
     powheg-fsrup-pythia8: m2D=172.78±0.09 jsf2D=0.995±0.001 m1D=172.33±0.06 mHyb=172.64±0.07 jsfHyb=0.996±0.001
 powheg-hdampDOWN-pythia8: m2D=172.56±0.06 jsf2D=0.999±0.001 m1D=172.49±0.04 mHyb=172.54±0.05 jsfHyb=0.999±0.000
   powheg-hdampUP-pythia8: m2D=172.45±0.06 jsf2D=1.001±0.001 m1D=172.52±0.04 mHyb=172.47±0.05 jsfHyb=1.001±0.000
   powheg-isrdown-pythia8: m2D=172.52±0.06 jsf2D=1.000±0.001 m1D=172.51±0.04 mHyb=172.52±0.05 jsfHyb=1.000±0.000
     powheg-isrup-pythia8: m2D=172.52±0.06 jsf2D=1.001±0.001 m1D=172.60±0.04 mHyb=172.54±0.05 jsfHyb=1.001±0.000
    powheg-pythia8-evtgen: m2D=172.67±0.14 jsf2D=1.000±0.001 m1D=172.66±0.09 mHyb=172.67±0.12 jsfHyb=1.000±0.001
          powheg_herwigpp: m2D=168.09±0.12 jsf2D=1.014±0.001 m1D=169.23±0.08 mHyb=168.43±0.10 jsfHyb=1.010±0.001
                   puDown: m2D=172.53±0.05 jsf2D=0.999±0.000 m1D=172.48±0.03 mHyb=172.51±0.04 jsfHyb=1.000±0.000
                     puUp: m2D=172.38±0.05 jsf2D=1.002±0.000 m1D=172.52±0.03 mHyb=172.43±0.04 jsfHyb=1.001±0.000
                scaleDown: m2D=172.47±0.05 jsf2D=1.000±0.000 m1D=172.50±0.03 mHyb=172.48±0.04 jsfHyb=1.000±0.000
                  scaleUp: m2D=172.39±0.05 jsf2D=1.001±0.000 m1D=172.50±0.03 mHyb=172.43±0.04 jsfHyb=1.001±0.000
source:down_CorrelationGroupIntercalibration: m2D=172.46±0.05 jsf2D=0.999±0.000 m1D=172.35±0.03 mHyb=172.43±0.04 jsfHyb=0.999±0.000
source:down_CorrelationGroupMPFInSitu: m2D=172.46±0.05 jsf2D=0.998±0.000 m1D=172.27±0.03 mHyb=172.40±0.04 jsfHyb=0.998±0.000
source:down_CorrelationGroupUncorrelated: m2D=172.58±0.05 jsf2D=0.990±0.000 m1D=171.73±0.03 mHyb=172.32±0.04 jsfHyb=0.993±0.000
source:down_SubTotalPileUp: m2D=172.56±0.05 jsf2D=0.996±0.000 m1D=172.25±0.03 mHyb=172.47±0.04 jsfHyb=0.997±0.000
source:down_TotalNoFlavorNoTime: m2D=172.58±0.05 jsf2D=0.989±0.000 m1D=171.67±0.03 mHyb=172.30±0.04 jsfHyb=0.992±0.000
source:up_CorrelationGroupIntercalibration: m2D=172.44±0.05 jsf2D=1.003±0.000 m1D=172.65±0.03 mHyb=172.50±0.04 jsfHyb=1.002±0.000
source:up_CorrelationGroupMPFInSitu: m2D=172.45±0.05 jsf2D=1.003±0.000 m1D=172.73±0.03 mHyb=172.53±0.04 jsfHyb=1.002±0.000
source:up_CorrelationGroupUncorrelated: m2D=172.35±0.05 jsf2D=1.011±0.000 m1D=173.27±0.03 mHyb=172.62±0.04 jsfHyb=1.008±0.000
 source:up_SubTotalPileUp: m2D=172.35±0.05 jsf2D=1.005±0.000 m1D=172.76±0.03 mHyb=172.47±0.04 jsfHyb=1.003±0.000
source:up_TotalNoFlavorNoTime: m2D=172.36±0.05 jsf2D=1.012±0.000 m1D=173.34±0.03 mHyb=172.65±0.04 jsfHyb=1.008±0.000
                    topPt: m2D=172.46±0.05 jsf2D=1.000±0.000 m1D=172.44±0.03 mHyb=172.46±0.04 jsfHyb=1.000±0.000
             trigger down: m2D=172.46±0.05 jsf2D=1.001±0.000 m1D=172.50±0.03 mHyb=172.47±0.04 jsfHyb=1.000±0.000
          trigger mu base: m2D=172.46±0.05 jsf2D=1.000±0.000 m1D=172.50±0.03 mHyb=172.47±0.04 jsfHyb=1.000±0.000
              trigger off: m2D=172.46±0.05 jsf2D=1.000±0.000 m1D=172.50±0.03 mHyb=172.47±0.04 jsfHyb=1.000±0.000
               trigger up: m2D=172.46±0.05 jsf2D=1.001±0.000 m1D=172.50±0.03 mHyb=172.47±0.04 jsfHyb=1.000±0.000

== Defined comparisons:
                       CR: m2D= 0.37      jsf2D=-0.002       m1D= 0.22      mHyb= 0.33      jsfHyb=-0.001
       CR def to CR erdON: m2D=-0.20±0.08 jsf2D=+0.007±0.001 m1D=+0.42±0.05 mHyb=-0.01±0.07 jsfHyb=+0.005±0.001
      CR def to GM erdOFF: m2D=-0.09±0.08 jsf2D=+0.000±0.001 m1D=-0.06±0.05 mHyb=-0.08±0.07 jsfHyb=+0.000±0.001
```

```
           CR def to GM erdON: m2D=+0.17±0.08 jsf2D=+0.006±0.001 m1D=+0.64±0.05 mHyb=+0.31±0.07 jsfHyb=+0.004±0.001
         CR erdON to GM erdON: m2D=+0.37±0.09 jsf2D=-0.002±0.001 m1D=+0.22±0.06 mHyb=+0.33±0.07 jsfHyb=-0.001±0.001
   CR erdON to QCDinsp erdON: m2D=-0.11±0.09 jsf2D=-0.001±0.001 m1D=-0.21±0.06 mHyb=-0.14±0.07 jsfHyb=-0.001±0.001
                    FSR var.: m2D=+0.23±0.07 jsf2D=-0.004±0.001 m1D=-0.12±0.05 mHyb=+0.12±0.06 jsfHyb=-0.003±0.000
                              m2D=-0.07±0.07 jsf2D=+0.003±0.001 m1D=+0.19±0.04 mHyb=+0.01±0.06 jsfHyb=+0.002±0.000
                    ISR var.: m2D=+0.06±0.08 jsf2D=+0.000±0.001 m1D=+0.10±0.05 mHyb=+0.07±0.07 jsfHyb=+0.000±0.001
                              m2D=+0.07±0.08 jsf2D=-0.001±0.001 m1D=+0.01±0.05 mHyb=+0.05±0.07 jsfHyb=-0.000±0.001
                  Isolation: m2D=+0.00±0.00 jsf2D=-0.000±0.000 m1D=+0.00±0.00 mHyb=+0.00±0.00 jsfHyb=-0.000±0.000
                              m2D=+0.00±0.00 jsf2D=-0.000±0.000 m1D=-0.00±0.00 mHyb=+0.00±0.00 jsfHyb=-0.000±0.000
           JEC (quad. sum): m2D= 0.12      jsf2D= 0.011       m1D= 0.82      mHyb= 0.17      jsfHyb= 0.008
   JEC: Flavor (linear sum): m2D=-0.39±0.00 jsf2D=+0.001±0.000 m1D=-0.31±0.00 mHyb=-0.37±0.00 jsfHyb=+0.001±0.000
                              m2D=+0.39±0.00 jsf2D=-0.001±0.000 m1D=+0.31±0.00 mHyb=+0.37±0.00 jsfHyb=-0.001±0.000
     JEC: Intercalibration: m2D=-0.01±0.00 jsf2D=+0.002±0.000 m1D=+0.15±0.00 mHyb=+0.04±0.00 jsfHyb=+0.001±0.000
                              m2D=+0.01±0.00 jsf2D=-0.002±0.000 m1D=-0.16±0.00 mHyb=-0.04±0.00 jsfHyb=-0.001±0.000
           JEC: MPFInSitu: m2D=-0.01±0.00 jsf2D=+0.003±0.000 m1D=+0.23±0.00 mHyb=+0.07±0.00 jsfHyb=+0.002±0.000
                              m2D=+0.00±0.00 jsf2D=-0.003±0.000 m1D=-0.23±0.00 mHyb=-0.07±0.00 jsfHyb=-0.002±0.000
               JEC: PileUp: m2D=-0.10±0.00 jsf2D=+0.004±0.000 m1D=+0.26±0.00 mHyb=+0.01±0.00 jsfHyb=+0.003±0.000
                              m2D=+0.11±0.00 jsf2D=-0.004±0.000 m1D=-0.25±0.00 mHyb=+0.00±0.00 jsfHyb=-0.003±0.000
   JEC: TotalNoFlavorNoTime: m2D=-0.10±0.00 jsf2D=+0.011±0.000 m1D=+0.84±0.00 mHyb=+0.18±0.00 jsfHyb=+0.008±0.000
                              m2D=+0.12±0.00 jsf2D=-0.011±0.000 m1D=-0.83±0.00 mHyb=-0.17±0.00 jsfHyb=-0.008±0.000
         JEC: Uncorrelated: m2D=-0.11±0.00 jsf2D=+0.011±0.000 m1D=+0.77±0.00 mHyb=+0.15±0.00 jsfHyb=+0.007±0.000
                              m2D=+0.12±0.00 jsf2D=-0.011±0.000 m1D=-0.77±0.00 mHyb=-0.15±0.00 jsfHyb=-0.007±0.000
                         JER: m2D=-0.06±0.00 jsf2D=+0.001±0.000 m1D=+0.04±0.00 mHyb=-0.03±0.00 jsfHyb=+0.001±0.000
                              m2D=+0.07±0.00 jsf2D=-0.001±0.000 m1D=-0.04±0.00 mHyb=+0.04±0.00 jsfHyb=-0.001±0.000
               JER both syst: m2D=-0.34±0.00 jsf2D=+0.006±0.000 m1D=+0.17±0.00 mHyb=-0.18±0.00 jsfHyb=+0.004±0.000
                              m2D=+0.38±0.00 jsf2D=-0.007±0.000 m1D=-0.16±0.00 mHyb=+0.22±0.00 jsfHyb=-0.005±0.000
   JER re +sys expV2 HS comb: m2D=-0.16±0.00 jsf2D=+0.003±0.000 m1D=+0.09±0.00 mHyb=-0.08±0.00 jsfHyb=+0.002±0.000
                              m2D=+0.18±0.00 jsf2D=-0.003±0.000 m1D=-0.08±0.00 mHyb=+0.10±0.00 jsfHyb=-0.002±0.000
JER re +sys expV2 newCentrVal: m2D=-0.38±0.00 jsf2D=+0.007±0.000 m1D=+0.19±0.00 mHyb=-0.21±0.00 jsfHyb=+0.005±0.000
                                    m2D=+0.00±0.00 jsf2D=-0.000±0.000 m1D=-0.02±0.00 mHyb=-0.00±0.00 jsfHyb=-0.000±0.000
JER re +sys expV2 newCentrVal centr_shift: m2D=-0.20±0.00 jsf2D=+0.004±0.000 m1D=+0.09±0.00 mHyb=-0.11±0.00 jsfHyb=+0.002±0.000
```

```
JER re +sys expV2 newCentrVal wrt new centr: m2D=-0.18±0.00 jsf2D=+0.003±0.000 m1D=+0.10±0.00 mHyb=-0.10±0.00 jsfHyb=+0.002±0.000
                                             m2D=+0.20±0.00 jsf2D=-0.004±0.000 m1D=-0.11±0.00 mHyb=+0.11±0.00 jsfHyb=-0.003±0.000
       Lepton Identification: m2D=+0.00±0.00 jsf2D=-0.000±0.000 m1D=+0.00±0.00 mHyb=+0.00±0.00 jsfHyb=-0.000±0.000
                              m2D=+0.00±0.00 jsf2D=-0.000±0.000 m1D=+0.00±0.00 mHyb=+0.00±0.00 jsfHyb=-0.000±0.000
                     PDF RMS: m2D= 0.01      jsf2D= 0.000       m1D= 0.01      mHyb= 0.01      jsfHyb= 0.000
                      PDF as: m2D=+0.00±0.00 jsf2D=-0.000±0.000 m1D=+0.00±0.00 mHyb=+0.00±0.00 jsfHyb=-0.000±0.000
                              m2D=-0.00±0.00 jsf2D=-0.000±0.000 m1D=-0.00±0.00 mHyb=-0.00±0.00 jsfHyb=-0.000±0.000
                PDF envelope: m2D= 0.03      jsf2D= 0.000       m1D= 0.02      mHyb= 0.03      jsfHyb= 0.000
                   PDF total: m2D= 0.01      jsf2D= 0.000       m1D= 0.01      mHyb= 0.01      jsfHyb= 0.000
                      Pileup: m2D=-0.07±0.00 jsf2D=+0.001±0.000 m1D=+0.02±0.00 mHyb=-0.04±0.00 jsfHyb=+0.001±0.000
                              m2D=+0.07±0.00 jsf2D=-0.001±0.000 m1D=-0.02±0.00 mHyb=+0.05±0.00 jsfHyb=-0.001±0.000
                  Trigger AJ: m2D= 0.01      jsf2D=-0.000       m1D=-0.00      mHyb= 0.01      jsfHyb=-0.000
               Trigger AJ mu: m2D=+0.01±0.00 jsf2D=-0.000±0.000 m1D=-0.00±0.00 mHyb=+0.01±0.00 jsfHyb=-0.000±0.000
              Trigger AJ off: m2D=+0.01±0.00 jsf2D=-0.000±0.000 m1D=-0.00±0.00 mHyb=+0.01±0.00 jsfHyb=-0.000±0.000
                  Trigger LJ: m2D=+0.00±0.00 jsf2D=-0.000±0.000 m1D=+0.00±0.00 mHyb=+0.00±0.00 jsfHyb=-0.000±0.000
                              m2D=+0.00±0.00 jsf2D=-0.000±0.000 m1D=-0.00±0.00 mHyb=+0.00±0.00 jsfHyb=-0.000±0.000
                   Tune var.: m2D=-0.06±0.07 jsf2D=+0.001±0.001 m1D=+0.00±0.05 mHyb=-0.04±0.06 jsfHyb=+0.001±0.000
                              m2D=+0.02±0.07 jsf2D=-0.000±0.001 m1D=+0.00±0.05 mHyb=+0.01±0.06 jsfHyb=-0.000±0.000
                aMCatNLOFXFX: m2D=+0.16±0.21 jsf2D=+0.002±0.002 m1D=+0.32±0.13 mHyb=+0.21±0.18 jsfHyb=+0.001±0.001
        aMCatNLOFXFX no fNeg: m2D=+0.16±0.12 jsf2D=+0.002±0.001 m1D=+0.32±0.08 mHyb=+0.21±0.10 jsfHyb=+0.001±0.001
                       b Tag: m2D=+0.03±0.00 jsf2D=-0.000±0.000 m1D=+0.01±0.00 mHyb=+0.02±0.00 jsfHyb=-0.000±0.000
                              m2D=-0.02±0.00 jsf2D=+0.000±0.000 m1D=-0.01±0.00 mHyb=-0.02±0.00 jsfHyb=+0.000±0.000
                 b Tag Cjets: m2D=-0.01±0.00 jsf2D=+0.000±0.000 m1D=-0.00±0.00 mHyb=-0.01±0.00 jsfHyb=+0.000±0.000
                              m2D=+0.01±0.00 jsf2D=-0.000±0.000 m1D=+0.00±0.00 mHyb=+0.01±0.00 jsfHyb=-0.000±0.000
        b frag Bowler-Lund: m2D=-0.06±0.00 jsf2D=+0.001±0.000 m1D=-0.01±0.00 mHyb=-0.05±0.00 jsfHyb=+0.000±0.000
                              m2D=+0.05±0.00 jsf2D=-0.000±0.000 m1D=+0.01±0.00 mHyb=+0.04±0.00 jsfHyb=-0.000±0.000
           b frag Peterson: m2D=-0.03±0.00 jsf2D=+0.000±0.000 m1D=+0.00±0.00 mHyb=-0.02±0.00 jsfHyb=+0.000±0.000
             b jet modeling: m2D= 0.08      jsf2D= 0.001       m1D= 0.04      mHyb= 0.06      jsfHyb= 0.001
                    b misTag: m2D=-0.00±0.00 jsf2D=+0.000±0.000 m1D=-0.00±0.00 mHyb=-0.00±0.00 jsfHyb=+0.000±0.000
                              m2D=+0.01±0.00 jsf2D=-0.000±0.000 m1D=+0.00±0.00 mHyb=+0.01±0.00 jsfHyb=-0.000±0.000
               b semilep br: m2D=-0.02±0.00 jsf2D=-0.000±0.000 m1D=-0.02±0.00 mHyb=-0.02±0.00 jsfHyb=-0.000±0.000
```

```
                            m2D=+0.04±0.00 jsf2D=-0.000±0.000 m1D=+0.04±0.00 mHyb=+0.04±0.00 jsfHyb=-0.000±0.000
                b tagging: m2D= 0.03      jsf2D= 0.000       m1D= 0.01      mHyb= 0.02      jsfHyb= 0.000
            background AJ: m2D= 0.01      jsf2D= 0.000       m1D= 0.00      mHyb= 0.01      jsfHyb= 0.000
            background LJ: m2D=-0.02±0.00 jsf2D=+0.000±0.000 m1D=+0.01±0.00 mHyb=-0.01±0.00 jsfHyb=+0.000±0.000
                           m2D=-0.02±0.00 jsf2D=+0.000±0.000 m1D=+0.01±0.00 mHyb=-0.01±0.00 jsfHyb=+0.000±0.000
         background mW AJ: m2D=+0.01±0.00 jsf2D=-0.000±0.000 m1D=-0.00±0.00 mHyb=+0.01±0.00 jsfHyb=-0.000±0.000
                           m2D=-0.01±0.00 jsf2D=+0.000±0.000 m1D=+0.00±0.00 mHyb=-0.01±0.00 jsfHyb=+0.000±0.000
         background mt AJ: m2D=-0.00±0.00 jsf2D=-0.000±0.000 m1D=-0.00±0.00 mHyb=-0.00±0.00 jsfHyb=-0.000±0.000
                           m2D=+0.00±0.00 jsf2D=-0.000±0.000 m1D=+0.00±0.00 mHyb=+0.00±0.00 jsfHyb=-0.000±0.000
              calibration: m2D=+0.03±0.00 jsf2D=+0.000±0.000 m1D=+0.03±0.00 mHyb=+0.03±0.00 jsfHyb=+0.000±0.000
                   evtgen: m2D=+0.21±0.00 jsf2D=-0.001±0.000 m1D=+0.16±0.00 mHyb=+0.20±0.00 jsfHyb=-0.000±0.000
            flavor bottom: m2D=-0.31±0.00 jsf2D=+0.000±0.000 m1D=-0.31±0.00 mHyb=-0.31±0.00 jsfHyb=+0.000±0.000
                           m2D=+0.31±0.00 jsf2D=-0.000±0.000 m1D=+0.31±0.00 mHyb=+0.31±0.00 jsfHyb=-0.000±0.000
             flavor charm: m2D=+0.03±0.00 jsf2D=-0.000±0.000 m1D=-0.01±0.00 mHyb=+0.02±0.00 jsfHyb=-0.000±0.000
                           m2D=-0.03±0.00 jsf2D=+0.000±0.000 m1D=+0.01±0.00 mHyb=-0.02±0.00 jsfHyb=+0.000±0.000
             flavor gluon: m2D=-0.22±0.00 jsf2D=+0.003±0.000 m1D=+0.02±0.00 mHyb=-0.15±0.00 jsfHyb=+0.002±0.000
                           m2D=+0.21±0.00 jsf2D=-0.003±0.000 m1D=-0.02±0.00 mHyb=+0.14±0.00 jsfHyb=-0.002±0.000
             flavor light: m2D=+0.11±0.00 jsf2D=-0.001±0.000 m1D=-0.01±0.00 mHyb=+0.07±0.00 jsfHyb=-0.001±0.000
                           m2D=-0.10±0.00 jsf2D=+0.001±0.000 m1D=+0.01±0.00 mHyb=-0.07±0.00 jsfHyb=+0.001±0.000
                   h_damp: m2D=-0.01±0.08 jsf2D=+0.000±0.001 m1D=+0.02±0.05 mHyb=+0.00±0.07 jsfHyb=+0.000±0.001
                           m2D=+0.10±0.08 jsf2D=-0.001±0.001 m1D=-0.01±0.05 mHyb=+0.07±0.07 jsfHyb=-0.001±0.001
     madgraphMLM pythia8: m2D=+0.79±0.15 jsf2D=+0.000±0.001 m1D=+0.80±0.10 mHyb=+0.79±0.13 jsfHyb=+0.000±0.001
                      muF: m2D=-0.00±0.00 jsf2D=-0.000±0.000 m1D=-0.02±0.00 mHyb=-0.01±0.00 jsfHyb=-0.000±0.000
                           m2D=+0.01±0.00 jsf2D=+0.000±0.000 m1D=+0.02±0.00 mHyb=+0.01±0.00 jsfHyb=+0.000±0.000
                      muR: m2D=+0.01±0.00 jsf2D=-0.000±0.000 m1D=+0.01±0.00 mHyb=+0.01±0.00 jsfHyb=-0.000±0.000
                           m2D=-0.01±0.00 jsf2D=+0.000±0.000 m1D=-0.01±0.00 mHyb=-0.01±0.00 jsfHyb=+0.000±0.000
                  muR muF: m2D=+0.00±0.00 jsf2D=-0.000±0.000 m1D=-0.01±0.00 mHyb=-0.00±0.00 jsfHyb=-0.000±0.000
                           m2D=-0.01±0.00 jsf2D=+0.000±0.000 m1D=+0.01±0.00 mHyb=-0.00±0.00 jsfHyb=+0.000±0.000
muR muF anti (not recomm): m2D=+0.01±0.00 jsf2D=+0.000±0.000 m1D=+0.03±0.00 mHyb=+0.02±0.00 jsfHyb=+0.000±0.000
                           m2D=-0.01±0.00 jsf2D=-0.000±0.000 m1D=-0.02±0.00 mHyb=-0.02±0.00 jsfHyb=-0.000±0.000
                    muR/F: m2D= 0.01      jsf2D= 0.000       m1D= 0.02      mHyb= 0.01      jsfHyb= 0.000
```

```
powheg herwigpp: m2D=-4.36±0.13 jsf2D=+0.014±0.001 m1D=-3.27±0.09 mHyb=-4.03±0.11 jsfHyb=+0.010±0.001
           stat: m2D=+0.08±0.00 jsf2D=+0.001±0.000 m1D=+0.05±0.00 mHyb=+0.07±0.00 jsfHyb=+0.001±0.000
         top pt: m2D=+0.01±0.00 jsf2D=-0.001±0.000 m1D=-0.06±0.00 mHyb=-0.01±0.00 jsfHyb=-0.001±0.000
```

B.3 Shift plots for combination

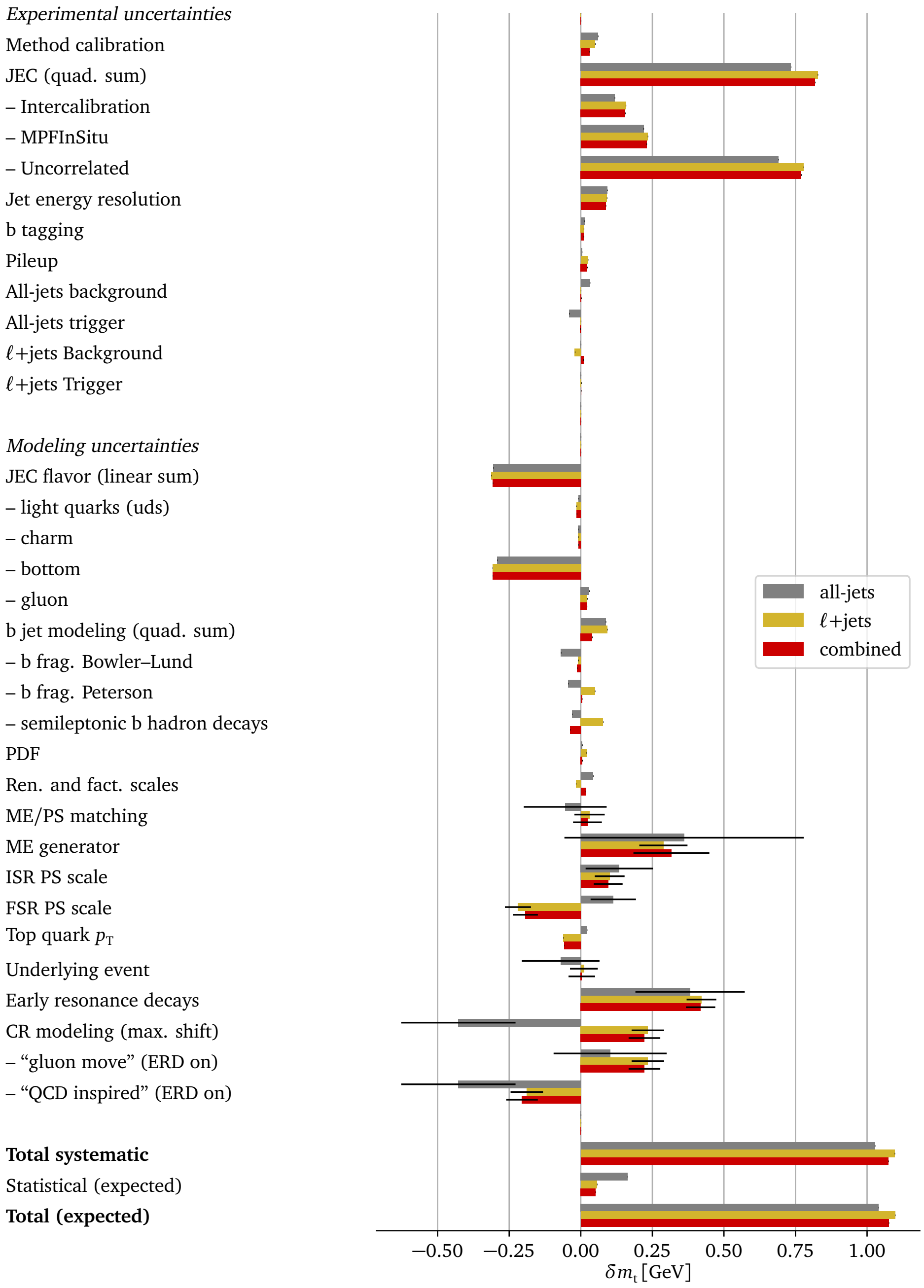

Figure B.1: The sizes of the uncertainty components for the 1D top quark mass measurement. The three bars for each component represent the measurements using the all-jets channel, the lepton+jets channel, and combined measurent. For two-sided uncertainties, the largest of the two shifts is shown, using the sign of the up-variation. Shifts that have an associated statistical uncertainty are presented with the corresponding error bars.

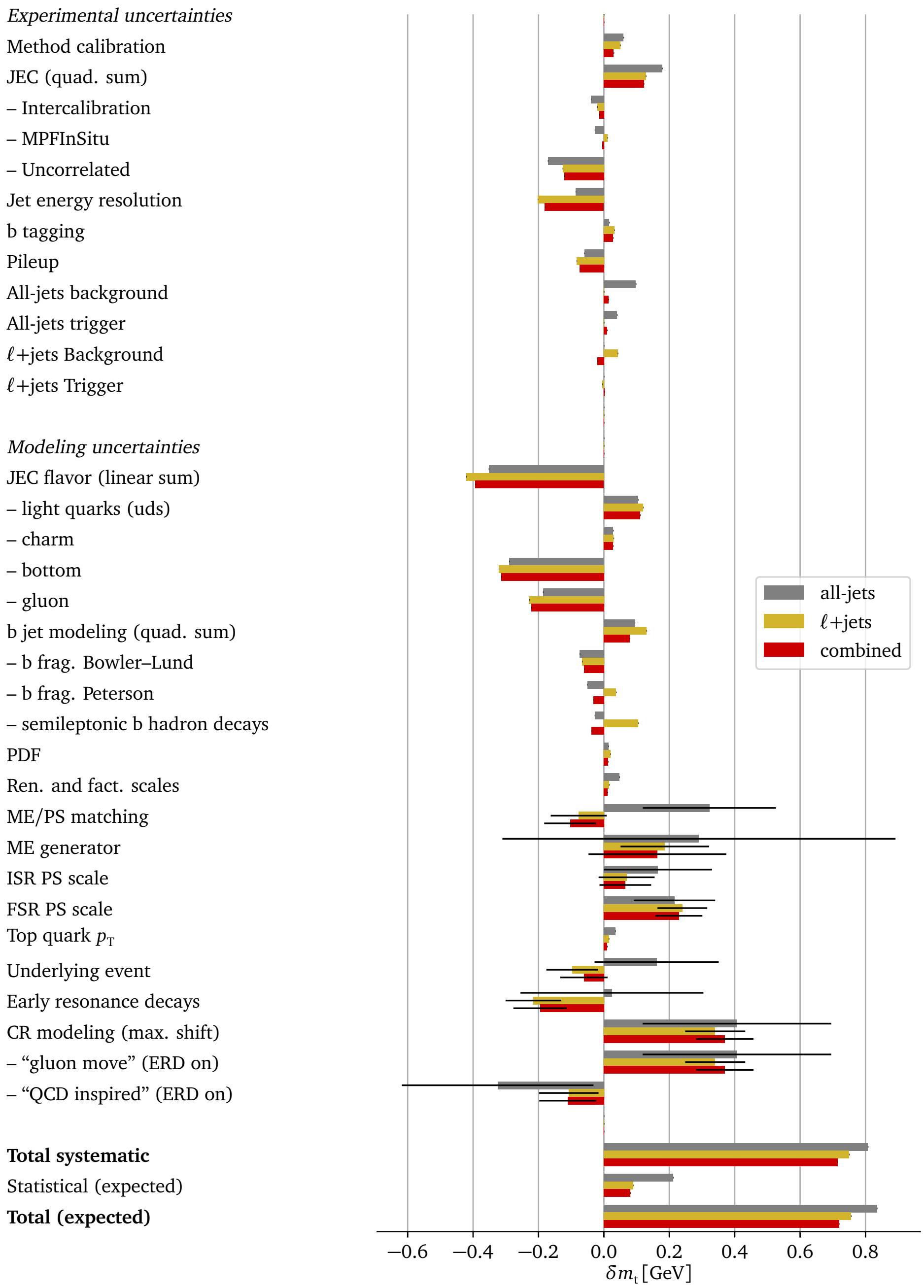

Figure B.2: The sizes of the uncertainty components for the 2D top quark mass measurement. The three bars for each component represent the measurements using the all-jets channel, the lepton+jets channel, and combined measurement. For two-sided uncertainties, the largest of the two shifts is shown, using the sign of the up-variation. Shifts that have an associated statistical uncertainty are presented with the corresponding error bars.

Appendix C

BLUE combination

C.1 Source code

Listing C.1: Python script defining the input covariance matrices used for the BLUE method as described in Section 5.3.3. The `blue_combine` package [160] is used to perform the BLUE method. The variable `reduce_corr` is used to toggle the usage of reduced correlations.

```
#!/usr/bin/env python3

try:
    import blue_combine as blue
except ImportError as e:
    print('The blue_combine module is needed!')
    print('Installation instructions: https://github.com/jolange/BLUE-py\n')
    raise e

from math import sqrt
import numpy as np
from collections import OrderedDict

# reduce_corr = True
reduce_corr = False
n = 2
measurements = blue.Measurements([172.250, 172.340])

# correlation matrices for 0% and 100% correlation
UNCORR = np.identity(n)
CORR = np.ones((n, n))

components = OrderedDict()
source =  blue.CovarianceMatrix.from_correlation_matrix
#                               LJ    AJ
components['FitCal']  = source([0.05, 0.06], UNCORR, reduce_corr)
components['intJES']  = source([0.04, 0.04], CORR,   reduce_corr)
components['MPFJES']  = source([0.07, 0.08], CORR,   reduce_corr)
components['uncJES']  = source([0.16, 0.12], CORR,   reduce_corr)
components['JER']     = source([0.12, 0.04], CORR,   reduce_corr)
```

```
components['BTag']    = source([0.03, 0.02], CORR,   reduce_corr)
components['PU']      = source([0.05, 0.04], CORR,   reduce_corr)
components['BKG']     = source([0.02, 0.07], UNCORR, reduce_corr)
components['Trigger'] = source([0.00, 0.02], UNCORR, reduce_corr)
components['flJES']   = source([0.39, 0.34], CORR,   reduce_corr)
components['bMod']    = source([0.12, 0.09], CORR,   reduce_corr)
components['PDF']     = source([0.02, 0.01], CORR,   reduce_corr)
components['Q']       = source([0.01, 0.04], CORR,   reduce_corr)
components['ME/PS']   = source([0.07, 0.24], CORR,   reduce_corr)
components['MCGen']   = source([0.20, 0.00], CORR,   reduce_corr)
components['ISR']     = source([0.07, 0.14], CORR,   reduce_corr)
components['FSR']     = source([0.13, 0.18], CORR,   reduce_corr)
components['topPt']   = source([0.01, 0.03], CORR,   reduce_corr)
components['UE']      = source([0.07, 0.17], CORR,   reduce_corr)
components['ERD']     = source([0.07, 0.24], CORR,   reduce_corr)
components['CR']      = source([0.31, 0.36], CORR,   reduce_corr)
components['Stat']    = source([0.08, 0.20], UNCORR, reduce_corr)

E = sum(components.values())
combination = blue.BLUE(measurements, E)

print('Total covariance matrix:')
print(E)
print('Total correlation matrix:')
print(E.correlation_matrix())
print('BLUE combination:')
print(combination)

print()
print('Uncertainty components:')
alpha = combination.alpha
sigma = 0
for comp, E_i in components.items():
    sigma_i = alpha.T * E_i * alpha
    sigma += sigma_i
    print('%-8s %.2f' % (comp, sqrt(sigma_i)))
print('total: %.4f' % sqrt(sigma))
```

Appendix D

Technical details of the global electroweak fit

Whenever the global electroweak fit, described in Chapter 6, is performed without the Higgs boson mass measurement as input, the Higgs boson mass is not completely free, but allowed to vary within $10\,\mathrm{GeV} \leq m_\mathrm{H} \leq 1\,\mathrm{TeV}$. This is, because in this range the theory parametrization approximates the result for the m_W prediction to better than 0.5 MeV [37]. Therefore, this is also what has been done by the Gfitter Group in their fits:

```
<Parameter
    Name       = "MH"
    Value      = "[10:1000]"
    ScanRange  = "[10:1000]"
    FitLimits  = "[10:1000]"
    PreFitScan = "[10:1000]"
    Active     = "T"
   />
```

The validity statement is true only if all other input values in the parametrization vary at most within 2σ [37]. For the top quark mass, 1σ was of the order of 5 GeV at that time [176]. The global fit "without the m_t measurement" has been re-evaluated with the top quark mass constrained to ±5 GeV around the nominal value of $m_\mathrm{t} = 172.26\,\mathrm{GeV}$, i.e., $167.26 \leq m_\mathrm{t} \leq 177.26\,\mathrm{GeV}$:

```
<Parameter
    Name       = "mt"
    Value      = "[167.26:177.26]"
    <!-- [...] -->
    Active     = "T"
    />
```

The result is shown in Fig. D.1 as the filled contour areas. The contours shown in Fig. 6.3 are included as dashed lines here. An artificial cut-off can be observed, showing that the more constrained m_t window has an impact.

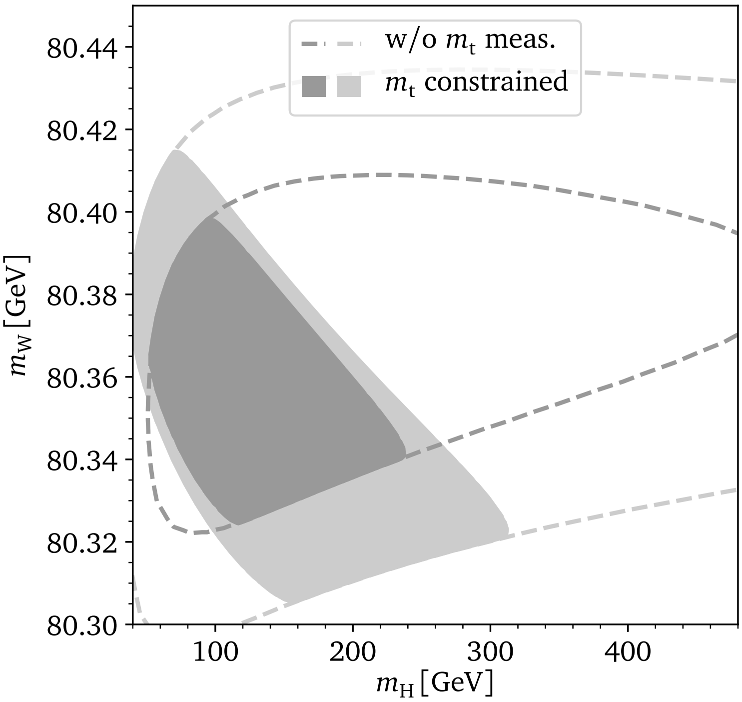

Figure D.1: Two-dimensional parameter scans of the global fit for m_W and m_H. Two concentric contours are shown for $\Delta\chi^2 = 2.3$ and 5.99, corresponding to 68% and 95% CL, respectively. For the dashed contours, the m_t measurements are excluded from the fit, like shown before in Fig. 6.3. For the filled gray contours, m_t is constrained to $167.26 \leq m_t \leq 177.26$ GeV.

Since it is not necessary to have an extremely precise parametrization for these studies, it can be checked up to which top quark mass it is a useful parametrization at all, and where it breaks down. For this, the `FctOfFreePara` functionality of GFITTER is used to get m_W as a function of m_t:

```
<Actions
    <!-- [...] -->
    FctOfFreePara  = "T:mt:Nbins=100"
    <!-- [...] -->
 />
<Parameter
    Name       = "mt"
    Value      = "172.26 +- 0.61_statsyst +- 0.5_syst"
    ScanRange  = "[2:1100]"
    <!-- [...] -->
    Active     = "T"
 />
```

The result is shown in Fig. D.2. The m_W prediction rises slightly with growing m_t and reaches a maximum at $m_t \approx 400$ GeV. It then falls steeply and even turns negative at around $m_t \approx 1.1\,\text{TeV}$. At least up to $m_t \approx 300\,\text{GeV}$ the prediction is reasonable, though, so the range $2 \leq m_t \leq 300\,\text{GeV}$ has been used in Chapter 6 and the dashed contours in Fig. D.1. In fact, constraining the top quark mass to $m_t \leq 200\,\text{GeV}$ is already sufficient to get the full area.

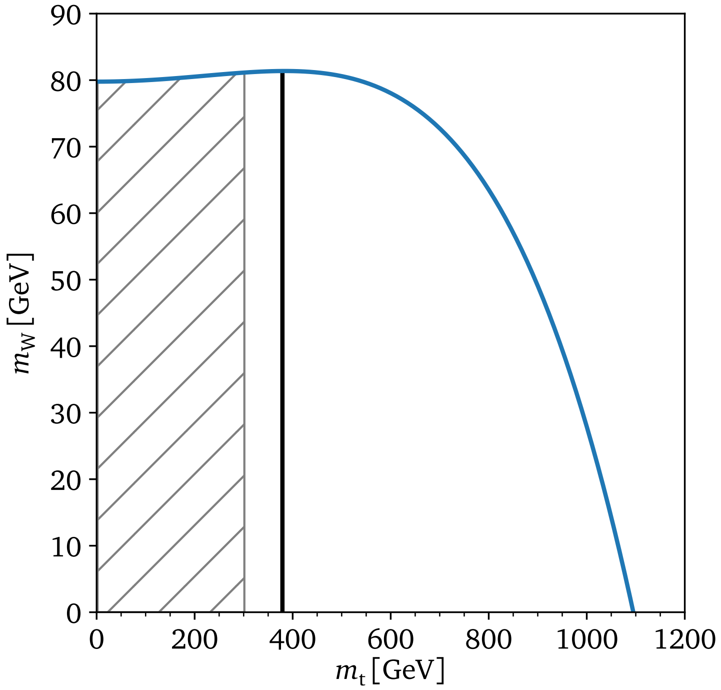

Figure D.2: The W boson mass as a function of m_t as obtained with the parametrization implemented in GFITTER [37, 38]. The vertical black line marks the maximum of the curve, while the gray hashed region represents the interval in which m_t is free in the fits "without the m_t measurement".

Table D.1: Input values for the global electroweak fit as used for the results presented in Chapter 6. The values are taken from Ref. [38], where further details on the definitions parameters and origins of the values can be found. The value for m_t in this list is not used in Chapter 6, but the result of the measurement presented in Chapter 5.

Parameter	Input value
M_H [GeV]	125.1 ± 0.2
M_W [GeV]	80.379 ± 0.013
Γ_W [GeV]	2.085 ± 0.042
M_Z [GeV]	91.1875 ± 0.0021
Γ_Z [GeV]	2.4952 ± 0.0023
σ^0_had [nb]	41.540 ± 0.037
R^0_ℓ	20.767 ± 0.025
$A^{0,\ell}_\mathrm{FB}$	0.0171 ± 0.0010
A_ℓ	0.1499 ± 0.0018
$\sin^2 \theta^\ell_\mathrm{eff}(Q_\mathrm{FB})$	0.2324 ± 0.0012
$\sin^2 \theta^\ell_\mathrm{eff}(\mathrm{Tevt.})$	0.23148 ± 0.00033
A_c	0.670 ± 0.027
A_b	0.923 ± 0.020
$A^{0,c}_\mathrm{FB}$	0.0707 ± 0.0035
$A^{0,b}_\mathrm{FB}$	0.0992 ± 0.0016
R^0_c	0.1721 ± 0.0030
R^0_b	0.21629 ± 0.00066
$\overline{m}_\mathrm{c}$ [GeV]	$1.27^{+0.07}_{-0.11}$
$\overline{m}_\mathrm{b}$ [GeV]	$4.20^{+0.17}_{-0.07}$
m_t [GeV]	172.47 ± 0.68
$\Delta\alpha^{(5)}_\mathrm{had}(M_Z^2)$	2760 ± 9

References

[1] CMS Collaboration, “Measurement of the top quark mass in the all-jets final state at $\sqrt{s} = 13$ TeV and combination with the lepton+jets channel”, *Eur. Phys. J. C* **79** (2019) 313, `doi:10.1140/epjc/s10052-019-6788-2`, `arXiv:1812.10534`.

[2] CMS Collaboration, “Measurement of the top quark mass in the all-jets final state at $\sqrt{s} = 13$ TeV”, CMS Physics Analysis Summary CMS-PAS-TOP-17-008, 2018.

[3] J. Lange (on behalf of the CMS Collaboration), “Top quark mass measurement in the $\mathrm{t\bar{t}}$ all-jets final state with the CMS experiment at $\sqrt{s} = 13$ TeV”, in *Proceedings of the 11th International Workshop on Top Quark Physics (TOP2018) Bad Neuenahr, Germany, September 16-21, 2018 (SLAC eConf C1809161)*, `arXiv:1812.05394`.

[4] J. Lange et al., “Measurement of the top quark mass in the all-jets final state at 13 TeV”, CMS Analysis Note CMS AN-2017/064 v10 [CMS internal], 2017.

[5] J. Lange et al., “Combined measurement of the top quark mass in the lepton+jets and all-jets final states at 13 TeV”, CMS Analysis Note CMS AN-2018/076 v9 [CMS internal], 2018.

[6] CMS Collaboration, “Observation of a new boson at a mass of 125 GeV with the CMS experiment at the LHC”, *Phys. Lett. B* **716** (2012) 30, `doi:10.1016/j.physletb.2012.08.021`, `arXiv:1207.7235`.

[7] ATLAS Collaboration, “Observation of a new particle in the search for the Standard Model Higgs boson with the ATLAS detector at the LHC”, *Phys. Lett. B* **716** (2012) 1, `doi:10.1016/j.physletb.2012.08.020`, `arXiv:1207.7214`.

[8] ATLAS Collaboration, CMS Collaboration, “Combined Measurement of the Higgs Boson Mass in pp Collisions at $\sqrt{s} = 7$ and 8 TeV with the ATLAS and CMS Experiments”, *Phys. Rev. Lett.* **114** (2015) 191803, `doi:10.1103/PhysRevLett.114.191803`, `arXiv:1503.07589`.

[9] CMS Collaboration, “Precise determination of the mass of the Higgs boson and tests of compatibility of its couplings with the standard model predictions using proton collisions at 7 and 8 TeV”, *Eur. Phys. J. C* **75** (2015), no. 5, 212, `doi:10.1140/epjc/s10052-015-3351-7`, `arXiv:1412.8662`.

[10] M. Persic, P. Salucci, and F. Stel, “The Universal rotation curve of spiral galaxies: 1. The Dark matter connection”, *Mon. Not. Roy. Astron. Soc.* **281** (1996) 27, `doi:10.1093/mnras/281.1.27,10.1093/mnras/278.1.27`, `arXiv:astro-ph/9506004`.

[11] D. Clowe et al., “A direct empirical proof of the existence of dark matter”, *Astrophys. J.* **648** (2006) L109, `doi:10.1086/508162`, `arXiv:astro-ph/0608407`.

[12] Particle Data Group, “Review of Particle Physics”, *Phys. Rev. D* **98** (2018) 030001, `doi:10.1103/PhysRevD.98.030001`.

[13] Wikipedia User:Cush, “File:Standard Model of Elementary Particles.svg”, `https://en.wikipedia.org/wiki/File:Standard_Model_of_Elementary_Particles.svg`, Version 14:41, 17 September 2019.

[14] CMS Collaboration, “Evidence for the 125 GeV Higgs boson decaying to a pair of τ leptons”, *JHEP* **05** (2014) 104, `doi:10.1007/JHEP05(2014)104`, `arXiv:1401.5041`.

[15] CMS Collaboration, “Search for the standard model Higgs boson produced through vector boson fusion and decaying to $b\overline{b}$”, *Phys. Rev. D* **92** (2015) 032008, `doi:10.1103/PhysRevD.92.032008`, `arXiv:1506.01010`.

[16] CMS Collaboration, “Evidence for the direct decay of the 125 GeV Higgs boson to fermions”, *Nature Phys.* **10** (2014) 557, `doi:10.1038/nphys3005`, `arXiv:1401.6527`.

[17] CMS Collaboration, “Combined measurements of Higgs boson couplings in proton–proton collisions at $\sqrt{s} = 13\,\text{TeV}$”, *Eur. Phys. J. C* **79** (2019) 421, `doi:10.1140/epjc/s10052-019-6909-y`, `arXiv:1809.10733`.

[18] ATLAS, CMS Collaboration, “Measurements of the Higgs boson production and decay rates and constraints on its couplings from a combined ATLAS and CMS analysis of the LHC pp collision data at $\sqrt{s} = 7$ and 8 TeV”, *JHEP* **08** (2016) 045, `doi:10.1007/JHEP08(2016)045`, `arXiv:1606.02266`.

[19] CMS Collaboration, “Observation of $\mathrm{t\bar{t}H}$ production”, *Phys. Rev. Lett.* **120** (2018) 231801, `doi:10.1103/PhysRevLett.120.231801`, `arXiv:1804.02610`.

[20] CDF Collaboration, “Observation of top quark production in $\bar{p}p$ collisions”, *Phys. Rev. Lett.* **74** (1995) 2626, `doi:10.1103/PhysRevLett.74.2626`, `arXiv:hep-ex/9503002`.

[21] D0 Collaboration, “Observation of the top quark”, *Phys. Rev. Lett.* **74** (1995) 2632, `doi:10.1103/PhysRevLett.74.2632`, `arXiv:hep-ex/9503003`.

[22] S. P. Martin, “A Supersymmetry primer”, *Adv. Ser. Direct. High Energy Phys.* **18** (1998) 1, `doi:10.1142/9789812839657_0001`, `arXiv:hep-ph/9709356`.

[23] P. Ramond, “Dual theory for free fermions”, *Phys. Rev. D* **3** (1971) 2415, `doi:10.1103/PhysRevD.3.2415`.

[24] J. Wess and B. Zumino, “Supergauge transformations in four-dimensions”, *Nucl. Phys. B* **70** (1974) 39, `doi:10.1016/0550-3213(74)90355-1`.

[25] D. Z. Freedman, P. van Nieuwenhuizen, and S. Ferrara, “Progress toward a theory of supergravity”, *Phys. Rev. D* **13** (1976) 3214, `doi:10.1103/PhysRevD.13.3214`.

[26] P. Fayet, “Supergauge invariant extension of the Higgs mechanism and a model for the electron and its neutrino”, *Nucl. Phys. B* **90** (1975) 104, `doi:10.1016/0550-3213(75)90636-7`.

[27] A. H. Chamseddine, R. L. Arnowitt, and P. Nath, “Locally supersymmetric grand unification”, *Phys. Rev. Lett.* **49** (1982) 970, `doi:10.1103/PhysRevLett.49.970`.

[28] L. J. Hall, J. D. Lykken, and S. Weinberg, “Supergravity as the messenger of supersymmetry breaking”, *Phys. Rev. D* **27** (1983) 2359, `doi:10.1103/PhysRevD.27.2359`.

[29] G. L. Kane, C. F. Kolda, L. Roszkowski, and J. D. Wells, “Study of constrained minimal supersymmetry”, *Phys. Rev. D* **49** (1994) 6173, `doi:10.1103/PhysRevD.49.6173`, `arXiv:hep-ph/9312272`.

[30] A. Andreassen, W. Frost, and M. D. Schwartz, “Scale Invariant Instantons and the Complete Lifetime of the Standard Model”, *Phys. Rev. D* **97** (2018) 056006, `doi:10.1103/PhysRevD.97.056006`, `arXiv:1707.08124`.

[31] H. Flacher et al., “Revisiting the Global Electroweak Fit of the Standard Model and Beyond with Gfitter”, *Eur. Phys. J. C* **60** (2009) 543, `doi:10.1140/epjc/s10052-009-0966-6,10.1140/epjc/s10052-011-1718-y`, `arXiv:0811.0009`. [Erratum: *Eur. Phys. J. C* **71** (2011) 1718].

[32] M. Baak et al., “Updated Status of the Global Electroweak Fit and Constraints on New Physics”, *Eur. Phys. J. C* **72** (2012) 2003, `doi:10.1140/epjc/s10052-012-2003-4`, `arXiv:1107.0975`.

[33] M. Baak et al., “The electroweak fit of the standard model after the discovery of a new boson at the LHC”, *Eur. Phys. J. C* **72** (2012) 2205, `doi:10.1140/epjc/s10052-012-2205-9`, `arXiv:1209.2716`.

[34] M. Baak et al., “The global electroweak fit at NNLO and prospects for the LHC and ILC”, *Eur. Phys. J. C* **74** (2014) 3046, `doi:10.1140/epjc/s10052-014-3046-5`, `arXiv:1407.3792`.

[35] D. Yu. Bardin et al., “ZFITTER v.6.21: A Semianalytical program for fermion pair production in e+ e- annihilation”, *Comput. Phys. Commun.* **133** (2001) 229, `doi:10.1016/S0010-4655(00)00152-1`, `arXiv:hep-ph/9908433`.

[36] A. B. Arbuzov et al., “ZFITTER: A Semi-analytical program for fermion pair production in e+ e- annihilation, from version 6.21 to version 6.42”, *Comput. Phys. Commun.* **174** (2006) 728, `doi:10.1016/j.cpc.2005.12.009`, `arXiv:hep-ph/0507146`.

[37] M. Awramik, M. Czakon, A. Freitas, and G. Weiglein, “Precise prediction for the W boson mass in the standard model”, *Phys. Rev. D* **69** (2004) 053006, `doi:10.1103/PhysRevD.69.053006`, `arXiv:hep-ph/0311148`.

[38] J. Haller et al., “Update of the global electroweak fit and constraints on two-Higgs-doublet models”, *Eur. Phys. J. C* **78** (2018) 675, `doi:10.1140/epjc/s10052-018-6131-3`, `arXiv:1803.01853`.

[39] M. Czakon and A. Mitov, “Top++: A program for the calculation of the top-pair cross-section at hadron colliders”, *Comput. Phys. Commun.* **185** (2014) 2930, `doi:10.1016/j.cpc.2014.06.021`, `arXiv:1112.5675`.

[40] LHCtopWG, “Summary Plots”, `https://twiki.cern.ch/twiki/bin/view/LHCPhysics/LHCTopWGSummaryPlots?rev=55`, License: CC-BY-4.0 [accessed 27.05.2019].

[41] J. Gao, C. S. Li, and H. X. Zhu, “Top Quark Decay at Next-to-Next-to Leading Order in QCD”, *Phys. Rev. Lett.* **110** (2013), no. 4, 042001, `doi:10.1103/PhysRevLett.110.042001`, `arXiv:1210.2808`.

[42] D. Kovalskyi et al., “Fireworks: A Physics Event Display for CMS”, *J. Phys. Conf. Ser.* **219** (2010) 032014, `doi:10.1088/1742-6596/219/3/032014`.

[43] CMS Collaboration, “Physics Analysis Oriented Event Display (Fireworks / cmsShow)”, `https://twiki.cern.ch/twiki/bin/view/CMSPublic/WorkBookFireworks?rev=285`.

[44] P. Nason, “The Top Mass in Hadronic Collisions”, in *From My Vast Repertoire ...: Guido Altarelli’s Legacy*, A. Levy, S. Forte, and G. Ridolfi, eds., p. 123. 2019. `arXiv:1712.02796`.

[45] P. Nason, “Theory issues on top quark mass measurement; Top mass theory including follow-ups from previous meeting and from Top2019”, Open meeting of the LHCtopWG, 2019. `https://indico.cern.ch/event/843509/timetable/#12-top-mass-theory-including-f`.

[46] M. Butenschoen et al., “Top Quark Mass Calibration for Monte Carlo Event Generators”, *Phys. Rev. Lett.* **117** (2016) 232001, `doi:10.1103/PhysRevLett.117.232001`, `arXiv:1608.01318`.

[47] A. H. Hoang, “The Top Mass: Interpretation and Theoretical Uncertainties”, in *Proceedings, 7th International Workshop on Top Quark Physics (TOP2014): Cannes, France, September 28-October 3, 2014*, 2014, `arXiv:1412.3649`.

[48] S. Moch, “Precision determination of the top-quark mass”, *PoS* **LL2014** (2014) 054, `doi:10.22323/1.211.0054`, `arXiv:1408.6080`.

[49] A. H. Hoang, A. Jain, I. Scimemi, and I. W. Stewart, “Infrared Renormalization Group Flow for Heavy Quark Masses”, *Phys. Rev. Lett.* **101** (2008) 151602, `doi:10.1103/PhysRevLett.101.151602`, `arXiv:0803.4214`.

[50] CDF Collaboration, “Measurement of the top-quark mass in the all-hadronic channel using the full CDF data set”, *Phys. Rev. D* **90** (2014) 091101, `doi:10.1103/PhysRevD.90.091101`, `arXiv:1409.4906`.

[51] CMS Collaboration, “Measurement of the top-quark mass in all-jets $\mathrm{t\bar{t}}$ events in pp collisions at $\sqrt{s}$=7 TeV”, *Eur. Phys. J. C* **74** (2014) 2758, `doi:10.1140/epjc/s10052-014-2758-x`, `arXiv:1307.4617`.

[52] CMS Collaboration, “Measurement of the top quark mass using proton-proton data at $\sqrt{s} = 7$ and 8 TeV”, *Phys. Rev. D* **93** (2016) 072004, `doi:10.1103/PhysRevD.93.072004`, `arXiv:1509.04044`.

[53] ATLAS Collaboration, “Measurement of the top-quark mass in the fully hadronic decay channel from ATLAS data at $\sqrt{s} = 7\,\mathrm{TeV}$”, *Eur. Phys. J. C* **75** (2015) 158, `doi:10.1140/epjc/s10052-015-3373-1`, `arXiv:1409.0832`.

[54] ATLAS Collaboration, “Top-quark mass measurement in the all-hadronic $\mathrm{t\bar{t}}$ decay channel at $\sqrt{s} = 8$ TeV with the ATLAS detector”, *JHEP* **09** (2017) 118, `doi:10.1007/JHEP09(2017)118`, `arXiv:1702.07546`.

[55] ATLAS Collaboration, “Measurement of the top quark mass in the $t\bar{t} \to$ lepton+jets channel from $\sqrt{s} = 8$ TeV ATLAS data and combination with previous results”, (2018). `arXiv:1810.01772`. Submitted to *Eur. Phys. J. C*.

[56] CDF and D0 Collaborations, “Combination of CDF and D0 results on the mass of the top quark using up 9.7 fb^{-1} at the Tevatron”, FERMILAB-CONF-16-298-E, TEVEWWG/top2016/01, `arXiv:1608.01881`, 2016.

[57] CMS Collaboration, “Measurement of the top quark mass with lepton+jets final states using pp collisions at $\sqrt{s} = 13\,\mathrm{TeV}$”, *Eur. Phys. J. C* **78** (2018) 891, `doi:10.1140/epjc/s10052-018-6332-9`, `arXiv:1805.01428`.

[58] CMS Collaboration, “Measurement of the $\mathrm{t\bar{t}}$ production cross section, the top quark mass, and the strong coupling constant using dilepton events in pp collisions at $\sqrt{s} =$ 13 TeV”, *Eur. Phys. J. C* **79** (2019) 368, `doi:10.1140/epjc/s10052-019-6863-8`, `arXiv:1812.10505`.

[59] ATLAS Collaboration, “Measurement of the $t\bar{t}$ production cross-section and lepton differential distributions in $e\mu$ dilepton events from pp collisions at $\sqrt{s} = 13$ TeV with the ATLAS detector”, ATLAS Conferernce Note ATLAS-CONF-2019-041, CERN, 2019.

[60] CMS Collaboration, “Measurement of $\mathrm{t\bar{t}}$ normalised multi-differential cross sections in pp collisions at $\sqrt{s} = 13$ TeV, and simultaneous determination of the strong coupling strength, top quark pole mass, and parton distribution functions”, `arXiv:1904.05237`. Submitted to *Eur. Phys. J. C*.

[61] S. Fleming, A. H. Hoang, S. Mantry, and I. W. Stewart, “Jets from massive unstable particles: Top-mass determination”, *Phys. Rev. D* **77** (2008) 074010, `doi:10.1103/PhysRevD.77.074010`, `arXiv:hep-ph/0703207`.

[62] S. Fleming, A. H. Hoang, S. Mantry, and I. W. Stewart, “Top jets in the peak region: Factorization analysis with next-to-leading-log resummation”, *Phys. Rev. D* **77** (2008) 114003, `doi:10.1103/PhysRevD.77.114003`, `arXiv:0711.2079`.

[63] A. Jain, I. Scimemi, and I. W. Stewart, “Two-loop jet-function and jet-mass for top quarks”, *Phys. Rev. D* **77** (2008) 094008, `doi:10.1103/PhysRevD.77.094008`, `arXiv:0801.0743`.

[64] A. H. Hoang, A. Pathak, P. Pietrulewicz, and I. W. Stewart, “Hard matching for boosted tops at two loops”, *JHEP* **12** (2015) 059, `doi:10.1007/JHEP12(2015)059`, `arXiv:1508.04137`.

[65] A. H. Hoang, S. Mantry, A. Pathak, and I. W. Stewart, “Extracting a short distance top mass with light grooming”, *Phys. Rev. D* **100** (2019) 074021, `doi:10.1103/PhysRevD.100.074021`, `arXiv:1708.02586`.

[66] A. H. Hoang, C. Lepenik, and M. Stahlhofen, “Two-loop massive quark jet functions in SCET”, *JHEP* **08** (2019) 112, `doi:10.1007/JHEP08(2019)112`, `arXiv:1904.12839`.

[67] C. W. Bauer, S. Fleming, and M. E. Luke, “Summing Sudakov logarithms in $B \to X_s + \gamma$ in effective field theory”, *Phys. Rev. D* **63** (2000) 014006, `doi:10.1103/PhysRevD.63.014006`, `arXiv:hep-ph/0005275`.

[68] C. W. Bauer, S. Fleming, D. Pirjol, and I. W. Stewart, “An effective field theory for collinear and soft gluons: Heavy to light decays”, *Phys. Rev. D* **63** (2001) 114020, `doi:10.1103/PhysRevD.63.114020`, `arXiv:hep-ph/0011336`.

[69] C. W. Bauer and I. W. Stewart, "Invariant operators in collinear effective theory", *Phys. Lett. B* **516** (2001) 134, `doi:10.1016/S0370-2693(01)00902-9`, `arXiv:hep-ph/0107001`.

[70] C. W. Bauer, D. Pirjol, and I. W. Stewart, "Soft-collinear factorization in effective field theory", *Phys. Rev. D* **65** (2002) 054022, `doi:10.1103/PhysRevD.65.054022`, `arXiv:hep-ph/0109045`.

[71] CMS Collaboration, "Measurement of the jet mass distribution and top quark mass in hadronic decays of boosted top quarks in pp collisions at $\sqrt{s} = 13$ TeV", `arXiv:1911.03800`. Submitted to *Phys. Rev. Lett.*

[72] L. Evans and P. Bryant, "LHC Machine", *JINST* **3** (2008) S08001, `doi:10.1088/1748-0221/3/08/S08001`.

[73] CMS Collaboration, "The CMS experiment at the CERN LHC", *JINST* **3** (2008) S08004, `doi:10.1088/1748-0221/3/08/S08004`.

[74] ATLAS Collaboration, "The ATLAS Experiment at the CERN Large Hadron Collider", *JINST* **3** (2008) S08003, `doi:10.1088/1748-0221/3/08/S08003`.

[75] LHCb Collaboration, "The LHCb Detector at the LHC", *JINST* **3** (2008) S08005, `doi:10.1088/1748-0221/3/08/S08005`.

[76] ALICE Collaboration, "The ALICE experiment at the CERN LHC", *JINST* **3** (2008) S08002, `doi:10.1088/1748-0221/3/08/S08002`.

[77] E. Mobs, "The CERN accelerator complex. Complexe des accélérateurs du CERN", OPEN-PHO-ACCEL-2016-009, `https://cds.cern.ch/record/2197559`.

[78] CMS Collaboration, "Particle Kickers", `https://cds.cern.ch/record/1706606/` [accessed 2019-06-09].

[79] CMS Collaboration, "Public CMS Luminosity Information", `https://twiki.cern.ch/twiki/bin/view/CMSPublic/LumiPublicResults?rev=161`.

[80] T. Sakuma and T. McCauley, "Detector and Event Visualization with SketchUp at the CMS Experiment", *J. Phys. Conf. Ser.* **513** (2014) 022032, `doi:10.1088/1742-6596/513/2/022032`, `arXiv:1311.4942`.

[81] Tai Sakuma, "CMS SketchUp file", `https://cms-docdb.cern.ch/cgi-bin/DocDB/ShowDocument?docid=5958` [accessed 2016-08-09].

[82] P. Adzic et al., "Energy resolution of the barrel of the CMS electromagnetic calorimeter", *JINST* **2** (2007) P04004, `doi:10.1088/1748-0221/2/04/P04004`.

[83] G. Bauer et al., "The CMS High Level Trigger System: Experience and future development", *J. Phys. Conf. Ser.* **396** (2012) 012008, `doi:10.1088/1742-6596/396/1/012008`.

[84] P. Bortignon, "The current CMS trigger / Description of the CMS Trigger Design and Performance", Talk at *Triggering Discoveries in High Energy Physics II*, 2018. `https://indico.cern.ch/event/659612/contributions/2836315/`.

[85] R. Brun and F. Rademakers, “ROOT: An object oriented data analysis framework”, *Nucl. Instrum. Meth. A* **389** (1997) 81, `doi:10.1016/S0168-9002(97)00048-X`.

[86] I. Antcheva et al., “ROOT: A C++ framework for petabyte data storage, statistical analysis and visualization”, *Comput. Phys. Commun.* **180** (2009) 2499, `doi:10.1016/j.cpc.2009.08.005`, `arXiv:1508.07749`.

[87] G. Petrucciani, A. Rizzi, and C. Vuosalo, “Mini-AOD: A New Analysis Data Format for CMS”, *J. Phys. Conf. Ser.* **664** (2015), no. 7, 072052, `doi:10.1088/1742-6596/664/7/072052`.

[88] F. Stober et al., “The swiss army knife of job submission tools: grid-control”, *J. Phys. Conf. Ser.* **898** (2017) 092052, `doi:10.1088/1742-6596/898/9/092052`, `arXiv:1707.03198`.

[89] CMS Collaboration, “Particle-Flow Event Reconstruction in CMS and Performance for Jets, Taus, and MET”, CMS Physics Analysis Summary CMS-PAS-PFT-09-001, CERN, Geneva, 2009.

[90] CMS Collaboration, “Commissioning of the Particle-flow Event Reconstruction with the first LHC collisions recorded in the CMS detector”, CMS Physics Analysis Summary CMS-PAS-PFT-10-001, CERN, Geneva, 2010.

[91] CMS Collaboration, “Particle-flow reconstruction and global event description with the CMS detector”, *JINST* **12** (2017) P10003, `doi:10.1088/1748-0221/12/10/P10003`, `arXiv:1706.04965`.

[92] M. Cacciari, G. P. Salam, and G. Soyez, “The anti-k_T jet clustering algorithm”, *JHEP* **04** (2008) 063, `doi:10.1088/1126-6708/2008/04/063`, `arXiv:0802.1189`.

[93] M. Cacciari, G. P. Salam, and G. Soyez, “FastJet user manual”, *Eur. Phys. J. C* **72** (2012) 1896, `doi:10.1140/epjc/s10052-012-1896-2`, `arXiv:1111.6097`.

[94] CMS Collaboration, “Particle-flow commissioning with muons and electrons from J/Psi and W events at 7 TeV”, CMS Physics Analysis Summary CMS-PAS-PFT-10-003, CERN, Geneva, 2010.

[95] CMS Collaboration, “Baseline muon selections for Run-II”, `https://twiki.cern.ch/twiki/bin/view/CMS/SWGuideMuonIdRun2?rev=57#Muon_Identification`.

[96] L. Gray for the CMS EGM POG, “GED Electron and Photon Reconstruction for Run 2”, Second EGM Global Event Description Workshop `https://indico.cern.ch/event/306030/contributions/704002/` [CMS internal], CERN, Geneva, 2014-03-24.

[97] CMS Collaboration, “Performance of Photon Reconstruction and Identification with the CMS Detector in Proton-Proton Collisions at $\sqrt{s} = 8$ TeV”, *JINST* **10** (2015), no. 08, P08010, `doi:10.1088/1748-0221/10/08/P08010`, `arXiv:1502.02702`.

[98] CMS Collaboration, “Performance of Electron Reconstruction and Selection with the CMS Detector in Proton-Proton Collisions at $\sqrt{s} = 8$ TeV”, *JINST* **10** (2015), no. 06, P06005, `doi:10.1088/1748-0221/10/06/P06005`, `arXiv:1502.02701`.

[99] CMS Collaboration, “Cut Based Photon ID for Run 2”, `https://twiki.cern.ch/twiki/bin/view/CMS/CutBasedPhotonIdentificationRun2?rev=50`.

[100] CMS Collaboration, “Cut Based Electron ID for Run 2”, `https://twiki.cern.ch/twiki/bin/view/CMS/CutBasedElectronIdentificationRun2?rev=63`.

[101] M. Cacciari and G. P. Salam, “Dispelling the N^3 myth for the k_t jet-finder”, *Phys. Lett. B* **641** (2006) 57, `doi:10.1016/j.physletb.2006.08.037`, `arXiv:hep-ph/0512210`.

[102] CMS Collaboration, “Performance of b tagging at $\sqrt{s} = 8$ TeV in multijet, $t\bar{t}$ and boosted topology events”, CMS Physics Analysis Summary CMS-PAS-BTV-13-001, 2013.

[103] CMS Collaboration, “Identification of heavy-flavour jets with the CMS detector in pp collisions at 13 TeV”, *JINST* **13** (2018) P05011, `doi:10.1088/1748-0221/13/05/P05011`, `arXiv:1712.07158`.

[104] CMS Collaboration, “Jet energy scale and resolution in the CMS experiment in pp collisions at 8 TeV”, *JINST* **12** (2017) P02014, `doi:10.1088/1748-0221/12/02/P02014`, `arXiv:1607.03663`.

[105] CMS Collaboration, “Jet Energy Resolution”, `https://twiki.cern.ch/twiki/bin/view/CMS/JetResolution?rev=72`.

[106] F. Siegert, “Monte-Carlo event generation for the LHC”, PhD thesis, CERN-THESIS-2010-302, Durham University, 2010. `http://etheses.dur.ac.uk/484/`.

[107] P. Nason, “A new method for combining NLO QCD with shower Monte Carlo algorithms”, *JHEP* **11** (2004) 040, `doi:10.1088/1126-6708/2004/11/040`, `arXiv:hep-ph/0409146`.

[108] S. Frixione, P. Nason, and C. Oleari, “Matching NLO QCD computations with parton shower simulations: the POWHEG method”, *JHEP* **11** (2007) 070, `doi:10.1088/1126-6708/2007/11/070`, `arXiv:0709.2092`.

[109] S. Alioli, P. Nason, C. Oleari, and E. Re, “A general framework for implementing NLO calculations in shower Monte Carlo programs: the POWHEG BOX”, *JHEP* **06** (2010) 043, `doi:10.1007/JHEP06(2010)043`, `arXiv:1002.2581`.

[110] J. M. Campbell, R. K. Ellis, P. Nason, and E. Re, “Top-pair production and decay at NLO matched with parton showers”, *JHEP* **04** (2015) 114, `doi:10.1007/JHEP04(2015)114`, `arXiv:1412.1828`.

[111] J. Alwall et al., “The automated computation of tree-level and next-to-leading order differential cross sections, and their matching to parton shower simulations”, *JHEP* **07** (2014) 079, `doi:10.1007/JHEP07(2014)079`, `arXiv:1405.0301`.

[112] J. Alwall et al., “Comparative study of various algorithms for the merging of parton showers and matrix elements in hadronic collisions”, *Eur. Phys. J.* **C53** (2008) 473–500, `doi:10.1140/epjc/s10052-007-0490-5`, `arXiv:0706.2569`.

[113] NNPDF Collaboration, “Parton distributions for the LHC Run II”, *JHEP* **04** (2015) 040, `doi:10.1007/JHEP04(2015)040`, `arXiv:1410.8849`.

[114] T. Sjöstrand, S. Mrenna, and P. Z. Skands, "A Brief Introduction to PYTHIA 8.1", *Comput. Phys. Commun.* **178** (2008) 852, `doi:10.1016/j.cpc.2008.01.036`, `arXiv:0710.3820`.

[115] P. Skands, "Pythia and Colour Reconnection(s)", Open meeting of the LHCtopWG, 2019. `https://indico.cern.ch/event/843509/timetable/#18-pythia-and-colour-reconnect`.

[116] J. R. Christiansen and P. Z. Skands, "String formation beyond leading colour", *JHEP* **08** (2015) 003, `doi:10.1007/JHEP08(2015)003`, `arXiv:1505.01681`.

[117] S. Argyropoulos and T. Sjöstrand, "Effects of color reconnection on $t\bar{t}$ final states at the LHC", *JHEP* **11** (2014) 043, `doi:10.1007/JHEP11(2014)043`, `arXiv:1407.6653`.

[118] M. Bähr et al., "Herwig++ physics and manual", *Eur. Phys. J. C* **58** (2008) 639, `doi:10.1140/epjc/s10052-008-0798-9`, `arXiv:0803.0883`.

[119] S. Gieseke, P. Kirchgaeßer, S. Plätzer, and A. Siodmok, "Colour Reconnection from Soft Gluon Evolution", *JHEP* **11** (2018) 149, `doi:10.1007/JHEP11(2018)149`, `arXiv:1808.06770`.

[120] GEANT4 Collaboration, "GEANT4—a simulation toolkit", *Nucl. Instrum. Meth. A* **506** (2003) 250, `doi:10.1016/S0168-9002(03)01368-8`.

[121] CMS Collaboration, "Jet Identification for the 13 TeV data Run2016", `https://twiki.cern.ch/twiki/bin/view/CMS/JetID13TeVRun2016?rev=7#Recommendations_for_the_13_TeV_d`.

[122] P. Skands, S. Carrazza, and J. Rojo, "Tuning PYTHIA 8.1: the Monash 2013 Tune", *Eur. Phys. J. C* **74** (2014) 3024, `doi:10.1140/epjc/s10052-014-3024-y`, `arXiv:1404.5630`.

[123] CMS Collaboration, "Investigations of the impact of the parton shower tuning in PYTHIA 8 in the modelling of $\mathrm{t\bar{t}}$ at $\sqrt{s} = 8$ and 13 TeV", CMS Physics Analysis Summary CMS-PAS-TOP-16-021, 2016.

[124] M. Czakon, P. Fiedler, and A. Mitov, "Total Top-Quark Pair-Production Cross Section at Hadron Colliders Through $O(\alpha\frac{4}{S})$", *Phys. Rev. Lett.* **110** (2013) 252004, `doi:10.1103/PhysRevLett.110.252004`, `arXiv:1303.6254`.

[125] ATLAS and CMS Collaborations, "NNLO+NNLL top-quark-pair cross sections, ATLAS-CMS recommended predictions for top-quark-pair cross sections using the Top++v2.0 program", `https://twiki.cern.ch/twiki/bin/view/LHCPhysics/TtbarNNLO?rev=16`.

[126] CMS Collaboration, "Methods to apply b-tagging efficiency scale factors", `https://twiki.cern.ch/twiki/bin/view/CMS/BTagSFMethods?rev=27`.

[127] CMS Collaboration, "Usage of b/c Tag Objects for 13 TeV Data in 2016 and 80X MC", `https://twiki.cern.ch/twiki/bin/view/CMS/BtagRecommendation80XReReco?rev=14`.

[128] J. D'Hondt et al., "Fitting of event topologies with external kinematic constraints in CMS", CMS NOTE 2006/023, 2006.

[129] "Jet resolution functions for the kinematic fit", `https://github.com/cms-sw/cmssw/blob/CMSSW_8_0_X/TopQuarkAnalysis/TopObjectResolutions/python/stringResolutions_etEtaPhi_Fall11_cff.py`.

[130] DELPHI Collaboration, "Measurement of the mass and width of the W boson in e^+e^- collisions at $\sqrt{s} = 161 - 209$ GeV", *Eur. Phys. J. C* **55** (2008) 1, `doi:10.1140/epjc/s10052-008-0585-7`, `arXiv:0803.2534`.

[131] D0 Collaboration, "Measurement of the top quark mass in the lepton + jets channel using the ideogram method", *Phys. Rev. D* **75** (2007) 092001, `doi:10.1103/PhysRevD.75.092001`, `arXiv:hep-ex/0702018`.

[132] CDF Collaboration, "Measurement of the top-quark mass in all-hadronic decays in $p\bar{p}$ collisions at CDF II", *Phys. Rev. Lett.* **98** (2007) 142001, `doi:10.1103/PhysRevLett.98.142001`, `arXiv:hep-ex/0612026`.

[133] CMS Collaboration, "Measurement of the top-quark mass in $t\bar{t}$ events with lepton+jets final states in pp collisions at $\sqrt{s} = 7$ TeV", *JHEP* **12** (2012) 105, `doi:10.1007/JHEP12(2012)105`, `arXiv:1209.2319`.

[134] M. Seidel, "Measurement of Top Quark Mass and Jet Energy Scale at the CMS Experiment using the Ideogram Method", Diploma thesis, U. Hamburg, Dept. Phys., Hamburg, 2011.

[135] E. Schlieckau, "Measurement of Top-Quark Mass and Inclusive Top-Quark-Pair Production Cross Section in pp Collisions at $\sqrt{s} = 7/8$ TeV with CMS", PhD thesis, DESY-THESIS-2014-024, CERN-THESIS-2014-109, Universität Hamburg, Hamburg, 2014.

[136] M. Seidel, "Precise measurement of the top-quark mass at the CMS experiment using the ideogram method", PhD thesis, U. Hamburg, Dept. Phys., Hamburg, 2015.

[137] C. Garbers, "Measurement of the Top Quark Mass in the Muon+Jets Final State at $\sqrt{s}$=13 TeV", Master thesis, U. Hamburg, Dept. Phys., Hamburg, 2016.

[138] N. Kovalchuk, "Top quark mass measurement and color effects at the LHC", PhD Thesis DESY-THESIS-2018-007, U. Hamburg, Dept. Phys., Hamburg, 2018. `doi:10.3204/PUBDB-2018-01620`.

[139] W. Verkerke and D. P. Kirkby, "The RooFit toolkit for data modeling", *eConf* **C0303241** (2003) MOLT007, `arXiv:physics/0306116`.

[140] CMS Collaboration, "Jet energy scale uncertainty sources", `https://twiki.cern.ch/twiki/bin/view/CMS/JECUncertaintySources?rev=51`.

[141] ATLAS and CMS Collaborations, "Jet energy scale uncertainty correlations between ATLAS and CMS at 8 TeV", ATL-PHYS-PUB-2015-049, CMS-PAS-JME-15-001, 2015.

[142] A. Karavdina, J. Lange, and H. Stadie, "JER SFs uncertainty for 2016 top mass measurements", Jet Energy Corrections and Resolution Meeting, 2018. `https://indico.cern.ch/event/744309/#2-jer-sfs-uncertainty-for-2016`.

[143] CMS Collaboration, "Measurement of the inelastic proton-proton cross section at $\sqrt{s} = 13$ TeV", *JHEP* **07** (2018) 161, `doi:10.1007/JHEP07(2018)161`, `arXiv:1802.02613`.

[144] T. Sjöstrand, S. Mrenna, and P. Skands, "PYTHIA 6.4 physics and manual", *JHEP* **05** (2006) 026, `doi:10.1088/1126-6708/2006/05/026`, `arXiv:hep-ph/0603175`.

[145] ALEPH Collaboration, "Study of the fragmentation of b quarks into B mesons at the Z peak", *Phys. Lett. B* **512** (2001) 30, `doi:10.1016/S0370-2693(01)00690-6`, `arXiv:hep-ex/0106051`.

[146] DELPHI Collaboration, "A study of the b-quark fragmentation function with the DELPHI detector at LEP I and an averaged distribution obtained at the Z Pole", *Eur. Phys. J. C* **71** (2011) 1557, `doi:10.1140/epjc/s10052-011-1557-x`, `arXiv:1102.4748`.

[147] Particle Data Group, "Review of particle physics", *Chin. Phys. C* **40** (2016) 100001, `doi:10.1088/1674-1137/40/10/100001`.

[148] M. Czakon, D. Heymes, and A. Mitov, "High-precision differential predictions for top-quark pairs at the LHC", *Phys. Rev. Lett.* **116** (2016) 082003, `doi:10.1103/PhysRevLett.116.082003`, `arXiv:1511.00549`.

[149] CMS Collaboration, "Measurement of differential cross sections for top quark pair production using the lepton+jets final state in proton-proton collisions at 13 TeV", *Phys. Rev. D* **95** (2017) 092001, `doi:10.1103/PhysRevD.95.092001`, `arXiv:1610.04191`.

[150] CMS Collaboration, "Measurement of normalized differential $\mathrm{t}\bar{\mathrm{t}}$ cross sections in the dilepton channel from pp collisions at $\sqrt{s} = 13$ TeV", *JHEP* **04** (2018) 060, `doi:10.1007/JHEP04(2018)060`, `arXiv:1708.07638`.

[151] J. Heinrich and L. Lyons, "Systematic errors", *Ann. Rev. Nucl. Part. Sci.* **57** (2007) 145, `doi:10.1146/annurev.nucl.57.090506.123052`.

[152] R. Frederix and S. Frixione, "Merging meets matching in MC@NLO", *JHEP* **12** (2012) 061, `doi:10.1007/JHEP12(2012)061`, `arXiv:1209.6215`.

[153] N. Kovalchuk et al., "Measurement of the top-quark mass in $\mathrm{t}\bar{\mathrm{t}}$ events with lepton+jets final states in pp collisions at $\sqrt{s} = 13$ TeV using 2016 data", CMS Analysis Note CMS AN-2016/327 [CMS internal], 2016.

[154] N. Kovalchuk et al., "Top quark mass from ttbar lepton+jets 2016 data", CMS CADI entry TOP-17-007 [CMS internal].

[155] J. Lange et al., "Top quark mass from ttbar fully hadronic 2016 data", CMS CADI entry TOP-17-008 [CMS internal].

[156] D0 Collaboration, "Direct measurement of the top quark mass at D0", *Phys. Rev. D* **58** (1998) 052001, `doi:10.1103/PhysRevD.58.052001`, `arXiv:hep-ex/9801025`.

[157] L. Lyons, D. Gibaut, and P. Clifford, "How to Combine Correlated Estimates of a Single Physical Quantity", *Nucl. Instrum. Meth. A* **270** (1988) 110, `doi:10.1016/0168-9002(88)90018-6`.

[158] A. Valassi, "Combining correlated measurements of several different physical quantities", *Nucl. Instrum. Meth. A* **500** (2003) 391, `doi:10.1016/S0168-9002(03)00329-2`.

[159] ATLAS, CDF, CMS, D0 Collaboration, "First combination of Tevatron and LHC measurements of the top-quark mass", `arXiv:1403.4427`.

[160] "blue_combine: Python package for the Best Linear Unbiased Estimate (BLUE) method", `https://github.com/jolange/BLUE-py`.

[161] ATLAS Collaboration, "Measurement of the W-boson mass in pp collisions at $\sqrt{s} = 7$ TeV with the ATLAS detector", *Eur. Phys. J. C* **78** (2018) 110, `doi:10.1140/epjc/s10052-018-6354-3,10.1140/epjc/s10052-017-5475-4`, `arXiv:1701.07240`. [Erratum: *Eur. Phys. J. C* **78** (2018) 898].

[162] Tevatron Electroweak Working Group, "2012 Update of the Combination of CDF and D0 Results for the Mass of the W Boson", `arXiv:1204.0042`.

[163] LEP Electroweak Working Group, "Electroweak Measurements in Electron-Positron Collisions at W-Boson-Pair Energies at LEP", *Phys. Rept.* **532** (2013) 119, `doi:10.1016/j.physrep.2013.07.004`, `arXiv:1302.3415`.

[164] D0 Collaboration, "Precise measurement of the top-quark mass from lepton+jets events at D0", *Phys. Rev. D* **84** (2011) 032004, `doi:10.1103/PhysRevD.84.032004`, `arXiv:1105.6287`.

[165] T. Makela and M. Voutilainen, "Reproducing the D0 b-JES", Open meeting of the LHCtopWG, 2018. `https://indico.cern.ch/event/746611/timetable/#5-studies-of-the-d0-b-jet-cali`.

[166] CMS Collaboration, "Determination of the top-quark mass from the m(lb) distribution in dileptonic ttbar events at sqrt(s) = 8 TeV", CMS Physics Analysis Summary CMS-PAS-TOP-14-014, 2014.

[167] CMS Collaboration, "Measurement of the top quark mass using charged particles in pp collisions at $\sqrt{s} = 8$ TeV", *Phys. Rev. D* **93** (2016) 092006, `doi:10.1103/PhysRevD.93.092006`, `arXiv:1603.06536`.

[168] CMS Collaboration, "Measurement of the mass of the top quark in decays with a J/ψ meson in pp collisions at 8 TeV", *JHEP* **12** (2016) 123, `doi:10.1007/JHEP12(2016)123`, `arXiv:1608.03560`.

[169] ATLAS Collaboration, "Measurement of the top quark mass using a leptonic invariant mass in pp collisions at $sqrts = 13$ TeV with the ATLAS detector", ATLAS Conferernce Note ATLAS-CONF-2019-046, CERN, 2019.

[170] W. T. Giele, D. A. Kosower, and P. Z. Skands, "Higher-Order Corrections to Timelike Jets", *Phys. Rev. D* **84** (2011) 054003, `doi:10.1103/PhysRevD.84.054003`, `arXiv:1102.2126`.

[171] S. Mrenna and P. Skands, "Automated Parton-Shower Variations in Pythia 8", *Phys. Rev. D* **94** (2016) 074005, `doi:10.1103/PhysRevD.94.074005`, `arXiv:1605.08352`.

[172] C. Garbers, PhD thesis, U. Hamburg, Dept. Phys., Hamburg, *Expected to be completed in 2020*.

[173] C. Garbers, J. Lange, P. Schleper, and H. Stadie, "A profiled likelihood approach to measure the top quark mass", CMS Analysis Note CMS AN-2019/284 [CMS internal], 2019 *(work in progress)*.

[174] T. Lange, "Applications of Deep Neural Networks in a Top Quark Mass Measurement at the LHC", Master thesis CMS-TS-2018-004, CERN-THESIS-2018-065, U. Hamburg, Dept. Phys., Hamburg, 2018.

[175] H. Stadie, C. Garbers, J. Lange, and P. Schleper, "A profiled likelihood approach to measure the top quark mass", CMS Analysis Note CMS AN-2018/261 v2 [CMS internal], 2018.

[176] P. S. Wells, "Experimental tests of the standard model", *Eur. Phys. J. C* **33** (2004) 5, `doi:10.1140/epjcd/s2004-03-1692-8`.

List of Figures

List of Tables

Eidesstattliche Versicherung / Declaration on oath

Hiermit versichere ich an Eides statt, die vorliegende Dissertationsschrift selbst verfasst und keine anderen als die angegebenen Hilfsmittel und Quellen benutzt zu haben. Die eingereichte schriftliche Fassung entspricht der auf dem elektronischen Speichermedium.

Die Dissertation wurde in der vorgelegten oder einer ähnlichen Form nicht schon einmal in einem früheren Promotionsverfahren angenommen oder als ungenügend beurteilt.

Hamburg, den ________________

____
Johannes Lange